PHD

LOW-COORDINATE Ni(I) COMPLEXES FOR MAGNETIC APPLICATIONS

Blackaby, Will

Award date:
2020

Awarding institution:
University of Bath

LOW-COORDINATE Ni(I) COMPLEXES FOR MAGNETIC APPLICATIONS

William John Mark Blackaby

A thesis submitted in partial fulfilment of the requirements for the degree of

Doctor of Philosophy

University of Bath

Department of Chemistry

September 2019

Signed…… Date……

CONTENTS

ACKNOWLEDGMENTS

Firstly, I would like to thank the boss, Professor Mike Whittlesey, for allowing me the opportunity to work in his lab, along the well-trodden path of MChem student turning to PhD student. I am grateful for Mike's enthusiasm for research, the support, and reading through countless drafts. I have learnt so much from working with Mike, and go forward with the simple (but effective) mantra - JFDI…

I have been fortunate enough to work with brilliant post-docs Drs Ian Riddlestone, (Lady) Sara Sabater, Maia Espinal, and Fedor Miloserdov, as well as excellent PhD students Lee Collins, Mat Cybulski, Jon Hall, and Connie Isaac, who have all been a pleasure to work and socialise with over the last four years.

I would also like to thank various collaborators from the department at Bath; Dr Mary Mahon for all things related to X-ray diffraction, Dr John Lowe for NMR spectroscopy (and baked goods), Dr Vera Krewald and Dr Elizaveta Suturina for the computational work, and Professor Frank Marken for help with setting up, running, and analysing the cyclic voltammetry. Many thanks to the collaborators from further afield; Professor Damien Murphy, Dr Emma Richards, and Dr Andrea Folli from the University of Cardiff for running EPR spectroscopy, Professor Stuart Macgregor and Sam Neale from Heriot-Watt University for performing calculations on the hydrophosphination catalysis, Professor Stephen Hill and Dr Sam Greer from the National High Magnetic Field Laboratory in Tallahassee for the FTIR and high-field EPR, and Professor Muralee Murugesu, Katie Harriman and the whole Murugesu group from the University of Ottawa for introducing me to the joys of SQUID magnetometry and for all the help during my secondment to Canada.

Finally, I would like to thank my loved ones. To Poppy, and my wonderful parents, I am so grateful for your continued love and support.

ABSTRACT

This thesis describes the synthesis and characterisation of a range of two- and three-coordinate mono- and dinuclear Ni(I) complexes featuring six- and seven-membered ring-expanded N-heterocyclic carbene (RE-NHC) ligands, and examines their reactivity, electronic structure, and magnetic properties.

A series of trigonal planar three-coordinate Ni(RE-NHC)(PPh_3)Br compounds bearing N-aryl and N-alkyl six- and seven-membered RE-NHCs were prepared *via* the comproportionation of Ni(COD)$_2$ and Ni(PPh_3)$_2$Br$_2$ in the presence of the free RE-NHC. The reactivity of Ni(6Mes)(PPh_3)Br with halide abstracting agents gave T-shaped [Ni(6Mes)(PPh_3)(THF)]PF_6 and the mono-bromide bridged dimer [{Ni(6Mes)(PPh_3)}$_2$(μ-Br)]BAr^F_4, both of which reacted with CO to form T-shaped [Ni(6Mes)(PPh_3)(CO)]$^+$. The use of an alternative synthetic route led to the formation of Ni(RE-NHC)(PCy_3)Br compounds. Through use of EPR spectroscopy and DFT calculations, the geometry of the three-coordinate Ni(I) complexes was shown to be determined by electronic effects rather than sterics, whereby a change in the *d*-orbital character of the SOMO caused a change in the observed g_2 values and structural geometries.

The three-coordinate Ni(I) compounds were used as precursors to form linear two-coordinate *bis*-NHC complexes, either the homoleptic [Ni(RE-NHC)$_2$]Br species, or heteroleptic [Ni(RE-NHC)(NHC')]Br derivatives. Solution magnetic moment measurements gave values larger than those expected for a d^9 ion. These unusual data were validated by SQUID analysis, which revealed room temperature magnetic susceptibilities larger than the predicted spin-only value. Computational studies predicted the electronic structure of linear Ni(I) complexes to have a low-lying excited state and two degenerate orbitals making up the HOMO. This orbital arrangement leads to unquenched orbital angular momentum, resulting in magnetic anisotropy and the large observed magnetic moment and susceptibility values, suggestive of single ion magnet (SIM) behaviour. The dynamic magnetic properties of the homoleptic and heteroleptic species were investigated with SQUID measurements. In all cases, field-induced slow magnetic relaxation was observed, and relaxation times were used to derive parameters for Orbach, Raman, direct, and quantum tunnelling of magnetisation (QTM) relaxation mechanisms.

Two-coordinate species of type $[Ni(RE\text{-}NHC)(PCy_3)]^+$ were formed by halide abstraction from $Ni(RE\text{-}NHC)(PCy_3)Br$. The reactivity of the two-coordinate species was probed through the addition of P^tBu_3 (leading to PCy_3 substitution), and CO, which formed T-shaped Ni(I)-carbonyl compounds. Cyclic voltammetry on $[Ni(RE\text{-}NHC)(PR_3)]^+$ showed irreversible oxidation and reduction waves, while magnetic moment measurements suggested magnetic anisotropy of the Ni(I) ion. SQUID analysis again revealed SIM behaviour, although the spin reversal barrier was lower than those in the *bis*-NHC complexes.

During investigations into Ni-NHC catalysed hydrophosphination of alkynes with secondary phosphines, it emerged that the NHCs themselves were able to perform catalysis in the absence of a metal with excellent conversions. DFT calculations provided a mechanism whereby the NHC acts as a Brønsted base to afford an imidazolium phosphide, which then undergoes nucleophilic attack at the terminal alkyne carbon. Extension of the study to the use of cyclic(alkyl)(amino)carbenes (CAAC) showed dependence of catalytic activity on substituent size, the smaller diethyl substituted CAAC proving inactive in contrast to bulkier analogues which displayed excellent activity.

ABBREVIATIONS

Analytical

$\%V_{bur}$	Percentage buried volume
A	Superhyperfine coupling constant
ac	Alternating current
B	Magnetic flux density
br	Broad
ca.	Circa
CASSCF	Complete active space self-consistent field
CV	Cyclic voltammetry
CW EPR	Continuous wave electron paramagnetic resonance
d	Doublet
D	Diffusion coefficient
D	Axial zero-field splitting parameter
dc	Direct current
DFT	Density functional theory
E	Transverse/rhombic zero-field splitting parameter
E_p	Potential voltage
E_p^{ox}	Oxidation voltage
EPR	Electron paramagnetic resonance
E_p^{red}	Reduction voltage
equiv.	Equivalents
ESI-MS	Electrospray ionisation mass spectrometry
ESI-TOF	Electrospray ionisation time-of-flight
FT	Fourier transform
g	*g* factor in EPR
g_e	Free electron spin *g* value
H	External reverse magnetic field
HEP	Huynh's electronic parameter
HF	High field
HOMO	Highest occupied molecular orbital
HPLC	High performance liquid chromatography

I	Current
i-	*Ipso*-
I_p^{ox}	Oxidation current
I_p^{red}	Reduction current
IR	Infrared
J	Exchange coupling constant
k_B	Boltzmann constant
LF	Low field
LUMO	Lowest unoccupied molecular orbital
m	Multiplet
M	Magnetisation in SQUID data
m-	*Meta*-
MO	Molecular orbital
M_S	Magnetisation saturation
NBO	Natural bond order
${}^{n}J_{XY}$	Coupling constant of X to Y across n bonds
NMR	Nuclear magnetic resonance
o-	*Ortho*-
p-	*Para*-
PCS	Pseudocontact shift
$p\mathrm{K_a}$	$-\log_{10}$ of the acid dissociation constant ($\mathrm{K_a}$)
q	Quartet
QTM	Quantum tunnelling of magnetisation
quin	Quintet
s	Singlet
sept	Septet
SIM	Single ion magnet
SMM	Single molecular magnet
SOMO	Singly occupied molecular orbital
SQUID	Superconducting quantum interference device
t	Triplet
t	Time
T	Temperature

T_B	Blocking temperature
TEP	Tolman electronic parameter
U_{eff}	Effective energy barrier
ZFS	Zero-field splitting
α	Distribution of relaxation times
δ	NMR chemical shift
ν	Frequency
τ	Relaxation time
χ'	In-phase component of the magnetic susceptibility
χ''	Out-of-phase component of the magnetic susceptibility
χ_S	Isothermal magnetic susceptibility
χ_T	Adiabatic magnetic susceptibility
χT	Molar susceptibility per molecule defined as M/H (magnetic susceptibility) at temperature T

Units

%	Percentage
°	Degree
µA	Microamp
μ_B	Bohr magneton
µL	Microlitre
A	Amp
Å	Ångström
atm	Atmosphere
cm^{-1}	Wavenumber
e^-	Electron
eV	Electron volt
g	Gram
GHz	Gigahertz
hr	Hour
Hz	Hertz
K	Kelvin
kcal	Kilocalorie

m	Metre
M	Molar concentration
m/z	Mass-to-charge ratio
mg	Milligram
MHz	Megahertz
min	Minute
mL	Millilitre
mM	Millimolar
mm	Millimetre
mmol	Millimole
mol	Mole
mT	Millitesla
Oe	Oersted
ppm	Parts per million
s	Second
T	Tesla
V	Volt
W	Watt

Chemical

μ-L	Bridging ligand L
18-crown-6	1,4,7,10,13,16-hexaoxacyclooctadecane
2.2.2-crypt	4,7,13,16,21,24-hexaoxa-1,10-diazabicyclo[8.8.8]hexacosane
5MesDAC	1,3-*bis*(2,4,6-trimethylphenyl)-4,5-diketoimidazol-2-ylidene
6Cy	1,3-*bis*(cyclohexyl)-3,4,5,6-tetrahydropyrimid-2-ylidene
6Et	1,3-*bis*(diethyl)-3,4,5,6-tetrahydropyrimid-2-ylidene
6^{i}Bu	1,3-*bis*(isobutyl)-3,4,5,6-tetrahydropyrimid-2-ylidene
6^{i}Pr	1,3-*bis*(isopropyl)-3,4,5,6-tetrahydropyrimid-2-ylidene
6Mes	1,3-*bis*(2,4,6-trimethylphenyl)-3,4,5,6-tetrahydropyrimid-2-ylidene
6MesDAC	1,3-*bis*(2,4,6-trimethylphenyl)-4,6-diketo-5,5-dimethylpyrimidin-2-ylidene

6^{m}Xyl	1,3-*bis*(3,5-dimethylphenyl)-3,4,5,6-tetrahydropyrimid-2-ylidene
6^{n}Pent	1,3-*bis*(neopentyl)-3,4,5,6-tetrahydropyrimid-2-ylidene
6^{o}Tol	1,3-*bis*(2-methylphenyl)-3,4,5,6-tetrahydropyrimid-2-ylidene
6^{t}Bu	1,3-*bis*(*tert*-butyl)-3,4,5,6-tetrahydropyrimid-2-ylidene
6Xyl	1,3-*bis*(2,6-dimethylphenyl)-3,4,5,6-tetrahydropyrimid-2-ylidene
6Xyl-*p*-Br	1,3-*bis*(4-bromo-2,6-dimethylphenyl)-3,4,5,6-tetrahydropyrimid-2-ylidene
7^{i}Bu	1,3-*bis*(isobutyl)-4,5,6,7-tetrahydro-[1,3]-diazepin-2-ylidene
7Mes	1,3-*bis*(2,4,6-trimethylphenyl)-4,5,6,7-tetrahydro-[1,3]-diazepin-2-ylidene
7MesDAC	1,3-*bis*(2,4,6-trimethylphenyl)-4,7-diketobenzo[e][1,3]diazepin-2-ylidene
7^{m}Xyl	1,3-*bis*(3,5-dimethylphenyl)-4,5,6,7-tetrahydro-[1,3]-diazepin-2-ylidene
7^{n}Pent	1,3-*bis*(neopentyl)-4,5,6,7-tetrahydro-[1,3]-diazepin-2-ylidene
7^{o}Tol	1,3-*bis*(2-methylphenyl)-4,5,6,7-tetrahydro-[1,3]-diazepin-2-ylidene
7Xyl	1,3-*bis*(2,6-dimethylphenyl)-4,5,6,7-tetrahydro-[1,3]-diazepin-2-ylidene
7Xyl-*p*-Br	1,3-*bis*(4-bromo-2,6-dimethylphenyl)-4,5,6,7-tetrahydro-[1,3]-diazepin-2-ylidene
Ad	1-adamantyl
Ar	Aryl group
asym-PhobP^{t}Bu	(1R,6S,9R)-9-(*tert*-butyl)-9-phosphabicyclo[4.2.1]nonane
BAr$^{F}{}_{4}$	Tetrakis(3,5-*bis*(trifluoromethyl)phenyl)borate
CAAC	Cyclic(alkyl)(amino)carbene
Cg-P^{t}Bu	(1S,3R,5R,7S)-8-(*tert*-butyl)-1,3,5,7-tetramethyl-2,4,6-trioxa-8-phosphaadamantane
CN	Cyano/Nitrile
COD	Cycloocta-1,5-diene
Cp	Cyclopentadienyl

Cp*	1,2,3,4,5-pentamethylcyclopentadienyl
Cy	Cyclohexyl
$^{Cyt\mathrm{Bu}}$CAAC	1-[(2,6-Diisopropyl)phenyl]-3-(4-*tert*-butylcyclohexyl)-5,5-dimethyl-2-pyrrolidinylidene
DAC	Diamidocarbene
DIPP	Diisopropylphenyl
dme	Dimethoxyethane
DMSO-d_6	Deuterated dimethylsulfoxide
E	Generic heteroatom
^{Et2}CAAC	1-[(2,6-Diisopropyl)phenyl]-3,3-diethyl-5,5-dimethyl-2-pyrrolidinylidene
HBPin	Pinacolborane
IAd	1,3-diadamantylimidazol-2-ylidene
^{i}Bu	Isobutyl
ICy	1,3-dicyclohexylimidazol-2-ylidene
IEt$_2$Me$_2$	1,3-diethyl-4,5-dimethylimidazol-2-ylidene
I^{i}Pr$_2$	1,3-diisopropylimidazol-2-ylidene
I^{i}Pr$_2$Me$_2$	1,3-diisopropyl-4,5-dimethylimidazol-2-ylidene
IMe$_2$	1,3-dimethylimidazol-2-ylidene
IMe$_4$	1,3,4,5-tetramethylimidazol-2-ylidene
IMes	1,3-*bis*(2,4,6-trimethylphenyl)imidazol-2-ylidene
IMes^{Cl2}	4,5-dichloro-1,3-*bis*(2,4,6-trimethylphenyl)imidazol-2-ylidene
IMes^{Me2}	4,5-dimethyl-1,3-*bis*(2,4,6-trimethylphenyl)imidazol-2-ylidene
Ind	Indenyl
IPh	1,3-diphenylimidazol-2-ylidene
IPr	1,3-*bis*(2,6-diisopropylphenyl)imidazol-2-ylidene
^{i}Pr	Isopropyl
I^{t}Bu	1,3-di-*tert*-butylimidazol-2-ylidene
L	Generic ligand
M	Metal
^{Me2}CAAC	1-[(2,6-Diisopropyl)phenyl]-3,3-dimethyl-5,5-dimethyl-2-pyrrolidinylidene

^{Menthyl}CAAC	1-[(2,6-Diisopropyl)phenyl]-3-(1-isopropyl-3-methylcyclohexyl)-5,5-dimethyl-2-pyrrolidinylidene
Mes	2,4,6-trimethylphenyl
Naph	Naphthalene
^{n}Bu	Normal butyl
NHC	N-heterocyclic carbene
^{n}Pent	Neopentyl
Py	Pyridyl group
R	Aryl or alkyl group
RE-NHC	Ring-expanded N-heterocyclic carbene
SIMes	1,3-*bis*(2,4,6-trimethylphenyl)imidazolin-2-ylidene
SIPh	1,3-diphenylimidazolin-2-ylidene
SIPr	1,3-*bis*(2,6-diisopropylphenyl)imidazolin-2-ylidene
SI^{t}Bu	1,3-di-*tert*-butylimidazolin-2-ylidene
sym-PhobP^{t}Bu	9-(*tert*-butyl)-9-phosphabicyclo[3.3.1]nonane
^{t}Bu	*Tert*-butyl
TIPP	Triisopropylphenyl
Tol	2-methylphenyl
X	Halide group
Xyl	2,6-dimethylphenyl
η^{n}-L	η binding mode of ligand L with n atoms
κ^{n}-L	κ binding mode of ligand L with n atoms

CHAPTER 1

1 INTRODUCTION

1.1 Nickel(I) Chemistry

Nickel chemistry covers a vast range of areas, with the use of a variety of ligands to form organometallic complexes with varying oxidation states, coordination numbers and geometries. As with most transition metals, nickel complexes are widely used for homogeneous catalytic processes.[1-6] The most common oxidation states found in nickel chemistry are Ni(0) or Ni(II) and, for many years, the Ni(I) state was considered to be unstable.[7] Recent rapid growth of the number of characterised Ni(I) examples has been driven by their relevance to catalysis and biological chemistry,[8-11] for example, in the active site of nickel based cofactor F_{430} from the enzyme methylcoenzyme M reductase (MCR) involved in the metabolism of bacteria,[12-16] or in acetyl coenzyme A synthase (ACS) which is used in conjunction with carbon monoxide dehydrogenase (CODH) for physiological carbon cycling (Figure 1.1).[17-19]

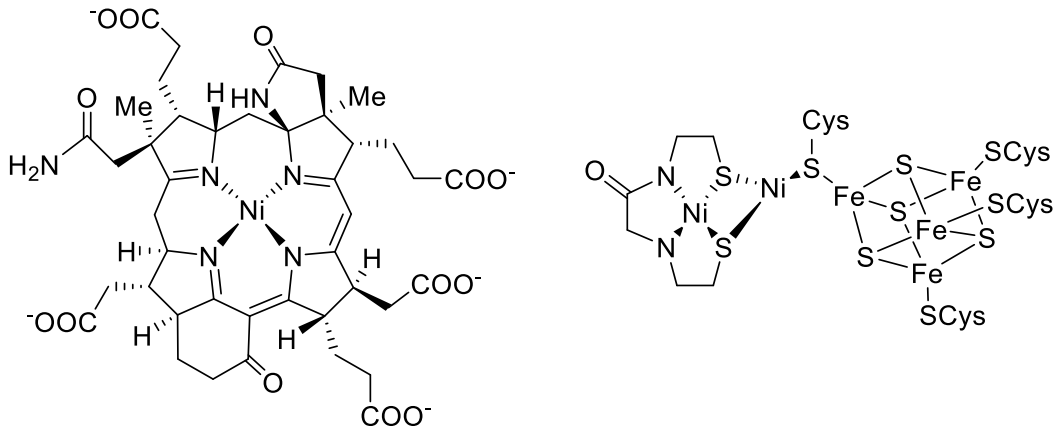

Figure 1.1 Cofactor F_{430} in the MCR enzyme active site (left) and the ACS active site (right).

In terms of organometallic chemistry, there is an interest in developing the chemistry of nickel complexes to replace the use of more expensive palladium and platinum catalysts, which inevitably led to investigations into the properties of Ni(I) species.[6, 20-22] The main routes to forming Ni(I) complexes involve the reduction or oxidation of Ni(II) and Ni(0) species respectively, the comproportionation of Ni(0) and Ni(II) complexes, or the spontaneous formation of a Ni(I) state due to the instability of a Ni(II) or Ni(0) starting precursor material.[23] Successfully isolated Ni(I) species often

contain, but are not limited to, bulky or bidentate phosphines,[24-35] or other chelating ligands such as *β*-diketiminates.[36-44]

Synthesis of the first Ni(I) species was reported by Bellucci in 1914, the so-called Bellucci's salt, a dimeric cyano compound $K_4[Ni_2(CN)_6]$ **i**, formed from the chemical reduction of $K_2[Ni(CN)_4]$ with sodium amalgam (Scheme 1.1).[45] Subsequent reports provided addition structural information about the salt through X-ray, IR, and Raman data,[46-52] however, the actual structure of the compound was confirmed by single crystal X-ray diffraction only in 1970.[53-55]

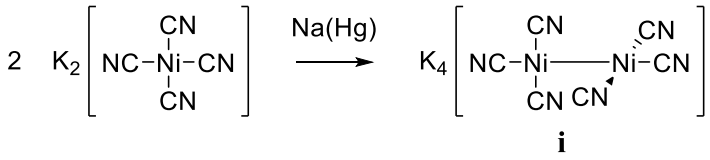

i

Scheme 1.1 Synthesis of first known Ni(I) species **i**.

The first report of a three-coordinate Ni(I) complex was in 1972 by Bradley *et al.* while studying the effects of using phosphines to stabilise nickel dialkylamide compounds.[56] Although the reaction between $Ni(PPh_3)_2Cl_2$ and $LiN(SiMe_3)_2$ did not produce the desired dialkylamide species, it did generate the novel three-coordinate trigonal planar *bis*-PPh_3 Ni(I) compound, $Ni(PPh_3)_2(N(SiMe_3)_2)$ **ii** (Scheme 1.2). Bradley reported subsequent Ni(I) species isolated from reactions of NiL_nCl_2 with $LiN(SiMe_3)_2$ to form the corresponding $NiL_n(N(SiMe_3)_2)$ (n = 2, L = PMe_2Ph, $PMePh_2$, PEt_2Ph, $PEtPh_2$, and PEt_3; n = 1, L = $Ph_2PCH_2CH_2PPh_2$) compounds. Compound **ii** had a magnetic moment of 1.9 μ_B, representing one unpaired electron and confirming the +1 oxidation state.

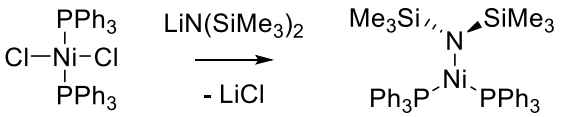

ii

Scheme 1.2 Synthesis of three-coordinate Ni(I) species **ii**.

Soon after, more examples of $Ni(PR_3)_2X$ species were reported, but they were characterised as either oligomers (R = Ph, X = Br, Cl),[57] or dimers with a square-planar geometry around the nickel (R = Cy, X = Br, Cl).[58] In 1964 Heimbach proposed that

$Ni(PPh_3)_2X$ species were formed during comproportionation reactions between $Ni(PPh_3)_2(C_2H_4)$ and $Ni(PPh_3)_2X_2$.[59] Four-coordinate $Ni(PPh_3)_3X$ derivatives were also reported in the same work, although structural characterisation of both the three- and four-coordinate species was not confirmed until much later; $Ni(PPh_3)_3Br$ in 1983,[60] $Ni(PPh_3)_3Cl$ and $Ni(PPh_3)_2Cl{\cdot}THF$ in 2000,[61] and $Ni(PPh_3)_2Cl$ in 2002.[62] Measurements run with a superconducting quantum interference device (SQUID) indicated that compound **ii** and $Ni(PPh_3)_2Cl{\cdot}THF$ displayed field induced slow magnetic relaxation and single ion magnet (SIM) behaviour (*vide infra*).[63]

Closely related $Ni(P^iPr_3)_2X$ (X = Cl, Br, I) compounds were reported to form *via* the same synthetic route proposed by Heimbach, with room temperature magnetic moments of 2.1 – 2.2 μ_B supporting the presence of one unpaired electron.[33] The trigonal planar compounds were found to be precursors to a Ni(0)-dinitrogen compound $[Ni(P^iPr_3)_2]_2(\mu\text{-}N_2)$, itself a useful synthon towards making a wide range of Ni(I) species through subsequent reaction with silanes, phosphines, and thiols.[33, 64]

Other examples of planar three-coordinate Ni(I) species were reported by Hillhouse *et al.*, by treatment of dimeric precursor $[Ni(dtbpe)(\mu\text{-}Cl)]_2$ **iii** with lithium alkyls, phosphides, anilides, and potassium silyls to afford a range of monomeric Ni(I) complexes (Scheme 1.3).[24-27, 31] In all cases, the Ni(I) alkyl, amido, silyl, and phosphido complexes were fully characterised by X-ray crystallography, EPR spectroscopy, and magnetic moment measurements, confirming the presence of an unpaired electron and a Ni(I) ion.

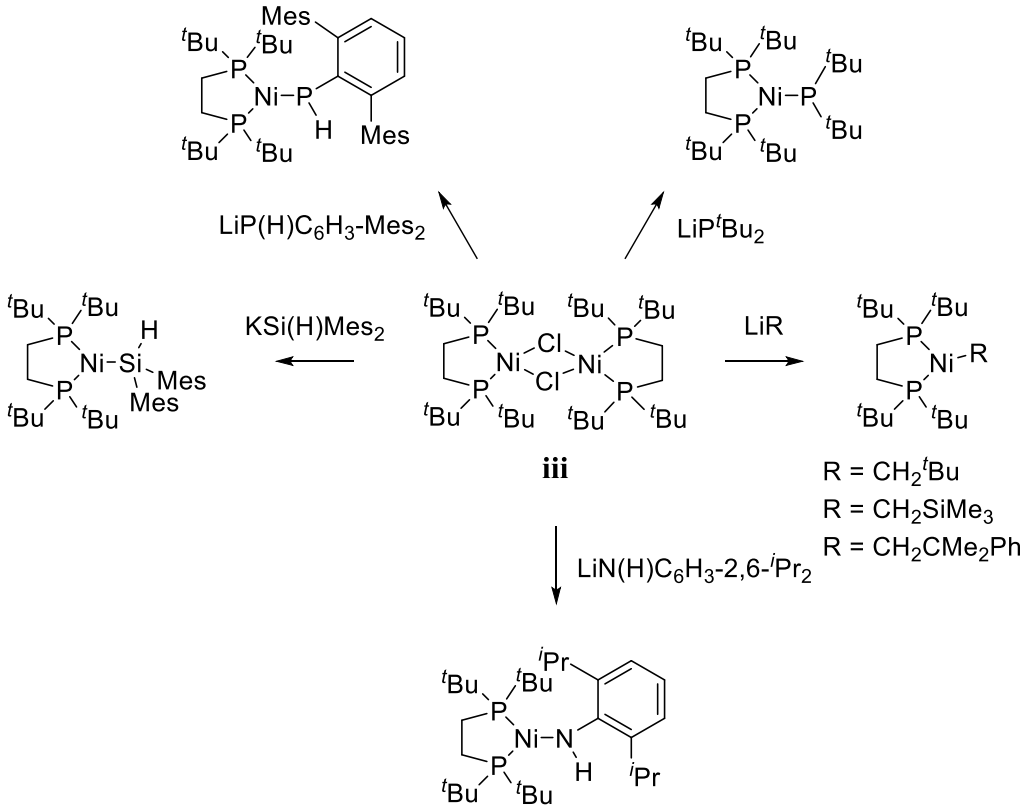

Scheme 1.3 Synthesis of a variety of Ni(I) species from dimer **iii**.

1.2 Carbenes

Carbenes are neutral organic species with six electrons in the valence shell of carbon, and either a singlet or triplet ground state (*vide infra*). They are divalent species with a wide array of substituents, ranging from simple hydrogen atoms (to afford methylene, CH_2), to large cyclic heteroatom-containing rings. As the carbenic carbon is not compliant with the octet rule, carbenes are considered electron deficient and hence highly reactive. The first reported attempt to form a carbene occurred in 1835 by Dumas, with efforts to prepare methylene by dehydration of methanol.[65] Work in the 1950s and 1960s by Doering and Fischer introduced carbenes to organic and organometallic chemistry,[66, 67] and research undertaken by Wanzlick and Breslow demonstrated an increase in carbene stability by having electron-donating atoms neighbouring the carbenic carbon.[68, 69] The first successful isolation of a stable carbene species was by Bertrand,[70] achieved by thermolysis of a (silyl)(phosphino)diazomethane precursor to produce the (silyl)(phosphino)carbene species **iv** (Scheme 1.4).

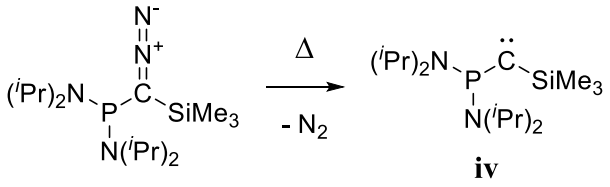

iv

Scheme 1.4 Synthesis of the first stable carbene **iv**.

The ground state configuration of the two non-bonding valence electrons of the carbon will affect the reactivity of the carbenic centre. In the case of a linear arrangement, the geometry implies an *sp*-hybridised carbene centre and the two electrons are located in two degenerate orbitals p_x and p_y (Figure 1.2). Upon bending of the molecule, the carbene centre becomes sp^2-hybridised and the degeneracy is broken, whereby the p_y remains unchanged (referred to as the p_π orbital due to being perpendicular to the plane of the carbene), and the p_x orbital is stabilised as it gains more *s* character (now called the σ orbital).[71] The ground state spin multiplicity of the carbene centre is determined by the energy gap between the σ and p_π orbitals.[72, 73] When the difference in energy between the orbitals was greater than 2.0 eV, both non-bonding electrons occupied the same orbital – either the σ (more stable) or p_π. This is known as the singlet state because the electrons are paired and total spin (S) = 0, therefore a multiplicity of 1 ($2S + 1 = 1$). When the energy gap falls below 1.5 eV, the electrons occupy different orbitals. This configuration is called the triplet state, as the unpaired electrons give a total spin (S) = 1 and a multiplicity of 3 ($2S + 1 = 3$).

The nature of the carbene substituents impacts on the energy gap between the frontier orbitals, which dictates the electron configuration and thus the observed geometry around the carbenic centre.

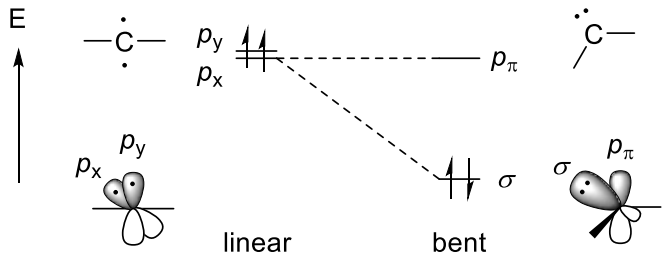

Figure 1.2 Difference in geometries and non-bonding frontier orbital energies of singlet and triplet carbenes.[71]

1.2.1 N-heterocyclic Carbenes

N-heterocyclic carbenes (NHCs) are a particular class of carbenes, most commonly with two nitrogen atoms adjacent to the carbenic carbon which forms part of a three- to eight-membered ring system. The N-substituents typically contain alkyl or aryl groups, allowing for control over the stereoelectronic properties.[74] As well as the carbenic centre and neighbouring nitrogen atoms, NHCs also contain a carbon backbone that can be either saturated (denoted with the prefix SI) or unsaturated (with the prefix I), as most frequently encountered in five-membered ring NHCs. Wanzlick was the first to attempt preparation of these nitrogen containing carbenes, when attempting to remove $HCCl_3$ from 1,3-diphenyl-2-(trichloromethyl)imidazolidine to produce SIPh **v** (Scheme 1.5).[75, 76] However, the monomeric NHC was in fact isolated as its dimeric form (**vi**). It was proposed that the carbene and dimer were in equilibrium, although later studies by two independent groups seemed to disprove the presence of such an equilibrium through dissociation reactions between mixtures of two different NHC species.[77, 78] A subsequent investigation did indeed show the presence of an equilibrium, forming mixed dimers when heating two different NHC dimer species above 373 K.[79] Wanzlick continued to study the N-phenyl system, and demonstrated the reaction of the imidazolium perchlorate salt $[IPhH]ClO_4$ with mercury(II) acetate to form one of the first known NHC - *d*-block metal compounds **vii** (Scheme 1.5).[80]

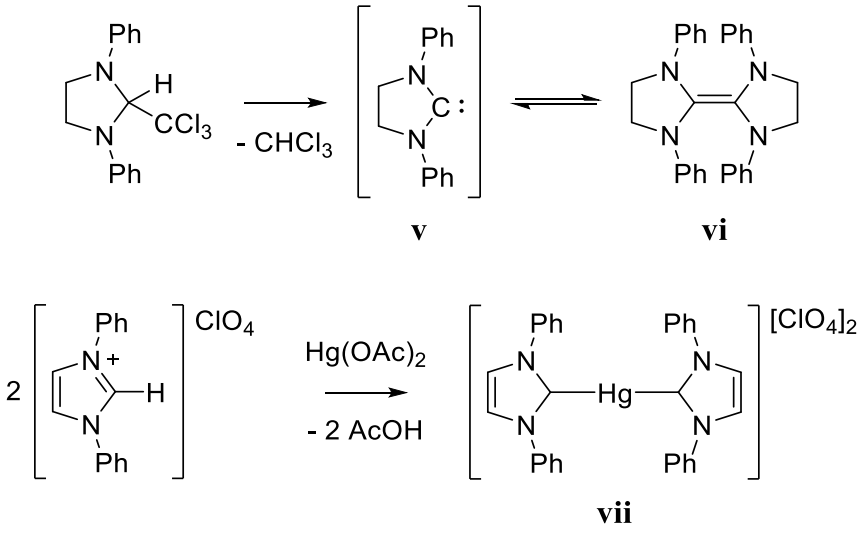

Scheme 1.5 First attempted isolation of NHC **v** (top), and synthesis of NHC-Hg(II) compound **vii** (bottom).

The first free stable NHC was isolated by Arduengo *et al*. with the deprotonation of the imidazolium salt [IAdH]Cl with NaH to form the singlet carbene IAd **viii** (Scheme 1.6).[81] The product was remarkably stable (in absence of air and water) and showed no decomposition up to 513 K, likely due to the bulky adamantyl groups preventing the formation of the corresponding dimer. Formation of the N-methyl substituted IMe_2 and IMe_4 species (the latter was also isolated) demonstrated that carbene stability was not dictated entirely by steric factors.[82] It was another six years before an air stable NHC was synthesised (also by Arduengo) with the reaction between IMes and CCl_4 in THF to form $IMes^{Cl2}$ **ix** (Scheme 1.6).[83]

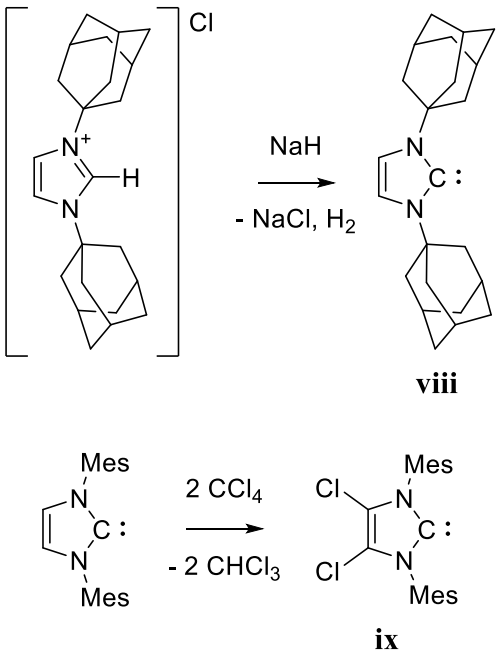

Scheme 1.6 Synthesis of the first stable, isolable NHC **viii** (top), and the first air and moisture stable NHC **ix** (bottom).

The thermodynamic stability of NHCs can be explained by the presence of two nitrogen atoms, which have the dual effect of inductive and mesomeric stabilisation. The inductive stabilisation arises from the fact that nitrogen is σ-electron withdrawing and this has a stabilising effect on the filled σ orbital (Figure 1.3, left). The mesomeric effect comes the π-electron donating ability of the nitrogen substituents, where the energy of the vacant p_π orbital is increased through interaction with the lone pair of electrons in a symmetrical combination of p orbitals, forming molecular orbitals b_1 and $p_\pi(b_1)$ (Figure

1.3, right). The combination of the inductive and mesomeric effects creates a large enough $\sigma - p_\pi$ gap (HOMO – LUMO gap) to stabilise the singlet ground state.

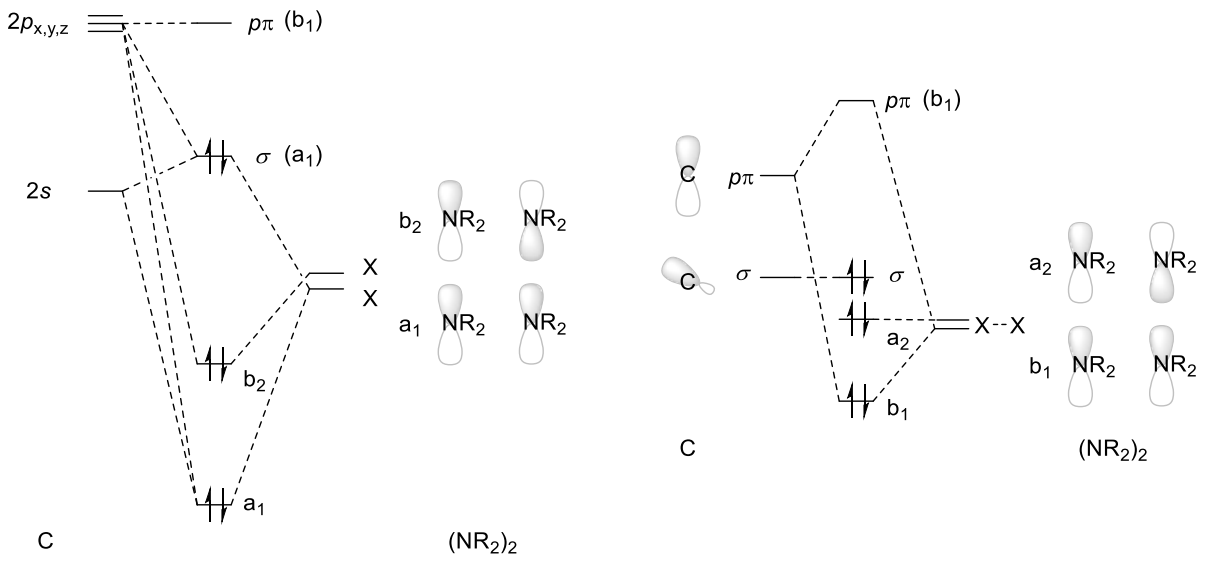

Figure 1.3 Molecular orbital diagram showing influence of the inductive effect of σ-donation (left) and the mesomeric effect of π-donation (right) arising from the neighbouring diamino groups.[71]

As well as increasing the energy of the p_π orbital, the π-donation from the nitrogen substituents creates a three-centre-four-electron bond where the N-C_{NHC} bond develops some partial multiple bond character. This enables NHCs to have multiple resonance forms, further enhancing the NHC stability (Figure 1.4).

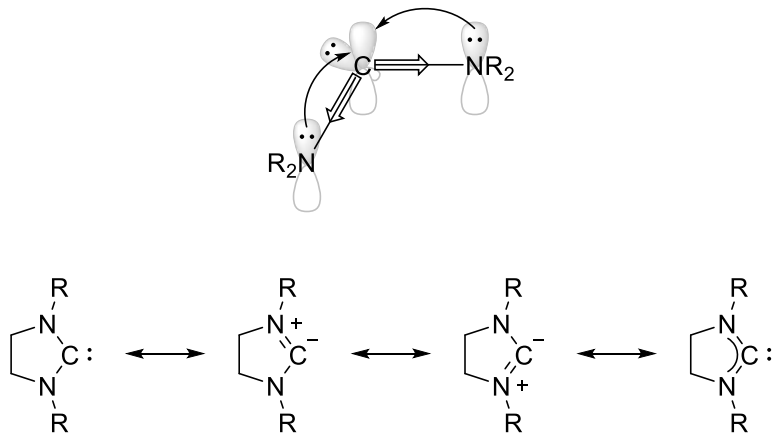

Figure 1.4 Electronic stabilisation of diamino substituents in NHCs, and resonance forms arising from the π-donation mesomeric effect.

NHCs are considered to be strong σ-donors, and are often compared to phosphines (also neutral, two electron σ-donors). They have been frequently used as ligands in transition metal organometallic complexes as replacements for their phosphine counterparts.[84] They are able to coordinate to a wide variety of transition metals and most commonly used in catalysis, where the improved nucleophilicity of the NHC can help stabilise low-coordinate and reactive species.[85, 86] A further benefit to using NHCs over phosphines is the remarkable tunability of the electronic and steric profiles, due to the modular preparation of the ligands allowing for functionalisation of the N-substituents and backbone ring positions with relative ease.

As previously mentioned, NHCs are σ-donor singlet state carbenes bearing π-electron donating nitrogen substituents, so they could be considered to bond to transition metal complexes similarly to Fischer type carbene complexes. A fundamental difference between a Fischer type interaction and NHC bonding arises from the π-donation from the nitrogen lone pairs (mesomeric stabilisation), causing the empty p_π orbital to be high in energy, thus preventing or reducing the amount of π-backbonding associated with Fischer type complexes.[85, 87, 88] Previous studies have shown group 10 metals with completely filled *d*-orbitals forming bonds through σ orbital interactions.[89] However, subsequent reports have shown that non-negligible π-backbonding can occur in a wide variety of NHC-transition metal chemistry.[90-94] In one case, electron-poor rhodium(III) and iridium(III) complexes were stabilised by π-donation from the NHC to the metal centres.[95] These π-accepting and donating abilities could perhaps be considered another benefit of using NHCs over phosphines, with strong NHC-metal bonds leading to excellent stability of reactive metal fragments.

Since the early 2000s there has been a significant effort to widen the scope of NHCs beyond the simple five-membered ring imidazole based diaminocarbenes, leading to the development of new classes of carbene ligands such as cyclic(alkyl)(amino)carbenes (CAACs),[96, 97] diamidocarbenes (DACs),[98, 99] and ring-expanded NHCs (RE-NHCs) (Figure 1.5).[100-104]

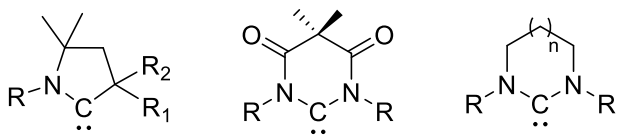

R = alkyl or aryl, and R_1, R_2 = alkyl

Figure 1.5 Structures of CAACs (left), DACs (middle) and RE-NHCs (right).

1.2.2 Ring-Expanded NHCs

The term RE-NHC is normally applied to any NHCs with ring sizes larger than the five-membered imidazole ring compounds, with the most common variants containing six- to eight-membered rings.[105] Examples with nine- and ten-membered rings have also been very recently reported.[106] Prepared *via* the synthesis of a formamidine precursor, and subsequent reaction with a dihaloalkane with a chain length corresponding to the desired ring size, this results in the formation of an air and moisture stable salt, which can be deprotonated to form the desired RE-NHC (Scheme 1.7).[102]

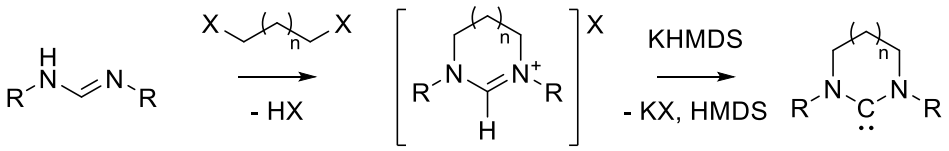

Scheme 1.7 Synthesis of six-membered RE-NHC from formamidine precursor.

As a result of the ring expansion, the carbene ligands exhibit unique steric and electronic profiles. The internal angles of a RE-NHC are significantly larger than a five-membered ring counterpart. For example, in Rh(NHC)(COD)Cl complexes the IMes N-C_{NHC}-N bond angle = 107.29(12)°, whereas in the six-membered analogue 6Mes it is 117.0(4)°, and in the seven-membered ring derivative 7Mes, it is 118.0(3)°.[107] The wider angle allows greater steric protection of the metal centre by the N-substituents of the carbenes, and can lead to better stabilisation of low-coordinate transition metal complexes with potentially superior catalytic activity.[103, 108-110] On the other hand, having the ligand closer to the metal centre can lead to alternative reaction pathways, such as cyclometallation, which would potentially have a negative effect on catalytic efficiency.[111-113] As a consequence of the larger N-C_{NHC}-N angle, there is a decrease in *s* character of the σ orbital (Figure 1.2), which leads to an increase in the energy of the orbital. This makes RE-NHCs better σ-donors than NHCs, as well as having a smaller HOMO – LUMO gap.

1.2.3 DACs

DACs were first reported in 2009 as NHCs with carbonyl functionality in the carbene backbone, α to each nitrogen.[114] The nitrogen substituents still donate some π-electron density into the vacant p_π orbital of the carbene centre, however, there is now a

competing process of π-donation from the nitrogen atoms into the π^* of the carbonyl groups. This reduced electron donation into the carbenic p_π orbital results in a lowering of the energy of the LUMO, and thus better π-backbonding capabilities. The X-ray structure of 6MesDAC showed an average C_{NHC}-N bond length of 1.371(3) Å, significantly longer than that of the analogous 6Mes (1.3464(12) Å). This reflects the reduction of the mesomeric stabilisation effect leading to less multiple bond character of the N-C_{NHC}-N bond.[102, 115] Various transition metal complexes featuring 5MesDAC, 6MesDAC, and 7MesDAC have been reported to utilise the additional π-backbonding capabilities to form strong DAC-metal bonds,[116-119] while the six-membered derivative has also been shown to perform insertion reactions with a range of boranes, amines, aromatic C-H bonds, silanes, and phosphines.[120-124]

1.2.4 CAACs

CAACs were first developed by Bertrand in 2005, whereby one of the amino substituents in an NHC is replaced with an alkyl group.[96] The replacement of the electronegative nitrogen with a more electron-donating carbon leads to CAACs being electron-rich and better σ-donors than NHCs. The nitrogen/carbon exchange also reduces the amount of electron-donation into the p_π orbital (the LUMO), and this reduction of competing donation makes CAACs good π-acceptors. These changes in electronic properties has led to the extensive use of CAACs as ligands in organometallic chemistry,[96, 125, 126] and also to them displaying interesting "transition-metal like" activation of small molecule E-H bonds (Scheme 1.8).[127-130] As well as improved σ-donor and π-acceptor abilities, the presence of a quaternary carbon atom next to the carbene centre allows for even more steric control of the substituents.

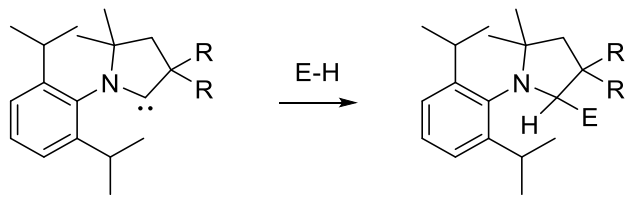

(E = H, BPin, CCl_3, CCPh, SiH_2Ph, $SiHPh_2$, NH_2, PPhH, PPh_2)

Scheme 1.8 Activation of E-H bonds by CAACs.

1.3 Ni(I)-NHC Chemistry

The relevance of NHCs to Ni(I) chemistry started with the synthesis of two dimeric species; [Ni(IPr)(μ-Cl)]$_2$ **x** (known as Sigman's dimer) and [Ni(SIPr)(μ-Cl)]$_2$.[131] These dimers were formed from the comproportionation of Ni(COD)$_2$ and Ni(dme)Cl$_2$ in the presence of IPr or SIPr respectively (Scheme 1.9). Analysis of the crystal structure of **x** revealed a Ni-Ni distance of 2.5194(5) Å, and diamagnetic ^{1}H NMR spectra confirmed the presence of a Ni-Ni bond (by indicating that the nickel was Ni(II)). These complexes were found to be useful precursors for a range of Ni-IPr and -SIPr containing compounds. For example, when investigating potential Ni-NHC mechanisms for Kumada coupling, Matsubara formed the dimers [Ni(IPr)]$_2$(μ-*p*-tol)(μ-Cl) and [Ni(IPr)]$_2$(μ-*p*-tol)$_2$ from the reaction between **x** and *p*-tolMgCl.[132]

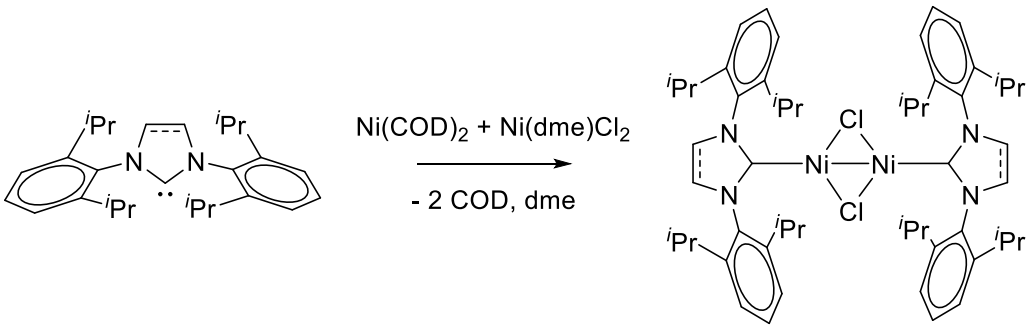

x: NHC = IPr

Scheme 1.9 Synthesis of [Ni(IPr)(μ-Cl)]$_2$ **x** and [Ni(SIPr)(μ-Cl)]$_2$.

1.3.1 Three-coordinate Ni(I)-NHC Compounds

Matsubara *et al*. reported a *bis*-NHC species Ni(IPr)$_2$Cl **xii** as a monomeric, three-coordinate 15e$^-$ complex.[133] This complex was formed during an investigation into using the Ni(0) precursor Ni(IPr)$_2$ **xi** for the Negishi cross coupling of aryl halides (Scheme 1.10), with compound **xi** having previously shown catalytic activity in a variety of other cross coupling reactions.[134-136] Paramagnetic ^{1}H NMR spectra and magnetic susceptibility measurements proved the presence of a d^9 metal centre in **xii**, while X-ray crystallographic analysis revealed a T-shaped geometry with no stabilising hydrogen bonding or agostic interactions. In solution, **xii** existed in equilibrium with Sigman's dimer **x** and free IPr, indicating the labile nature of the NHC ligand.[133] The addition of 2 equiv. (equivalents) of PPh$_3$ to **x** led to the formation of the Y-shaped compound Ni(IPr)(PPh$_3$)Cl **xiii** (Scheme 1.10).[137] The difference in geometries of **xii** and **xiii** was

attributed to different electronic properties rather than just steric factors. Sigman's dimer **x** was also reported to form two other Ni(IPr)(L)Cl species (L = $P(OPh)_3$, pyridine) under the same conditions as **xiii**.[138]

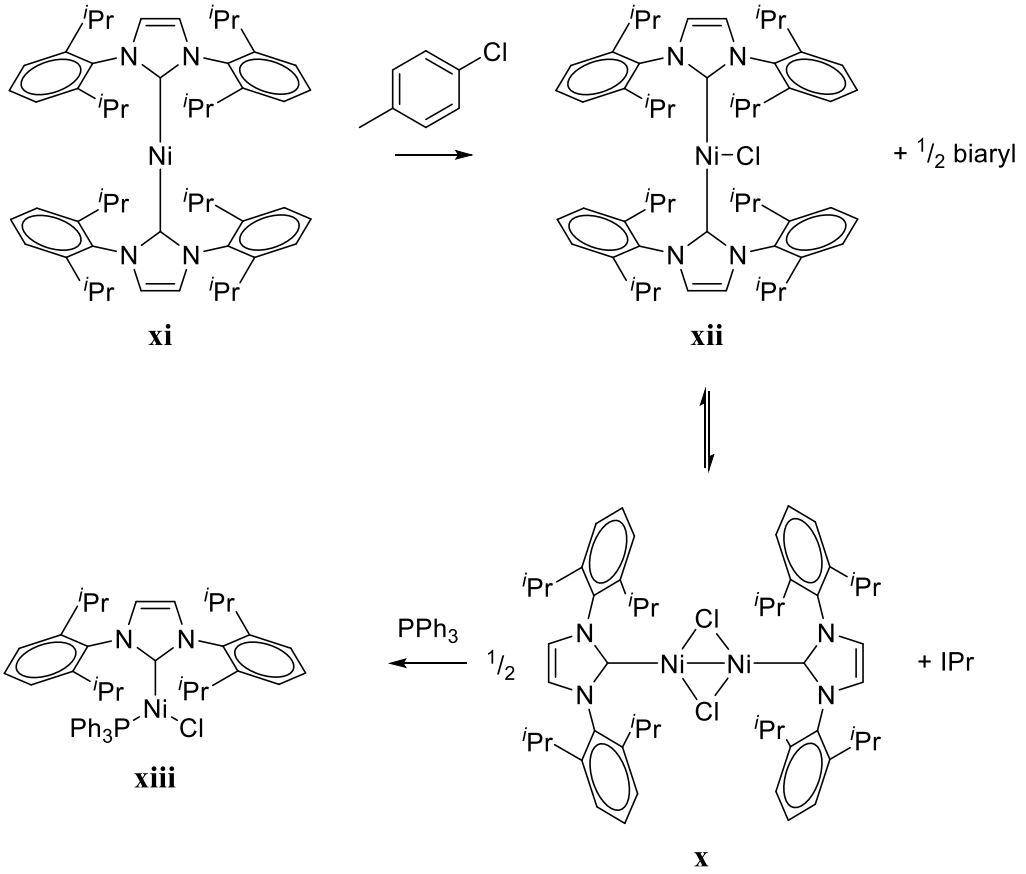

Scheme 1.10 Synthesis of three-coordinate Ni(I) species **xii** and **xiii** from Ni(0) compound **xi** and Sigman's dimer **x**.

N-mesityl derivatives $Ni(IMes)_2X$ (X = Cl, Br)[i] **xv** were reported by Louie *et al.* during attempts to form $Ni(IMes)_2(Ar)X$ species from the reaction of $Ni(IMes)_2$ **xiv** with aryl halides (Scheme 1.11).[139] The same compounds could also be formed from ligand substitution of $Ni(PPh_3)_2(Ar)X$ (Ar = Ph, *p*-MeOPh, *p*-F_3CPh) with IMes (Scheme 1.11).[139] Characterisation of compounds $\mathbf{xv_a}$ and $\mathbf{xv_b}$ by X-ray crystallography showed the same T-shaped geometry seen for $Ni(IPr)_2Cl$ **xii**. The synthesis of mixed phosphine-NHC species $Ni(IMes)(PPh_3)X$ (X = Cl, Br) **xvi** occurred *via* the comproportionation of

[i] $Ni(IMes)_2I$ was also formed from a reaction of PhI with **xiv**, but not from the ligand substitution route with IMes.

$Ni(COD)_2$ and $Ni(PPh_3)_2X_2$ in the presence of IMes (Scheme 1.11).[138] The Y-shaped geometries of **xvi$_a$** and **xvi$_b$** were analogous to $Ni(IPr)(PPh_3)Cl$ **xiii**, in that the change in geometry compared to the *bis*-NHC derivatives was due to a change in electronic properties.

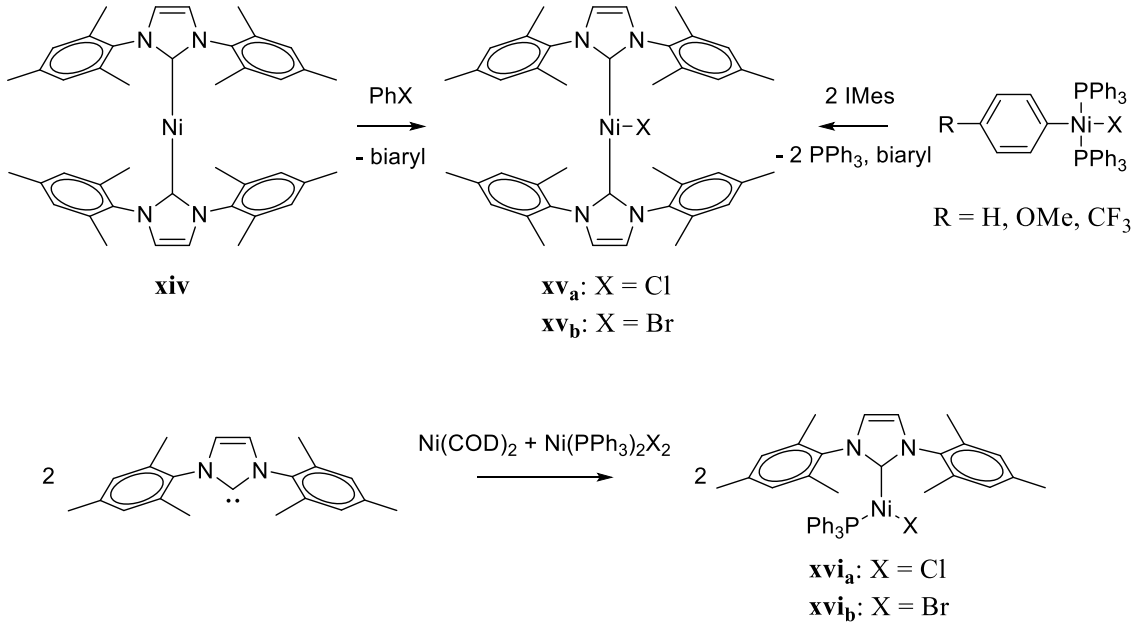

Scheme 1.11 Synthesis of *bis*-NHC Ni(I) species **xv$_a$** and **xv$_b$** by either reaction with aryl halides or ligand substitution routes (top), and mixed NHC-phosphine Ni(I) complexes **xvi$_a$** and **xvi$_b$** *via* the comproportionation route (bottom).

These three-coordinate Ni(I)-NHC complexes have all shown catalytic activity in a range of cross coupling reactions. $Ni(IPr)_2Cl$ **xii** was shown to mediate Kumada coupling between an aryl Grignard (PhMgCl) and aryl bromides (4-Br-anisole and 4-Br-biphenyl) to form coupled products which were isolated in near-quantitative yields.[133] $Ni(IPr)(PPh_3)Cl$ **xiii** displayed similar levels of activity for the same Kumada cross coupling, as well as Buchwald-Hartwig amination of aryl halides with diphenylamine.[137] $Ni(IMes)_2X$ species **xv$_a$** and **xv$_b$** were used as Kumada cross coupling catalysts between MesMgBr and aryl halides (PhCl and PhBr), and also showed capacity for Suzuki cross coupling of aryl bromides (4-Br-anisole and 4-Br-$PhCF_3$) and phenylboronic acid.[139] $Ni(IMes)(PPh_3)Cl$ **xvi$_a$** was also able to perform Suzuki cross coupling with 4-Br-benzophenone.[138]

Scheme 1.12 shows a generic catalytic cycle with the expected coordination and oxidation states of the nickel species involved in Kumada or Suzuki cross coupling

reactions. These same catalysts can also be used for reductive coupling,[140] cycloadditions,[141] transfer hydrogenation[142] and C-H/C-C/C-F bond activations.[86] However, Louie proposes an alternative mechanism based on the results of the work pertaining to Kumada and Suzuki cross coupling with $Ni(IMes)_2X$ catalysts **xv$_a$** and **xv$_b$** (Scheme 1.12).[139] Stoichiometric reactions between catalyst precursors and cross coupling reagents suggested an initial transmetallation step followed by oxidative addition and reductive elimination, consistent with other reports of Ni(I) catalysis starting with this transformation.[143, 144]

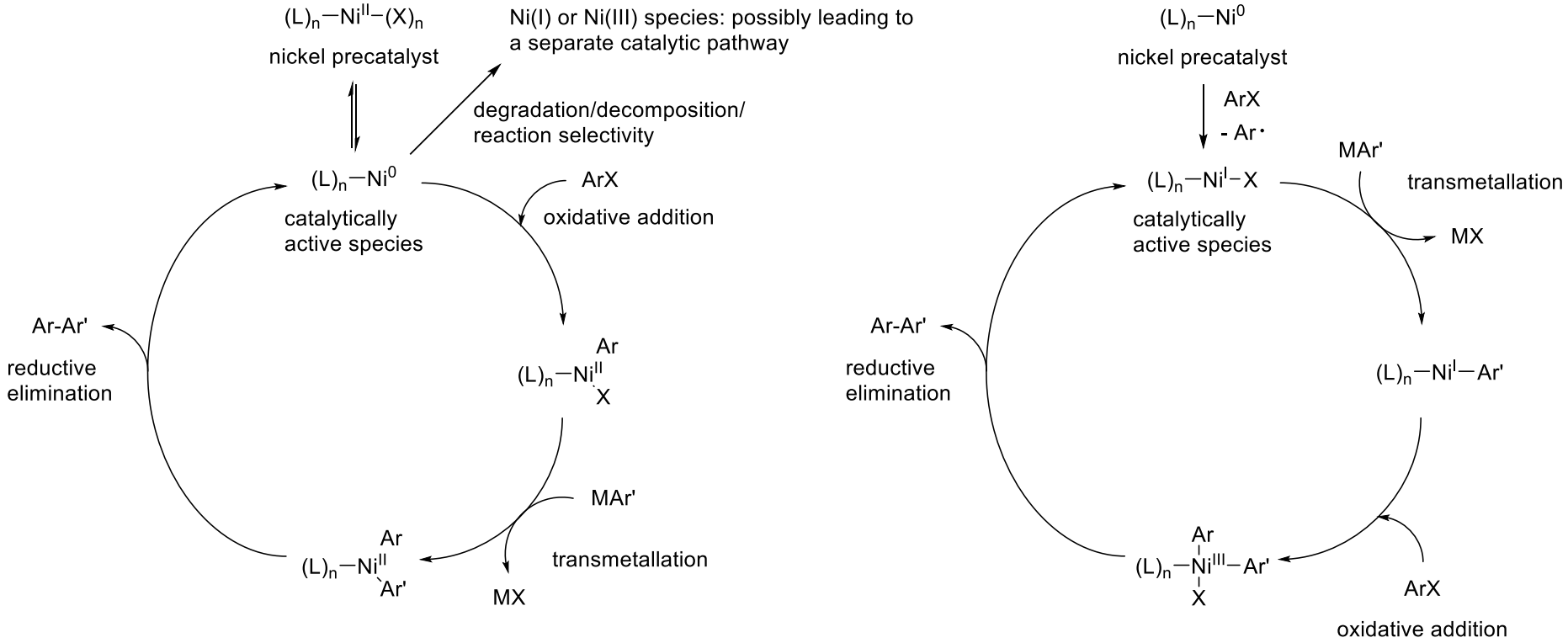

Scheme 1.12 Generic catalytic cycle for cross coupling with nickel (left) and proposed catalytic cycle for Ni(I) in coupling reactions.

1.3.2 Two-coordinate Ni(I)-NHC Compounds

Two-coordinate Ni(I)-NHC species are generally formed with one neutral NHC ligand and one negatively charged amido or alkyl ligand, with the first few examples of this type of complex reported by Hillhouse *et al.* (Scheme 1.13).[145, 146] Starting from Sigman's dimer **x**, treatment with $NaN(SiMe_3)_2$ and $LiN(H)(C_6H_3\text{-}2,6\text{-}^iPr_2)$ gave rise to the NHC-amide Ni(I) compounds $Ni(IPr)(N(SiMe_3)_2)$ **xvii** and $Ni(IPr)(N(H)(C_6H_3\text{-}2,6\text{-}^iPr_2)$ **xviii** respectively.[145] A few years later it was shown that the salt metathesis between dimer **x** and either $Mg(CH(SiMe_3)_2)Cl$ or $LiC_6H_3\text{-}2,6\text{-}Mes_2$ generated the two-coordinate NHC-alkyl species $Ni(IPr)(CH(SiMe_3)_2)$ **xix** and $Ni(IPr)(C_6H_3\text{-}2,6\text{-}Mes_2)$ **xx**.[146] Magnetic susceptibility measurements confirmed the Ni(I) oxidation state, while structural analysis of compounds **xvii** – **xx** revealed no short contacts or stabilising interactions between the nickel centre and NHC/amide/alkyl ligands. C_{NHC}-Ni-L bond angles of 178.7(8)°, 163.2(2)/167.4(2)°, 174.81(10)°, and 175.97(8)° were determined for compounds **xvii** to **xx** respectively.

Subsequent use of the terphenylamide salts $LiN(H)(C_6H_3\text{-}2,6\text{-}Mes_2)$ and $LiN(H)(C_6H_3\text{-}2,6\text{-}(C_6H_3\text{-}2,6\text{-}^iPr_2)_2))$ to generate more NHC-amide Ni(I) species from Sigman's dimer **x** led to the formation of $Ni(IPr)(N(H)(C_6H_3\text{-}2,6\text{-}Mes_2))$ and $Ni(IPr)(N(H)(C_6H_3\text{-}2,6\text{-}(C_6H_3\text{-}2,6\text{-}^iPr_2)_2))$.[147] These bulky amide containing species differ slightly from those in Scheme 1.13, due to the stabilising Ni-C_{ipso} interactions from the terphenyl wingtips. This results in significant bending of the C_{NHC}-Ni-amide bond angles compared to those in **xvii** – **xx** (112.17(9)° and 116.41(9)°). The steric congestion around the nickel centre is also inferred by elongation of the Ni-C_{NHC}/Ni-N bond lengths relative to those of **xviii** (1.949(2)/1.936(2) Å and 1.959(2)/1.953(2) Å *vs.* 1.878(5)/1.831(4) Å). A similar case of an Ni-C_{ipso} interaction was reported for the NHC-thiolate species $Ni(IMes)(S(C_6H_3\text{-}2,6\text{-}Mes_2))$.[148] The reaction between the phosphine containing precursor $Ni(PPh_3)(S(C_6H_3\text{-}2,6\text{-}Mes_2))$ (which also featured Ni-C_{ipso} stabilisation) and IMes formed this two-coordinate Ni(I) species, which displayed a significantly bent C_{NHC}-Ni-S bond angle (106.55(7)°) due to the terphenyl group interaction.

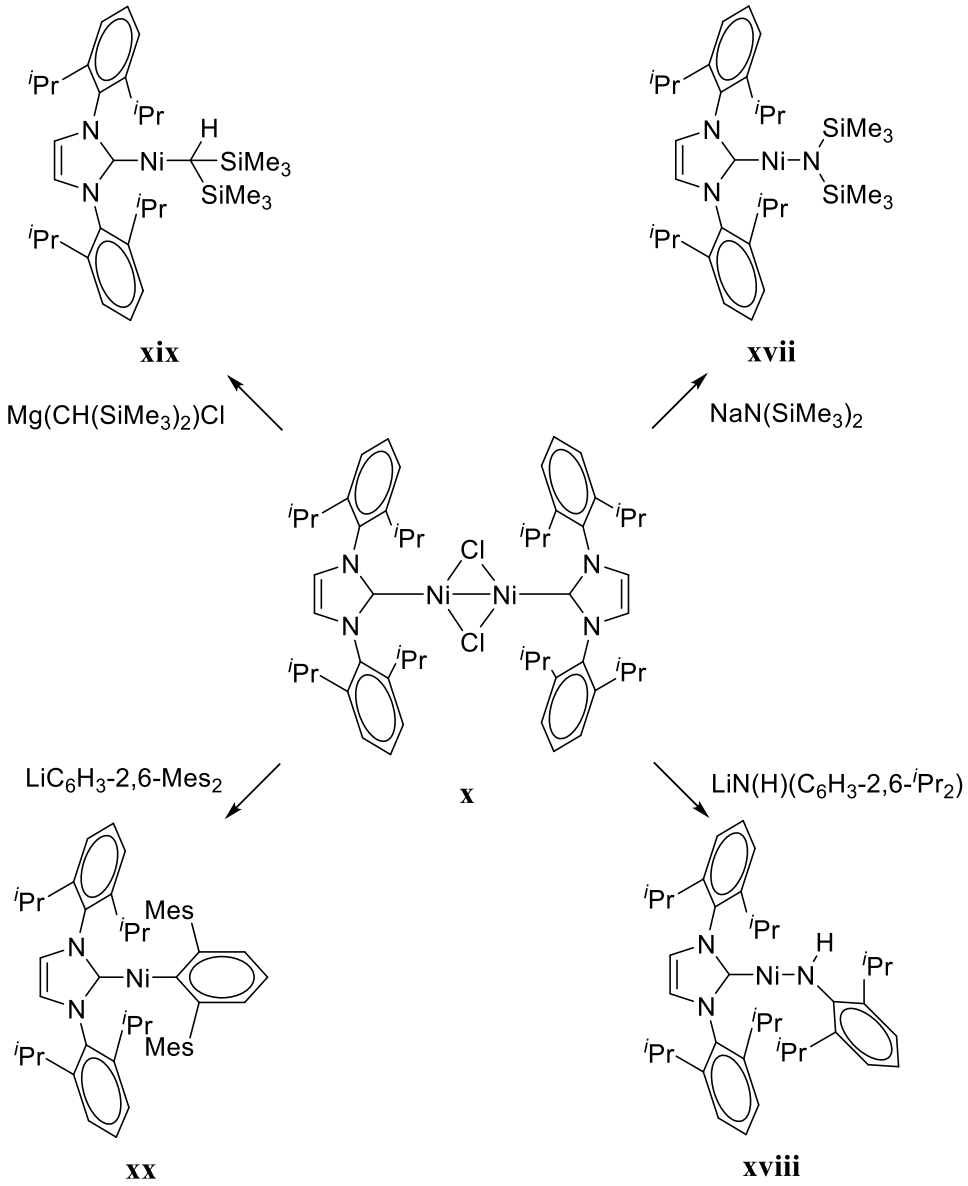

Scheme 1.13 Synthesis of two-coordinate Ni(I) species **xvii** – **xx** from Sigman's dimer **x**.

Tilley *et al.* reported the synthesis of another NHC-amide species, Ni(IPr)(N(SiMe$_3$)(C$_6$H$_3$-2,6-^{i}Pr$_2$)) **xxiii**, arising from the substitution of one amide group from the two-coordinate species Ni(N(SiMe$_3$)(C$_6$H$_3$-2,6-^{i}Pr$_2$))$_2$ **xxi** alongside reduction of the Ni(II) precursor (Scheme 1.14).[149, 150] A later publication by the same team showed an alternative route to forming **xxiii** *via* the ligand substitution of the nickelate **xxii** (formed from chemical reduction of **xxi** with KC$_8$) (Scheme 1.14).[151] Analysis of the molecular structure of **xxiii** revealed a near-linear arrangement of the C$_{NHC}$-Ni-N bond (173.01(7)°) and no stabilisation interactions between ligands and nickel. Subsequent proton transfer from the bulky phenol reagent 2,6-di-*tert*-butyl-4-methylphenol gave

Ni(IPr)(OC$_6$H$_2$-2,6-^{t}Bu$_2$-4-Me) **xxiv** (Scheme 1.14), which had an average C$_{NHC}$-Ni-O bond angle of 168.16°.

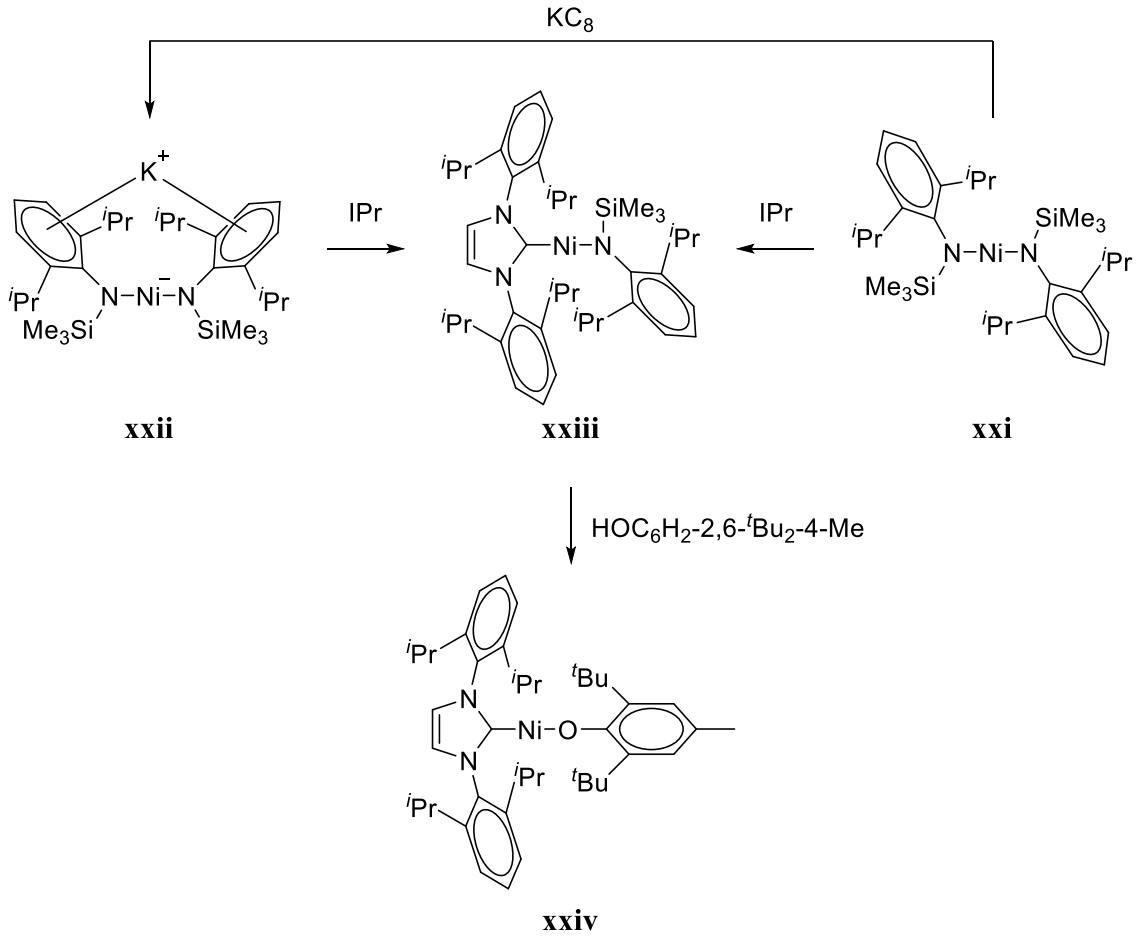

xxii **xxiii** **xxi** **xxiv**

Scheme 1.14 Synthesis of NHC-amide Ni(I) complex **xxiii** from reduction of *bis*-amide species **xxi** or ligand substitution of **xxii**, followed by formation of NHC-aryloxide compound **xxiv**.

In a slight variation to the IPr-amide chemistry mentioned above, a series of Ni(I) NHC-amidate species were prepared by the reaction between the bromide derivative of Sigman's dimer (first generated by Hillhouse *et al.*[146]) and sodium amidate salts bearing different bulky alkyl groups (Scheme 1.15).[152] The structures of the Ni(I) amidate products **xxv** – **xxvii** were dependent on the substituents of the amidate salt. The reaction involving amidate salts with bulky ^{t}Bu and C$_6$H$_3$-2,6-^{i}Pr$_2$ groups formed compound **xxv** which featured a κ^1-*O* binding mode of the amidate, along with an η^2-π interaction with the aryl ring. The crystal structure of **xxv** revealed a non-linear C$_{NHC}$-Ni-O bond angle (107.90(8)°) due to the π interaction. Removal of the aryl ring and changing of the groups

to ^{t}Bu/^{i}Pr and ^{i}Pr/^{i}Pr produced the κ^1-*N* binding mode of the amidate in compounds **xxvi** and **xxvii**, and far wider C_{NHC}-Ni-N bond angles (172.12(4)° and 169.0(5)°). Notably, **xxvi** features a δ-*bis*(C-H) agostic interaction between two protons from the ^{t}Bu group and the nickel centre, the first reported such example in Ni(I) chemistry. Substitution of the ^{t}Bu with a second ^{i}Pr moiety formed two-coordinate species **xxvii** free of stabilising agostic interactions.

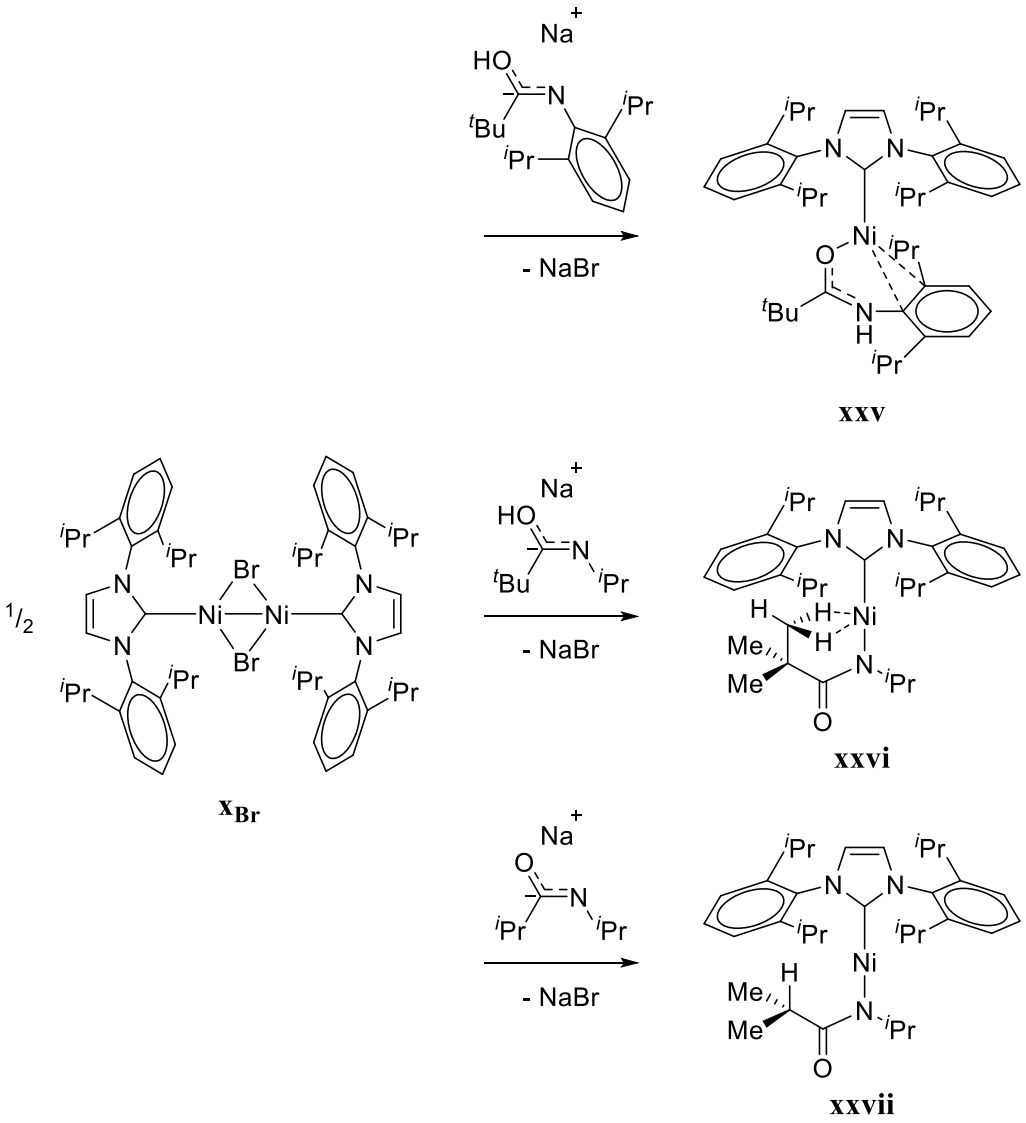

Scheme 1.15 Synthesis of Ni(I) NHC-amidate species **xxv** – **xxvii** from reaction of $\mathbf{x_{Br}}$ with sodium amidate salts.

Although not technically a two-coordinate system, a range of Ni(I) NHC-cyclopentadienyl (Cp) species have been reported and used as synthons for a wide range of Ni(0)- and Ni(II)-Cp compounds.[153-157] One route to the formation of such species was

reported by Hazari *et al*. *via* the salt metathesis between either the IPr or SIPr versions of Sigman's dimer and 2 equiv. of sodium cyclopentadienyl, to give the monomeric 17e$^-$ Ni(I) compounds **xxviii** and **xxix** (Scheme 1.16).[158] The same synthetic route was used to form closely related Ni(I) NHC-indenyl (Ind) species with lithium indenyl. Use of a single equiv. of NaCp or LiInd (½ equiv. per Ni centre) generated Cp- and Ind-bridged dimers [Ni(NHC)]$_2$(μ-Cp)(μ-Cl) and [Ni(NHC)]$_2$(μ-Ind)(μ-Cl) (NHC = IPr, SIPr).[158] Wolf and Whittlesey presented an alternative route to forming the pseudo-two-coordinate NHC-Cp species by the reduction of Ni(II)-halide species with KC_8 to form Ni(IPr)Cp, Ni(IMes)Cp, Ni(IPr)Cp*, Ni(6Mes)Cp, Ni(7Mes)Cp, and Ni(6MesDAC)Cp compounds **xxviii** and **xxx** – **xxxiv** (Scheme 1.16).[153, 159]

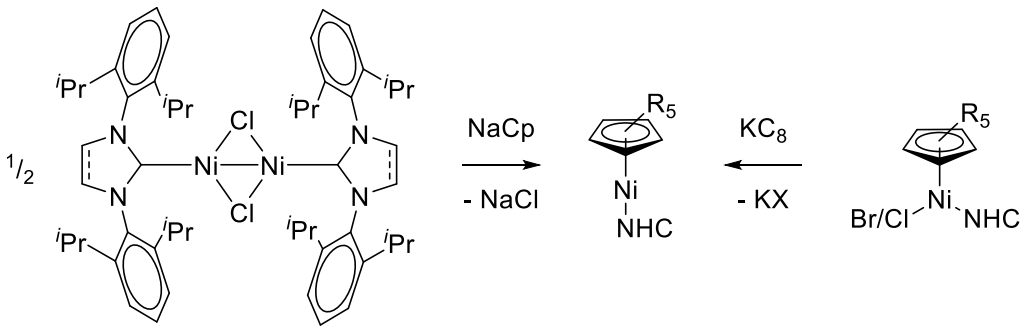

xxviii: NHC = IPr, R = H
xxix: NHC = SIPr, R = H
xxx: NHC = IMes, R = H
xxxi: NHC = IPr, R = Me
xxxii: NHC = 6Mes, R = H
xxxiii:NHC = 7Mes, R = H
xxxiv:NHC = 6MesDAC, R = H

Scheme 1.16 Synthesis of Ni(I)-cyclopentadienyl compounds **xxviii** – **xxxiv** from salt metathesis and chemical reduction routes.

1.4 Two-coordinate Transition Metal Chemistry

The chemistry of stable, open shell (d^1 – d^9) two-coordinate transition metal complexes is relatively scarce, being one of the least researched areas of coordination chemistry. Their rarity is due to the fact that any isolated examples are commonly extremely air and moisture sensitive, meaning further investigation into small molecule activation or further coordination is hindered. Another contributing factor to their scarcity is the difficulty in isolating coordinatively unsaturated monomeric species while preventing aggregation into structures in which the metal has a higher coordination

number.[160] An example of this is with transition metal dihalide species, which can be two-coordinate in the gas phase but then form six-coordinate structures in the solid state.[161] The main strategy to successfully form and isolate low-coordinate, unsaturated complexes is to utilise bulky ligand systems, with most examples to date using sterically encumbered alkyl, aryl, amido, alkoxo and thiolato compounds.[160, 162] Since the development of coordination chemistry in the late 19th century, there have been investigations into increasing the steric bulk of ligands to make low-coordinate complexes.[163] A milestone introduction of the bulky silylamido group $N(SiMe_3)_2$ in 1963 led to proposed $M[N(SiMe_3)_2]_n$ complexes (n = 2, M = Mn, Co, Ni; n = 3, M = Cr and Fe).[164, 165] The three-coordinate $Fe[N(SiMe_3)_2]_3$ was finally characterised by X-ray crystallography a few years later in 1969.[166] The other three-coordinate first row transition metal analogues soon followed,[167, 168] along with work by Lappert *et al.* using the isoelectronic $CH(SiMe_3)_2$ ligand.[169, 170] The isolation of two-coordinate species was much slower, the first fully characterised example $Mn[C(SiMe_3)_3]_2$ appearing only in 1985.[171] Another manganese complex ($Mn(CH_2{}^tBu)_2$) was characterised at the same time, although in the vapour phase at *ca.* 413 K.[172] Soon after, iron and cobalt amido examples were reported and characterised, both in solid and gas phase.[173, 174]

1.4.1 Magnetism of Two-coordinate Transition Metal Compounds

In the 2012 review by Power on two-coordinate transition metal complexes, it was noted that only 18 of 80 structurally characterised examples showed a highly linear geometry (interligand angle greater than 170°), while the others varied greatly in their deviation from linearity.[160] It has been reported that complexes with linear geometry show interesting magnetic properties, such as highly anisotropic magnetic fields and zero field splitting.[175-177] Figure 1.6 shows the *d*-orbital splitting arrangement for a typical linear geometry ($D_{\infty h}$ crystal field) assuming σ-interactions between metal and ligand only, and where the two ligands are conventionally aligned along the z axis. When an odd number of electrons occupy a degenerate orbital (either $d_{x2\text{-}y2}/d_{xy}$ or d_{xz}/d_{yz}) this can result in first order orbital angular momentum, which remains unquenched by the ligand field due to no ligands directly interacting with the degenerate orbitals and removes the requisite degeneracy.

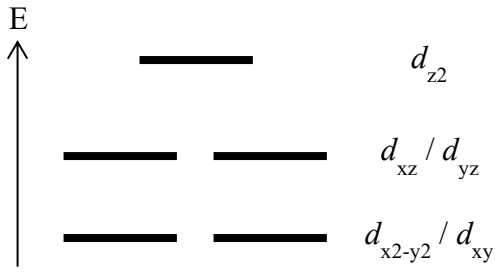

Figure 1.6 The *d*-orbital splitting arrangement in $D_{\infty h}$ crystal field.

Complexes with magnetic anisotropy have been shown to demonstrate single ion magnetic (SIM) behaviour, however it is not the case that all molecules with magnetic anisotropy will be SIMs.[178] This magnetic anisotropy means that each individual molecule will contain a magnetic moment of preferred orientation, independent of an external field, which ultimately leads to an overall net magnetisation within the bulk material.[179] When a magnetic field (*B*) is applied, this net magnetisation will orientate itself to match the field direction, however, when the applied magnetic field is removed, the amount of magnetisation remaining (remnant magnetisation) is relative to how well the SIM performs. A SIM will exhibit the ability to retain magnetisation for relatively long periods of time (~ 10^{-6} – 10^{-11} s) in the absence of the applied magnetic field, however this is invariably at low temperatures. SIMs possess an energy barrier to "relax" and reorient their magnetic moment, known as the effective energy barrier (U_{eff}), and the magnitude of this barrier is a good measure by which to compare different SIMs. Complexes which have a larger barrier usually exhibit SIM behaviour at higher temperatures.[179]

The U_{eff} value is usually determined from magnetic susceptibility measurements in a very small ac magnetic field, and can be performed either in a zero static dc field, or an applied dc field if required.[179, 180] In-phase (χ') and out-of-phase (χ'') components of magnetic susceptibility are measured as functions of temperature and ac frequency (ν), and the inability of a given system to follow progressively faster oscillating magnetic fields suggests the presence of an energy barrier to the magnetisation, causing the χ' signals to diminish and the χ'' to increase.[181] The peak maximum of the χ'' curve can be used to determine relaxation time (τ) from using Equation 1.1, and a relationship between τ and temperature may be established through an Arrhenius plot of $\ln(\tau)$ *vs.* T^{-1}. The U_{eff} value can then be extracted from the linear fit of the plot with Equation 1.2, where preexponential factor τ_0 is the relaxation time for reversal at $T = \infty$.

Equations 1.1 and 1.2

$$\tau = \frac{1}{2\pi\nu}$$

$$\tau = \tau_0 \exp^{\left(\frac{U_{eff}}{k_B T}\right)}$$

A second measure of SIM properties is to analyse the field dependence of magnetisation over a range of low temperatures. A SIM will retain its magnetisation when first subjected to a reverse magnetic field (*H*) and then subsequently returned to zero field conditions, and thus display non-zero values of magnetisation (*M*). This magnetism retention is known as magnetic hysteresis, and it is temperature and sweep-rate dependent, with a maximum temperature called the blocking temperature (T_B) at which this hysteresis is observed.[179]

The Arrhenius plots of a given system are rarely linear across the full temperature range, and this deviation from linearity is caused by a collection of magnetic relaxation pathways that are not thermally activated processes. These additional relaxation pathways come from interactions between the spin system and the lattice system, and these interactions are called phonons. Three different types of spin-lattice relaxation processes are commonly encountered for in SIM chemistry; direct, Raman, and Orbach, and SIMs can also feature quantum tunnelling of magnetisation (QTM), whereby the magnetisation "tunnels" through the energy barrier.

The electronic structure of transition metal ions (particularly first row) is conventionally governed by electron repulsion and ligand field interactions, with spin-orbit coupling normally of lower magnitude and significance.[182] In transition metal SIMs where the orbital angular momentum is quenched by the ligand field, the projection of the spin (*S*) along the main magnetic axis leads to $2S + 1$ quantised states, denoted M_S. In linear two-coordinate species where the ligand field does not fully quench the spin-orbit coupling, an orbital angular momentum contribution to the magnetic moment (*L*) must be accounted for, and together with the spin contribution, forms the total angular momentum (*J*) and M_J microstates. The U_{eff} value can be thought of as the height of the barrier to spin reversal of a system from $-M_S$ to $+M_S$ (or vice versa), whereas the relaxation pathways provide shortcuts that involve tunnelling through the barrier or excitation to an intermediate $\pm M_S$ state followed by relaxation. When the spin ground state of an ion is greater than ½ (*i.e.* more than one unpaired electron) then zero field splitting (ZFS)

occurs, lifting the degeneracy of the M_S states in the absence of a magnetic field. The magnetic behaviour of SIMs is governed by the *D* and *E* terms which correspond to the axial and transverse/rhombic ZFS parameters respectively. Ultimately, the U_{eff} value for a SIM can be estimated by Equations 1.3 and 1.4, but experimentally derived U_{eff} values deviate away from this estimate due to the presence of alternative relaxation pathways.

Equations 1.3 and 1.4 U_{eff} estimates for integer spin systems (top) and half-integer spin systems (bottom).

$$U_{eff} = |D|S^2$$

$$U_{eff} = |D|\left(S^2 - \frac{1}{4}\right)$$

1.4.2 Low-coordinate Iron and Cobalt SIMs

Two-coordinate transition metal SIMs have emerged in recent years,[181-183] with the linear geometry used as a strategy to maximising the magnetic anisotropy, which in itself is a result of the ligand field failing to quench the magnetism arising from the linear arrangement of ligands. So far, many iron and cobalt (and chromium) examples have set reasonably high U_{eff} barriers (< 200 cm^{-1}), with d^7 Fe(I) and Co(II) examples showing the most desirable unquenched orbital magnetic moments along with large enough spins ($S = {}^3/_2$), resulting in large magnetic anisotropy. A few recent examples from the literature are mentioned in more detail below.

1.4.2.1 Cobalt

Bis-NHC Co(I) d^8 species $[Co(NHC)_2)]BPh_4$ (NHC = IMes, SIMes) **xxxv** and **xxxvi** were formed from the halide abstraction of Co(I)-chloride precursors with $NaBPh_4$, while $[Co(IAd)_2]BAr^F{}_4$ **xxxvii** was prepared from the reaction of $Co(IAd)(PPh_3)Cl$ with $NaBAr^F{}_4$ and IAd (Figure 1.7).[184, 185] X-ray diffraction revealed linear geometries (C_{NHC}-Co-C_{NHC} bonds = 178.4(1) – 180°) and torsion angles between the planes of the NHCs of 39.6°, 35.0°, and 90° respectively. Room temperature χT values of 3.65 and 3.26 cm^3 K mol^{-1} for the mesityl derivatives **xxxv** and **xxxvi** indicated unquenched orbital angular momentum due to significant deviation from the spin-only value expected of a $S = 1$ system (1.00 cm^3 K mol^{-1}), while the adamantyl analogue **xxxvii** gave a value of 1.94 cm^3 K mol^{-1}. The calculated *D* and *E* values appeared to suggest the possibility of

slow magnetic relaxation, however, no out-of-phase (χ'') ac susceptibility signals were observed under zero static field. Application of a 2000 Oe dc field revealed χ'' peaks for compound **xxxv** only, in the temperature range of 2 – 10 K, and the frequency dependent data was fitted with the generalised Debye model to generate relaxation times. The plot of τ *vs.* T^{-1} was fitted with the Arrhenius law to give U_{eff} and τ_0 values of 21.3 cm^{-1} (6.6×10^{-6} s) for the high temperature region data, while at low temperatures, the Raman and QTM processes dominated and caused deviation from the linear Arrhenius regime. No slow magnetic relaxation was seen for **xxxvi** and **xxxvii** under any dc field strength. This was likely due to the difference in the saturation of the NHC backbone making SIMes a better π-acceptor than IMes, thereby inducing a stronger *d*-π interaction and reducing the magnetic anisotropy of the Co(I) centre in **xxxvi**. In the second case, the perpendicular torsion angle between IAd ligands appeared to quench the spin-orbit coupling and significantly reduce the anisotropy.

The d^7 Co(II) NHC-imido species **xxxviii** – **xl** were formed from the reaction of Co(0)-olefin precursors with dimesitylphenyl azide, and X-ray structures displayed C_{NHC}-Co-N bond angles of 173.0(3)°, 177.5(2)/179.3(2)°, and 175.7(2)° respectively (Figure 1.7).[186, 187] The room temperature χT values of 3.86, 3.72, and 3.74 cm^3 K mol^{-1} far exceeded the spin-only values for an $S = {}^3/_2$ ion (1.875 cm^3 K mol^{-1}), and suggested a significant orbital contribution to the magnetic moment despite the high covalency of the Co-N bond.[187] Compounds **xxxviii** – **xl** displayed χ'' signals under a zero applied dc field, and relaxation times derived from the Debye model were used to find parameters for the direct, Raman, and Orbach relaxation processes. U_{eff} values were determined to be 297, 288, and 413 cm^{-1}, and represent some of the highest barrier values for transition metal SIMs. The excellent magnetic properties were believed to be due to the magnetic anisotropy of the Co-N fragment and a strong exchange coupling between the atoms that reduces the QTM of relaxation.

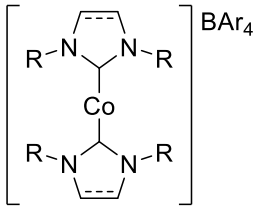

xxxv: NHC = IMes, R = Mes
xxxvi: NHC = SIMes, R = Mes
xxxvii: NHC = IAd, R = Ad

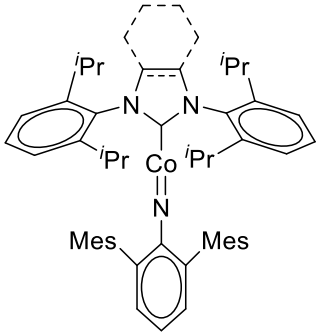

xxxviii: NHC = IPr
xxxix: NHC = CyIPr
xl: NHC = SIPr

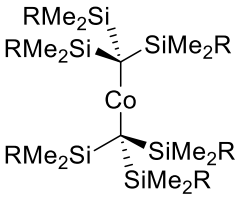

xli: R = ONaph

Figure 1.7 Examples of two-coordinate cobalt species **xxxv** – **xli** that showed SIM behaviour.

Another two-coordinate Co(II) species **xli** was reportedly formed *via* a salt metathesis of $CoBr_2$ and $KC(SiMe_2ONaph)_3$.[188] Ligand field analysis revealed a so-called non-Aufbau 3*d*-orbital arrangement, represented as $(d_{x2\text{-}y2},d_{xy})^3(d_{xz},d_{yz})^3(d_{z2})^1$. Using naphthalene based ligands with reduced basicity led to a very weak ligand field, which resulted in spin-orbital coupling and electron repulsion dictating the electronic structure of **xli**, and hence the high spin state arrangement of electrons. X-ray structure analysis revealed sp^3-CH$\cdots\pi$ and sp^2-CH$\cdots\pi$ interactions between naphthalene rings and methyl groups, helping to stabilise **xli**. A χT value of 4.89 cm^3 K mol^{-1} was significantly higher than the spin-only expected value, but more in agreement with the value obtained with fully unquenched orbital contribution (5.47 cm^3 K mol^{-1}). Rather than fitting the high temperature magnetic relaxation data extracted from ac susceptibility measurements to determine a U_{eff} value, IR spectroscopy in the presence of applied magnetic fields was used to experimentally derive the energy gap between ground and first excited states. Transmission spectra was collected at 4.2 K under applied fields ranging from 0 to 11 T, and a peak at 450 cm^{-1} was assigned to the transition between the ground and excited states. This value represents the highest U_{eff} value of a transition metal complex to date, and with this compound having a weak ligand field, completely unquenched orbital angular momentum, and maximal magnetic anisotropy it is possible that this value is the realistic maximum barrier for 3*d* compounds.

1.4.2.2 Iron

The pseudo-two-coordinate Fe(I) compound Fe($I^iPr_2Me_2$)(Cp^{R5}) **xlii** (R = C_6H_4-4-Et) was formed from the chemical reduction of the corresponding Fe(II)-bromide precursor with KC_8 (Figure 1.8).[189] It was reported as the first example of a 15e$^-$ Fe(I)-Cp species, and had a C_{NHC}-Fe-Cp bond angle of 166.2.11(8)° and 171.19(8)° for each crystallographically independent molecule. The first indication of SIM behaviour came from Mossbauer spectroscopy, which implied the compound had unquenched orbital angular momentum. The ac susceptibility measurements showed no χ'' signals under zero field, presumably due to rapid QTM enabled by the bent structure. Measurements under a 1000 Oe dc field produced χ'' signals up to 7 K, and fits of the temperature dependent data to the Arrhenius law yielded U_{eff} and τ_0 values of 63.6 cm^{-1} (6.8 × 10^{-10} s).

Use of CAACs as ligands for low-coordinate transition metal complexes has generated a number of Cr, Mn, Fe, and Co compounds.[183, 190-192] *Bis*-CAAC Fe(I) species **xliii** and **xliv** were reported by Roesky *et al*., with **xliv** formed from the reaction between **xliii** and $LiB(C_6F_5)_4 \cdot 2.5Et_2O$ (Figure 1.8).[193] The geometry around the Fe in **xliii** was trigonal planar, while the C-Fe-C bond angle in cation **xliv** was 180° due to the Fe being located at a crystallographic inversion centre. The d^7 compounds had room temperature χT values of 2.93 and 2.79 cm^3 K mol^{-1}, which are higher than the spin-only value and indicative of significant orbital angular momentum. Simulation of the ZFS parameters gave D values of 20.4 cm^{-1} for **xliii** and -22.0 cm^{-1} for **xliv**, and the fact that the two compounds gave opposite signs for the anisotropy was confirmed independently by high-field EPR spectroscopy (HF-EPR). The presence of slow magnetic relaxation was confirmed by ac susceptibility measurements under applied dc fields. Compound **xliii** gave χ'' signals under a 500 Oe dc field, leading to an energy barrier value of 22.4 cm^{-1}. The linear species **xliv** required a 3000 Oe dc field to produce frequency dependent χ'' peaks, and an upper limit estimate of 20 cm^{-1} was derived for the U_{eff} due to only a few data points available for the Arrhenius plot.

Moving away from the use of NHCs and CAACs, the linear Fe(I)-amide species [Fe($N(SiMe_3)_2)_2$]KL **xlv** and **xlvi** (L = 18-crown-6, 2.2.2-crypt) were formed from reduction of Fe(II) *bis*-amide precursors in the presence of a crown ether (Figure 1.8).[194, 195] Room temperature χT values of 3.89 and 3.78 cm^3 K mol^{-1}, as well as temperature dependence of the χT product as low temperatures, pointed to reasonable magnetic anisotropy. Slow magnetic relaxation was observed for both compounds in the absence

of an applied dc field up to 22 K. U_{eff} values of 43 and 64 cm^{-1} and τ_0 times of 4.6×10^{-6} and 8.9×10^{-6} s were thought to suggest that through-barrier relaxation processes were operating across the full temperature range, leading to relatively low barrier values.

A closely related two-coordinate Fe(I) species $[Fe(C(SiMe_3)_3)_2]K(2.2.2\text{-crypt})$ **xlvii** (Figure 1.8) reported by Long *et al.* exhibits the highest U_{eff} barrier (226 cm^{-1}) for any iron based SIMs to date.[196] Made from the reduction of $Fe(C(SiMe_3)_3)_2$ with KC_8 in the presence of 2.2.2-cryptand, the compound displayed a linear C-Fe-C bond angle (179.2(2)°). *Ab initio* ligand field analysis provided a *d*-orbital splitting arrangement of $(d_{z2})^2(d_{x2-y2},d_{xy})^3(d_{xz},d_{yz})^2$, which was vastly different to the isostructural and isoelectronic Co(II) species **xli**.[188] The different orbital arrangement was due to mixing of the Fe $3d_{z2}$ and 4*s* orbitals, and resulted in unquenched orbital momentum (room temperature χT of 3.39 cm^3 K mol^{-1}). Frequency dependent χ'' signals were observed up to 29 K in a zero applied field and plotting of the high temperature data to the Arrhenius law resulted in the large U_{eff} value, while at lower temperatures the QTM process was shown to dominate the magnetic relaxation pathway.

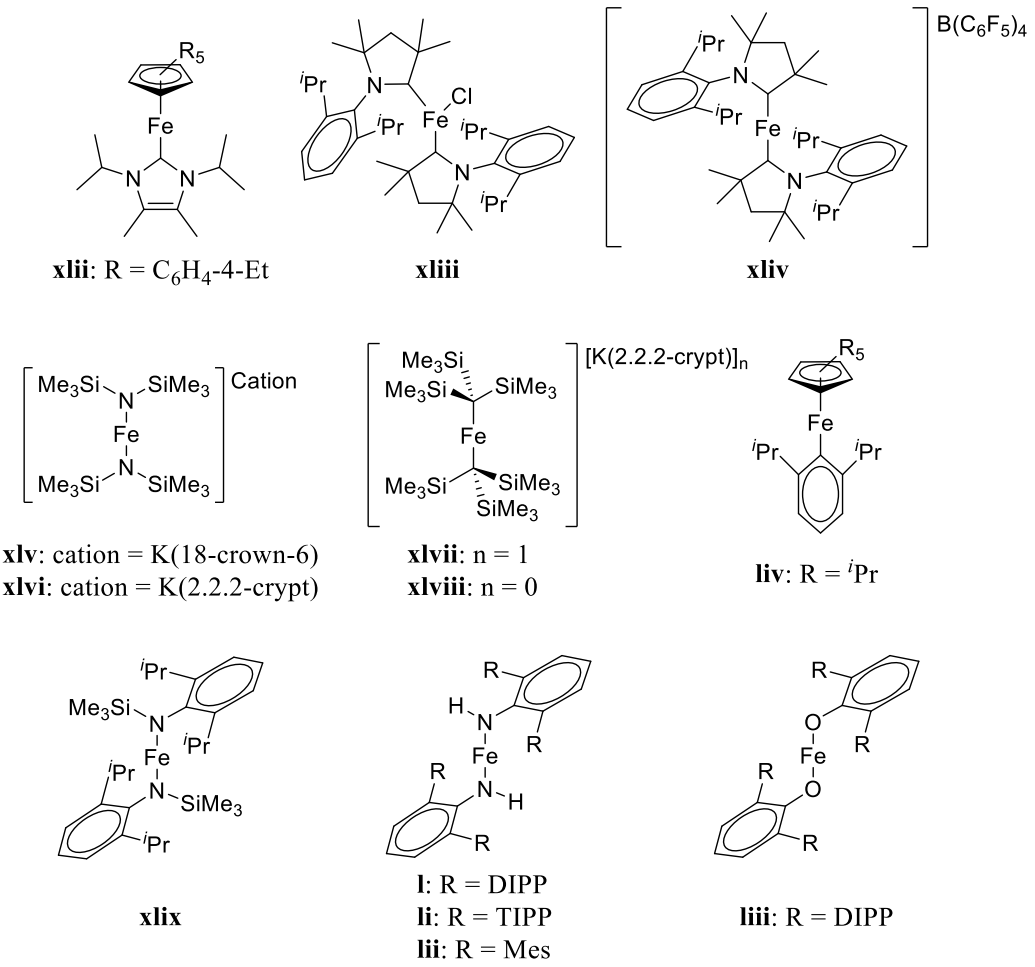

Figure 1.8 Examples of low-coordinate iron species **xlii** – **liv** that showed SIM behaviour (DIPP = C_6H_3-2,6-^{i}Pr$_2$, TIPP = C_6H_2-2,4,6-^{i}Pr$_3$).

The magnetic properties of the neutral Fe(II) analogue of **xlvii**, **xlviii**, and a series of two-coordinate *bis*-amide and *bis*-aryloxide Fe(II) compounds **xlix** – **liii** were investigated as part of a study into Fe(II) SIMs.[197, 198] Compounds **xlix** and **l** were formed *via* the salt elimination reaction between $FeCl_2$ and Li(L) (L = N(SiMe$_3$)(C_6H_3-2,6-^{i}Pr$_2$), N(H)(C_6H_3-2,6-(C_6H_3-2,6-^{i}Pr$_2$)$_2$)), while structural parameters of **xlviii**,[199, 200] **li** and **lii**,[177] and **liii**[201] were taken from previous publications. L-Fe-L bond angles for each compound were exactly 180° as the Fe was located on a special position, with the exception of compound **lii** which had a bent geometry and an N-Fe-N angle of 140.9(2)°. The static magnetic properties of compounds **xlviii** – **liii** were analysed by dc susceptibility measurements, with room temperature χT values that were higher than the spin-only value (S = 2; 3.00 cm^3 K mol^{-1}; with the exception of the bent species **lii**, 2.88 cm^3 K mol^{-1}), suggesting the presence of magnetic anisotropy. As expected, compounds **xlviii** – **li** and **liii** displayed slow magnetic relaxation under an applied dc field, while χ'' signals for **lii**

were not observed at any field strength. Each Fe(II) compound required an applied dc field to induce the SIM behaviour, and the field strength was determined from peak maxima of τ *vs*. H plots. Once the optimal field for each compound was set, temperature and frequency dependent χ'' signals were observed and used to derive U_{eff} and τ_0 values (181 – 43 cm^{-1} and $1 \times 10^{-11} – 3 \times 10^{-7}$ s), and parameters for the field and temperature dependent relaxation processes. It was shown that the Orbach process was not dominant, and that direct, Raman, and through-barrier relaxation pathways were present.

A d^6 Fe(II) pseudo-two-coordinate compound Fe(Cp^{R5})(C_6H_3-2,6-^{i}Pr$_2$) **liv** (R = ^{i}Pr) exhibited a near-linear Cp-Fe-C bond angle (177°) (Figure 1.8).[202] Simulation of the ZFS parameters yielded a very large negative D value (-51.4 cm^{-1}), based upon the χT value of 3.41 cm^3 K mol^{-1}, and so compound **liv** was expected to have a reasonably high spin reversal barrier. The ac susceptibility measurements confirmed the presence of slow magnetic relaxation, but only when under an applied field to suppress the QTM process. Compound **liv** appeared to have two separate relaxation process, with χ'' peak maxima at high frequency under small dc fields (< 750 Oe), before a low frequency χ'' peak maxima appears at larger dc fields (> 2000 Oe). Measurement of the temperature dependence of dynamic susceptibility occurred at both 750 Oe and 2500 Oe up to 15 K, leading to U_{eff} values of 28.0 cm^{-1} under 750 Oe and 99.7 cm^{-1} under the 2500 Oe field.

1.5 Previous Work

Scheme 1.17 showcases the chemistry done by previous members of the Whittlesey group (Poulten, Page) involving Ni(I) complexes stabilised by large-ring (or ring-expanded) carbenes.[112, 119, 203-205] All of the studies originate from the three-coordinate species Ni(6Mes)(PPh_3)Br (shown in the centre of Scheme 1.17). This thesis focuses on further investigating the interesting magnetic properties of the two-coordinate *bis*-NHC system (highlighted at the bottom of Scheme 1.17), and the effect that altering the nature of the carbene ligands has on the magnetic behaviour. This entailed (i) preparing and studying the reactivity of a range of new three-coordinate Ni(I) precursors (Chapter 2), (ii) the characterisation of the electronic and magnetic properties of homoleptic two-coordinate *bis*-NHC species (Chapter 3), and (iii) the preparation of two-coordinate Ni(I) complexes featuring two different NHCs or an NHC and a phosphine (Chapter 4). A side project on the use of NHCs themselves as catalysts for the hydrophosphination of alkynes is described in Chapter 5.

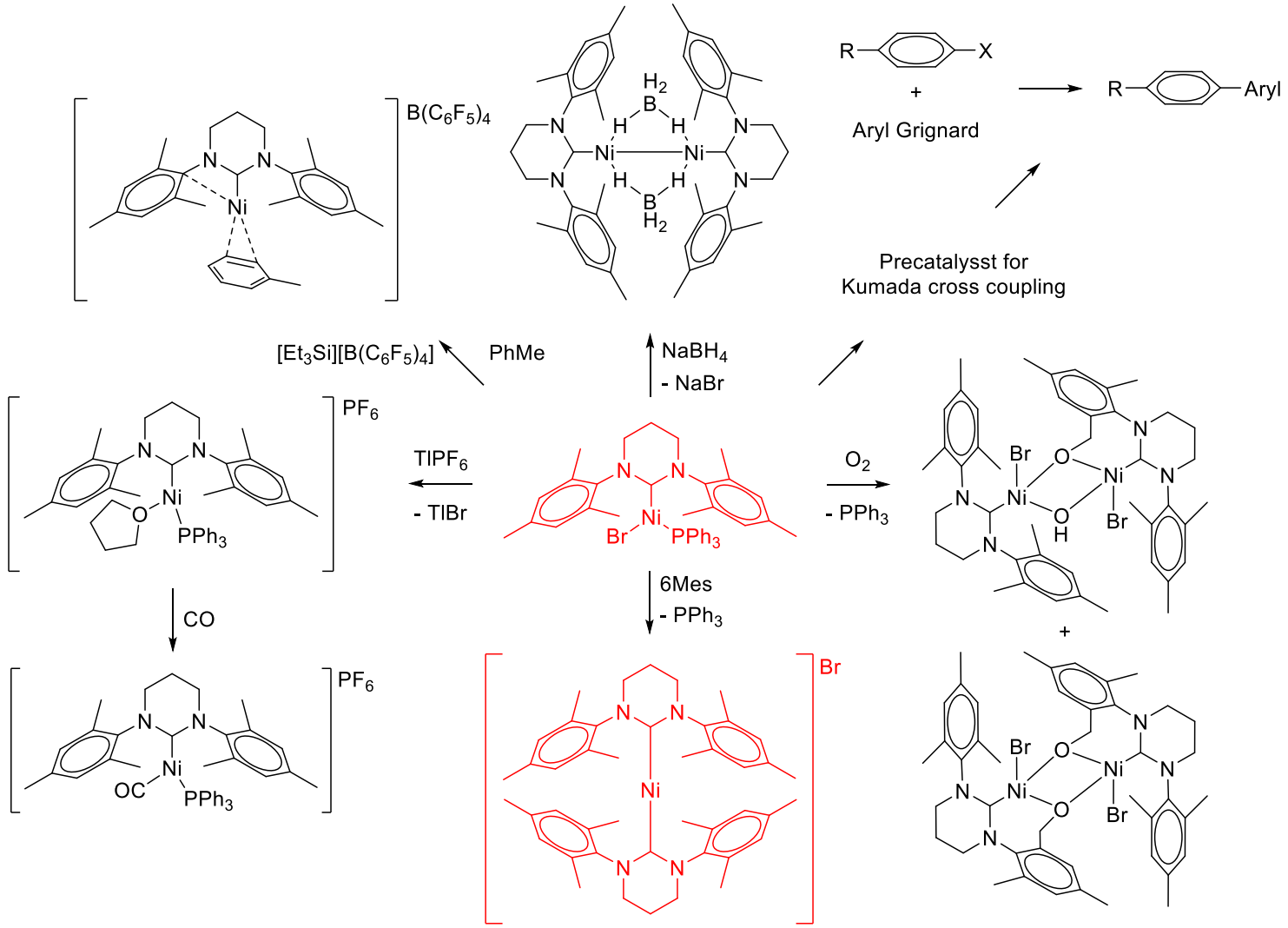

Scheme 1.17 Summary of Ni(I) chemistry undertaken by previous members of the group; Poulten, Page, *et al.*[112, 119, 203-205]

1.6 References

1. M. L. H. Green and H. Munakata, *J. Chem. Soc., Dalton Trans.*, 1974, 269-272.
2. C. A. Tolman, *Chem. Rev.*, 1977, **77**, 313-348.
3. C. A. Tolman, R. J. McKinney, W. C. Seidel, J. D. Druliner and W. R. Stevens, *Adv. Catal.*, 1985, **33**, 1-46.
4. G. Wilke, *Angew. Chem. Int. Ed.*, 1988, **27**, 185-206.
5. W. Keim, *Angew. Chem. Int. Ed.*, 1990, **29**, 235-244.
6. S. Z. Tasker, E. A. Standley and T. F. Jamison, *Nature*, 2014, **509**, 299-309.
7. F. A. Cotton, G. Wilkinson, C. A. Murillo and M. Bochmann, *Advanced Inorganic Chemistry*, John Wiley & Sons Ltd, Chichester, U.K., 6th edn., 1999.
8. K. Nag and A. Chakravorty, *Coord. Chem. Rev.*, 1980, **33**, 87-147.
9. L. Sacconi, F. Mani and A. Benici, in *Comprehensive coordination chemistry: the synthesis, reactions, properties and applications of coordination compounds*, ed. G.Wilkinson, Pergamon, Oxford, 1987.
10. F. Meyer and H. Kozlowski, in *Comprehensive Coordination Chemistry*, ed. J. A. Meyer and T. J. McCleverty, Pergamon, Oxford, 2nd edn., 2003, vol. 6, ch. 3, 247-554.
11. P. Zimmermann and C. Limberg, *J. Am. Chem. Soc.*, 2017, **139**, 4233-4242.
12. J. Harmer, C. Finazzo, R. Piskorski, S. Ebner, E. C. Duin, M. Goenrich, R. K. Thauer, M. Reiher, A. Schweiger, D. Hinderberger and B. Jaun, *J. Am. Chem. Soc.*, 2008, **130**, 10907-10920.
13. X. Li, J. Telser, R. C. Kunz, B. M. Hoffman, G. Gerfen and S. W. Ragsdale, *Biochemistry*, 2010, **49**, 6866-6876.
14. S. Scheller, M. Goenrich, R. Boecher, R. K. Thauer and B. Jaun, *Nature*, 2010, **465**, 606-U697.
15. S. Scheller, M. Goenrich, S. Mayr, R. K. Thauer and B. Jaun, *Angew. Chem. Int. Ed.*, 2010, **49**, 8112-8115.
16. J. Nishigaki, T. Matsumoto and K. Tatsumi, *Inorg. Chem.*, 2012, **51**, 5173-5187.
17. D. J. Evans, *Coord. Chem. Rev.*, 2005, **249**, 1582-1595.
18. S. W. Ragsdale, *Chem. Rev.*, 2006, **106**, 3317-3337.
19. M. Can, F. A. Armstrong and S. W. Ragsdale, *Chem. Rev.*, 2014, **114**, 4149-4174.
20. F. Han, *Chem. Soc. Rev.*, 2013, **42**, 5270-5298.
21. V. P. Ananikov, *ACS Catal.*, 2015, **5**, 1964-1971.

22. N. Hazari, P. R. Melvin and M. M. Beromi, *Nat. Rev. Chem.*, 2017, **1**, 1-16.
23. C. Lin and P. P. Power, *Chem. Soc. Rev.*, 2017, **46**, 5347-5399.
24. D. J. Mindiola and G. L. Hillhouse, *J. Am. Chem. Soc.*, 2001, **123**, 4623-4624.
25. R. Melenkivitz, D. J. Mindiola and G. L. Hillhouse, *J. Am. Chem. Soc.*, 2002, **124**, 3846-3847.
26. D. J. Mindiola, R. Waterman, D. M. Jenkins and G. L. Hillhouse, *Inorg. Chim. Acta*, 2003, **345**, 299-308.
27. K. D. Kitiachvili, D. J. Mindiola and G. L. Hillhouse, *J. Am. Chem. Soc.*, 2004, **126**, 10554-10555.
28. J. Langer, R. Fischer, H. Goerls, N. Theyssen and D. Walther, *Z. Anorg. Allg. Chem.*, 2007, **633**, 557-562.
29. M. J. Ingleson, B. C. Fullmer, D. T. Buschhorn, H. Fan, M. Pink, J. C. Huffman and K. G. Caulton, *Inorg. Chem.*, 2008, **47**, 407-409.
30. Y. Xiong, S. Yao, E. Bill and M. Driess, *Inorg. Chem.*, 2009, **48**, 7522-7524.
31. V. M. Iluc and G. L. Hillhouse, *J. Am. Chem. Soc.*, 2010, **132**, 11890-11892.
32. J. Cornella, E. Gomez-Bengoa and R. Martin, *J. Am. Chem. Soc.*, 2013, **135**, 1997-2009.
33. R. Beck, M. Shoshani, J. Krasinkiewicz, J. A. Hatnean and S. A. Johnson, *Dalton Trans.*, 2013, **42**, 1461-1475.
34. G. Yin, I. Kalvet, U. Englert and F. Schoenebeck, *J. Am. Chem. Soc.*, 2015, **137**, 4164-4172.
35. L. M. Guard, M. Mohadjer Beromi, G. W. Brudvig, N. Hazari and D. J. Vinyard, *Angew. Chem. Int. Ed.*, 2015, **54**, 13352-13356.
36. P. L. Holland, T. R. Cundari, L. L. Perez, N. A. Eckert and R. J. Lachicotte, *J. Am. Chem. Soc.*, 2002, **124**, 14416-14424.
37. N. A. Eckert, E. M. Bones, R. J. Lachicotte and P. L. Holland, *Inorg. Chem.*, 2003, **42**, 1720-1725.
38. D. Zhang, G. Jin, L. Weng and F. Wang, *Organometallics*, 2004, **23**, 3270-3275.
39. N. A. Eckert, A. Dinescu, T. R. Cundari and P. L. Holland, *Inorg. Chem.*, 2005, **44**, 7702-7704.
40. G. C. Bai, P. R. Wei and D. W. Stephan, *Organometallics*, 2005, **24**, 5901-5908.
41. E. Kogut, H. L. Wiencko, L. B. Zhang, D. E. Cordeau and T. H. Warren, *J. Am. Chem. Soc.*, 2005, **127**, 11248-11249.
42. S. Pfirrmann, C. Limberg and B. Ziemer, *Dalton Trans.*, 2008, 6689-6691.

43. Y. Tsai, *Coord. Chem. Rev.*, 2012, **256**, 722-758.
44. C. Chen, S. M. Bellows and P. L. Holland, *Dalton Trans.*, 2015, **44**, 16654-16670.
45. I. Bellucci and R. Corelli, *Z. Anorg. Allg. Chem.*, 1914, **86**, 88-104.
46. J. W. Eastes and W. M. Burgess, *J. Am. Chem. Soc.*, 1942, **64**, 1187-1189.
47. R. Nast and W. Pfab, *Naturwissenschaften*, 1952, **39**, 300-300.
48. M. F. A. El-Sayed and R. K. Sheline, *J. Am. Chem. Soc.*, 1956, **78**, 702-706.
49. W. M. Burgess, J. W. Eastes, W. E. Parker and J. Kleinberg, *Inorg. Synth.*, 1957, **5**, 197-201.
50. W. P. Griffith and G. Wilkinson, *J. Inorg. Nucl. Chem.*, 1958, **7**, 295-297.
51. J. R. Miller, in *Adv. Inorg. Chem. Radiochem.*, eds. H. J. Emeléus and A. G. Sharpe, Academic Press, 1962, vol. 4, pp. 133-195.
52. W. P. Griffith and A. J. Wickham, *J. Chem. Soc. A*, 1969, 834-839.
53. O. Jarchow, H. Schulz and R. Nast, *Angew. Chem. Int. Ed.*, 1970, **9**, 71-71.
54. O. Jarchow, *Z. Anorg. Allg. Chem.*, 1971, **383**, 40-48.
55. O. Jarchow, *Z. Kristallogr.*, 1972, **136**, 122.
56. D. C. Bradley, M. B. Hursthouse, R. J. Smallwood and A. J. Welch, *J. Chem. Soc., Chem. Comm.*, 1972, 872-873.
57. M. F. Lappert and G. Speier, *J. Organomet. Chem.*, 1974, **80**, 329-339.
58. M. Aresta, C. F. Nobile and A. Sacco, *Inorg. Chim. Acta*, 1975, **12**, 167-178.
59. P. Heimbach, *Angew. Chem. Int. Ed.*, 1964, **3**, 648-649.
60. C. Mealli, P. Dapporto, V. Sriyunyongwat and T. A. Albright, *Acta Crystallogr. Sect. C*, 1983, **39**, 995-996.
61. D. D. Ellis and A. L. Spek, *Acta. Crystallogr.*, 2000, **C56**, 1067-1070.
62. N. C. Norman, A. G. Orpen, M. J. Quayle and G. R. Whittell, *Acta. Crystallogr.*, 2002, **C58**, m160-m161.
63. W. Lin, T. Bodenstein, V. Mereacre, K. Fink and A. Eichhofer, *Inorg. Chem.*, 2016, **55**, 2091-2100.
64. R. Beck and S. A. Johnson, *Organometallics*, 2012, **31**, 3599-3609.
65. J. B. Dumas and E. Peligot, *Ann. Chim. Phys.*, 1835, **58**, 5.
66. W. von E. Doering and A. K. Hoffmann, *J. Am. Chem. Soc.*, 1954, **76**, 6162-6165.
67. E. O. Fischer and A. Maasbol, *Angew. Chem.*, 1964, **3**, 580-581.
68. R. Breslow, *J. Am. Chem. Soc.*, 1958, **80**, 3719-3726.
69. H. W. Wanzlick, *Angew. Chem. Int. Ed.*, 1962, **1**, 75-80.

70. A. Igau, H. Grutzmacher, A. Baceiredo and G. Bertrand, *J. Am. Chem. Soc.*, 1988, **110**, 6463-6466.
71. D. Bourissou, O. Guerret, F. P. Gabbaï and G. Bertrand, *Chem. Rev.*, 2000, **100**, 39-92.
72. R. Gleiter and R. Hoffmann, *J. Am. Chem. Soc.*, 1968, **90**, 5457-5460.
73. G. B. Schuster, *Adv. Phys. Org. Chem.*, 1986, **22**, 311-361.
74. R. Dicosimo and G. M. Whitesides, *J. Am. Chem. Soc.*, 1982, **104**, 3601-3607.
75. H. W. Wanzlick and E. Schikora, *Angew. Chem.*, 1960, **72**, 494-494.
76. H. Wanzlick and E. Schikora, *Chem. Ber.*, 1961, **94**, 2389-2393.
77. D. M. Lemal, R. A. Lovald and K. I. Kawano, *J. Am. Chem. Soc.*, 1964, **86**, 2518-2519.
78. H. E. Winberg, J. E. Carnahan, D. D. Coffman and M. Brown, *J. Am. Chem. Soc.*, 1965, **87**, 2055-2056.
79. M. K. Denk, K. Hatano and M. Ma, *Tetrahedron Lett.*, 1999, **40**, 2057-2060.
80. H. W. Wanzlick and H. J. Schönherr, *Angew. Chem. Int. Ed.*, 1968, **7**, 141-142.
81. A. J. Arduengo, III, R. L. Harlow and M. Kline, *J. Am. Chem. Soc.*, 1991, **113**, 361-363.
82. A. J. Arduengo, III, H. V. R. Dias, R. L. Harlow and M. Kline, *J. Am. Chem. Soc.*, 1992, **114**, 5530-5534.
83. A. J. Arduengo, III, F. Davidson, H. V. R. Dias, J. R. Goerlich, D. Khasnis, W. J. Marshall and T. K. Prakasha, *J. Am. Chem. Soc.*, 1997, **119**, 12742-12749.
84. C. M. Crudden and D. P. Allen, *Coord. Chem. Rev.*, 2004, **248**, 2247-2273.
85. W. A. Herrmann, *Angew. Chem. Int. Ed.*, 2002, **41**, 1290-1309.
86. S. Diez-Gonzalez, N. Marion and S. P. Nolan, *Chem. Rev.*, 2009, **109**, 3612-3676.
87. C. Boehme and G. Frenking, *J. Am. Chem. Soc.*, 1996, **118**, 2039-2046.
88. C. Heinemann, T. Muller, Y. Apeloig and H. Schwarz, *J. Am. Chem. Soc.*, 1996, **118**, 2023-2038.
89. J. C. Green, R. G. Scurr, P. L. Arnold and F. G. N. Cloke, *Chem. Commun.*, 1997, 1963-1964.
90. X. L. Hu, I. Castro-Rodriguez, K. Olsen and K. Meyer, *Organometallics*, 2004, **23**, 755-764.
91. H. Jacobsen, A. Correa, C. Costabile and L. Cavallo, *J. Organomet. Chem.*, 2006, **691**, 4350-4358.

92. M. D. Sanderson, J. W. Kamplain and C. W. Bielawski, *J. Am. Chem. Soc.*, 2006, **128**, 16514-16515.
93. H. Jacobsen, A. Correa, A. Poater, C. Costabile and L. Cavallo, *Coord. Chem. Rev.*, 2009, **253**, 687-703.
94. M. Alcarazo, T. Stork, A. Anoop, W. Thiel and A. Fürstner, *Angew. Chem. Int. Ed.*, 2010, **49**, 2542-2546.
95. N. M. Scott, R. Dorta, E. D. Stevens, A. Correa, L. Cavallo and S. P. Nolan, *J. Am. Chem. Soc.*, 2005, **127**, 3516-3526.
96. V. Lavallo, Y. Canac, C. Präsang, B. Donnadieu and G. Bertrand, *Angew. Chem. Int. Ed.*, 2005, **44**, 5705-5709.
97. R. Jazzar, R. D. Dewhurst, J. Bourg, B. Donnadieu, Y. Canac and G. Bertrand, *Angew. Chem. Int. Ed.*, 2007, **46**, 2899-2902.
98. L. P. Spencer, S. Winston and M. D. Fryzuk, *Organometallics*, 2004, **23**, 3372-3374.
99. L. P. Spencer and M. D. Fryzuk, *J. Organomet. Chem.*, 2005, **690**, 5788-5803.
100. M. Mayr, K. Wurst, K. H. Ongania and M. R. Buchmeiser, *Chem. Eur. J.*, 2004, **10**, 1256-1266.
101. R. Jazzar, H. Liang, B. Donnadieu and G. Bertrand, *J. Organomet. Chem.*, 2006, **691**, 3201-3205.
102. M. Iglesias, D. J. Beetstra, J. C. Knight, L. L. Ooi, A. Stasch, S. Coles, L. Male, M. B. Hursthouse, K. J. Cavell, A. Dervisi and I. A. Fallis, *Organometallics*, 2008, **27**, 3279-3289.
103. A. Binobaid, M. Iglesias, D. J. Beetstra, B. Kariuki, A. Dervisi, I. A. Fallis and K. J. Cavell, *Dalton Trans.*, 2009, 7099-7112.
104. W. Y. Lu, K. J. Cavell, J. S. Wixey and B. Kariuki, *Organometallics*, 2011, **30**, 5649-5655.
105. J. Li, W. Shen and X. Li, *Curr. Org. Chem.*, 2012, **16**, 2879-2891.
106. A. Cervantes-Reyes, F. Rominger, M. Rudolph and A. S. K. Hashmi, *Chem. Eur. J.*, 2019, **25**, 11745-11757.
107. M. Iglesias, D. J. Beetstra, B. Kariuki, K. J. Cavell, A. Dervisi and I. A. Fallis, *Eur. J. Inorg. Chem.*, 2009, 1913-1919.
108. S. K. Schneider, W. A. Herrmann and E. Herdtweck, *J. Mol. Catal. A: Chem.*, 2006, **245**, 248-254.
109. J. J. Dunsford and K. J. Cavell, *Dalton Trans.*, 2011, **40**, 9131-9135.

110. J. J. Dunsford, K. J. Cavell and B. Kariuki, *J. Organomet. Chem.*, 2011, **696**, 188-194.
111. R. Armstrong, C. Ecott, E. Mas-Marza, M. J. Page, M. F. Mahon and M. K. Whittlesey, *Organometallics*, 2010, **29**, 991-997.
112. C. J. E. Davies, M. J. Page, C. E. Ellul, M. F. Mahon and M. K. Whittlesey, *Chem. Commun.*, 2010, **46**, 5151-5153.
113. H. Tsurugi, S. Fujita, G. Choi, T. Yarnagata, S. Ito, H. Miyasaka and K. Mashima, *Organometallics*, 2010, **29**, 4120-4129.
114. T. W. Hudnall and C. W. Bielawski, *J. Am. Chem. Soc.*, 2009, **131**, 16039-16041.
115. T. W. Hudnall, J. P. Moerdyk and C. W. Bielawski, *Chem. Commun.*, 2010, **46**, 4288-4290.
116. M. Braun, W. Frank, G. J. Reiss and C. Ganter, *Organometallics*, 2010, **29**, 4418-4420.
117. T. W. Hudnall, A. G. Tennyson and C. W. Bielawski, *Organometallics*, 2010, **29**, 4569-4578.
118. V. Cesar, N. Lugan and G. Lavigne, *Eur. J. Inorg. Chem.*, 2010, 361-365.
119. R. C. Poulten, I. Lopez, A. Llobet, M. F. Mahon and M. K. Whittlesey, *Inorg. Chem.*, 2014, **53**, 7160-7169.
120. J. P. Moerdyk and C. W. Bielawski, *Chem. Eur. J.*, 2013, **19**, 14773-14776.
121. J. P. Moerdyk, G. A. Blake, D. T. Chase and C. W. Bielawski, *J. Am. Chem. Soc.*, 2013, **135**, 18798-18801.
122. D. T. Chase, J. P. Moerdyk and C. W. Bielawski, *Org. Lett.*, 2014, **16**, 812-815.
123. D. N. Lastovickova, J. P. Moerdyk, A. R. Kelley and C. W. Bielawski, *J. Phys. Org. Chem.*, 2015, **28**, 75-78.
124. D. N. Lastovickova and C. W. Bielawski, *Organometallics*, 2016, **35**, 706-712.
125. D. R. Anderson, V. Lavallo, D. J. O'Leary, G. Bertrand and R. H. Grubbs, *Angew. Chem. Int. Ed.*, 2007, **46**, 7262-7265.
126. V. Lavallo, G. D. Frey, B. Donnadieu, M. Soleilhavoup and G. Bertrand, *Angew. Chem. Int. Ed.*, 2008, **47**, 5224-5228.
127. G. D. Frey, J. D. Masuda, B. Donnadieu and G. Bertrand, *Angew. Chem. Int. Ed.*, 2010, **49**, 9444-9447.
128. M. Soleilhavoup and G. Bertrand, *Acc. Chem. Res.*, 2015, **48**, 256-266.
129. S. Roy, K. C. Mondal and H. W. Roesky, *Acc. Chem. Res.*, 2016, **49**, 357-369.

130. M. Melaimi, R. Jazzar, M. Soleilhavoup and G. Bertrand, *Angew. Chem. Int. Ed.*, 2017, **56**, 10046-10068.
131. B. R. Dible, M. S. Sigman and A. M. Arif, *Inorg. Chem.*, 2005, **44**, 3774-3776.
132. K. Matsubara, H. Yamamoto, S. Miyazaki, T. Inatomi, K. Nonaka, Y. Koga, Y. Yamada, L. F. Veiros and K. Kirchner, *Organometallics*, 2017, **36**, 255-265.
133. S. Miyazaki, Y. Koga, T. Matsumoto and K. Matsubara, *Chem. Commun.*, 2010, **46**, 1932-1934.
134. K. Matsubara, K. Ueno and Y. Shibata, *Organometallics*, 2006, **25**, 3422-3427.
135. K. Matsubara, K. Ueno, Y. Koga and K. Hara, *J. Org. Chem.*, 2007, **72**, 5069-5076.
136. K. Matsubara, S. Miyazaki, Y. Koga, Y. Nibu, T. Hashimura and T. Matsumoto, *Organometallics*, 2008, **27**, 6020-6024.
137. S. Nagao, T. Matsumoto, Y. Koga and K. Matsubara, *Chem. Lett.*, 2011, **40**, 1036-1038.
138. K. Matsubara, Y. Fukahori, T. Inatomi, S. Tazaki, Y. Yamada, Y. Koga, S. Kanegawa and T. Nakamura, *Organometallics*, 2016, **35**, 3281-3287.
139. K. Zhang, M. Conda-Sheridan, S. R. Cooke and J. Louie, *Organometallics*, 2011, **30**, 2546-2552.
140. A. Velian, S. Lin, A. J. M. Miller, M. W. Day and T. Agapie, *J. Am. Chem. Soc.*, 2010, **132**, 6296-6297.
141. T. N. Tekavec, G. Zuo, K. Simon and J. Louie, *J. Org. Chem.*, 2006, **71**, 5834-5836.
142. M. Vogt, B. de Bruin, H. Berke, M. Trincado and H. Gruetzmacher, *Chem. Sci.*, 2011, **2**, 723-727.
143. T. J. Anderson, G. D. Jones and D. A. Vicic, *J. Am. Chem. Soc.*, 2004, **126**, 8100-8101.
144. G. D. Jones, J. L. Martin, C. McFarland, O. R. Allen, R. E. Hall, A. D. Haley, R. J. Brandon, T. Kanovalova, P. J. Desrochers, P. Pulay and D. A. Vicic, *J. Am. Chem. Soc.*, 2006, **128**, 13175-13183.
145. C. A. Laskowski and G. L. Hillhouse, *J. Am. Chem. Soc.*, 2008, **130**, 13846-13847.
146. C. A. Laskowski, D. J. Bungum, S. M. Baldwin, S. A. Del Ciello, V. M. Iluc and G. L. Hillhouse, *J. Am. Chem. Soc.*, 2013, **135**, 18272-18275.

147. C. A. Laskowski, G. R. Morello, C. T. Saouma, T. R. Cundari and G. L. Hillhouse, *Chem. Sci.*, 2013, **4**, 170-174.
148. M. Ito, T. Matsumoto and K. Tatsumi, *Inorg. Chem.*, 2009, **48**, 2215-2223.
149. M. I. Lipschutz and T. D. Tilley, *Chem. Commun.*, 2012, **48**, 7146-7148.
150. M. I. Lipschutz, X. Yang, R. Chatterjee and T. D. Tilley, *J. Am. Chem. Soc.*, 2013, **135**, 15298-15301.
151. M. I. Lipschutz and T. D. Tilley, *Organometallics*, 2014, **33**, 5566-5570.
152. D. D. Beattie, E. G. Bowes, M. W. Drover, J. A. Love and L. L. Schafer, *Angew. Chem. Int. Ed.*, 2016, **55**, 13290-13295.
153. S. Pelties, D. Herrmann, B. de Bruin, F. Hartl and R. Wolf, *Chem. Commun.*, 2014, **50**, 7014-7016.
154. S. Pelties and R. Wolf, *Organometallics*, 2016, **35**, 2722-2727.
155. U. Chakraborty, F. Urban, B. Muehldorf, C. Rebreyend, B. de Bruin, N. van Velzen, S. Harder and R. Wolf, *Organometallics*, 2016, **35**, 1624-1631.
156. U. Chakraborty, B. Mühldorf, N. J. C. van Velzen, B. de Bruin, S. Harder and R. Wolf, *Inorg. Chem.*, 2016, **55**, 3075-3078.
157. U. Chakraborty, M. Modl, B. Mühldorf, M. Bodensteiner, S. Demeshko, N. J. C. van Velzen, M. Scheer, S. Harder and R. Wolf, *Inorg. Chem.*, 2016, **55**, 3065-3074.
158. J. G. Wu, A. Nova, D. Balcells, G. W. Brudvig, W. Dai, L. M. Guard, N. Hazari, P. H. Lin, R. Pokhrel and M. K. Takase, *Chem. Eur. J.*, 2014, **20**, 5327-5337.
159. S. Pelties, E. Carter, A. Folli, M. F. Mahon, D. M. Murphy, M. K. Whittlesey and R. Wolf, *Inorg. Chem.*, 2016, **55**, 11006-11017.
160. P. P. Power, *Chem. Rev.*, 2012, **112**, 3482-3507.
161. M. Hargittai, *Coord. Chem. Rev.*, 1988, **91**, 35-88.
162. P. P. Power, *J. Organomet. Chem.*, 2004, **689**, 3904-3919.
163. A. Werner, *Z. Anorg. Chem.*, 1893, **3**, 267-330.
164. H. Bürger and U. Wannagat, *Monatsh. Chem.*, 1963, **94**, 1007-1012.
165. H. Bürger and U. Wannagat, *Monatsh. Chem.*, 1964, **95**, 1099-1102.
166. D. C. Bradley, M. B. Hursthouse and P. F. Rodesiler, *Chem. Commun.*, 1969, 14-15.
167. P. G. Eller, D. C. Bradley, M. B. Hursthouse and D. W. Meek, *Coord. Chem. Rev.*, 1977, **24**, 1-95.
168. S. Alvarez, *Coord. Chem. Rev.*, 1999, **193–195**, 13-41.

169. G. K. Barker and M. F. Lappert, *J. Organomet. Chem.*, 1974, **76**, C45-C46.
170. P. B. Hitchcock, M. F. Lappert, R. G. Smith, R. A. Bartlett and P. P. Power, *J. Chem. Soc., Chem. Commun.*, 1988, 1007-1009.
171. N. H. Buttrus, C. Eaborn, P. B. Hitchcock, J. D. Smith and A. C. Sullivan, *J. Chem. Soc., Chem. Commun.*, 1985, 1380-1381.
172. R. A. Andersen, A. Haaland, K. Rypdal and H. V. Volden, *J. Chem. Soc., Chem. Commun.*, 1985, 1807-1808.
173. R. A. Bartlett and P. P. Power, *J. Am. Chem. Soc.*, 1987, **109**, 7563-7564.
174. R. A. Andersen, K. Faegri, J. C. Green, A. Haaland, M. F. Lappert, W. P. Leung and K. Rypdal, *Inorg. Chem.*, 1988, **27**, 1782-1786.
175. W. M. Reiff, A. M. LaPointe and E. H. Witten, *J. Am. Chem. Soc.*, 2004, **126**, 10206-10207.
176. W. M. Reiff, C. E. Schulz, M. Whangbo, J. I. Seo, Y. S. Lee, G. R. Potratz, C. W. Spicer and G. S. Girolami, *J. Am. Chem. Soc.*, 2009, **131**, 404-405.
177. W. Alexander Merrill, T. A. Stich, M. Brynda, G. J. Yeagle, J. C. Fettinger, R. D. Hont, W. M. Reiff, C. E. Schulz, R. D. Britt and P. P. Power, *J. Am. Chem. Soc.*, 2009, **131**, 12693-12702.
178. F. Neese and D. A. Pantazis, *Faraday Discuss.*, 2011, **148**, 229-238.
179. R. A. Layfield, *Organometallics*, 2014, **33**, 1084-1099.
180. G. A. Craig and M. Murrie, *Chem. Soc. Rev.*, 2015, **44**, 2135-2147.
181. J. M. Frost, K. L. Harriman and M. Murugesu, *Chem. Sci.*, 2016, **7**, 2470-2491.
182. M. Feng and M. Tong, *Chem. Eur. J.*, 2018, **24**, 7574-7594.
183. F. Guo, A. K. Bar and R. A. Layfield, *Chem. Rev.*, 2019, **119**, 8479-8505.
184. Z. Mo, D. Chen, X. Leng and L. Deng, *Organometallics*, 2012, **31**, 7040-7043.
185. Y. Meng, Z. Mo, B. Wang, Y. Zhang, L. Deng and S. Gao, *Chem. Sci.*, 2015, **6**, 7156-7162.
186. J. Du, L. Wang, M. Xie and L. Deng, *Angew. Chem. Int. Ed.*, 2015, **54**, 12640-12644.
187. X. Yao, J. Du, Y. Zhang, X. Leng, M. Yang, S. Jiang, Z. Wang, Z. Ouyang, L. Deng, B. Wang and S. Gao, *J. Am. Chem. Soc.*, 2017, **139**, 373-380.
188. P. C. Bunting, M. Atanasov, E. Damgaard-Møller, M. Perfetti, I. Crassee, M. Orlita, J. Overgaard, J. van Slageren, F. Neese and J. R. Long, *Science*, 2018, **362**, 1378.

189. U. Chakraborty, S. Demeshko, F. Meyer, C. Rebreyend, B. de Bruin, M. Atanasov, F. Neese, B. Mühldorf and R. Wolf, *Angew. Chem. Int. Ed.*, 2017, **56**, 7995-7999.

190. P. P. Samuel, K. C. Mondal, H. W. Roesky, M. Hermann, G. Frenking, S. Demeshko, F. Meyer, A. C. Stückl, J. H. Christian, N. S. Dalal, L. Ungur, L. F. Chibotaru, K. Pröpper, A. Meents and B. Dittrich, *Angew. Chem. Int. Ed.*, 2013, **52**, 11817-11821.

191. G. Ung, J. Rittle, M. Soleilhavoup, G. Bertrand and J. C. Peters, *Angew. Chem. Int. Ed.*, 2014, **53**, 8427-8431.

192. P. P. Samuel, R. Neufeld, K. Chandra Mondal, H. W. Roesky, R. Herbst-Irmer, D. Stalke, S. Demeshko, F. Meyer, V. C. Rojisha, S. De, P. Parameswaran, A. C. Stückl, W. Kaim, J. H. Christian, J. K. Bindra and N. S. Dalal, *Chem. Sci.*, 2015, **6**, 3148-3153.

193. P. P. Samuel, K. C. Mondal, N. Amin Sk, H. W. Roesky, E. Carl, R. Neufeld, D. Stalke, S. Demeshko, F. Meyer and L. Ungur, *J. Am. Chem. Soc.*, 2014, **136**, 11964-11971.

194. C. G. Werncke, P. C. Bunting, C. Duhayon, J. R. Long, S. Bontemps and S. Sabo-Etienne, *Angew. Chem. Int. Ed.*, 2015, **54**, 245-248.

195. C. G. Werncke, E. Suturina, P. C. Bunting, L. Vendier, J. R. Long, M. Atanasov, F. Neese, S. Sabo-Etienne and S. Bontemps, *Chem. Eur. J.*, 2016, **22**, 1668-1674.

196. J. M. Zadrozny, D. J. Xiao, M. Atanasov, G. J. Long, F. Grandjean, F. Neese and J. R. Long, *Nat. Chem.*, 2013, **5**, 577-581.

197. J. M. Zadrozny, M. Atanasov, A. M. Bryan, C. Lin, B. D. Rekken, P. P. Power, F. Neese and J. R. Long, *Chem. Sci.*, 2013, **4**, 125-138.

198. M. Atanasov, J. M. Zadrozny, J. R. Long and F. Neese, *Chem. Sci.*, 2013, **4**, 139-156.

199. T. Viefhaus, W. Schwarz, K. Hübler, K. Locke and J. Weidlein, *Z. Anorg. Allg. Chem.*, 2001, **627**, 715-725.

200. A. M. LaPointe, *Inorg. Chim. Acta*, 2003, **345**, 359-362.

201. C. Ni and P. P. Power, *Chem. Commun.*, 2009, 5543-5545.

202. D. Weismann, Y. Sun, Y. Lan, G. Wolmershäuser, A. K. Powell and H. Sitzmann, *Chem. Eur. J.*, 2011, **17**, 4700-4704.

203. R. C. Poulten, M. J. Page, A. G. Algarra, J. J. Le Roy, I. Lopez, E. Carter, A. Llobet, S. A. Macgregor, M. F. Mahon, D. M. Murphy, M. Murugesu and M. K. Whittlesey, *J. Am. Chem. Soc.*, 2013, **135**, 13640-13643.

204. M. J. Page, W. Y. Lu, R. C. Poulten, E. Carter, A. G. Algarra, B. M. Kariuki, S. A. Macgregor, M. F. Mahon, K. J. Cavell, D. M. Murphy and M. K. Whittlesey, *Chem. Eur. J.*, 2013, **19**, 2158-2167.

205. W. J. M. Blackaby, S. Sabater, R. C. Poulten, M. J. Page, A. Folli, V. Krewald, M. F. Mahon, D. M. Murphy, E. Richards and M. K. Whittlesey, *Dalton Trans.*, 2018, **47**, 769-782.

CHAPTER 2

2 SYNTHESIS OF THREE-COORDINATE Ni(RE-NHC)(PR_3)Br COMPOUNDS

Some of the work in this chapter has been published previously in:

W. J. M. Blackaby, S. Sabater, R. C. Poulten, M. J. Page, A. Folli, V. Krewald, M. F. Mahon, D. M. Murphy, E. Richards and M. K. Whittlesey, *Dalton Trans.*, 2018, **47**, 769-782.

Compounds **2.1**, **2.3**, **2.5**, **2.7**, **2.9**, **2.12**, **2.17**, **2.19** and **2.20** were synthesised by previous members of the group, and remade (*via* published or modified synthetic routes) by Blackaby.[1-4] Compounds **I** and **II** were made by previous members of the group.

2.1 Background

2.1.1 Synthesis and Characterisation of Ni(6Mes)(PPh_3)Br (2.1)

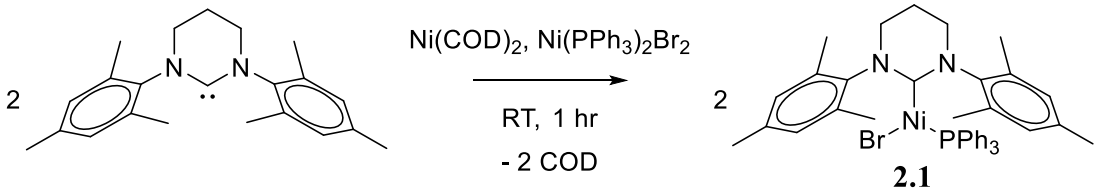

2.1

Scheme 2.1 Synthesis of Ni(6Mes)(PPh_3)Br **2.1**.

In 2010, Whittlesey and co-workers reported the use of the six-membered ring-expanded NHC (RE-NHC) 6Mes for the stabilisation of the novel, three-coordinate, $15e^-$ Ni(I) compound, Ni(6Mes)(PPh_3)Br **2.1** (Scheme 2.1).[1] The reported synthesis of this air- and moisture-sensitive compound involved a comproportionation reaction of $Ni(COD)_2$ and $Ni(PPh_3)_2Br_2$ in the presence of 6Mes (2 equiv.), generated *in-situ* from the reaction of [6MesH]BF_4 and $KN(SiMe_3)_2$. Due to reproducibility issues, a more reliable procedure involved isolating free 6Mes before subsequent reaction with the nickel reagents in THF at room temperature for 1 hr. Compound **2.1** could be isolated as a bright yellow solid in 84% yield. The ^{1}H NMR spectrum (Figure 2.1) showed a series of broad and paramagnetically shifted resonances between δ 30 to -17 ppm. Integration and therefore assignment of individual peaks was not possible. Moreover, $^{31}P\{^1H\}$ NMR spectroscopy

did not show any signal for PPh_3 (bound or free). A room temperature solution magnetic moment of 2.1 μ_B was recorded in C_6H_6 *via* the Evans method, consistent with the presence of a single unpaired electron.

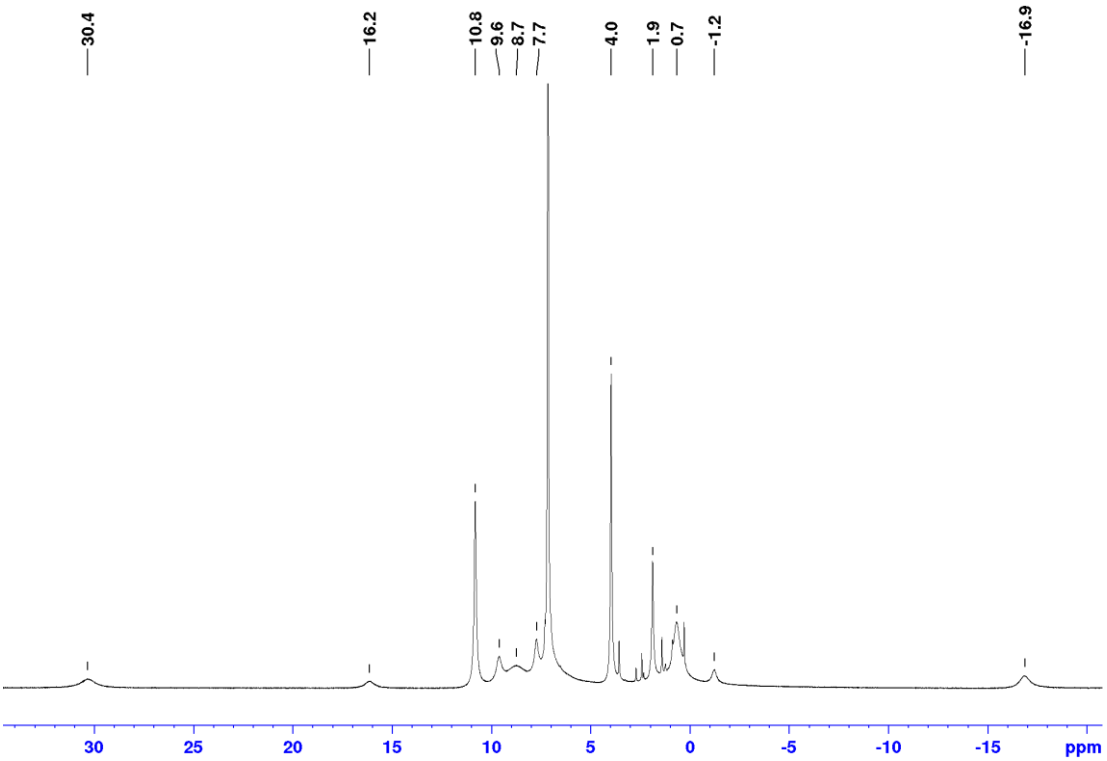

Figure 2.1 ^{1}H NMR spectrum (C_6D_6, 500 MHz, 298 K) of compound **2.1**.

X-ray crystallography revealed a distorted trigonal planar structure for **2.1** (Figure 2.2) with the sum of internal angles equalling 360.00(9)° (C_{NHC}-Ni-P: 117.01(6)°, C_{NHC}-Ni-Br: 133.46(6)°, P-Ni-Br: 109.531(19)°).

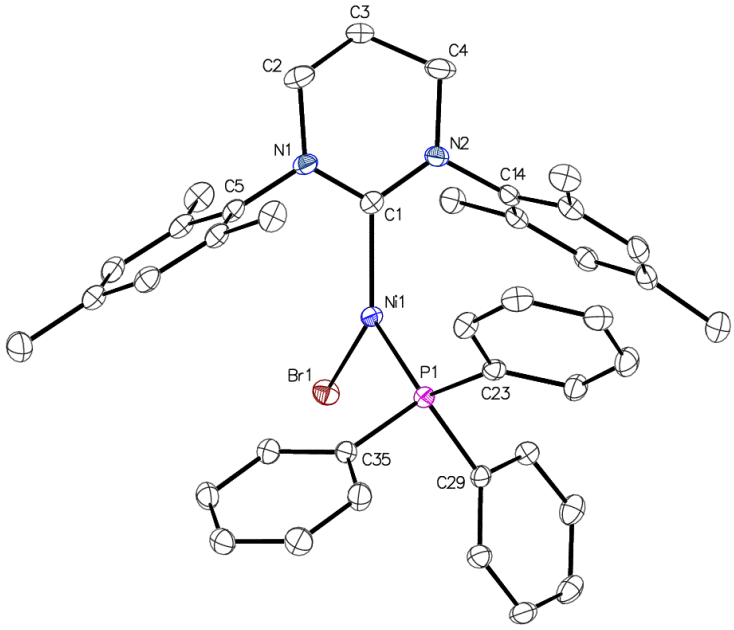

Figure 2.2 Molecular structure of compound **2.1**. Thermal ellipsoids are set at 30% probability. All hydrogen atoms have been omitted for clarity.

This distorted trigonal planar geometry has been observed in other mono-NHC Ni(I) compounds, such as Ni(IPr)(PPh_3)Cl (**xiii**), Ni(IMes)(PPh_3)Cl (**xvi$_a$**), and Ni(IMes)(PPh_3)Br (**xvi$_b$**), which feature C_{NHC}-Ni-X bond angles in the range 131.03(9) – 134.2(1)° (selected bond angles in Table 2.1).[5, 6] However, the geometry contrasts with the *bis*-NHC Ni(I) species Ni(IPr)$_2$Cl (**xii**) and Ni(IMes)$_2$X (**xv**) (X = Cl, Br, I), which are T-shaped and display C_{NHC}-Ni-C_{NHC} bond angles of 166.46(16) – 168.26(12)° (Table 2.1).[7-9] The use of RE-NHCs with bulky aryl N-substituents leads to an increase in steric demands of the carbene ligand, likely leading to the sterics influencing the geometry significantly. It has also been reported that electronics can impact upon the geometry in d^9 systems.[10] For example, β-diketiminate Ni(I) and Cu(II) compounds usually form Y-shaped structures due to the bidentate ligand, but when an electron-withdrawing ligand is involved (such as CO) the geometry changed to T-shaped (*e.g.*, Ni(L)(CO); L = HC(C(Me)NC_6H_3(^{i}Pr)$_2$)$_2$).[10]

Table 2.1 Selected bond angles for various three-coordinate Ni(I)-NHC compounds.

Compound	**C_{NHC}-Ni-P (°)**	**C_{NHC}-Ni-X (°)**	**P-Ni-X (°)**	**C-Ni-C (°)**
2.1	117.01(6)	133.46(6)	109.531(19)	-
Ni(IPr)(PPh_3)Cl[5]	112.1(1)	134.2(1)	113.31(4)	-
Ni(IMes)(PPh_3)Cl[6]	111.6(1)	132.8(1)	115.31(5)	-
Ni(IMes)(PPh_3)Br[6]	112.76(9)	131.03(9)	115.95(3)	-
$Ni(IPr)_2Cl$[7]	-	96.34(10)/95.47(10)	-	168.18(15)
$Ni(IMes)_2Cl$[8]	-	83.8(3)/82.7(3)	-	166.47(10)
$Ni(IMes)_2Br$[8]	-	97.58(11)/95.94(12)	-	166.46(16)
$Ni(IMes)_2I$[8]	-	96.74(8)/94.97(8)	-	168.26(12)

The X-band (~ 9.5 GHz) continuous wave (CW) EPR spectrum of **2.1** (measured at Cardiff University by collaborators Prof. Damien Murphy, Dr. Emma Richards, and Dr. Andrea Folli) was collected in frozen THF/toluene (10:1) at 140 K (Figure 2.3).[2, 4]

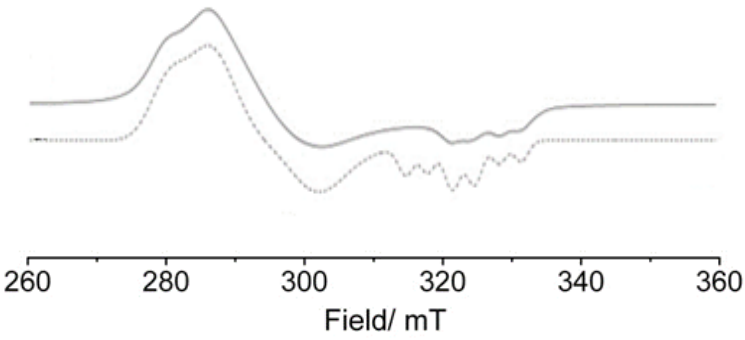

Figure 2.3 Experimental (solid line) and simulated (dashed line) X-band CW EPR spectra (THF/toluene, 140 K) of compound **2.1**.

The EPR measurement afforded a spectrum that displayed a rhombic *g* profile (whereby each *g* value is different) with broadening of linewidths due to the large superhyperfine coupling to EPR-active ^{31}P and $^{79,81}Br$ nuclei. The spin Hamiltonian parameters of **2.1** are displayed in Table 2.2. The magnitude of the *g* values can offer an insight into the location of the unpaired electron.[2] The g_2 and g_3 values were significantly

greater than the g_1 value, suggesting that the lone unpaired electron could be localised in a singly occupied molecular orbital (SOMO) with $3d_{z2}$ character. This was based on the reported DFT calculations on a model three-coordinate Ni(I) compound $[Ni(CO)(H_2O)_2]^+$, whereby the SOMO was calculated to be predominantly $3d_{z2}$ (with some $3d_{x2-y2}$ mixing) resulting in *g* values of 2.017, 2.249, and 2.357, comparable to those of **2.1** (Table 2.2).[11] DFT calculations performed by Prof. Stuart Macgregor and Dr Andrés Algarra at Heriot-Watt University revealed that the SOMO of **2.1** was indeed made up of $3d_{z2}$ and $3d_{x2-y2}$ character, in agreement with the experimental EPR data.[2] The other set of parameters displayed in Table 2.2 are the superhyperfine coupling constants (*A* values), resulting from the unpaired electron coupling to the ligand nuclei. The EPR spectrum showed considerable hyperfine coupling to the coordinated phosphine ligand, with large *A* values of an isotropic nature, reflecting a high degree of Ni-P covalency.[2, 4] Additional hyperfine coupling can be observed to the bromide ligand, though line broadening occurred due to unresolved superhyperfine coupling from both the ^{31}P and ^{79,81}Br nuclei.

Table 2.2 Spin Hamiltonian parameters (*g* values and ^{31}P superhyperfine coupling constants – numbers in brackets are ^{79,81}Br superhyperfine coupling constants) for compound **2.1**.

Compound	g_1	g_2	g_3	A_1 **(MHz)**	A_2 **(MHz)**	A_3 **(MHz)**
2.1	2.050	2.265	2.365	184 (-6)	194 (-27)	250 (70)

To probe the magnetic properties of **2.1**, SQUID measurements were performed (measured by Prof. Muralee Murugesu and Jennifer Le Roy, University of Ottawa). Initially, compound **2.1** was subjected to dc magnetic susceptibility measurements under a 1000 Oe field in the temperature range 1.8 to 300 K. The measured room temperature magnetic susceptibility (χT) value of 0.76 cm^3 K mol^{-1} was significantly higher than the theoretical spin-only value of 0.375 cm^3 K mol^{-1} for a d^9 ion, suggesting significant magnetic anisotropy of the Ni(I) centre. As the temperature was lowered, the χT value steadily decreased until, at *ca*. 10 K, the value notably dropped to a minimum of 0.35 cm^3 K mol^{-1}. This deviation may be a consequence of antiferromagnetic intermolecular interactions between Ni(I) centres, magnetic anisotropy (as identified from the room temperature χT measurements) or the thermal depopulation of excited states.

The field dependence of the magnetisation (M) was examined at 1.8, 3, 5, and 7 K increments and at magnetic fields ranging from 0 to 7 T to yield the *M vs. H* plot in Figure 2.4. At each temperature increment, field dependence of the magnetisation was observed, with near-saturation and a magnetisation value of 1.16 μ_B at 1.8 K under a 7 T field. Moreover, the reduced magnetisation plot (*M vs. H* T^{-1}) displayed curves that do not overlay, signifying potential magnetic anisotropy within the compound (and/or low energy excited states). In an effort to evaluate the slow relaxation of magnetisation in **2.1**, ac susceptibility measurements were performed using the SQUID magnetometer. Under both zero and small (1000 Oe) applied dc fields, no out-of-phase signal in the temperature dependence measurement was observed, most likely due to rapid relaxation *via* QTM. This implied that **2.1** did not show any SIM behaviour. Other examples of nickel species displaying magnetic anisotropy without being SIMs have been reported,[12-17] in particular the Ni(I) species $Ni(PPh_3)_3Cl$,[18] which also exhibited rapid relaxation due to QTM.

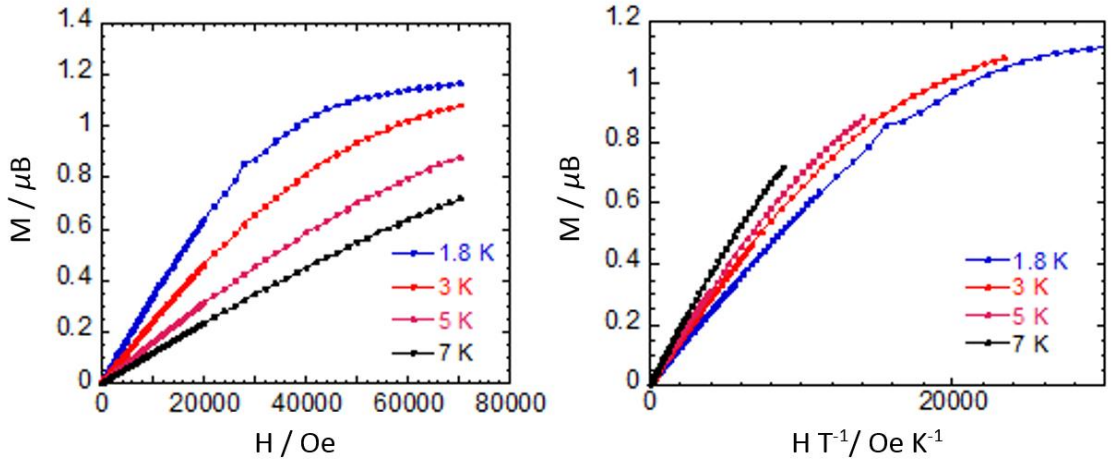

Figure 2.4 Field dependence of the magnetisation (*M vs. H*) (left) and reduced magnetisation (*M vs. H* T^{-1}) (right) for compound **2.1**.

2.2 Synthesis and Characterisation of Ni(RE-NHC)(PPh_3)Br Compounds

Following the successful synthesis and characterisation of **2.1**, the next objective was to better understand the structure and bonding properties of analogous three-coordinate Ni(I) species through the following:

- Synthesis of a range of N-aryl RE-NHCs with different aryl ring substitution patterns and different carbene ring sizes.

- Synthesis of N-alkyl RE-NHC analogues to examine to effect of introducing a flexible N-substituent compared to the more rigid aryl species.
- Subsequent use of new N-aryl and -alkyl RE-NHCs in the synthesis of Ni(I) compounds.
- Varying the phosphine, from PPh_3, through substitution and/or alternative synthetic routes to determine the importance of the phenyl-substituted phosphine in terms of electronic and steric effects.
- Continuation of attempts to perform bromide abstraction on compound **2.1** (and other three-coordinate Ni(I) complexes) in order to form two-coordinate [Ni(RE-NHC)$(PR_3)]^+$ species.
- Any successfully synthesised two- and three-coordinate Ni(I) compounds would be characterised with extensive spectroscopic and computational analysis.

2.2.1 Use of RE-NHCs with N-aryl Substituents

Adopting the same synthetic procedure used for **2.1**, the six- and seven-membered ring NHC compounds **2.2** – **2.9** shown in Scheme 2.2 were prepared. All eight Ni(I) compounds were isolated as bright yellow solids in yields of 32 – 82%, with the exception of the diamidocarbene species **2.9**, which appeared as a dark brown powder. Compounds **2.3**, **2.5**, **2.7**, and **2.9** have been previously reported by the Whittlesey group,[2, 3] while compounds **2.2**, **2.4**, **2.6** and **2.8** were new.

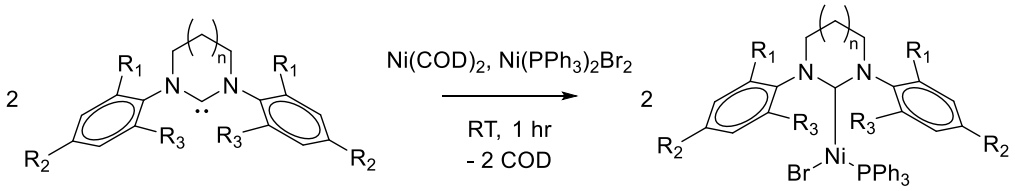

2.2 - 2.8

2.2: RE-NHC = 6Xyl, n = 1, R_1/R_3 = Me, R_2 = H
2.3: RE-NHC = 6^{o}Tol, n = 1, R_1 = Me, R_2/R_3 = H
2.4: RE-NHC = 6Xyl-*p*-Br, n = 1, R_1/R_3 = Me, R_2 = Br
2.5: RE-NHC = 7Mes, n = 2, $R_1/R_2/R_3$ = Me
2.6: RE-NHC = 7Xyl, n = 2, R_1/R_3 = Me, R_2 = H
2.7: RE-NHC = 7^{o}Tol, n = 2, R_1 = Me, R_2/R_3 = H
2.8: RE-NHC = 7Xyl-*p*-Br, n = 2, R_1/R_3 = Me, R_2 = Br

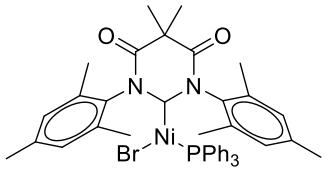

2.9

Scheme 2.2 Syntheses and formulae of the three-coordinate Ni(RE-NHC)(PPh_3)Br compounds **2.2** – **2.9**.

Compounds **2.2** – **2.9** all displayed paramagnetic ^{1}H NMR spectra, with broad signals in the range δ 32 to -20 ppm. As for **2.1**, integration and assignment of signals was again impossible. Similarly, no peaks were again observable in the ^{31}P{^{1}H} NMR spectra. The room temperature solution magnetic moments of compounds **2.2** – **2.9** were within the range of 1.7 – 2.1 μ_B (Evans method in C_6H_6).

Compounds **2.2** – **2.8** displayed comparable high air- and moisture-sensitivity as **2.1**, with solutions turning rapidly from yellow to pink/purple when exposed to air; compound **2.9** went from dark orange/brown to virtually colourless.[i] Exposure of **2.5** to O_2 formed single and double C-H bond activated Ni(II) compounds analogous to those made from **2.1**. The reaction between **2.3**, **2.7**, and O_2 did not result in the oxidation of the carbene ligand but, instead, gave *bis*-halide Ni(RE-NHC)(PPh_3)Br_2 species as the only isolable products of the reactions. Compound **2.9** reacted differently again, with the formation of a nickel phosphine oxide species Ni($OPPh_3$)$_2Br_2$ and the urea, 6MesDAC=O.

[i] Previously reported work in the group showed that the yellow to purple colour change resulting from reaction of compound **2.1** with O_2 was commensurate with the formation of the C-H bond activated Ni(II) products [Ni(6Mes)(Br)(μ-OH)(μ-O-6Mes')NiBr] and [Ni(Br)(μ-O-6Mes')$_2$NiBr].[3]

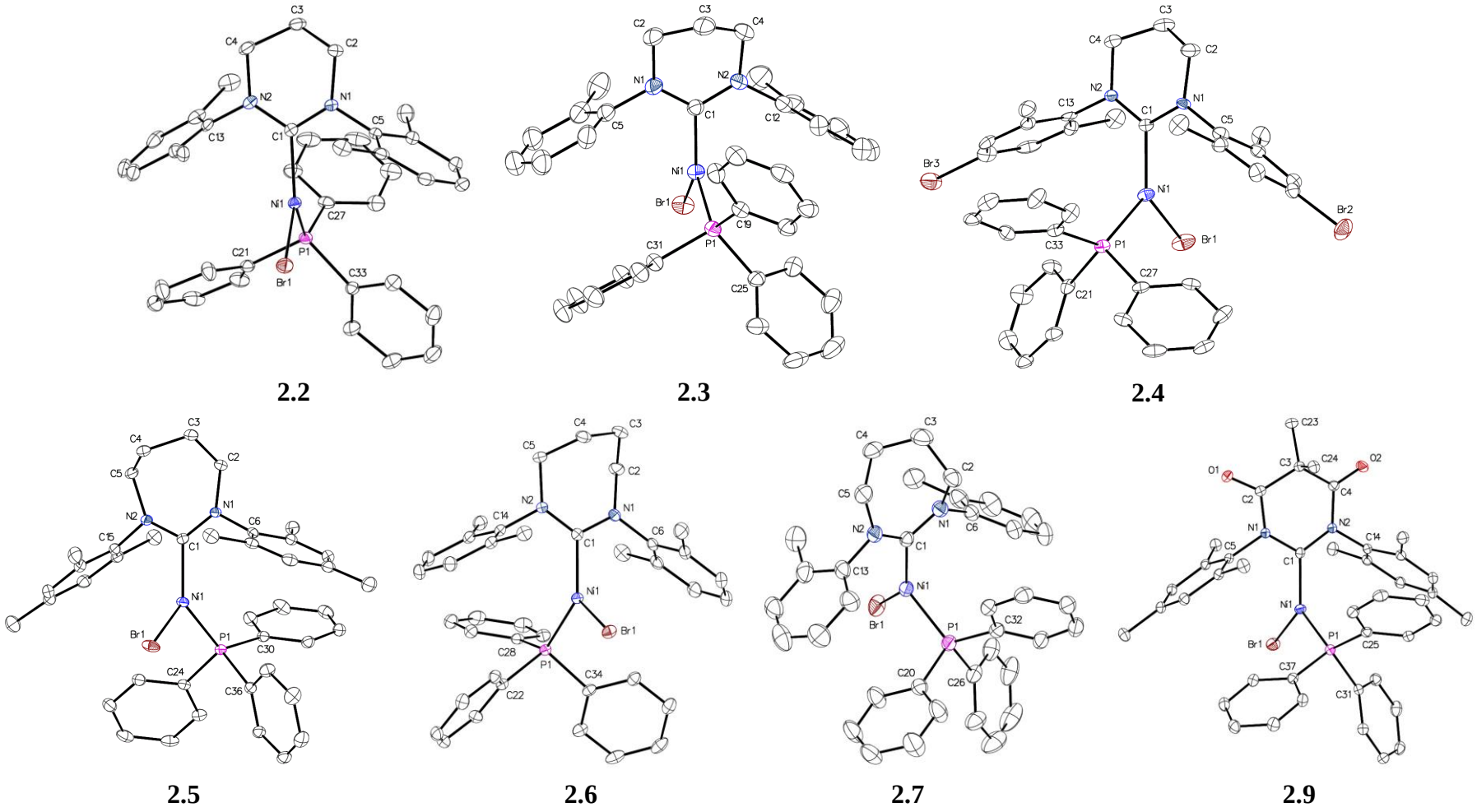

Figure 2.5 Molecular structures of compounds **2.2** – **2.7** and **2.9**. Thermal ellipsoids are set at 30% probability. All hydrogen atoms have been omitted for clarity.

Recrystallisation of **2.2** – **2.7** and **2.9** from either THF/hexane or C_6H_6/hexane led to isolation of crystals suitable for X-ray crystallography. Molecular structures of the series of compounds can be seen in Figure 2.5, with selected bond lengths and angles given in Table 2.3. All cases exhibited the same distorted trigonal planar structure as **2.1**, with large C_{NHC}-Ni-Br bond angles that deviate from the expected 120° (127.54(6) – 138.82(12)°). To accommodate this angle deviation, seven-membered RE-NHCs (and, to an extent, six-membered) exhibited a twisted backbone, with the largest distance between the out-of-plane atom and the mean plane of the RE-NHC being measured in the 7Mes analogue **2.5** (1.316 Å *vs.* 0.638 Å in **2.1**). The N-C_{NHC}-N bond angles increased with expansion of the RE-NHC ring size (116.33(16) – 116.9(4)° for **2.1** – **2.3** compared to 118.26(19) – 118.5(2)° for **2.5** – **2.7**). The Ni-C_{NHC} bond lengths were typical of this class of Ni(I)-NHC compounds, with values in the range of 1.925(3) – 1.9596(18) Å.[9, 19] The Ni-C_{NHC} distance in **2.9** was notably shorter (1.8702(18) Å *vs.* 1.942(2) Å in **2.1**) due to the poorer electron-donating and increased π-accepting ability of the diamidocarbene.[20-26]

Efforts to further alter the steric profile of the N-aryl substituents with the synthesis of the previously unreported *m*-Me aryl substituted RE-NHCs 6^{m}Xyl and 7^{m}Xyl failed to produce any isolable Ni(I) products. Indeed, the ^{1}H NMR spectra of reaction mixtures never showed the presence of any paramagnetic species. The lack of clean Ni(I) products may reflect the need for *o*-aryl substituents to provide the stabilisation necessary to form the three-coordinate Ni(I) species **2.1** – **2.9**.

Attempts were also made to introduce substituents onto the aryl groups to try and modify the electronic parameters of the RE-NHCs. The introduction of an electron-withdrawing *p*-Br group on the aryl ring (as shown in compounds **2.4** and **2.8**) was successful, although attempts to incorporate a *p*-nitrile group failed. While the initial formamidine precursor could be formed, the next steps to form the pyrimidinium and diazepinium salts only yielded unreacted starting materials or decomposition products.

Table 2.3 Selected bond lengths and angles for compounds **2.1** – **2.7**, **2.9**, **2.13**, **2.14**, and **2.16**.

Compound	**Ni-C_{NHC} (Å)**	**Ni-P (Å)**	**Ni-Br (Å)**	**N-C_{NHC}-N (°)**	**C_{NHC}-Ni-P (°)**	**C_{NHC}-Ni-Br (°)**	**P-Ni-Br (°)**
Ni(6Mes)(PPh_3)Br (**2.1**)	1.942(2)	2.2188(6)	2.3331(3)	116.48(19)	117.01(6)	133.46(6)	109.531(19)
Ni(6Xyl)(PPh_3)Br (**2.2**)	1.9596(18)	2.2151(5)	2.3502(3)	116.33(16)	117.15(5)	133.28(5)	109.434(16)
Ni(6^{o}Tol)(PPh_3)Br (**2.3**)	1.926(4)	2.1806(1)	2.3969(6)	116.9(4)	106.70(12)	138.82(12)	114.48(3)
Ni(6Xyl-*p*-Br)(PPh_3)Br (**2.4**)	1.944(9)	2.222(3)	2.3325(16)	117.3(8)	121.6(3)	132.9(3)	105.49(8)
Ni(7Mes)(PPh_3)Br (**2.5**)	1.9553(19)	2.2165(5)	2.3525(3)	118.49(17)	122.04(6)	134.00(5)	103.915(17)
Ni(7Xyl)(PPh_3)Br (**2.6**)	1.949(2)	2.2324(6)	2.3778(3)	118.26(19)	120.71(6)	127.54(6)	111.747(19)
Ni(7^{o}Tol)(PPh_3)Br (**2.7**)	1.925(3)	2.1890(8)	2.3498(5)	118.5(2)	110.07(8)	138.13(8)	111.66(2)
Ni(6MesDAC)(PPh_3)Br (**2.9**)	1.8702(18)	2.2614(5)	2.3029(3)	115.68(15)	118.99(5)	127.66(5)	113.352(16)
Ni(6^{i}Bu)(PPh_3)Br (**2.13**)	1.950(3)	2.1823(9)	2.3093(5)	117.2(3)	102.88(9)	126.48(9)	130.63(3)
Ni(6^{n}Pent)(PPh_3)Br (**2.14**)	1.949(3)	2.1840(9)	2.3155(6)	117.5(3)	99.75(9)	138.58(9)	121.66(3)
Ni(7^{n}Pent)(PPh_3)Br (**2.16**)	1.953(5)	2.2068(13)	2.4486(7)	116.2(4)	110.24(14)	132.36(14)	116.83(4)

2.2.2 Use of RE-NHCs with N-alkyl Substituents

RE-NHCs with N-alkyl substituents were used in an effort to try to access Ni(RE-NHC)(PPh_3)Br species with less bulk. In general, there is a paucity of isolable transition metal complexes bearing N-alkyl RE-NHCs, with only a few examples[i] based on ruthenium,[27-29] rhodium,[30-32] palladium,[30, 33-35] iridium,[31] gold,[36, 37] and copper[38] known in the literature.

As the free N-alkyl RE-NHCs could only be isolated as oils, they were more readily generated by *in-situ* deprotonation of either the BF_4 or PF_6 salts with $KN(SiMe_3)_2$ prior to comproportionation with Ni(0) and Ni(II) precursors. Initial studies with 6Et and 6^{i}Pr (Scheme 2.3) failed to produce the desired three-coordinate Ni(I) products but gave instead the four-coordinate square-planar Ni(II) compounds **2.10** and **2.11** (Appendix 1, Figure A1.1). The lack of any three-coordinate species is consistent with the findings for the *m*-substituted N-aryl RE-NHCs that significant steric encumbrance in the RE-NHCs is a requirement. Increasing the bulk of the N-alkyl groups to cyclohexyl rings (6Cy) did yield ^{1}H NMR spectra (of crude reaction mixtures of 6Cy and the nickel precursors) displaying paramagnetically shifted resonances, but no clean compound(s) could be isolated. The use of different solvents and/or reaction temperatures led to the same outcome.

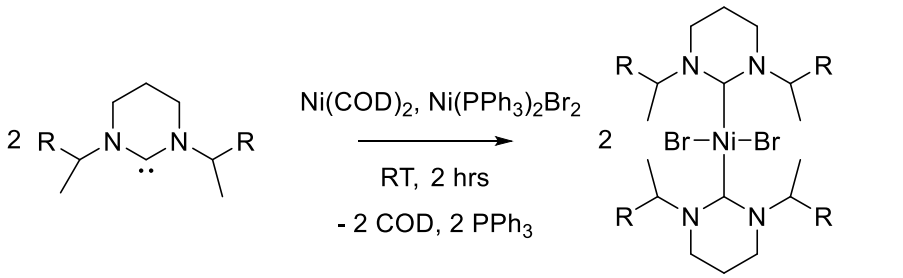

2.10: RE-NHC = 6Et, R = H
2.11: RE-NHC = 6^{i}Pr, R = Me

Scheme 2.3 Synthesis of four-coordinate Ni(II) compounds **2.10** and **2.11**.

The use of the bulkier 6^{t}Bu ligand also failed to give the desired Ni(I) species, but now formed small amounts of Ni(6^{t}Bu)'Br **2.12**, stabilised by additional C-H activated and agostically bonded ^{t}Bu groups (Figure 2.6). The bond lengths (Ni-H6A: 2.05(2) Å,

[i] Excluding pincer ligands and RE-NHCs with N-benzyl substituents.

Ni-H6B: 1.98(2) Å) and angles (Ni-H6A-C: 94.399°, Ni-H6B-C: 97.162°) are within the parameters generally accepted for an agostic interaction.[39] The ^{1}H NMR spectrum did not display any notable shift of the signal for the protons involved (δ 0.54 ppm, s, 9H), due to either the absence of the agostic interaction in solution, or alternatively, rapid exchange between the agostic/non-agostic ^{t}Bu methyl groups on the NMR timescale. **2.12** was only ever isolated as a few single crystals; this held back attempts to perform further studies on this very interesting product.

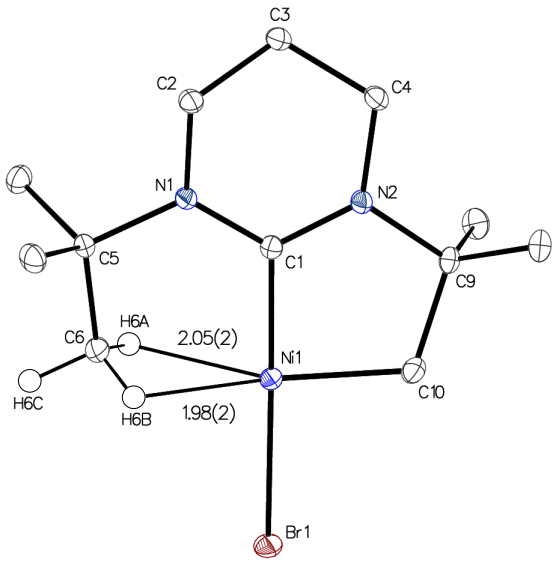

Figure 2.6 Molecular structure of compound **2.12**. Thermal ellipsoids are set at 30% probability. All hydrogen atoms, except those involved in agostic interactions, have been omitted for clarity.

Following the unsuccessful attempts with 6Et, 6^{i}Pr, and 6Cy, a move towards pendant-like N-alkyl substituents featuring a CH_2 linkage between the N atom and alkyl chain was undertaken (Scheme 2.4). It was hoped that this would afford more steric bulk in the N-alkyl arms, and potentially lead to formation of the desired three-coordinate Ni(I) compounds. Indeed, using the neopentyl functionalised carbenes 6^{n}Pent and 7^{n}Pent described by Cavell *et al.*,[31] along with the previously unreported isobutyl analogues 6^{i}Bu and 7^{i}Bu, Ni(I) compounds **2.13** – **2.16** could be synthesised *via* the same comproportionation route used for the formation of **2.1** (Scheme 2.4).

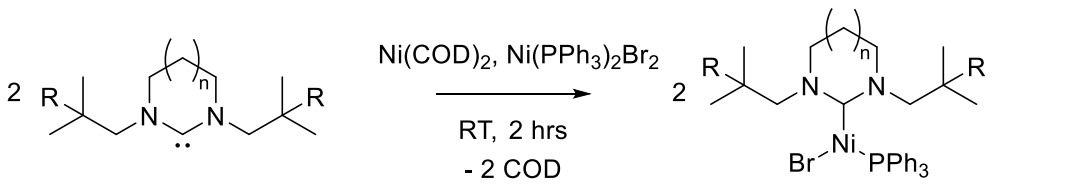

2.13: RE-NHC = 6^{i}Bu, n = 1, R = H
2.14: RE-NHC = 6^{n}Pent, n = 1, R = Me
2.15: RE-NHC = 7^{i}Bu, n = 2, R = H
2.16: RE-NHC = 7^{n}Pent, n = 2, R = Me

Scheme 2.4 Synthesis of three-coordinate Ni(I) compounds **2.13** – **2.16**.

The ^{1}H NMR spectra for compounds **2.13** – **2.16** displayed broad and paramagnetically shifted signals in the range δ 24 to -18 ppm. Again, integration and peak assignments were not possible, and no resonances were visible in the ^{31}P{^{1}H} NMR spectra. A room temperature solution magnetic moment for compound **2.14** of 1.6 μ_B was recorded in THF using the Evans method.

2.13, **2.14**, and **2.16** were isolated as yellow X-ray quality crystals from C_6H_6/hexane, whereas **2.15** could not be isolated cleanly, affording instead orange crystals of the *bis*-carbene Ni(II) side product Ni(7^{i}Bu)$_2$Br$_2$. Similarly, upon leaving recrystallisation vials of compounds **2.14** and **2.16** for multiple weeks, dark orange crystals of Ni(6^{n}Pent)$_2$Br$_2$ and Ni(7^{n}Pent)$_2$Br$_2$ were formed. X-ray crystallography of these three Ni(II) compounds revealed the same square-planar geometries seen in **2.10** and **2.11** (Appendix 1, Figure A1.1).

Molecular structures of **2.13**, **2.14**, and **2.16** (Figure 2.7) displayed a distorted trigonal planar geometry, with the sum of internal angles of each compound being 359.99(13)°, 359.99(13)°, and 359.43(20)° respectively. Selected bond lengths and angles are displayed in Table 2.3. As with the N-aryl analogues, the C_{NHC}-Ni-Br bond angles deviate from 120° (126.48(9) – 138.58(9)°). In the six-membered ring derivatives **2.13** and **2.14**, the isobutyl and neopentyl substituents adopt a *cis* conformation relative to each other, with both N-alkyl groups directed away from the neighbouring PPh_3 ligand. This allows the PPh_3 to move away from the bromide ligand and create a wider P-Ni-Br bond angle (**2.13**: 130.63(3)°, **2.14**: 121.66(3)°; *cf.* **2.1**: 109.531(19)°). Conversely, in the seven-membered derivative **2.16**, the neopentyl groups are *trans* to one another, most likely due to the backbone twisting inherent to seven-membered heterocycles. The appearance of different conformations with different ring sizes was also reported by Cavell in Rh(I) and Ir(I) complexes of 6^{n}Pent and 7^{n}Pent.[31] The N-C_{NHC}-N bond angle in

compound **2.16** is smaller than those in **2.13** and **2.14** (116.2(4)° *vs.* 117.2(3)/117.5(3)°), again likely due to the twisted ring and *trans* conformation of the neopentyl substituents.

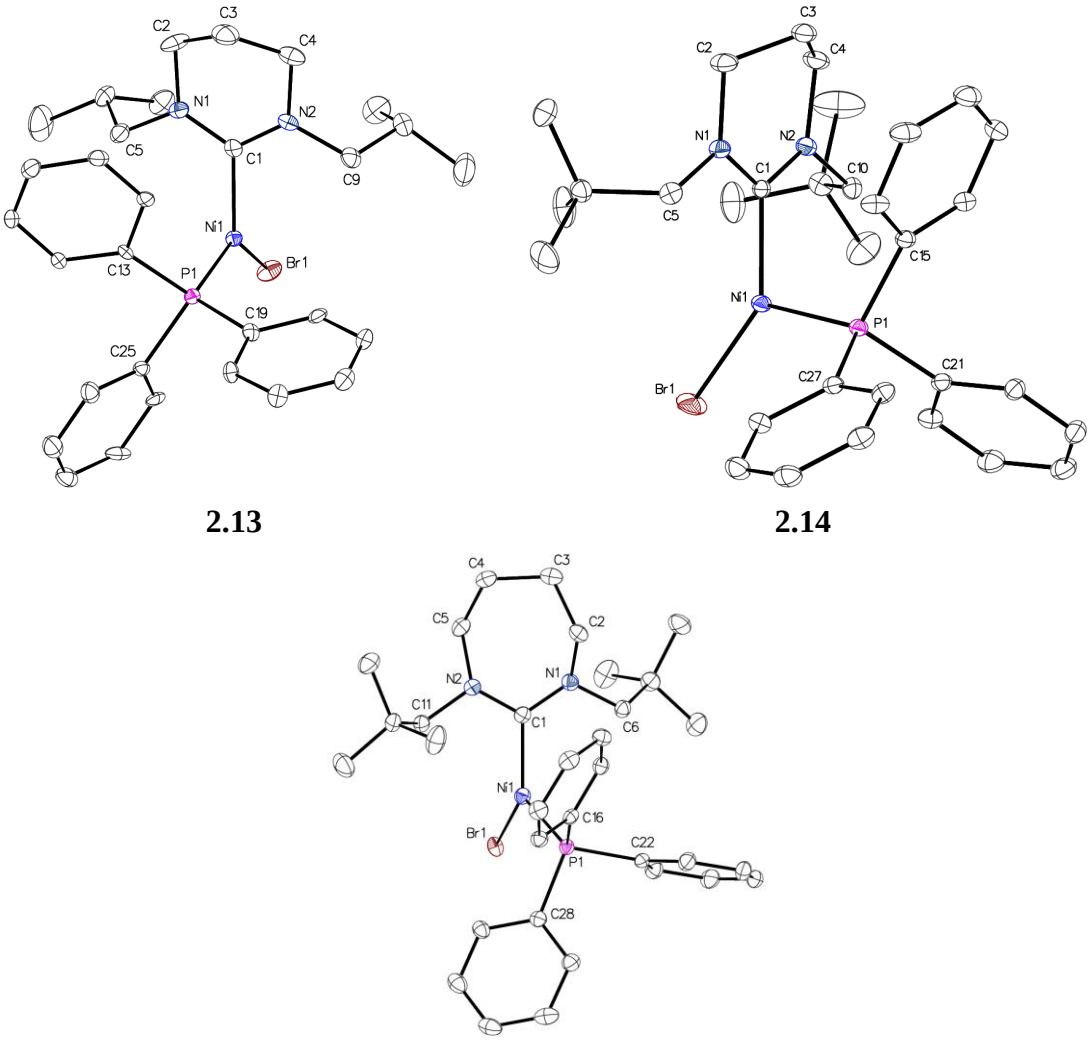

2.13 **2.14**

2.16

Figure 2.7 Molecular structures of compounds **2.13**, **2.14**, and **2.16**. Thermal ellipsoids are set at 30% probability. All hydrogen atoms have been omitted for clarity.

2.3 Reactivity of Ni(6Mes)(PPh$_3$)Br (2.1) with Halide Abstracting Agents

2.3.1 Use of Et_3Si^+, $NaBH_4$, $NaCNBH_3$, $NaNPh_2$, and $TlPF_6$

Previous efforts in the group have been directed at using compound **2.1** as a precursor to two-coordinate Ni(I) complexes by either abstraction of the bromide ligand, or substitution of both the bromide and phosphine ligands.[4] The results of these studies are shown in Scheme 2.5. Of particular interest was [Ni(6Mes)(PPh$_3$)(THF)]$^+$ **2.17** as this

would (upon elimination of THF) provide a potential route into a $[Ni(RE\text{-}NHC)(PR_3)]^+$ derivative of the targeted two-coordinate $[Ni(RE\text{-}NHC)_2]^+$ species (Chapter 3).

Poulten previously showed that treatment of **2.1** with $TlPF_6$ in THF gave **2.17** as a pale yellow solid in 85% yield (Scheme 2.5). X-ray crystallography revealed a three-coordinate distorted T-shaped geometry for the cation in **2.17** (Figure 2.8), with a C_{NHC}-Ni-P bond angle (158.59(6)°) far greater than in **2.1** (117.01(6)°). While compound **2.17** was of interest because of the potentially labile THF ligand, Poulten found that recrystallisation from a range of solvents (CH_2Cl_2, C_6H_6, C_6H_5F) did not yield the desired THF-free product. Not only was the use of highly toxic thallium salts a safety concern, but TlBr proved to be a troublesome side product that could not be completely removed during post-reaction work-ups, resulting in the formation of Ni(II) bromide products over prolonged reaction times. In light of these problems, a simpler route to halide abstraction was probed.

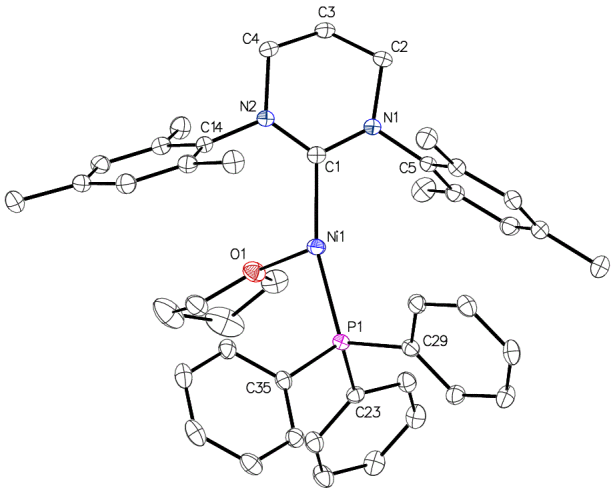

Figure 2.8 Molecular structure of the cation in **2.17**. Thermal ellipsoids are set at 30% probability. All hydrogen atoms have been omitted for clarity.

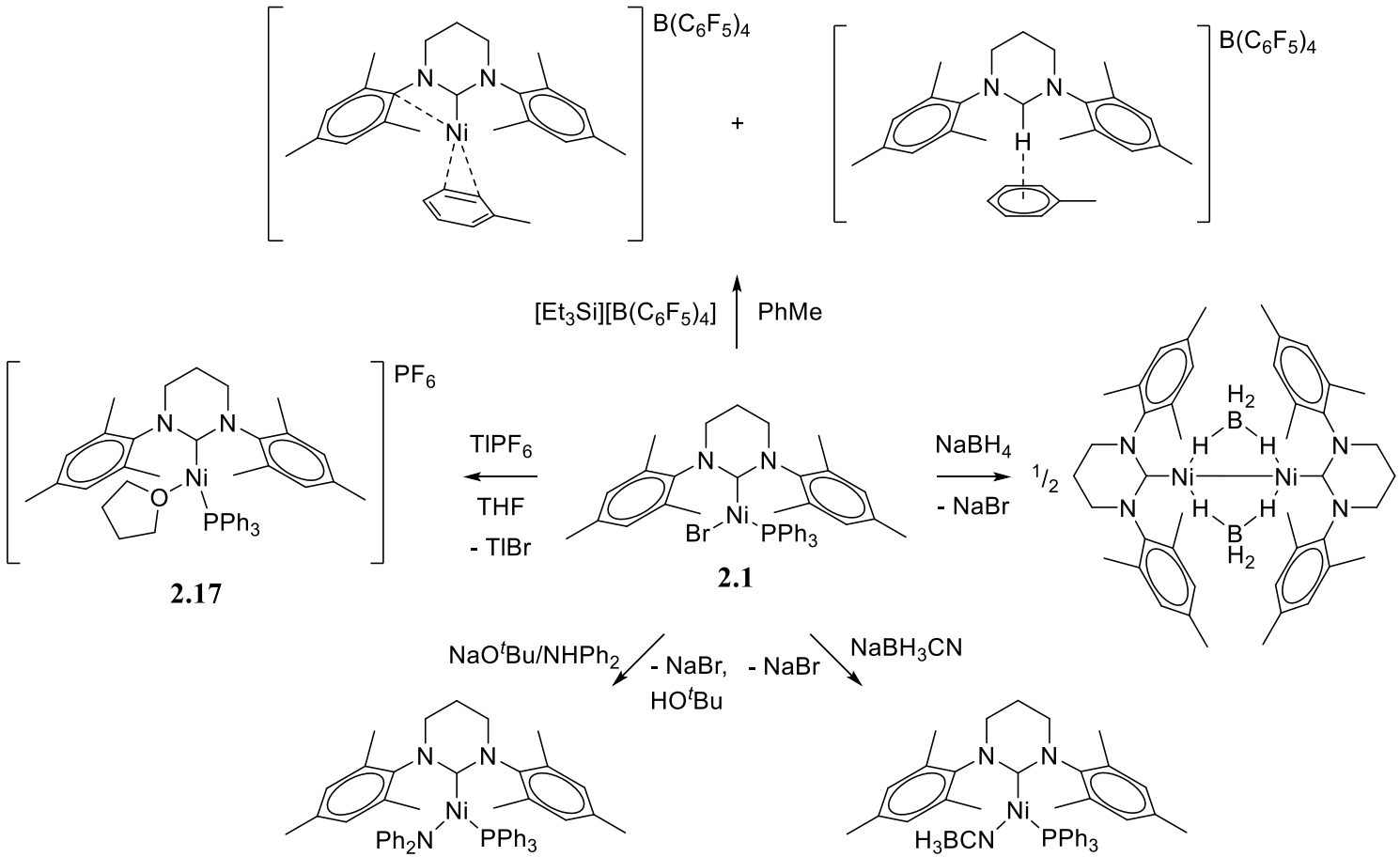

Scheme 2.5 Reactions between compound **2.1** and variety of halide abstraction reagents.

2.3.2 Reaction of 2.1 with $NaBAr^F_4$

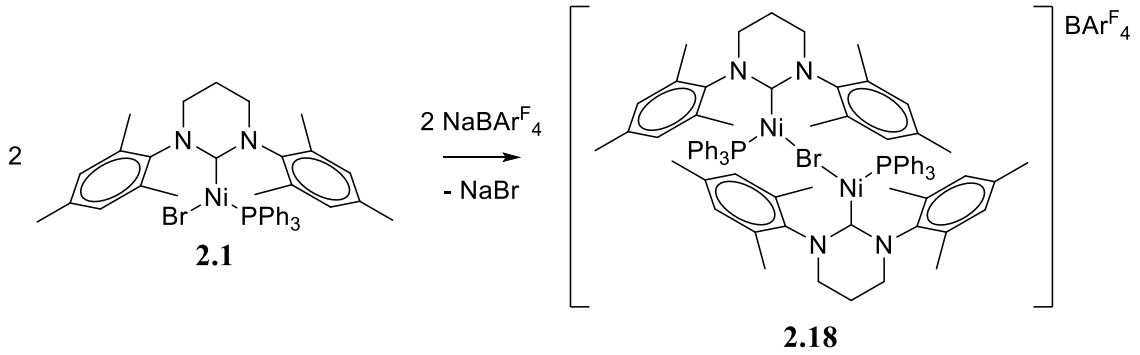

Scheme 2.6 Synthesis of the Ni(I) dimer **2.18**.

The reaction of **2.1** with $NaBAr^F_4$ in THF or C_6H_6 failed to yield any clean products, but upon changing the solvent to Et_2O, there was a colour change from yellow to orange and formation of an off-white precipitate (presumably NaBr). Ultimately, recrystallisation gave large orange crystals of the dimeric Ni(I) compound $[\{Ni(6Mes)(PPh_3)\}_2(\mu\text{-Br})]BAr^F_4$ **2.18** (Scheme 2.6).

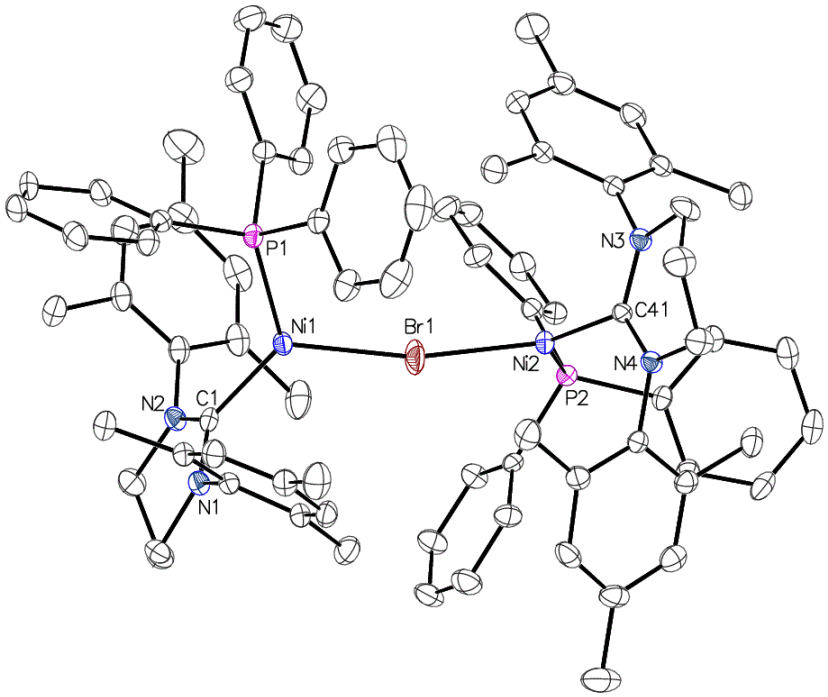

Figure 2.9 Molecular structure of compound **2.18** cation. Thermal ellipsoids are set at 30% probability. All hydrogen atoms have been omitted for clarity.

This compound featured a rare single bromide-bridge, with only a few examples of an unsupported Ni-Br-Ni moiety reported; the cationic Ni(II) allyl species [{Ni(η^3-C_3H_5)(PR_3)}$_2$(μ-Br)]X (R = ^{i}Pr, ^{t}Bu; X = $B(C_6F_5)_4$, BAr^F_4, Al{$OC(CF_3)_3$}$_4$),[40] and two examples featuring halide-bridged Ni(II) macrocycles.[41, 42]

X-ray crystallography revealed the bromide was located approximately midway between the two {Ni(6Mes)(PPh_3)} fragments (Ni1-Br1: 2.3803(6) Å and Ni2-Br1: 2.3688(6) Å), with a Ni-Br-Ni angle of 167.64(3)° (Figure 2.9). The Ni-Br bond lengths were similar to those in [{Ni(η^3-C_3H_5)(P^iPr_3)}$_2$(μ-Br)](Al{$OC(CF_3)_3$}$_4$) (Ni-Br: 2.3564(5) Å and 2.3674(5) Å), although this exhibited a more acute Ni-Br-Ni angle (118.01(2)°).[40] This difference most likely arises from the presence of the two bulky ligands on each nickel centre (6Mes and PPh_3) in **2.18**, compared to the single bulky P^iPr_3 and small allyl groups, leading to the two nickel fragments being pushed apart in **2.18**. The Ni···Ni distances in the two compounds supports this; 4.721 Å in **2.18**, 4.049 Å for the allyl compound. The presence of the bulky ligands also caused the nickel fragments to adopt a staggered arrangement along the Ni-Br-Ni axis. A plane featuring Br-Ni-P-C_{NHC} atoms can be drawn for each fragment, revealing an angle of *ca*. 46.8° between the two planes. Each {Ni(6Mes)(PPh_3)Br} moiety can be viewed as having a distorted trigonal planar geometry, with selected bond lengths and angles for starting material **2.1** and each half of **2.18** compared in Table 2.4. Compound **2.18** displayed smaller C_{NHC}-Ni-Br angles than **2.1** (122.1(11)°/123.75(10)° *vs.* 133.46(6)°), which was compensated by both the C_{NHC}-Ni-P and P-Ni-Br bond angles increasing slightly. The Ni-C_{NHC} and Ni-P distances in **2.1** and **2.18** are comparable, although the Ni-Br bond was elongated in the latter, presumably to alleviate any steric clash between the {Ni(6Mes)(PPh_3)} moieties.

Table 2.4 Selected bond lengths and angles for compounds **2.1** and **2.18**.

Compound	Ni(6Mes)(PPh_3)Br **(2.1)**	[{Ni(6Mes)(PPh_3)}$_2$(μ-Br)]$BAr^F{}_4$ **(2.18)**	
Ni-C_{NHC} (Å)	1.942(2)	1.937(4)	1.935(4)
Ni-P (Å)	2.2188(6)	2.2172(12)	2.2186(11)
Ni-Br (Å)	2.3331(3)	2.3803(6)	2.3688(6)
N-C_{NHC}-N (°)	116.48(19)	116.4(4)	116.0(3)
C_{NHC}-Ni-P (°)	117.01(6)	124.15(11)	124.72(11)
C_{NHC}-Ni-Br (°)	133.46(6)	122.16(11)	123.75(10)
P-Ni-Br (°)	109.531(19)	113.68(4)	111.39(4)

EPR spectroscopy (X-band, Et_2O/toluene, 140 K) appeared to show dissociation of **2.18** into two Ni(I) compounds, proposed to be a molecule of **2.1** and a molecule of [Ni(6Mes)(PPh_3)(OEt_2)]$BAr^F{}_4$ ((b), Figure 2.10). In frozen THF/toluene, signals for **2.1** and **2.17** ([Ni(6Mes)(PPh_3)(THF)]$^+$) were formed ((c), Figure 2.10).

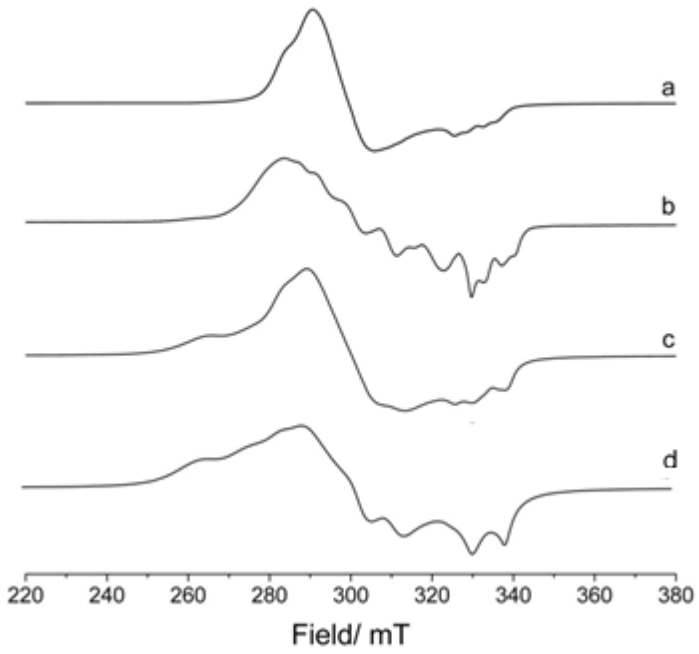

Figure 2.10 Experimental X-band CW EPR spectra (Et_2O/toluene, 140 K) showing appearance of **2.1** (a) in the spectrum of dissolved **2.18** (b). The spectrum of **2.18** in frozen THF/toluene (c) is shown against that of **2.17** in the same solvent mixture (d).

DFT calculations (by Dr Vera Krewald, University of Bath) revealed Mulliken spin populations of 0.78 on each nickel centre in **2.18**, showing that a +1 oxidation state was an accurate representation for the two nickel oxidation states. DFT predicted antiferromagnetic coupling (S = 0) at room temperature, with the exchange coupling constant (J) between the two nickel atoms calculated based on the molecular structure coordinates with optimised hydrogen atom positions. Different density functions calculated vastly different exchange constants (TPSSh: -97.6 cm^{-1}, B3LYP: -76.1 cm^{-1}, M06: -69.3 cm^{-1}, PBE0: -64.3 cm^{-1}) which showed that J values can be difficult to calculate with DFT and should be determined experimentally through SQUID techniques. However, the magnitude of the constants were weak enough to still allow population of the high spin (S = 1) ferromagnetically coupled state. The Boltzmann population distribution analysis showed the high spin state to have *ca*. 40% population at 300 K (Appendix 6). This was borne out experimentally, whereby the ^{1}H NMR spectroscopy displayed paramagnetic signals, indicating the presence of Ni(I) centres. Spectra collected in Et_2O were dominated by solvent peaks, while the use of THF-d_8 led to the appearance of peaks suggestive of **2.17** (*cf*. EPR spectra), reflecting the fact that **2.18** was not formed when using THF as a reaction solvent. A room temperature solution magnetic moment of 2.5 μ_B was measured *via* the Evans method in Et_2O, while a solid state magnetic moment of 2.4 μ_B was recorded using a Gouy balance. The values are consistent with the presence of two separate Ni(I) centres.

2.4 Synthesis and Characterisation of $[Ni(6Mes)(PPh_3)(CO)]^+$ (2.19)

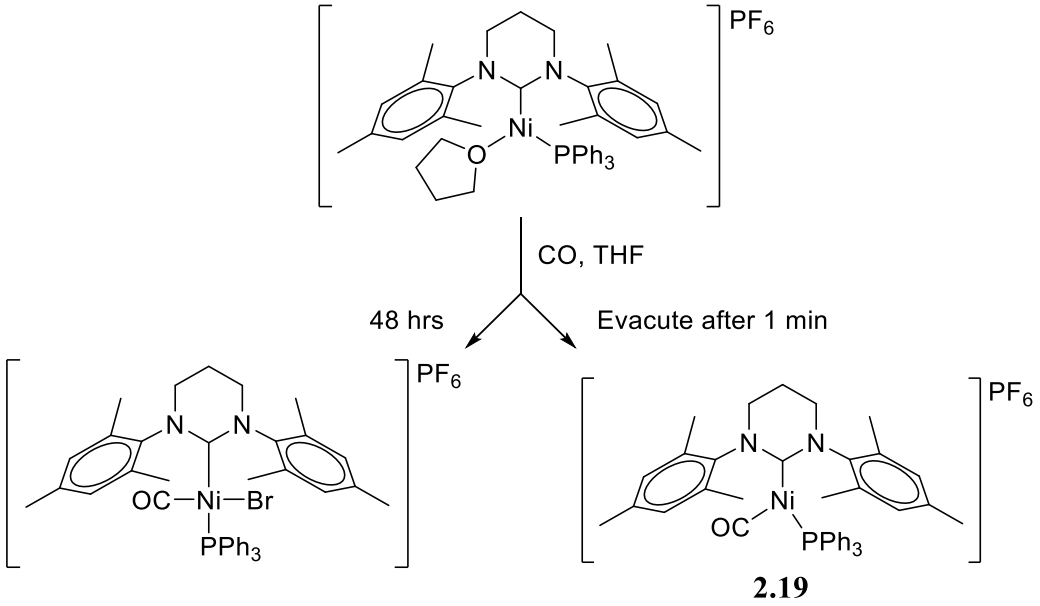

Scheme 2.7 Synthesis of Ni(I) carbonyl compound **2.19** (right), and the Ni(II) product formed after prolonged reaction time (left).

Successful synthesis of the desired low-coordinate nickel carbene-phosphine complex (albeit as the THF solvate **2.17**, and bromide-bridging dimer **2.18**) led to a reactivity study towards small molecules. Poulten had found that exposure of **2.17** to CO in THF brought about an immediate colour change from pale yellow to bright green, resulting from formation of the Ni(I) carbonyl compound $[Ni(6Mes)(PPh_3)(CO)]PF_6$. However, as **2.17** could not be completely separated from the TlBr formed during its synthesis, $[Ni(6Mes)(PPh_3)(CO)Br]PF_6$ was generated over prolonged reaction times (Scheme 2.7). Poulten showed this could be circumvented by rapid removal (< 1 min) of all volatiles after CO addition, followed by recrystallisation of the resulting residue from THF/hexane. This appeared to prevent the colour change to yellow for long enough to form crystals from the green solution. $[Ni(6Mes)(PPh_3)(CO)]PF_6$ **2.19** was isolated as green crystals in 79% yield (Scheme 2.7). The X-ray structure of **2.19** showed a distorted T-shaped geometry, with a C_{NHC}-Ni-P bond angle of 151.93(9)° (Figure 2.11). The bond angle was only slightly smaller than that in the starting material **2.17** (158.59(6)°), showing that substitution of THF by CO caused a minimal structural change.

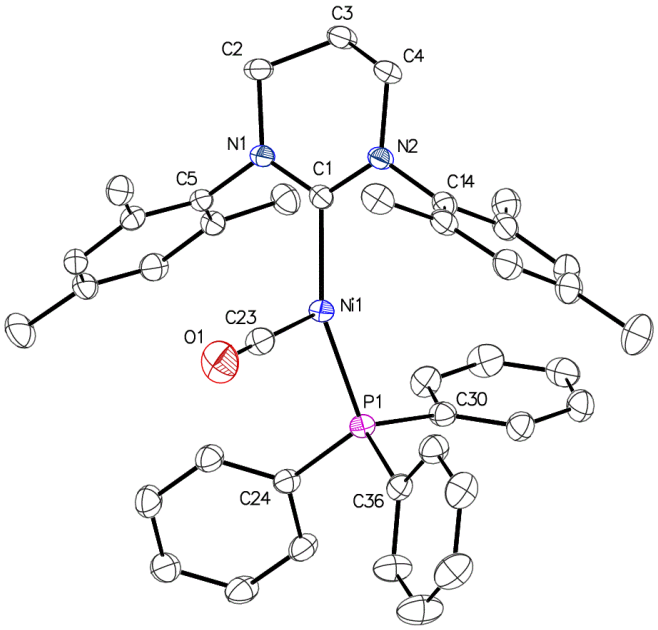

Figure 2.11 Molecular structure of the cation in **2.19**. Thermal ellipsoids are set at 30% probability. All hydrogen atoms have been omitted for clarity.

Following on from the work by Poulten, detailed spectroscopic characterisation of **2.19** was undertaken. FTIR spectroscopy on **2.19** showed a carbonyl signal at 2035 cm^{-1} in THF (Appendix 4), comparable to the few other reported Ni(I) carbonyl species (1927 – 2026 cm^{-1}).[10, 43-48] Compound **2.19** displayed a paramagnetic ^{1}H NMR spectrum with signals between δ 17 and 2 ppm, and no signal for the PPh_3 group in the $^{31}P\{^{1}H\}$ NMR spectrum. $^{13}C\{^{1}H\}$ NMR spectra recorded using a high sensitivity cryoprobe failed to show any ^{13}C resonance for the carbonyl group. However, treatment of **2.19** with 1 atm of ^{13}CO led to the emergence of an isotopically enhanced signal at δ 198.1 ppm after just 5 min (Appendix 3). The ^{13}C chemical shift of ^{13}CO in THF-d_8 is δ 184.5 ppm,[49] implying that the lower field signal was due to **2.19-^{13}CO**.

The measured magnetic moment for **2.19** (1.8 μ_B in THF-d_8 determined by the Evans method) was as expected for a Ni(I) centre.

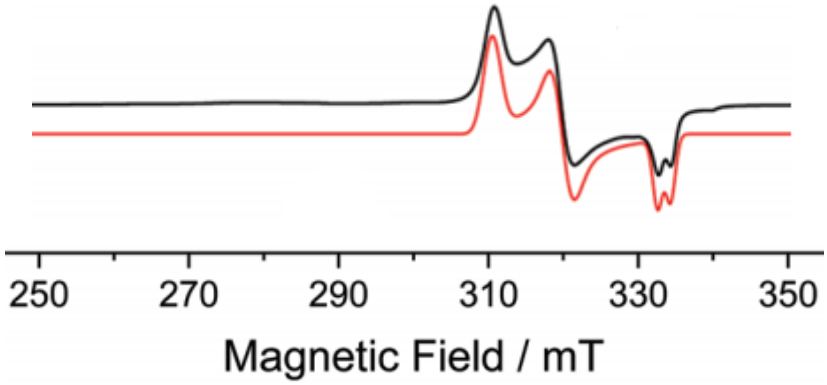

Figure 2.12 Experimental (black line) and simulated (red line) X-band CW EPR spectra (THF/toluene, 140 K) of compound **2.19**.

The EPR spectra of **2.19** displayed a rhombic profile (Figure 2.12) with a g_1 value lower than the g_2 and g_3 values (Table 2.5). While this trend was seen in the X-band EPR spectrum of **2.1**, the difference in g_1 to g_2/g_3 for the carbonyl compound was far smaller. The size of the superhyperfine coupling constants seen for **2.19** are also of interest, with *A* values an order of magnitude smaller than the *A* values of **2.1**. The DFT derived ^{31}P nucleus spin density was very small, likely due to the presence of the electron-withdrawing CO ligand and reflected in the fact that the superhyperfine coupling values were also small.

Table 2.5 Spin Hamiltonian parameters (*g* values and ^{31}P superhyperfine coupling constants) for compound **2.19**.

Compound	g_1	g_2	g_3	A_1 **(MHz)**	A_2 **(MHz)**	A_3 **(MHz)**
2.19	2.035	2.121	2.185	21	29	48

The bromide-bridged compound **2.18** was also a precursor for the Ni(I)-CO compound. Exposure to 1 atm of CO in THF led to the diagnostic instantaneous colour change to bright green. IR spectroscopy of the reaction mixture gave a strong carbonyl signal at 2036 cm^{-1}, indicative of [Ni(6Mes)(PPh$_3$)(CO)]$^+$ (Appendix 4).

2.5 Electronic Structure Analysis of Compounds 2.1, 2.17, 2.19, Ni(6Mes)(PPh_3)($NCBH_3$), and Ni(6Mes)(PPh_3)(NPh_2)[4]

Using a combination of DFT and EPR the electronic structures of compounds **2.1**, **2.17**, **2.19**, Ni(6Mes)(PPh_3)($NCBH_3$) (denoted compound **I**), and Ni(6Mes)(PPh_3)(NPh_2) (**II**) previously synthesised by Page, Poulten and Sabater were analysed. While the geometry of organometallic complexes can be influenced by steric demands of the ligands involved, previous work by Pietrzyk has shown that the electronic effects of the ligands also contribute to the observed geometry.[11, 50] As previously mentioned, the *β*-diketiminate Ni(I) compound reported by Holland *et al*. exhibited a change of geometry upon ligation of a CO ligand, with DFT calculations revealing the difference in electronics led to the geometry change.[10] Three-coordinate organometallic species tend to adopt an ideal trigonal planar geometry to ease steric repulsion between ligands, however, d^9 systems can become distorted and form either T-shaped or Y-shaped geometries due to a first-order Jahn-Teller effect removing the degeneracy of the d_{xy} and $d_{x2\text{-}y2}$ orbitals.[11, 50, 51] Figure 2.13 shows the molecular orbital diagram expected for a three-coordinate d^9 organometallic species, where the z-axis is perpendicular to the metal-ligand plane, in this case the "Ni-C_{NHC}-P-L" plane. When considering the changes in geometry as a result of purely electronic factors, and forgoing sterics, in the case where the d_{xy} orbital is stabilised (*i.e.*, by the presence of an electron-withdrawing ligand such as CO), the T-shaped geometry is preferred and the SOMO is predominantly $d_{x2\text{-}y2}$. Conversely, when the $d_{x2\text{-}y2}$ orbital becomes stabilised (or d_{xy} energy level raised by donation of electron density from ligands to metal centre) then a Y-shaped geometry will occur and the SOMO is mainly of d_{xy} character. DFT calculations to determine the contributions from the d_{xy} and $d_{x2\text{-}y2}$ orbitals to the SOMO of each compound ensued, revealing that the distorted T-shaped compounds (**2.17**, **2.19**, **II**) indeed featured a SOMO predominantly of $d_{x2\text{-}y2}$ character (Figure 2.15)

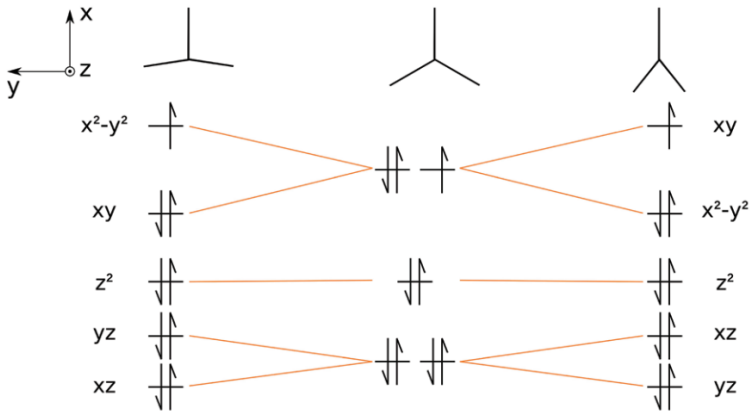

Figure 2.13 The *d*-orbital splitting arrangement in a *Cs* crystal field.

A review of the X-ray crystal structures of the compounds **2.1**, **2.17**, **2.19**, **I**, and **II** revealed that the P-Ni-L (L = Br, THF, CO, $NCBH_3$, NPh_2) bond angle vary by less than 10° (99.69(3) – 109.531(19)°). Conversely, the C_{NHC}-Ni-P and C_{NHC}-Ni-L bond angles vary significantly, and the size of the biggest angle dictates whether the Ni(I) species is classed as distorted trigonal planar or T-shaped geometry. As Figure 2.14 represents, compounds **2.1** and **I** have distorted trigonal planar geometries, and a ΔΔ(bond angle) of -93.0° and -95.2° respectively. The "ΔΔ(bond angle)" parameter denotes the difference between the largest angle and the sum of the two smaller angles around the Ni(I) centre (*i.e.*, ideal trigonal planar ΔΔ(bond angle) = -120° and ideal T-shaped geometry ΔΔ(bond angle) = 0°). Compounds **2.17** and **2.19** are considered to have distorted T-shaped geometry, with ΔΔ(bond angle) values of -46.8° and -56.1° respectively. Compound **II** also displayed a distorted T-shaped geometry (ΔΔ(bond angle) = -74.9°), however, this has been shown to be the result of a steric effect due to the presence of bulky N-bound phenyl groups. When replacing the N-phenyl groups with N-methyl groups, to form the hypothetical compound Ni(6Mes)(PPh_3)(NMe_2) (**II_{Me}**), DFT calculations predicted a geometry closer to trigonal planar (ΔΔ(bond angle) = -88.4°), with a reduction in the C_{NHC}-Ni-N bond angle and an increase in the C_{NHC}-Ni-P bond angle (Figure 2.14).

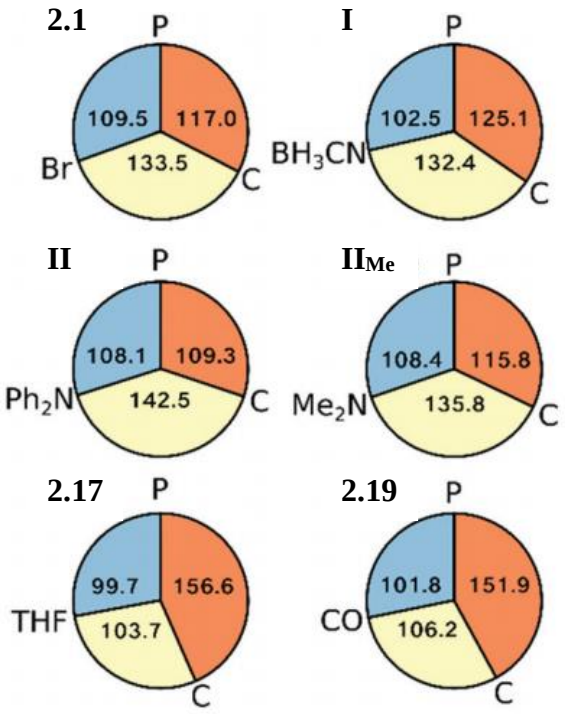

Figure 2.14 Pie charts depicting the X-ray crystal structure bond angles around the nickel in compounds **2.1**, **2.17**, **2.19**, **I**, **II**, and predicted angles of $\mathbf{II_{Me}}$.

Table 2.6 displays the *g* values gained from the X-band CW EPR spectra of the compounds of interest. Also featured is the difference between g_3, and g_2 and g_1, and the Δg_{rel} parameter. The "Δg_{rel}" parameter represents the magnitude of the difference between g_3 and g_2 values, as a percentage of the total difference between the g_3 and g_1 values (*i.e.*, 50% denotes a g_2 value intermediate between g_3 and g_1, and 100% would signify a g_2 value the same as g_1).[i] The displayed Δg_{rel} values reflect the link between the geometry of an organometallic complex and the experimentally observed EPR spectra and *g* values.

[i] Calculated according to the equation $\Delta g_{rel} = [(g_3 - g_2)/(g_3 - g_1)] \times 100$.

Table 2.6 Extracted g and Δg_{rel} values of compounds **2.1**, **2.17**, **2.19**, **I**, **II**, and $\mathbf{II_{Me}}$.

Compound	g_1	g_2	g_3	$g_3 - g_2$	$g_3 - g_1$	Δg_{rel} (%)
2.1	2.050	2.265	2.365	0.100	0.315	31.7
2.17	2.025	2.210	2.490	0.280	0.465	60.2
2.19	2.035	2.121	2.185	0.064	0.150	42.7
I	2.028	2.225	2.373	0.148	0.345	42.9
II	2.050	2.150	2.290	0.140	0.240	58.3
$\mathbf{II_{Me}}$	-	-	-	0.046	0.098	46.9

Combining the DFT computed d_{x2-y2}/d_{xy} contributions to the SOMO, EPR derived Δg_{rel} parameters, and the ΔΔ(bond angle) values obtained from the X-ray crystal structures, there is a connection between the experimental values and DFT calculations. Figure 2.15 shows that when the d_{xy} and d_{x2-y2} are near degenerate and both contributing to the compound SOMO, the geometries are close to trigonal planar (**2.1** and **I**). As the contribution of d_{x2-y2} to the SOMO increases (and d_{xy} contribution tends to zero), the geometry moves away from trigonal planar towards T-shaped (**2.17** and **2.19**). Interestingly, the hypothetical compound $\mathbf{II_{Me}}$ was predicted to have a SOMO with predominantly d_{xy} character (and distorted trigonal planar geometry), whereas the bulky analogue **II** was computed to have a far greater d_{x2-y2} contribution. This shows that the presence of bulky ligands dictating the geometry of an organometallic complex (sterics), will have an impact on the molecular orbital distribution (electronics).

Figure 2.15 also shows the connection between the geometry of a compound and its observed EPR spectra. Compounds with a geometry closer to trigonal planar exhibit Δg_{rel} values that represent g_2 and g_3 values significantly larger than the g_1 value. As the geometry moves towards T-shaped, the Δg_{rel} values increase, which shows that the g_2 value is shifting closer to the g_1 value. The average Δg_{rel} values for compounds with a distorted trigonal planar geometry (green; 40.5%) and distorted T-shaped geometry (blue; 53.7%) reflect this.

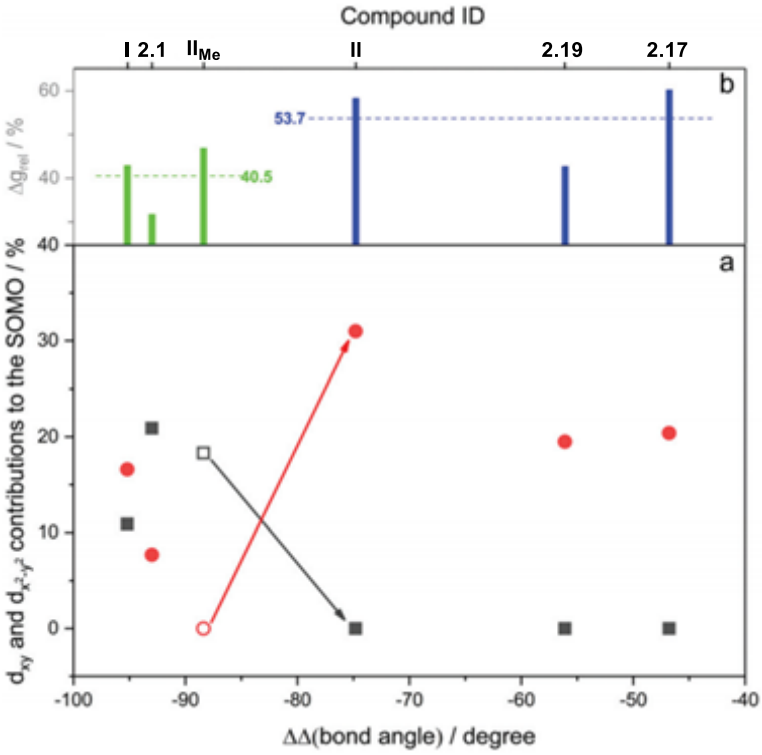

Figure 2.15 (a) d_{xy} and d_{x2-y2} contributions to the SOMO as a function of the ΔΔ(bond angle). Black squares refer to d_{xy} and red circles to d_{x2-y2}. Empty symbols refers to DFT derived *d*-orbital contributions from fully optimised structures rather than X-ray crystal structures. (b) Δg_{rel} values as a function of the ΔΔ(bond angle). Average Δg_{rel} values for Y (green) and T-shape (blue) geometries are also reported.

2.6 Synthesis and Characterisation of Ni(RE-NHC)(PR$_3$)Br Compounds

2.6.1 Reactivity of 2.1 with PCy$_3$

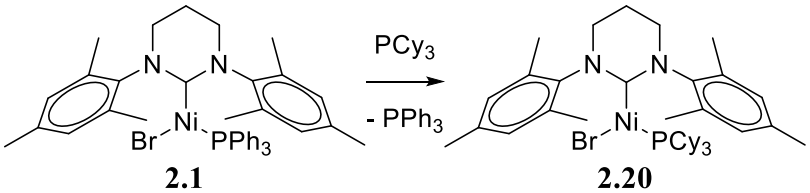

2.1 **2.20**

Scheme 2.8 Reaction between compound **2.1** and PCy$_3$.

The reaction between **2.1** and excess free PCy$_3$ in THF resulted in a colour change from bright yellow to a much paler yellow suspension. ^{1}H NMR spectroscopy of the reaction mixture showed the presence of new paramagnetic peaks, indicating the

formation of a new Ni(I) compound (Appendix 3), as well as the appearance of free PPh_3 in the $^{31}P\{^1H\}$ NMR spectrum. The new Ni(I) product was assumed to be the phosphine substituted compound Ni(6Mes)(PCy_3)Br **2.20** (Scheme 2.8). Isolation of the product *via* cannula filtration was followed by washing the solid with plenty of hexane to remove any remaining free PPh_3. The ^1H NMR spectrum showed that the substitution did not go to completion, as starting material **2.1** was still present. Longer reaction times and increased temperature did not improve the conversion, while recrystallisation from THF or C_6H_6 failed to separate the two organometallic products due to their similar solubilities.

2.6.2 Alternative Route to Synthesis of Ni(6Mes)(PCy_3)Br

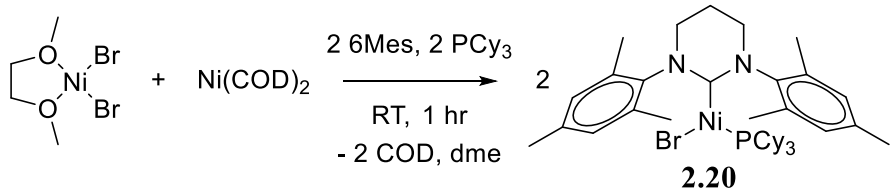

2.20

Scheme 2.9 Synthesis of compound **2.20** *via* an alternative route.

To overcome the problem of removing PPh_3 from compound **2.1**, Ni(dme)Br_2 was employed as a different source of Ni(II) for comproportionation. A mixture of Ni(dme)Br_2, Ni(COD)$_2$, 6Mes, and free PCy_3 in a ratio of 1:1:2:2 was stirred in C_6H_6 for 1 hr (Scheme 2.9). After removal of volatiles, the brown residue was recrystallised to afford **2.20** as a pale yellow solid in 75% isolated yield. The ^1H NMR spectrum of **2.20** displayed broad and paramagnetically shifted peaks in the range δ 36 to -2 ppm, analogous to the PPh_3 analogue **2.1** (*cf.* δ 30 to -17 ppm), yet $^{31}P\{^1H\}$ NMR spectroscopy still did not reveal any resonance for the phosphine ligand. The room temperature magnetic moment was 2.1 μ_B, recorded in C_6H_6 (Evans method).

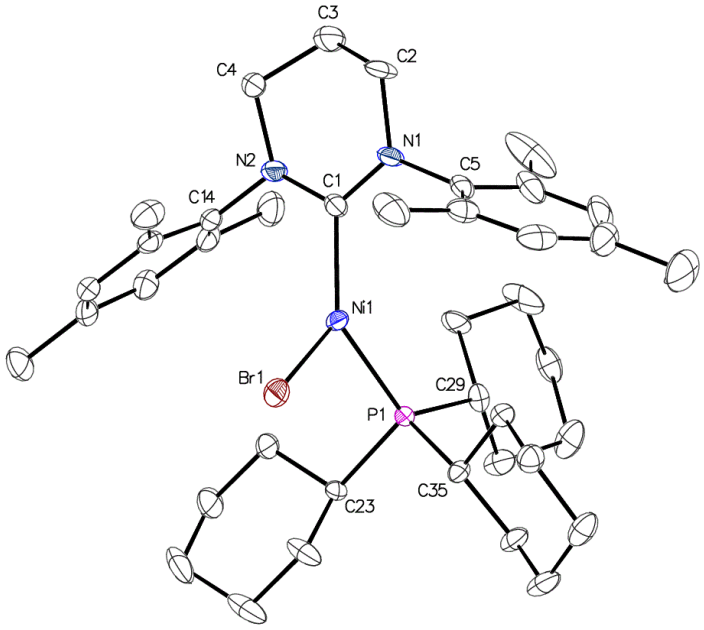

Figure 2.16 Molecular structure of compound **2.20**. Thermal ellipsoids are set at 30% probability. All hydrogen atoms have been omitted for clarity.

The X-ray structure of **2.20** is shown in Figure 2.16. As with **2.1** (Table 2.7), the C_{NHC}-Ni-P and C_{NHC}-Ni-Br bond angles were greater than the expected 120° (129.27(18)°/128.6(3)° and 128.81(18)°/124.9(4)° respectively), while the P-Ni-Br bond angle was more acute than that in **2.1** (101.74(4)°/106.00(5)°). Most notable is that the Ni-C_{NHC}, Ni-P, and Ni-Br distances were all longer in the PCy_3 derivative relative to the PPh_3 compound. It is assumed that this was due to the increased sterics of the cyclohexyl phosphine (Tolman cone angle (θ): PPh_3 = 145°; PCy_3 = 179°). The Ni-C_{NHC} bond length of one of the crystallographically independent molecules appeared especially long (1.987(10) Å). There is only one reported example with a longer Ni-C_{NHC} bond length; the cationic *tris*-NHC Ni(I) compound [Ni(L)]Cl (L = N{$(CH_2)_2$(NHC)}$_3$) featuring an average Ni-C_{NHC} bond length of 1.996(4) Å, and the authors reasoned this to be due to the ability of the NHC ligand to be capable of effective π-backbonding to electron-rich metal centres, or act as strong σ-donors to less electron-rich metals, such as the cationic Ni(I) example.[52]

Table 2.7 Selected bond lengths and angles for compounds **2.1** and **2.20**.

Compound	**2.1**	**2.20**[a]	
Ni-C_{NHC} (Å)	1.942(2)	1.969(5)	1.987(10)
Ni-P (Å)	2.2188(6)	2.2514(14)	2.2399(14)
Ni-Br (Å)	2.3331(3)	2.3757(11)	2.3444(11)
C_{NHC}-Ni-P (°)	117.01(6)	129.27(18)	128.6(3)
C_{NHC}-Ni-Br (°)	133.46(6)	128.81(18)	124.9(4)
P-Ni-Br (°)	109.531(19)	101.74(4)	106.00(5)
Σ of angles (°)	360.00(9)	359.82(26)	359.5(7)

[a] Two independent molecules in the unit cell.

2.6.3 Reactivity of 2.1 with Other Tertiary Phosphines

Treatment of compound **2.1** with a range of other tertiary phosphines P(*p*-tol)$_3$, P(*o*-tol)$_3$, P(C_6F_5)$_3$, and P(^{t}Bu)$_3$ (Figure 2.17) led to a reaction only for P(*p*-tol)$_3$. The $^{31}P\{^1H\}$ NMR spectra of each reaction mixture featuring the different phosphines was regularly monitored as reaction time and temperature was increased. The reaction between **2.1** and 2 equiv. of P(*p*-tol)$_3$ showed a ^{31}P resonance for free PPh_3 (δ -5.5 ppm) after 30 min at room temperature, although the ^1H NMR spectra of reaction mixtures after prolonged time (48 hrs) and applied heat (343 K) did not show the formation of clean product (*cf*. reaction between **2.1** and PCy_3). In an attempt to vary the substituents of the phosphine, phobanes (sym-PhobP^{t}Bu and asym-PhobP^{t}Bu)[53, 54] and an adamantyl-cage based phosphine (Cg-P^{t}Bu)[55, 56] donated by the Pringle group (University of Bristol), were tested (Figure 2.17). Using $^{31}P\{^1H\}$ NMR spectroscopy to follow the progress of reactions between **2.1** and the new phosphines, a signal for free PPh_3 failed to emerge in any reaction.

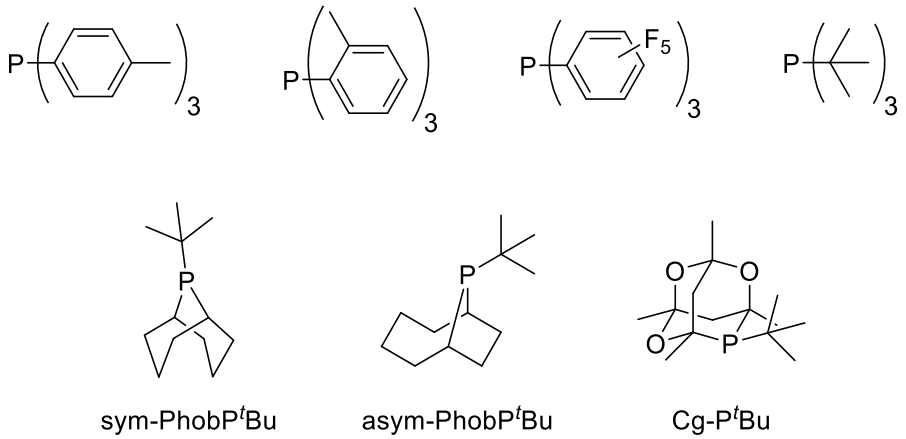

Figure 2.17 Tertiary phosphines used in attempted substitution reactions with **2.1**

The (lack of) reactivity of various PR_3 with **2.1** could be explained by the sterics and electronics of the tertiary phosphines. The Tolman electronic parameter (TEP) and cone angles of the phosphines are shown in Table 2.8.[57, 58] P(*o*-tol)$_3$ is significantly bulkier than both PPh_3 and PCy_3, which likely leads to a lack of reaction. P(*p*-tol)$_3$ has similar steric and electronic properties to PPh_3, so while substitution does occur, there is no driving force for the reaction. Although $P(C_6F_5)_3$ has a cone angle similar to PCy_3, the halogenated phosphine is far more electron-withdrawing, which possibly precluded any reaction.

Unfortunately, no crystal structures (and hence cone angle measurement) featuring sym-PhobP^{t}Bu, asym-PhobP^{t}Bu or Cg-P^{t}Bu have been reported, although one would expect each species to have significant steric bulk. Estimated cone angles for the phobanes and Cg-P^{t}Bu are featured in Table 2.8, based upon their reported *n*-butyl analogues.[54, 59] It is reasonable to expect the *tert*-butyl versions to have similar or even greater steric properties due to the branched nature of the C_4H_9 group. While the phobanes and adamantyl based phosphines are relatively bulky, they are potentially less so than PCy_3 (which readily reacts with **2.1**), although the flexible cyclohexyl rings of PCy_3 are able to bend and distort whereas the phobanes and cage-like phosphines appear more rigid and feasibly impeding any reactivity with **2.1**.

The electronic parameters of the phosphines also did not elucidate their reactivity, with the electron-donation strength of phobanes intermediate between PPh_3 and PCy_3, while Cg-P^{t}Bu was only slightly more electron-poor than PPh_3. This was shown by the $^1J_{PSe}$ coupling constants of selenium-phosphine adducts, whereby the magnitude of the

constant represents the electron-donating ability of the phosphine, with a smaller value indicating better donation (Table 2.8). [54, 59-61]

As with the formation of **2.20**, the substitution route did not provide adequate reactivity between **2.1** and phosphine. This led to the use of the featured tertiary phosphines *via* the alternative Ni(dme)Br_2 synthesis pathway.

Table 2.8 Tolman's electronic parameters (TEP), cone angles, and selenium adduct coupling constants of phosphines used.

Phosphine	**TEP (cm^{-1})**	**Cone angle (°)**	**$^1J_{PSe}$ (Hz)**
PPh_3	2069	145	733
PCy_3	2056	179	676
P(*p*-tol)$_3$	2067	145	-
P(*o*-tol)$_3$	2067	194	-
$P(C_6F_5)_3$	2091	184	-
P(^{t}Bu)$_3$	2056	182	-
sym-PhobP^{t}Bu	-	*ca*. 158[a]	678
asym-PhobP^{t}Bu	-	*ca*. 160[a]	705
Cg-P^{t}Bu	-	*ca*. 170[a]	*ca*. 752[a]

[a] Based on the reported PhobP^{n}Bu and Cg-P^{n}Bu analogues.

2.6.4 Alternative Route Using Other Tertiary Phosphines

Use of the P(*o*-tol)$_3$ in the alternative synthetic route established in section 2.6.2 initially formed a very dark green solution which gave a paramagnetic ^{1}H NMR spectrum, before plating out of what is assured to be Ni metal, preventing any isolation of the product(s). P(^{t}Bu)$_3$ also formed green solutions in C_6H_6, which ^{1}H NMR spectroscopy showed comprised of a mixture of free P(^{t}Bu)$_3$ and [Ni(6Mes)$_2$]Br (compound **3.1**, Chapter 3), together with unassignable peaks in the diamagnetic region of the spectra. While no new Ni(I) species seemed to be formed, this did appear to show a different

synthetic route to making the two-coordinate cationic Ni(I) species introduced later in Chapter 3.

Attempts at incorporating the phobanes sym-PhobP^{t}Bu and asym-PhobP^{t}Bu, and Cg-P^{t}Bu also did not yield the desired three-coordinate Ni(I) products. Reaction mixtures featuring the three bulky phosphines formed orange solutions in C_6H_6, and the ^{1}H NMR spectra in each case showed the diagnostic peaks for [Ni(6Mes)$_2$]Br. Recrystallisation of the Cg-P^{t}Bu reaction mixture led to the formation of pale orange crystals. X-ray crystallography showed that the [Ni(6Mes)$_2$]$^+$ cationic fragment had indeed formed, with the nickelate counterion [Ni(Cg-P^{t}Bu)Br$_2$]$^-$ (Figure 2.18). Although a Ni(I) – CgP^{t}Bu species was created, the formation of a three-coordinate nickelate compound rather than the neutral Ni(RE-NHC)(PR$_3$)Br species showed that the steric clash between carbene and phosphine was too great and it was not possible for a compound to feature both ligands. The same observation appeared in reactions involving the two phobanes and P(^{t}Bu)$_3$ (appearance of ^{1}H NMR signals diagnostic for the [Ni(6Mes)$_2$]$^+$ species). As previously stated, no known examples of Ni – Cg-P^{t}Bu compounds have been reported. The only nickel containing complexes involving the adamantyl based group use the phosphine as part of a bidentate ligand known as PAd-DalPhos, first reported by Stradiotto *et al*.[62]

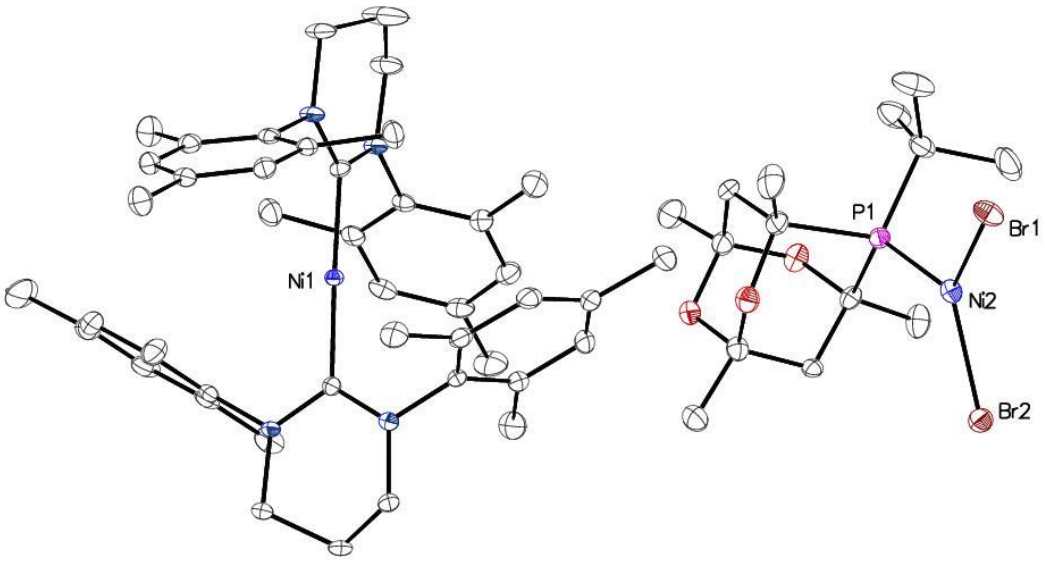

Figure 2.18 Molecular structure of [Ni(6Mes)$_2$][Ni(Cg-P^{t}Bu)Br$_2$]. Thermal ellipsoids are set at 30% probability. All hydrogen atoms have been omitted for clarity.

2.6.5 Synthesis of Ni(RE-NHC)(PCy$_3$)Br Compounds

Following the successful synthesis of compound **2.20**, a preliminary study of the formation of Ni(I) species with other RE-NHCs was pursued. The N-aryl RE-NHCs 6Xyl, 7Mes and 7Xyl brought about the formation of Ni(I) compounds **2.21** – **2.23** (Scheme 2.10), which were isolated as a pale yellow solids in yields between 28 – 61%. The three compounds displayed unassignable paramagnetic ^{1}H NMR spectra, with chemical shifts in the range δ 32 to -3 ppm. Magnetic moments of 2.1 – 2.2 μ_B were recorded in C_6H_6 at room temperature (Evans method). No material suitable for X-ray crystallography could be isolated for any of **2.21** – **2.23**, although, clean product formation was confirmed based on the successful onward reactivity discussed in Chapter 4.

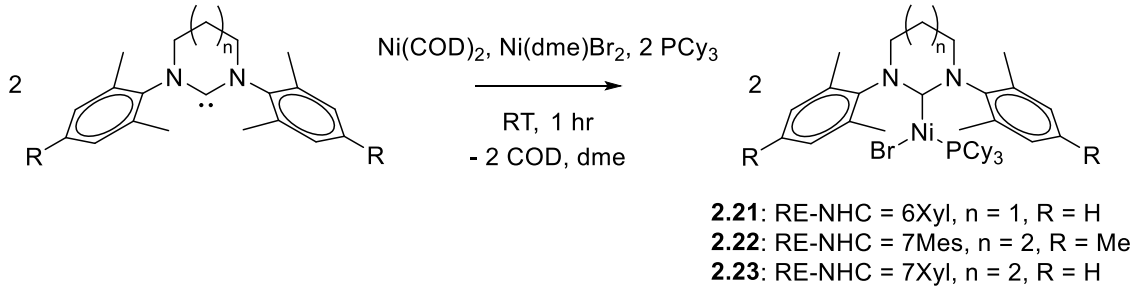

2.21: RE-NHC = 6Xyl, n = 1, R = H
2.22: RE-NHC = 7Mes, n = 2, R = Me
2.23: RE-NHC = 7Xyl, n = 2, R = H

Scheme 2.10 Synthesis of three-coordinate Ni(RE-NHC)(PCy$_3$)Br compounds **2.21** – **2.23**.

2.7 Summary

A series of trigonal planar Ni(RE-NHC)(PPh$_3$)Br compounds have been synthesised, incorporating a range of six- and seven- membered N-aryl and N-alkyl RE-NHCs. These compounds have been characterised by ^{1}H NMR spectroscopy, X-ray crystallography, and room temperature solution magnetic measurements (Evans method). While the use of N-aryl RE-NHCs led to successful formation of Ni(I) species, the synthesis of N-alkyl analogues proved more challenging, with a range of three and four-coordinate Ni(II) compounds characterised alongside the desired Ni(I) species.

Reactivity of Ni(6Mes)(PPh$_3$)Br **2.1** with a variety of halide abstracting agents yielded a series of new mono- and dinuclear nickel compounds which were characterised by ^{1}H NMR, X-ray crystallography, and EPR spectroscopy. Use of TlPF$_6$ in THF formed the T-shaped cationic THF bound compound **2.17**. Efforts to avoid working with toxic thallium salts led to the use of NaBAr$^F{}_4$, which formed the unusual bromide-bridged

nickel(I) dimer **2.18** in Et_2O. Exposure of both **2.17** and **2.18** to 1 atm CO gave the rare Ni(I)-CO species **2.19**.

The electronic structures of **2.1**, **2.17**, **2.19**, **I**, and **II** were examined using a combination of DFT calculations, EPR spectroscopy and X-ray crystallography. It was shown that the differences in geometry were dependent on the *d*-orbital character of the SOMO, whereby the SOMO of a T-shaped compound was expected to be predominantly d_{x2-y2}, whereas trigonal planar had more d_{xy} contribution. The effect of geometry on the *g* values of observed experimental EPR spectra was also examined. While all compounds showed rhombic EPR spectra with $g_1 < g_2 << g_3$ values, as the geometry moved from trigonal planar to T-shaped (and d_{x2-y2} contribution to the SOMO increases) the g_2 values shifted closer to g_1.

Efforts to substitute the PPh_3 within **2.1** with the bulkier PCy_3 led to the formation of compound **2.20**. Use of a variety of aryl and alkyl tertiary phosphines including bicyclic phobanes and adamantyl-cage based analogues did not lead to any new Ni(I) species. A new synthetic pathway featuring comproportionation of $Ni(COD)_2$ and $Ni(dme)Br_2$ in the presence of free RE-NHCs and PCy_3 led to clean formation of **2.20** and a series of $Ni(RE\text{-}NHC)(PCy_3)Br$ compounds, which were spectroscopically characterised. Use of other bulky and more rigid tertiary phosphines appeared to generate the cationic two-coordinate nickel species $[Ni(6Mes)_2]^+$ which was isolated in one case with $[Ni(Cg\text{-}P^tBu)Br_2]^-$ as the counterion.

2.8 References

1. C. J. E. Davies, M. J. Page, C. E. Ellul, M. F. Mahon and M. K. Whittlesey, *Chem. Commun.*, 2010, **46**, 5151-5153.
2. M. J. Page, W. Y. Lu, R. C. Poulten, E. Carter, A. G. Algarra, B. M. Kariuki, S. A. Macgregor, M. F. Mahon, K. J. Cavell, D. M. Murphy and M. K. Whittlesey, *Chem. Eur. J.*, 2013, **19**, 2158-2167.
3. R. C. Poulten, I. Lopez, A. Llobet, M. F. Mahon and M. K. Whittlesey, *Inorg. Chem.*, 2014, **53**, 7160-7169.
4. W. J. M. Blackaby, S. Sabater, R. C. Poulten, M. J. Page, A. Folli, V. Krewald, M. F. Mahon, D. M. Murphy, E. Richards and M. K. Whittlesey, *Dalton Trans.*, 2018, **47**, 769-782.
5. S. Nagao, T. Matsumoto, Y. Koga and K. Matsubara, *Chem. Lett.*, 2011, **40**, 1036-1038.
6. K. Matsubara, Y. Fukahori, T. Inatomi, S. Tazaki, Y. Yamada, Y. Koga, S. Kanegawa and T. Nakamura, *Organometallics*, 2016, **35**, 3281-3287.
7. S. Miyazaki, Y. Koga, T. Matsumoto and K. Matsubara, *Chem. Commun.*, 2010, **46**, 1932-1934.
8. K. Zhing, M. Conda-Sheridan, S. R. Cooke and J. Louie, *Organometallics*, 2011, **30**, 2546-2552.
9. C. Lin and P. P. Power, *Chem. Soc. Rev.*, 2017, **46**, 5347-5399.
10. N. A. Eckert, A. Dinescu, T. R. Cundari and P. L. Holland, *Inorg. Chem.*, 2005, **44**, 7702-7704.
11. P. Pietrzyk, K. Podolska and Z. Sojka, *J. Phys. Chem. A*, 2008, **112**, 12208-12219.
12. J. Krzystek, J. H. Park, M. W. Meisel, M. A. Hitchman, H. Stratemeier, L. C. Brunel and J. Telser, *Inorg. Chem.*, 2002, **41**, 4478-4487.
13. G. Rogez, J. N. Rebilly, A. L. Barra, L. Sorace, G. Blondin, N. Kirchner, M. Duran, J. van Slageren, S. Parsons, L. Ricard, A. Marvilliers and T. Mallah, *Angew. Chem. Int. Ed.*, 2005, **44**, 1876-1879.
14. F. Neese and D. A. Pantazis, *Faraday Discuss.*, 2011, **148**, 229-238.
15. R. Ruamps, L. J. Batchelor, R. Maurice, N. Gogoi, P. Jimenez-Lozano, N. Guihery, C. de Graaf, A. Barra, J. Sutter and T. Mallah, *Chem. Eur. J.*, 2013, **19**, 950-956.

16. R. Ruamps, R. Maurice, L. Batchelor, M. Boggio-Pasqua, R. Guillot, A. L. Barra, J. Liu, E. Bendeif, S. Pillet, S. Hill, T. Mallah and N. Guihery, *J. Am. Chem. Soc.*, 2013, **135**, 3017-3026.
17. R. A. Layfield, *Organometallics*, 2014, **33**, 1084-1099.
18. W. Lin, T. Bodenstein, V. Mereacre, K. Fink and A. Eichhofer, *Inorg. Chem.*, 2016, **55**, 2091-2100.
19. A. A. Danopoulos, T. Simler and P. Braunstein, *Chem. Rev*, 2019, **119**, 3730-3961.
20. T. W. Hudnall and C. W. Bielawski, *J. Am. Chem. Soc.*, 2009, **131**, 16039-16041.
21. T. W. Hudnall, J. P. Moerdyk and C. W. Bielawski, *Chem. Commun.*, 2010, **46**, 4288-4290.
22. T. W. Hudnall, A. G. Tennyson and C. W. Bielawski, *Organometallics*, 2010, **29**, 4569-4578.
23. M. Braun, W. Frank, G. J. Reiss and C. Ganter, *Organometallics*, 2010, **29**, 4418-4420.
24. J. P. Moerdyk and C. W. Bielawski, *Chem. Commun.*, 2014, **50**, 4551-4553.
25. V. Cesar, N. Lugan and G. Lavigne, *J. Am. Chem. Soc.*, 2008, **130**, 11286-11287.
26. V. Cesar, N. Lugan and G. Lavigne, *Eur. J. Inorg. Chem.*, 2010, 361-365.
27. E. Ö. Karaca, N. Gürbüz, H. Arslan, D. VanDerveer and İ. Özdemir, *Appl. Organomet. Chem.*, 2015, **29**, 475-480.
28. C. E. Ellul, J. P. Lowe, M. F. Mahon, P. R. Raithby and M. K. Whittlesey, *Dalton Trans.*, 2018, **47**, 4518-4523.
29. R. Armstrong, C. Ecott, E. Mas-Marza, M. J. Page, M. F. Mahon and M. K. Whittlesey, *Organometallics*, 2010, **29**, 991-997.
30. M. Mayr, K. Wurst, K. H. Ongania and M. R. Buchmeiser, *Chem. Eur. J.*, 2004, **10**, 1256-1266.
31. J. J. Dunsford, D. S. Tromp, K. J. Cavell, C. J. Elsevier and B. M. Kariuki, *Dalton Trans.*, 2013, **42**, 7318-7329.
32. N. Bramananthan, M. Carmona, J. P. Lowe, M. F. Mahon, R. C. Poulten and M. K. Whittlesey, *Organometallics*, 2014, **33**, 1986-1995.
33. S. K. Schneider, W. A. Herrmann and E. Herdtweck, *J. Mol. Catal. A: Chem.*, 2006, **245**, 248-254.
34. M. J. Spallek, D. Riedel, F. Rominger, A. S. K. Hashmi and O. Trapp, *Organometallics*, 2012, **31**, 1127-1132.

35. E. Ö. Karaca, N. Gürbüz, İ. Özdemir, H. Doucet, O. Şahin, O. Büyükgüngör and B. Çetinkaya, *Organometallics*, 2015, **34**, 2487-2493.
36. M. Bouché, M. Mordan, B. M. Kariuki, S. J. Coles, J. Christensen and P. D. Newman, *Dalton Trans.*, 2016, **45**, 13347-13360.
37. K. R. Sampford, J. L. Carden, E. B. Kidner, A. Berry, K. J. Cavell, D. M. Murphy, B. M. Kariuki and P. D. Newman, *Dalton Trans.*, 2019, **48**, 1850-1858.
38. B. Bantu, D. Wang, K. Wurst and M. R. Buchmeiser, *Tetrahedron*, 2005, **61**, 12145-12152.
39. M. Brookhart, M. L. H. Green and G. Parkin, *Proc. Nat. Acad. Sci. U. S. A.*, 2007, **104**, 6908.
40. D. Alberti, R. Goddard and K. Pörschke, *Organometallics*, 2005, **24**, 3907-3915.
41. J. C. A. Boeyens and E. Oosthuizen, *J. Crystallogr. Spectrosc. Res*, 1992, **22**, 3-7.
42. K. T. Szacilowski, P. Xie, A. Y. S. Malkhasian, M. J. Heeg, M. Y. Udugala-Ganehenege, L. E. Wenger and J. F. Endicott, *Inorg. Chem.*, 2005, **44**, 6019-6033.
43. P. Stavropoulos, M. Carrie, M. C. Muetterties and R. H. Holm, *J. Am. Chem. Soc.*, 1990, **112**, 5385-5387.
44. P. J. Schebler, B. S. Mandimutsira, C. G. Riordan, L. M. Liable-Sands, C. D. Incarvito and A. L. Rheingold, *J. Am. Chem. Soc.*, 2001, **123**, 331-332.
45. M. J. Ingleson, B. C. Fullmer, D. T. Buschhorn, H. Fan, M. Pink, J. C. Huffman and K. G. Caulton, *Inorg. Chem.*, 2008, **47**, 407-409.
46. B. Horn, S. Pfirrmann, C. Limberg, C. Herwig, B. Braun, S. Mebs and R. Metzinger, *Z. Anorg. Allg. Chem.*, 2011, **637**, 1169-1174.
47. C. Yoo, S. Oh, J. Kim and Y. Lee, *Chem. Sci.*, 2014, **5**, 3853-3858.
48. M. Abubekerov, L. Y. M. Eymann, T. L. Gianetti and J. Arnold, *Dalton Trans.*, 2016, **45**, 14581-14590.
49. D. Sellmann, R. Prakash, F. W. Heinemann, M. Moll and M. Klimowicz, *Angew. Chem. Int. Ed.*, 2004, **43**, 1877-1880.
50. P. Pietrzyk, K. Podolska and Z. Sojka, *Chem. Eur. J.*, 2009, **15**, 11802-11807.
51. S. Alvarez, *Coord. Chem. Rev.*, 1999, **193–195**, 13-41.
52. X. Hu, I. Castro-Rodriguez and K. Meyer, *Chem. Commun.*, 2004, 2164-2165.
53. M. Carreira, M. Charernsuk, M. Eberhard, N. Fey, R. van Ginkel, A. Hamilton, W. P. Mul, A. G. Orpen, H. Phetmung and P. G. Pringle, *J. Am. Chem. Soc.*, 2009, **131**, 3078-3092.

54. J. M. Lister, M. Carreira, M. F. Haddow, A. Hamilton, C. L. McMullin, A. G. Orpen, P. G. Pringle and T. E. Stennett, *Organometallics*, 2014, **33**, 702-714.
55. V. Gee, A. Guy Orpen, H. Phetmung, P. G. Pringle and R. I. Pugh, *Chem. Commun.*, 1999, 901-902.
56. J. H. Downing, J. Floure, K. Heslop, M. F. Haddow, J. Hopewell, M. Lusi, H. Phetmung, A. G. Orpen, P. G. Pringle, R. I. Pugh and D. Zambrano-Williams, *Organometallics*, 2008, **27**, 3216-3224.
57. C. A. Tolman, *J. Am. Chem. Soc.*, 1970, **92**, 2953-2956.
58. C. A. Tolman, *Chem. Rev.*, 1977, **77**, 313-348.
59. P. N. Bungu and S. Otto, *Dalton Trans.*, 2011, **40**, 9238-9249.
60. S. Otto, A. Ionescu and A. Roodt, *J. Organomet. Chem.*, 2005, **690**, 4337-4342.
61. P. N. Bungu and S. Otto, *J. Organomet. Chem.*, 2007, **692**, 3370-3379.
62. C. M. Lavoie, P. M. MacQueen, N. L. Rotta-Loria, R. S. Sawatzky, A. Borzenko, A. J. Chisholm, B. K. V. Hargreaves, R. McDonald, M. J. Ferguson and M. Stradiotto, *Nat. Commun.*, 2016, **7**, 11073.

CHAPTER 3

3 SYNTHESIS OF TWO-COORDINATE HOMOLEPTIC [Ni(RE-NHC)$_2$]Br COMPOUNDS

3.1 Background

3.1.1 Synthesis and Characterisation of [Ni(6Mes)$_2$]Br (3.1)

Following the successful formation of three-coordinate Ni(I) species with the use of sterically bulky RE-NHCs, and observing the range of nickel mono- and dinuclear compounds formed from the reactivity of compound **2.1** when exposed to a range of halide abstraction reagents and phosphines, the next logical step was to utilise the ring-expanded carbenes in an attempt to form even lower coordinate nickel species.

The substitution of phosphines by NHCs is well known, with various nickel examples reported. Hermann *et al*. showed that free ICy could substitute the weaker donor ligand PPh_3 in $Ni(PPh_3)_2X_2$ (X = Cl, Br) at room temperature to form the *bis*-carbene Ni(II) compound $Ni(ICy)_2X_2$.[1] Matsubara reported that IMes also formed the *bis*-carbene Ni(II) species $Ni(IMes)_2X_2$ whether one or two equiv. of NHC was used, whereas the use of the bulkier IPr carbene allowed more control over the substitution.[2] One equiv. of IPr formed the mono-carbene Ni(II) compound $Ni(IPr)(PPh_3)X_2$, which when exposed to a second equiv. of carbene gave $Ni(IPr)_2X_2$. The Whittlesey group have also reported an example, which featured RE-NHCs, whereby treatment of $Ni(PPh_3)_2Br_2$ with one equiv. of 6^{o}Tol or 7^{o}Tol formed Ni(II) compounds $Ni(6^oTol)(PPh_3)Br_2$ and $Ni(7^oTol)(PPh_3)Br_2$ respectively.[3] Using compound **2.1** (Ni(6Mes)(PPh_3)Br) as a starting material, it would be reasonable to predict that PPh_3 substitution would occur to give either three-coordinate $Ni(6Mes)_2Br$, analogous to $Ni(IPr)_2Cl$ (**xii**) and $Ni(IMes)_2X$ (**xv**) (X = Cl, Br, I) examples previously mentioned,[4, 5] or given the sterics of the RE-NHC, a two-coordinate species $[Ni(6Mes)_2]Br$. The latter was proved correct when the reaction between compound **2.1** and free 6Mes formed the novel cationic *bis*-carbene Ni(I) species $[Ni(6Mes)_2]Br$ **3.1** (Scheme 3.1).[6]

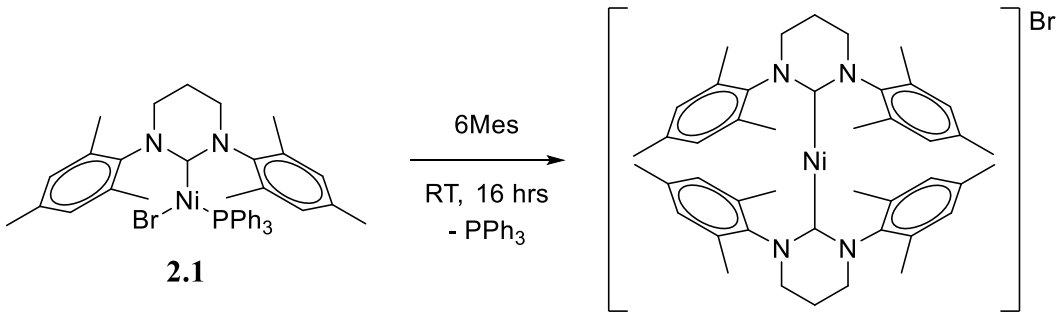

2.1 **3.1**

Scheme 3.1 Synthesis of [Ni(6Mes)$_2$]Br **3.1** from compound **2.1** and 6Mes.

The reaction involved combining compound **2.1** with free 6Mes in THF and stirring the reaction mixture overnight at room temperature. A gradual colour change occurred from yellow to an off-white suspension, which when allowed to settle, afforded a light brown solution and off-white precipitate. The solid was isolated, washed with diethyl ether to remove any remaining free phosphine and carbene, and recrystallised from CH_2Cl_2/hexane to give off-white crystalline material in 81% yield.

The ^{1}H NMR spectrum of compound **3.1** displayed paramagnetically shifted signals in the range δ 53 to -21 ppm, much wider than the spectrum of **2.1** (Figure 3.1). However, perhaps due to the widened nature of the spectrum, five distinct signals were observed, corresponding to the five proton environments within compound **3.1**. This allowed for integration and tentative assignment of the proton resonances. The broad singlet resonances at δ 52.6 (4H, NCH$_2$C*H*$_2$) and 50.1 ppm (8H, NC*H*$_2$) could be assigned to the carbene backbone protons, while the N-mesityl groups showed broad singlet signals at δ -10.6 (12H, *p*-C*H*$_3$), -12.8 (24H, *o*-C*H*$_3$) and -20.7 ppm (8H, *m*-C*H*$_{aryl}$).

As with the three-coordinate Ni(I) species in Chapter 2, room temperature effective magnetic moment measurements were performed on compound **3.1**. Solution measurements in CH_2Cl_2 *via* the Evans method gave a value of 3.3 μ_B, a value that is considerably higher than those observed for the three-coordinate Ni(I) species of Chapter 2 (*cf.* compound **2.1** with 2.1 μ_B). DFT calculations and subsequent SQUID measurements (details *vide infra*) explain the observed magnetic moment measurement.

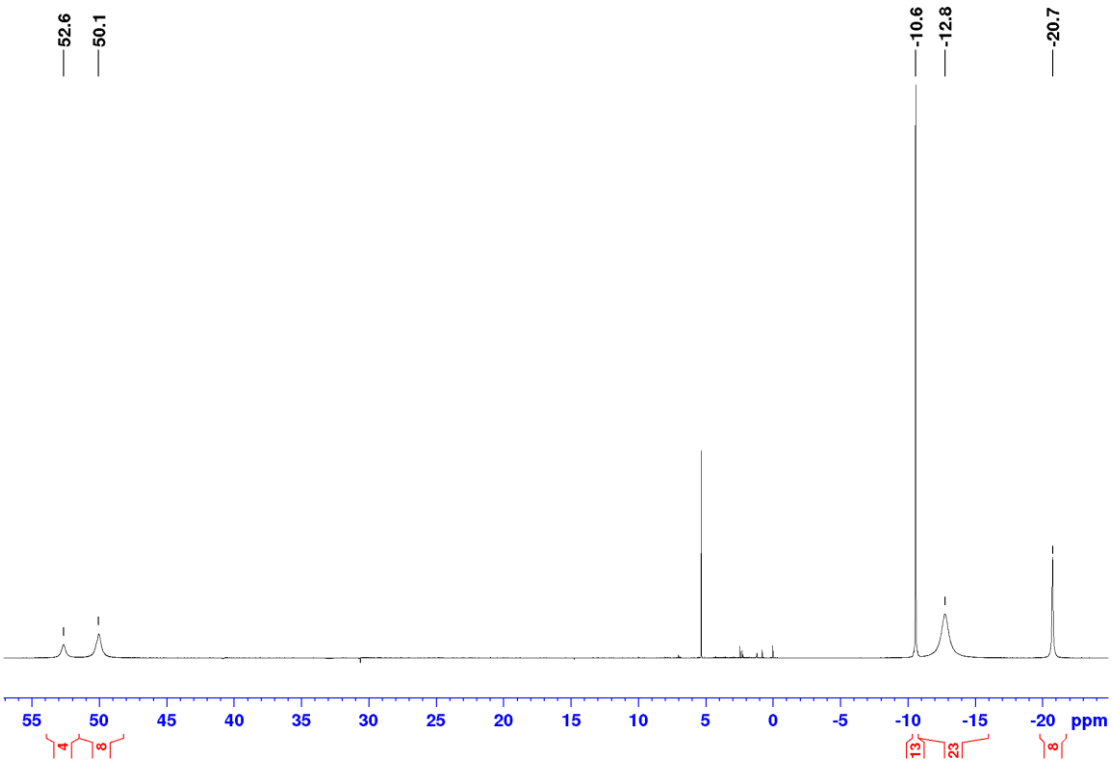

Figure 3.1 ^{1}H NMR spectrum (CD_2Cl_2, 500 MHz, 298 K) of compound **3.1**.

X-ray crystallography analysis of suitable crystals grown from CH_2Cl_2/hexane confirmed the two-coordinate structure of compound **3.1** (Figure 3.2). The cationic component showed a highly linear geometry, with a C_{NHC}-Ni-C_{NHC} bond angle of 179.27(13)°, and equal Ni-C_{NHC} bond lengths (1.939(3) and 1.941(3) Å). Remarkably, although the nickel is formally 13e$^-$ and highly electron deficient, no stabilising interactions between the Ni centre and N-substituent C-H bonds were observed. No close Ni-Ni contacts were observed in the X-ray data, with the shortest distance between two Ni(I) ions measured at 10.32 Å (pertinent to the magnetism section). To alleviate the steric clash between bulky N-mesityl groups, the 6Mes ligands were almost perpendicular to each other, with the angle between the two hypothetical N-C_{NHC}-N planes (denoted torsion angle, shown in Figure 3.2) measured at 77.84(11)°. The N-C_{NHC}-N bond angles in compound **3.1** were slightly larger than that seen in three-coordinate **2.1** (**3.1**: 117.6(2) and 117.3(3)°; **2.1**: 116.48(19)°), although the large estimated standard deviation values mean that they are not significantly different.

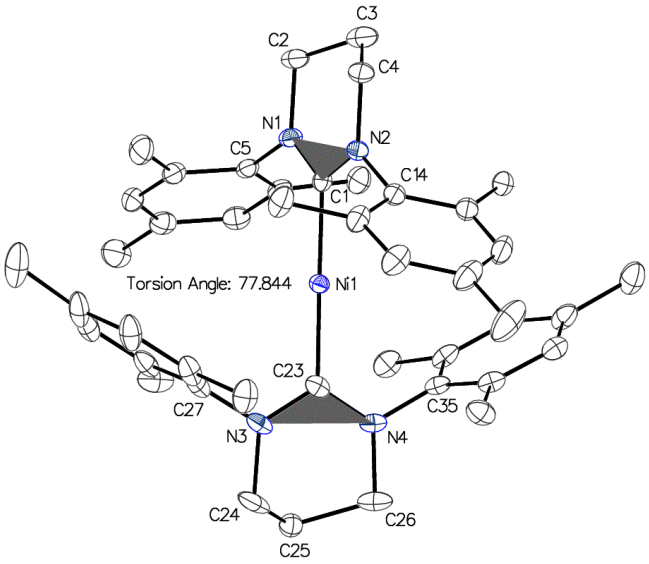

Figure 3.2 Molecular structure of the cation in compound **3.1**. Thermal ellipsoids are set at 30% probability. All hydrogen atoms have been omitted for clarity.

With the two carbene ligands providing encapsulation of the Ni(I) centre, the two-coordinate species demonstrated air and moisture stability when solutions of compound **3.1** were exposed to air. No obvious colour change occurred, and ^{1}H NMR spectra of samples left exposed for 30 min showed no change to the compound signals. Only after several hours did the pale yellow solution turn to brown, though the ^{1}H peaks of compound **3.1** could still be seen in the NMR spectra.

Other characterisation techniques such as cryoscopy and electrochemistry of compound **3.1** have been previously reported by Poulten.[6] Also featured in Poulten's work was the chemical reduction of **3.1** with powerful reducing agent KC_8 in THF. The resultant *bis*-carbene Ni(0) compound Ni(6Mes)$_2$ was isolated as a dark purple product and exhibited extreme air-sensitivity. X-ray structure analysis revealed a surprising decrease in Ni-C_{NHC} bond lengths from 1.941(3)/1.939(3) Å for **3.1** to 1.852(2)/1.868(3) Å for Ni(6Mes)$_2$. DFT calculations reproduced this observation (average Ni-C_{NHC}: 1.945 Å in **3.1** *vs.* 1.869 Å in Ni(6Mes)$_2$) but removed any suggestion that this was due to increased electron density on the nickel metal centre by showing analogous behaviour in $[Ni(NH_3)_2]^+$/$Ni(NH_3)_2$. Key here is that NH_3 is purely a σ-donor, and the calculated molecular orbital diagram showed an *sd*-hybridised orbital which was non-bonding with respect to the NH_3 ligands. Upon oxidation to Ni(I), the amount of *s* contribution decreased and the orbital gained some antibonding character, resulting in

elongation of the Ni-C bond.[6] A similar Ni-ligand bond length elongation was observed for the $Pd(P^tBu_3)_2$/$[Pd(P^tBu_3)_2]PF_6$ couple, wherein the Pd(0) compound underwent one electron oxidation with ferrocenium.[7] Ozerov *et al*. presented analogous work, involving the one electron oxidation of $M(P^tBu_3)_2$ (M = Pd, Pt) with trityl carborane salt $[Ph_3C]HCB_{11}Cl_{11}$ to form two-coordinate linear $[M(P^tBu_3)_2]HCB_{11}Cl_{11}$ compounds.[8] Rationalisation by only considering the energies and occupancy of molecular orbitals did not provide a satisfactory explanation to the observed M-P bond elongation, but, by including the consideration of attractive electrostatic and repulsive Pauli contributions, one can have a better understanding of the structural changes.

3.2 Synthesis and Characterisation of Other $[Ni(RE\text{-}NHC)_2]Br$ Compounds

No other *bis*-NHC Ni(I) species had been reported before or after the publication of compound **3.1** by the Whittlesey group. In fact, the only other isolated *bis*-NHC species involving nickel to be crystallographically reported have been eight examples of Ni(0) species featuring a range of IMes, IPr, I^{t}Bu, IMes^{Me2}, SI^{t}Bu, SIPr, and 6Mes ligands.[6, 9-14] Therefore, it was deemed pertinent to see the effect of varying the NHC ring size and N-group substituents, with the aim to achieve this through:

- Developing a robust synthetic pathway to forming new two-coordinate Ni(I) species, derived from the fact that Ni(6Mes)(PPh_3)Br (**2.1**) was successfully used as a reactive precursor to forming a two-coordinate Ni(I) complex (**3.1**), and the chemistry of Ni(RE-NHC)(PPh_3)Br analogues was similar to that of **2.1**.
- Any new two-coordinate species would undergo analysis of the structural, electronic, and magnetic properties to determine the impact of varying the nature of the RE-NHC.

Using the same synthetic procedure introduced in Scheme 3.1, a small series of two-coordinate compounds **3.2** – **3.4** were formed, featuring the RE-NHCs 6Xyl, 7Mes, and 7Xyl (Scheme 3.2). A THF solution of Ni(RE-NHC)(PPh_3)Br combined with the corresponding free RE-NHC (*i.e.* Ni(6Xyl)(PPh_3)Br with free 6Xyl) was stirred at room temperature overnight, with each reaction mixture forming a precipitate that was isolated as a pale yellow/off-white solid in yields of 54 – 77%.

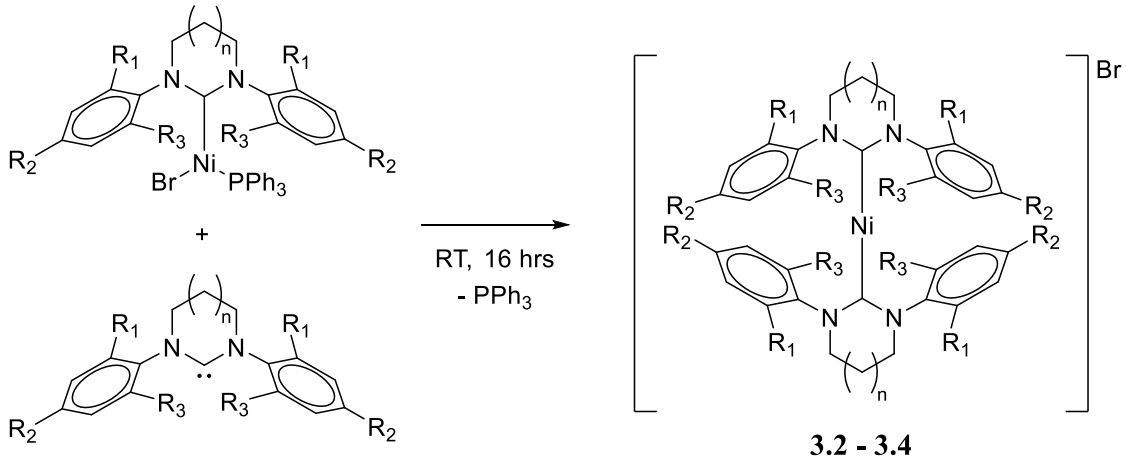

3.2: RE-NHC = 6Xyl, n = 1, R_1/R_3 = Me, R_2 = H
3.3: RE-NHC = 7Mes, n = 2, $R_1/R_2/R_3$ = Me
3.4: RE-NHC = 7Xyl, n = 2, R_1/R_3 = Me, R_2 = H

Scheme 3.2 Synthesis of two-coordinate [Ni(RE-NHC)$_2$]Br compounds **3.2** – **3.4**.

^{1}H NMR spectroscopy of compounds **3.2** – **3.4** displayed similarly broad and paramagnetic signals in the range δ 54 to -21 ppm, analogous to the spectrum of compound **3.1**. The ^{1}H peaks could be integrated and assigned in the same fashion as **3.1**, whereby the downfield signals (δ 40 – 60 ppm region) correspond to carbene backbone protons, while the three signals for the N-aryl substituents appeared significantly further upfield. The ^{1}H NMR spectrum of compound **3.2** showed two broad singlets for the carbene backbone protons at δ 54.4 (4H, NCH$_2$C*H*$_2$) and 52.1 ppm (8H, NC*H*$_2$), along with a very broad singlet at δ -13.3 ppm (24H *o*-C*H*$_3$) and singlet resonances at δ -15.6 (4H, *p*-C*H*$_{aryl}$) and -21.3 ppm (8H, *o*-C*H*$_{aryl}$) which correspond to the three different environments of the N-aryl group. Compound **3.3** displayed broad proton resonances at δ 49.2 (8H, NCH$_2$C*H*$_2$) and 38.7 ppm (8H, NC*H*$_2$) for the carbene backbone, and upfield signals corresponding to the N-mesityl substituents at δ -8.3 (12H, *p*-C*H*$_3$), -11.2 (24H *o*-C*H*$_3$), and -17.7 ppm (8H, C*H*$_{aryl}$). The third homoleptic species **3.4** showed a ^{1}H NMR spectrum with broad singlet peaks at δ 51.1 (8H, NCH$_2$C*H*$_2$) and 40.0 ppm (8H, NC*H*$_2$) for the carbene backbone protons, and singlets at δ -11.8 (24H *o*-C*H*$_3$), -14.1 (4H, *p*-C*H*$_{aryl}$), and -18.2 ppm (8H, *o*-C*H*$_{aryl}$) which arise from the N-aryl groups.

Room temperature solution magnetic moments of compounds **3.2** – **3.4** were measured in CH_2Cl_2 *via* the Evans method and displayed values in the range 3.0 to 3.3 μ_B, indicative of two unpaired electrons.

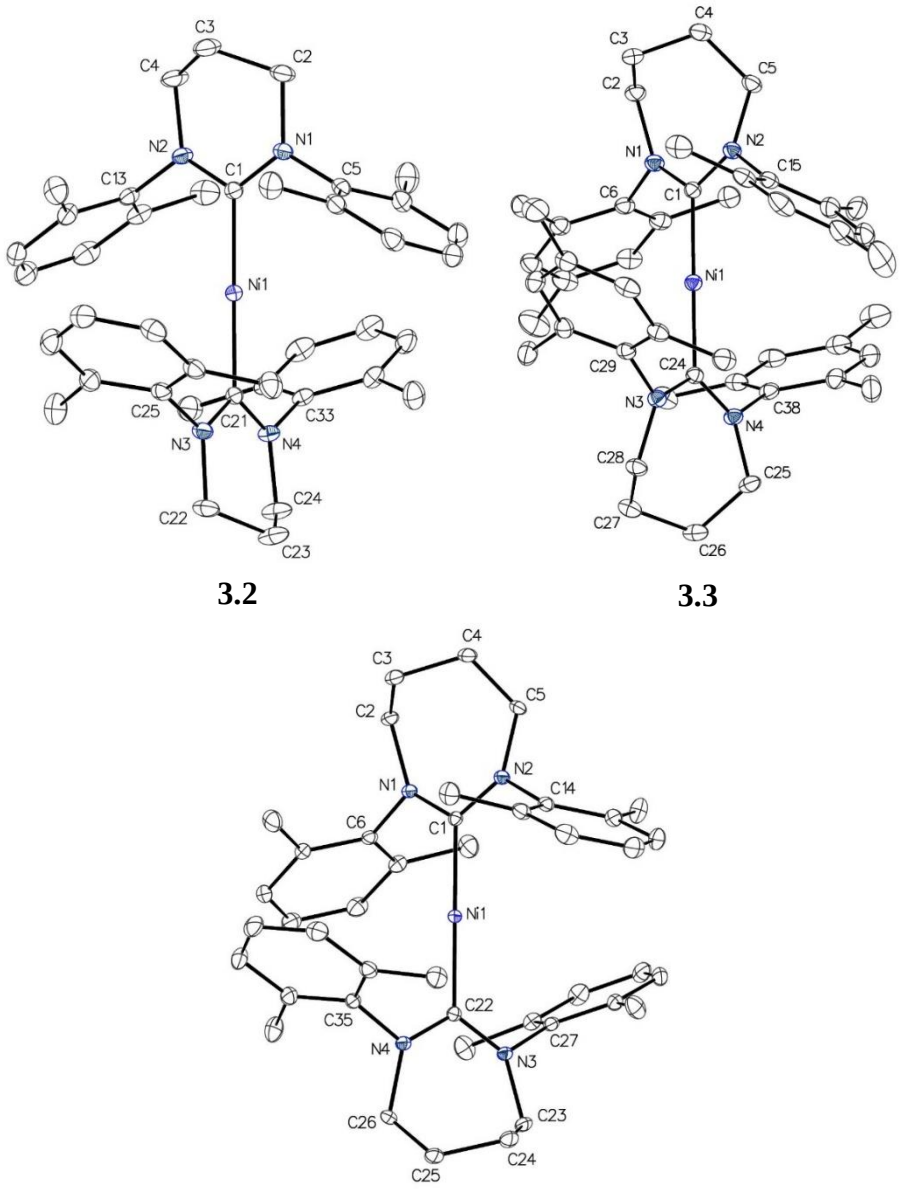

Figure 3.3 Molecular structures of the cations in **3.2** – **3.4**. Thermal ellipsoids are set at 30% probability. All hydrogen atoms have been omitted for clarity.

Recrystallisation of compounds **3.2** – **3.4** from CH_2Cl_2/hexane led to isolation of suitable crystals for X-ray crystallography, which revealed the same two-coordinate structure and linear geometry seen for **3.1** (Figure 3.3). Selected bond lengths and angles for compounds **3.1** – **3.4** are displayed in Table 3.1. Each new two-coordinate species showed a highly linear C_{NHC}-Ni-C_{NHC} arrangement, with bond angles between 178.92(11) – 179.78(15)°. The Ni-C_{NHC} bond lengths in compound **3.2** were close to those in **3.1** (**3.2**: 1.9431(19) Å, **3.1**: 1.941(3)/1.939(3) Å), while the seven-membered ring

counterparts **3.3**/**3.4** had marginally longer bond lengths (1.954(3)/1.959(3) Å and 1.9552(16) Å respectively). The range of bond lengths in compounds **3.1** – **3.4** was essentially unchanged from those in the three-coordinate starting materials (1.942(2) – 1.9596(18) Å), showing that the change of coordination number does not appear to affect the Ni-C_{NHC} distance. The N-C_{NHC}-N bond angles were as anticipated, with the seven-membered RE-NHCs showing a slightly wider angle than their six-membered analogues (**3.2**: 117.39(17)° *vs*. **3.4**: 118.28(15)°), although again, not significantly different when accounting for the estimated standard deviation. Just as for **3.1**, no short Ni-Ni contacts were observed in the structures of **3.2** – **3.4**, with the closest distances measured at 10.40 Å, 10.63 Å, and 10.42 Å respectively. Interestingly, the torsion angle between N-C_{NHC}-N planes along the C_{NHC}-Ni-C_{NHC} axis vary across the range of compounds, from 89.51(11)° in **3.2** to 68.08(10)° in **3.4**. The increase in torsion angle for the 7Mes derivative **3.3** (85.76(13)°) compared to the 6Mes derivative **3.1** probably reflects the ring expansion forcing the mesityl wing tips closer to the metal centre, thus increasing the opportunity for steric clash which can be alleviated by the carbenes residing at *ca*. 90°. However, why the 7Xyl carbenes in **3.4** are less staggered than the 6Xyl carbenes in **3.2** is unclear. Closer analysis of the packing arrangements of the crystal structures for the two compounds provided no clues.

Table 3.1 Selected bond lengths and angles for compounds **3.1** – **3.4**.

Compound	Ni-C_{NHC} (Å)	N-C_{NHC}-N (°)	C-Ni-C (°)	Torsion angle (°)
3.1	1.941(3)/1.939(3)	117.6(2)/117.3(3)	179.27(13)	77.84(11)
3.2[a]	1.9431(19)	117.39(17)	178.92(11)	89.51(11)
3.3	1.954(3)/1.959(3)	118.2(3)/119.2(3)	179.30(14)	85.76(13)
3.4[a]	1.9552(16)	118.28(15)	179.78(15)	68.08(10)

[a] Single values of Ni-C_{NHC} bond lengths and N-C_{NHC}-N bond angles are given when the nickel metal centre was located on a symmetry site.

Attempts to use compounds **2.3** and **2.7** (Ni(6^{o}Tol)(PPh_3)Br and Ni(7^{o}Tol)(PPh_3)Br) as precursors to two-coordinate species did not yield any products. Reaction mixtures of **2.3**/**2.7** and their corresponding free RE-NHC in THF did not change colour or form any precipitate after 48 hrs at room temperature, and ^{1}H NMR spectra of

the solutions showed no diagnostic signals for the two-coordinate species. This observation reflected the fact that the N-tolyl group was not sterically encumbered enough to stabilise the very low-coordinate compounds.

Similarly, efforts to incorporate the electron-withdrawing 6MesDAC were unsuccessful. NMR spectra of reaction mixtures of compound **2.9** and free 6MesDAC displayed starting material peaks and no new product peaks. Unlike the *o*-tol analogues, 6MesDAC should have provided the steric bulk necessary, on account of the N-mesityl wing tips. However, as previously mentioned, the presence of carbonyl groups in the carbene backbone make the ligand quite electron poor, which was perhaps the reason why no *bis*-6MesDAC species was observed as this would have resulted in a $13e^-$ compound with two significantly electron-withdrawing ligands.

The use of the N-aryl substituted carbenes 6Xyl-*p*-Br and 7Xyl-*p*-Br proved more successful. The reaction between **2.4**/6Xyl-*p*-Br and **2.8**/7Xyl-*p*-Br in THF led to the formation of yellow suspensions. ^{1}H NMR spectra of the reaction mixtures displayed signals that were diagnostic of *bis*-carbene compounds, namely [Ni(6Xyl-*p*-Br)$_2$]Br **3.5** and [Ni(7Xyl-*p*-Br)$_2$]Br **3.6**. The precipitates were isolated, but despite multiple recrystallisation attempts from CH_2Cl_2/hexane at both room temperature and 238 K, only oily residue and solid material too small for X-ray crystallography was produced.

Following on from the synthesis of three-coordinate Ni(I) compounds **2.13** – **2.16** with N-alkyl RE-NHCs (section 2.2.2), efforts were made to expand the number of characterised two-coordinate species to include such RE-NHCs. Attempts to introduce 6^{i}Bu, 6^{n}Pent, 7^{i}Bu, and 7^{n}Pent did not generate any new two-coordinate species. The ^{1}H NMR spectra of reactions showed unassignable signals in the diamagnetic region and no broad and shifted paramagnetic peaks. The lack of new products was probably due to the same reason that the N-tolyl analogue did not form, in that the sterics are suitable to make three-coordinate compounds while other bulky phosphine ligands are present (*e.g.*, PPh_3), but not effective at stabilising two-coordinate species.

3.3 Computational Studies of [Ni(RE-NHC)$_2$]Br Compounds 3.1 – 3.4

In spite of ^{1}H NMR spectroscopy and X-ray crystallography giving evidence that compounds **3.1** – **3.4** contained d^9 Ni(I) metal centres, the room temperature effective magnetic moment measurements appeared to contradict this, in yielding values between 2.7 – 3.3 μ_B, significantly greater than the moments expected of a compound with a single

unpaired electron (spin-only = 1.73 μ_B). Although previously described three-coordinate compounds from Chapter 2 have shown some deviation from the spin-only value due to inherent magnetic anisotropy (1.6 – 2.4 μ_B), the recorded values of the two-coordinate species **3.1** – **3.4** correspond closer to two unpaired electrons. DFT calculations (Prof Stuart Macgregor) performed as part of work undertaken by Poulten provided an explanation for these findings, whereby the electronic structure of compound **3.1** was predicted to comprise of five occupied metal based *d*-orbitals split in an approximate 2:1:2 pattern (Figure 3.4).[6]

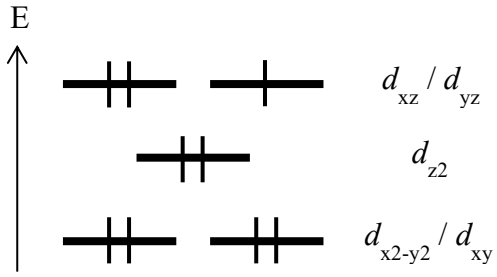

Figure 3.4 The predicted *d*-orbital splitting arrangement from DFT calculations of compound **3.1**.

This is in contrast to what is observed in typical linear ML_2 complexes, as mentioned in Chapter 1. Linear systems have been shown to exhibit an electronic arrangement where the five *d*-orbitals are split in a 1:2:2 pattern, and a HOMO comprised of the d_{z2} orbital, arising from crystal field theory (specifically from calculations of splitting components for the trigonal bipyramidal geometry, and then "removal" of trigonal planar environments to leave behind a linear system).[15, 16] The predicted splitting pattern for **3.1** was derived from DFT calculations (employing the BP86 functional) on the reduced Ni(0) analogue $Ni(6Mes)_2$, and then applied to the cationic species. The pattern placed orthogonal orbitals d_{xz} and d_{yz} as the highest energy orbitals, and close enough in energy to be considered degenerate. The unpaired electron of the d^9 ion is now in a degenerate set of orbitals that form the HOMO, and as a result, lead to interesting magnetic properties.

Table 3.2 Ligand field orbital splitting parameters for compounds **3.1** – **3.4** (computed at the SOC-CASSCF(9,5)/NEVPT2/def2-SVP level).

	Relative *d*-orbital energies (cm^{-1})					
Compound	**1**	**2**	**3**	**4**	**5**	**Δ*E*(4,5)**
3.1	0	226	2322	4071	4207	135
3.2	0	13	2140	4068	4077	9
3.3	0	245	2895	3521	3912	391
3.4	0	819	2682	4064	4321	257

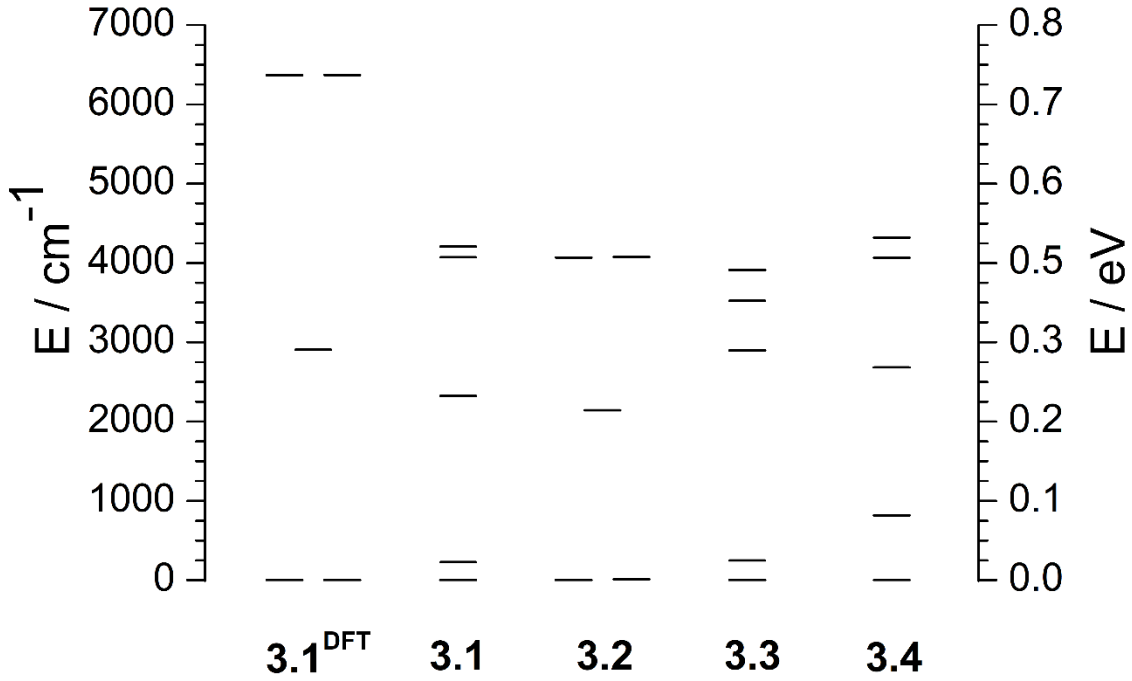

Figure 3.5 Energetic splitting of the ligand field orbitals of compounds **3.1** – **3.4** based on CASSCF, with the orbital splitting pattern of **3.1** from DFT to compare.

Subsequent computational work by Drs Vera Krewald and Elizaveta Suturina (University of Bath) was done on compounds **3.1** – **3.4**, whereby CASSCF calculations (derived from the X-ray crystal structures) produced ligand field orbital splitting parameters to describe the d^9 electronic configurations. The CASSCF results are summarised in Table 3.2 and Figure 3.5, with calculations done in a (9,5) active space using a def2-SVP basis set. The NEVPT2 correction was included to account for the

dynamical electron correlation. The first excited state for all Ni(I) compounds was very low in energy (< 391 cm^{-1}), meaning that the ground state is degenerate (as predicted from the initial DFT work). It is important to note that the CASSCF derived electronic structures have a different orbital order (d_{x2-y2}, $d_{xy} > d_{z2} > d_{xz}$, d_{yz}) to the DFT calculations (d_{xz}, $d_{yz} > d_{z2} > d_{x2-y2}$, d_{xy}). This is due to the fact that DFT is unable to predict the correct order of *d*-orbitals due to limitations in describing the wave functions relating to degenerate orbitals. *Ab initio* ligand field theory based on the CASSCF calculations show that the d_{xz}, d_{yz} orbitals are stabilised by backbonding to NHCs,[i] the d_{z2} orbital is stabilised by 3*d*-4*s* mixing, and the d_{x2-y2}, d_{xy} orbitals have minimal interaction with the carbenes and thus are highest in energy. This results in the unpaired electron residing in a degenerate set of orbitals that form the HOMO, giving rise to orbital angular momentum. As these linear Ni(I) compounds have the ligands located along the z-axis and thus unable to interact with the unpaired electron in the HOMO, the orbital angular momentum remains unquenched by the ligand field. Hence, an orbital contribution needs to be considered when calculating magnetic moments and susceptibilities.[17, 18] The maximum orbital contribution possible for compounds **3.1** – **3.4** is $L = 2$, arising from the fact that the unpaired electron is located in the d_{x2-y2}, d_{xy} set of orbitals which have the quantum number $M_L = \pm 2$.[19, 20] The orbital angular momentum leads to a spin-orbit coupling and magnetic anisotropy, large energy separation of the ground and first excited state, and SIM behaviour (*vide infra*).

3.4 *p*NMR Analysis of [Ni(RE-NHC)$_2$]Br Compounds 3.1 – 3.4

Although the ^{1}H NMR spectra of compounds **3.1** – **3.4** show a wide chemical shift range and broad peaks, analysis of the spectra can still give some interesting insight into the characterisation of the Ni(I) species. DFT calculations by Drs Krewald and Suturina were performed to give the optimised geometries of **3.1** – **3.4** in solution, from which the hyperfine parameters (*A* values) can be extracted. These parameters can be used to determine the paramagnetic shift with respect to a diamagnetic reference. From these *A* values, the contact shift and pseudocontact shift (PCS) contributions to the paramagnetic

[i] Note that the d_{xz}, d_{yz} orbitals are only degenerate for compound **3.2**, whereby the torsion angle between 6Xyl ligands is perpendicular. Compound **3.4** has the largest energy difference between the d_{xz} and d_{yz} orbitals, and the most acute torsion angle (Table 3.1), resulting in poorer overlap and poorer stabilisation between the Ni *d*-orbitals and NHC π-orbitals.

shift can be determined, which arise from through-bond and through-space interactions between the unpaired electron and the nucleus of interest. This coupling means that the nucleus experiences a large local magnetic field due to the unpaired electron relative to the external magnetic field from the spectrometer, giving rise to large shielding/deshielding of the nucleus and thus very large chemical shifts (*vs.* diamagnetic analogues). Once the paramagnetic shift has been determined, information about the magnetic susceptibility of the compounds can be found.

The DFT derived hyperfine parameters were assigned to all of the signals of each compound, and best fits of χ_{iso} and χ_{ax} were found by performing a linear least squares fit of the shift data to Equation 3.1. Once χ_{iso} and χ_{ax} values are known, the NMR shifts of each compound can be calculated.

Equation 3.1

$$\delta = (A_{iso}\chi_{iso} + A_{ax}\Delta\chi_{ax})\frac{10^{-28}}{\gamma_N \hbar \mu_0}$$

$$A_{iso} = \frac{A_{xx} + A_{yy} + A_{zz}}{3} \; and \; A_{ax} = \frac{2A_{zz} - A_{xx} - A_{yy}}{9}$$

The fit of ^{1}H NMR shifts indicated that the contact contribution (~ χ_{iso}) to the paramagnetic shift was significantly smaller than the PCS contribution (~ χ_{ax}). The contact contribution arises from the through-bond interaction between electron and nucleus, and it is proportional to the product of isotropic parts of hyperfine and magnetic susceptibility tensors. Conversely, the PCS contribution is from when there is anisotropy of both the magnetic susceptibility and hyperfine tensors, and so the electron-nucleus interaction becomes sensitive to the orientation of the unpaired electron and thus affected by the geometry (*i.e.*, through-space interaction). In most transition metal compounds where magnetic anisotropy is small, the PCS contribution is negligible, and so the paramagnetic shift can be calculated from just A_{iso} and χ_{iso}, which are known for each metal ion and can also be found experimentally (*e.g.*, from the Evans method). In the case of compounds **3.1** – **3.4**, significant magnetic anisotropy from the Ni(I) centre causes the PCS contribution to dominate, meaning that the paramagnetic shift is instead reliant on knowing $\Delta\chi_{ax}$, the axiality (anisotropy) of the magnetic susceptibility tensors which, in this work, was found from performing linear fits to Equation 3.1. The values of $\Delta\chi_{ax}$ are shown in Table 3.3, where the computed and experimental (extracted from NMR spectra)

anisotropy of the magnetic susceptibility agree reasonably well. The magnitude and sign of the $\Delta\chi_{ax}$ values indicate that the magnetic anisotropy of compounds **3.1** – **3.4** can be classed as easy-axis, meaning that the spin will preferentially align along the z-axis. The magnitude of the $\Delta\chi_{ax}$ value also represents the scale of the PCS contribution, so by setting the main magnetic axis to align with the Ni-C_{NHC} bond and plotting the $\Delta\chi_{ax}$ value against the A_{ax} coordinates (x, y, z), an isosurface of the PCS contribution can be generated (Figure 3.6 as an example). The blue region presents an increased shielding effect of the nuclei and the red region is increased deshielding. Comparison of the experimentally measured ^{1}H NMR shifts for compounds **3.1** – **3.4** and the paramagnetic shift values show good agreement across all the proton environments (Figure 3.7).

Table 3.3 Anisotropy of the magnetic susceptibility tensor extracted from the experimental room temperature NMR shifts compared to those computed with SOC-CASSCF.

	$\Delta\chi_{ax}(A^3)$		
Compound	**Experimental NMR data**	**NEVPT2 on optimised geometry**	**NEVPT2 on X-ray geometry**
3.1	0.15(1)	0.20	0.21
3.2	0.15(1)	0.18	0.21
3.3	0.13(1)	0.20	0.19
3.4	0.14(1)	0.20	0.21

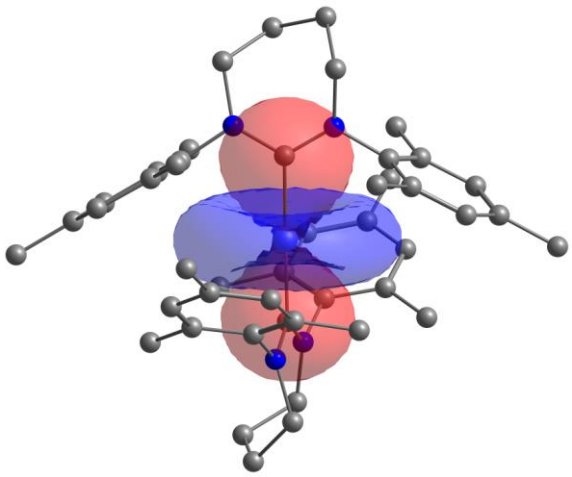

Figure 3.6 Isosurface of the pseudocontact shift for **3.3** showing that a positive shift (red) is expected for the CH_2 groups, and a negative shift (blue) for the mesityl groups.

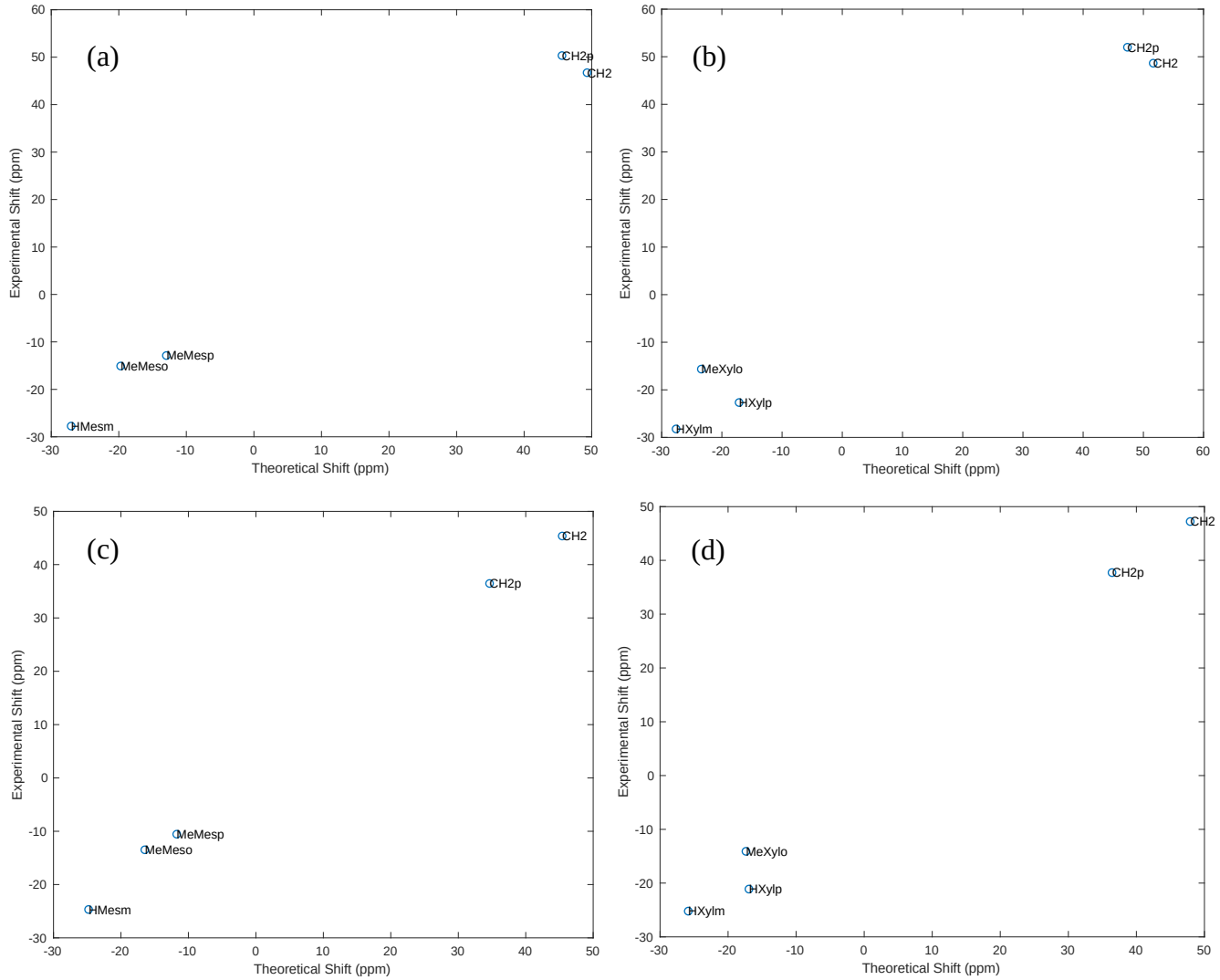

Figure 3.7 Comparison of the experimental and best fit paramagnetic shift for (a) **3.1**, (b) **3.2**, (c) **3.3**, (d) **3.4**.

3.5 EPR Spectroscopy of [Ni(RE-NHC)$_2$]Br Compounds 3.1 – 3.4

X-band EPR spectroscopy was undertaken to determine the spin Hamiltonian parameters of compounds **3.1** – **3.4**, with spectra featuring linewidth broadening due to significant *g* strain effects arising from the anisotropy of the *g* tensor.

EPR spectra of **3.1** – **3.4** were collected at 140 K in frozen CH_2Cl_2/toluene solutions, affording a strongly axial *g* profile which was split into the $g_{\|}$ (g_x, g_y) and $g_{\perp}$ (g_z) components. The $g_{\|}$ component can be seen in the spectra recorded at very low magnetic fields (Figure 3.8). Theoretical calculations predicted that the $g_{\perp}$ component would appear at higher fields, confirmed by X-band EPR spectra run at 10 K which display an extremely broad high field signal (Figure 3.9). The appearance of large *g* values is likely from the unquenched orbital angular momentum and subsequent spin-orbital coupling due to the orbital degeneracy.[21, 22] The resulting spin Hamiltonian parameters are displayed in Table 3.4, along with the CASSCF derived values based upon the X-ray crystal structure with optimised hydrogens.

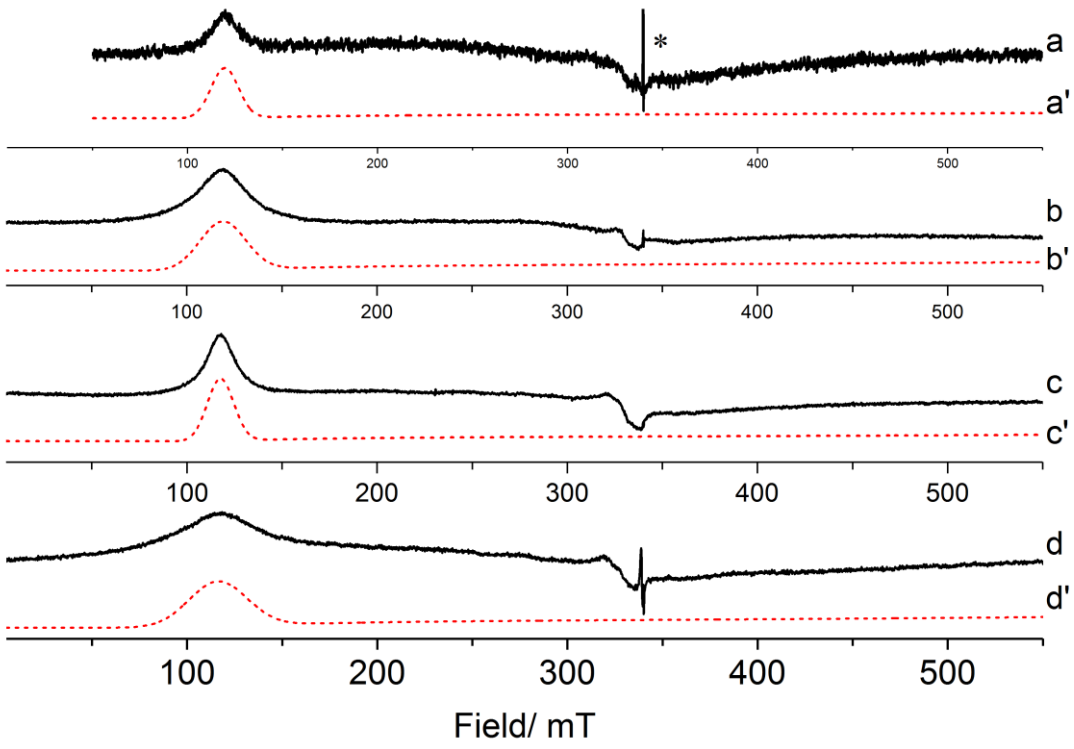

Figure 3.8 Experimental (solid line) and simulated (dashed line) X-band CW EPR spectra (CH_2Cl_2/toluene, 140 K) of (a) **3.1**, (b) **3.3**, (c) **3.2**, (d) **3.4**. Cavity artefacts and impurities in the quartz tube are marked with ∗.

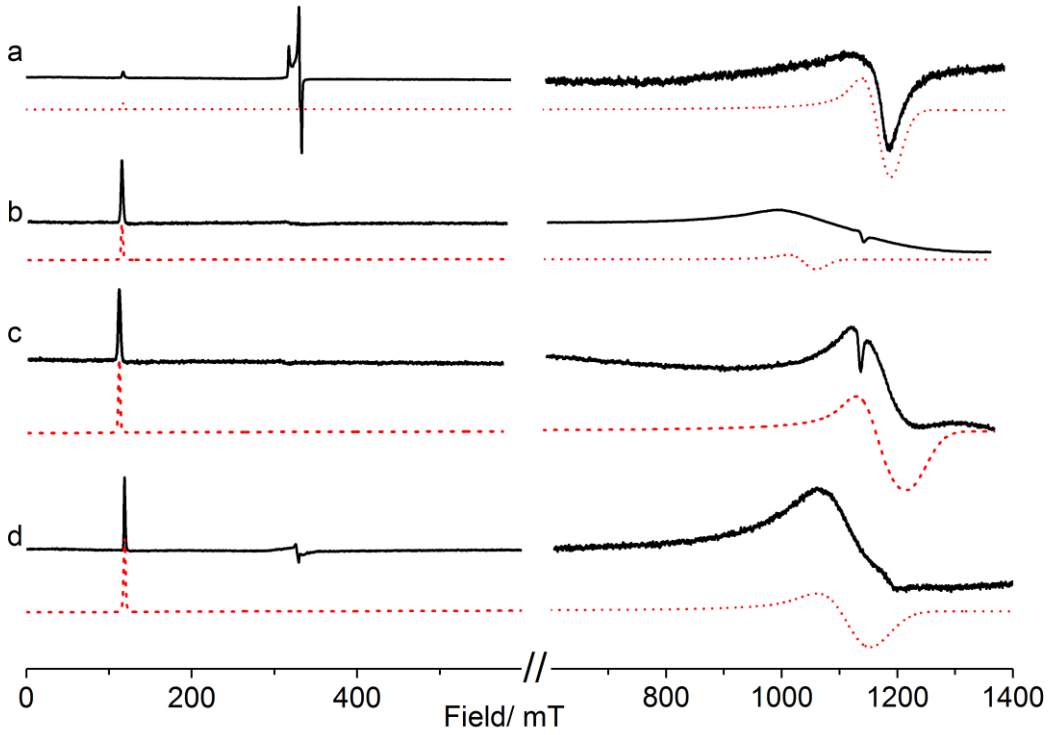

Figure 3.9 Experimental (solid line) and simulated (dashed line) X-band CW EPR spectra (CH_2Cl_2/toluene, 10 K) of (a) **3.1**, (b) **3.3**, (c) **3.2**, (d) **3.4**. A signal from the three-coordinate Ni(6Mes)(PPh_3)Br **2.1** precursor visible and centred near the free electron spin *g* value, g_e = 2.0023, in (a).

Table 3.4 Experimental and CASSCF calculated spin Hamiltonian parameters (*g* values) for compounds **3.1** – **3.4**.

Compound		g_x	g_y	g_z
3.1	*Expt.*	0.567	0.567	5.67
	Calc.	0.1170	0.1418	5.7135
3.2	*Expt.*	0.541	0.571	5.89
	Calc.	1.0457	1.1150	5.3494
3.3	*Expt.*	0.631	0.631	5.76
	Calc.	0.1461	0.1766	5.7174
3.4	*Expt.*	0.600	0.600	5.71
	Calc.	0.2001	0.2279	5.7744

3.6 Variable-field FTIR Spectroscopy of Compound 3.1

Given the large shift in effective *g* values away from the free ion value, and the expectation that this can only arise from a nearly orbitally degenerate state, FTIR spectroscopy performed by Prof. Stephen Hill and Dr Sam Greer (National High Magnetic Field Laboratory, Tallahassee) was employed in an attempt to measure this low-lying state. A complication in the determination of magnetic dipole transitions in the far-IR range is the additional presence of various vibrational modes. Transitions which are field independent arise from electric dipole transitions, while those with field dependent transitions are magnetic dipole allowed, so to separate the vibrational modes from transitions with a magnetic origin, the spectrum was recorded at multiple magnetic fields (0 – 17 T) at 4 K (Figure 3.10, (a)). The measurements revealed only a single transition with an appreciable field dependence, with a zero-field intercept of 643 cm^{-1}. The pair of transitions centred at ~ 612 cm^{-1} are essentially field independent and are therefore could be assigned to either the vibrational modes, or spin-phonon coupling. To observe the field dependent changes more clearly each recorded spectrum was divided by a reference spectrum recorded at 4 T larger field, and the resulting divided spectra were overlaid with a 2D false colour plot to show the evolution of the spectral features with increasing field (Figure 3.10, (b)). Examination of the field dependence of the magnetic transition showed a slight splitting of the feature as the field was increased. Note that the intensity pattern of this splitting is on the order of the standard deviation (grey outlines). The two resulting branches exhibit rates of change of 1.67 cm^{-1} T^{-1} and ~ 1.03 cm^{-1} T^{-1}. These values can be converted into effective *g* values between the ground and excited state by dividing by the Bohr magneton, β_e = 0.46686 cm^{-1} T^{-1}, yielding $\Delta\pm g_1 \sim 3.6$ and $\Delta\pm g_2 \sim 2.2$. The $\Delta\pm$ serves as a reminder that these effective transition *g* values are equal to either the sum or difference of the ground and excited state *g* values.

For comparison, CASSCF calculations were also used to predict the effective energy barrier (U_{eff}) value based upon the crystal structures with optimised hydrogen positions. Initial calculations computed at the SOC-CASSCF(9,5)/NEVPT2/def2-SVP level generated U_{eff} values of 1045, 1105, 854, and 1018 cm^{-1} for compounds **3.1** – **3.4** respectively. These values are higher than the variable-field IR measurement (**3.1**: 643 cm^{-1}) but attempts to improve the level of computational theory are ongoing, with the hope that a larger basis set will provide more accurate U_{eff} values.

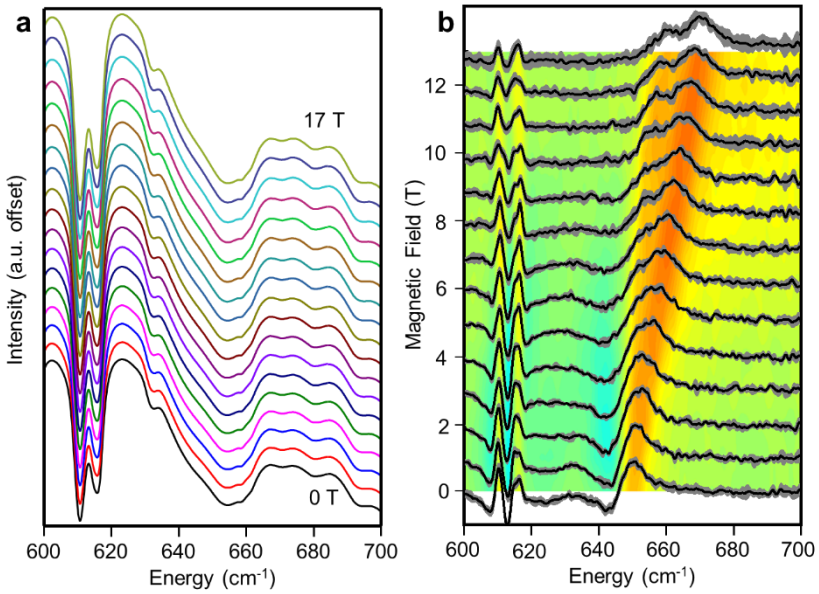

Figure 3.10 a) Averaged FTIR transmission spectra recorded on **3.1** at various fields from 0 T (bottom) to 17 T (top) in 1 T increments, b) FTIR spectra divided by reference spectra recorded at 4 T larger field. The data has been offset by the magnetic field of each recorded spectrum. The grey shading around each spectrum is the standard deviation of the four recorded spectra at each field. The bottom surface is a 2D false colour plot showing the evolution of the spectral feature with increasing applied field. The pair of features centred at ~ 612 cm^{-1} are field independent while the feature originating ~ 643 cm^{-1} displays pronounced field dependence.

3.7 Magnetism of [Ni(RE-NHC)$_2$]Br Compounds 3.1 – 3.4

SQUID measurements of compound **3.1** have been previously recorded and published by Poulten *et al.*[6] At the time of publication, **3.1** was the first example of a Ni(I) ion displaying SIM properties and, to date, no other such examples have been reported. Those findings are included in this section, followed by the work undertaken as an extension of those results (Debye fits of the ac susceptibility measurements and subsequent analysis of the dynamic magnetic properties *via* various relaxation pathways). Also featured is an investigation into the static and dynamic magnetic properties of the new compounds **3.2** – **3.4**.

3.7.1 Static Magnetic Properties

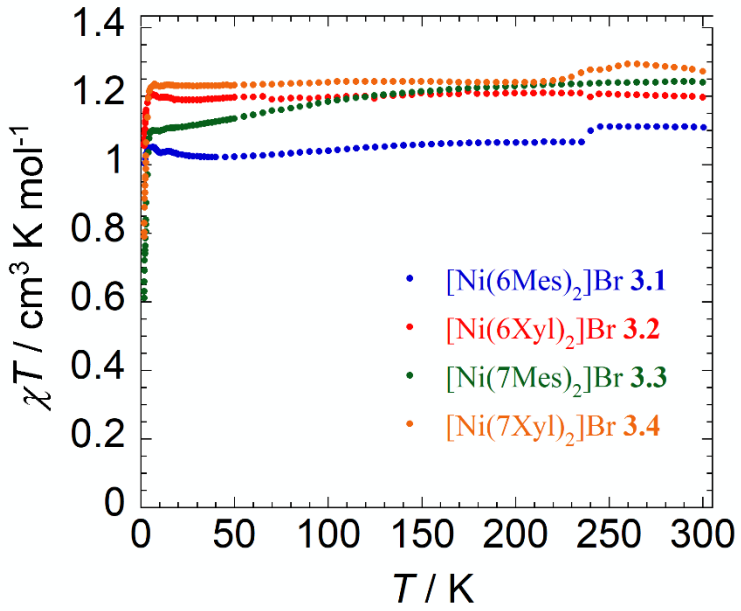

Figure 3.11 Temperature dependence of the χT product of compounds **3.1** – **3.4** under a 1000 Oe applied dc field (with χ being the molar magnetic susceptibility per molecule as defined by M/H).

The dc magnetic properties were measured on polycrystalline samples of **3.1** – **3.4** under a dc field of 1000 Oe in the temperature range 1.8 to 300 K (Figure 3.11). The room temperature (300 K) χT values of 1.11, 1.20, 1.24, and 1.27 cm^3 K mol^{-1} for compounds **3.1** to **3.4** respectively are significantly higher than the spin-only value of 0.375 cm^3 K mol^{-1} for a Ni(I) ion.[i] These high values concur with the large magnetic moments obtained from the Evans method measurements and can be attributed to the significant orbital contribution that needs to be considered for these linear compounds (*vide supra*). A revised expected χT value of 1.575 cm^3 K mol^{-1} for a Ni(I) ion[ii] with unquenched orbital angular momentum is in better agreement with the observed room temperature χT values of **3.1** – **3.4** (Table 3.5). The temperature dependence of χT for each compound was measured, with values remaining constant between 300 and 10 K, and a sharp drop below 10 K to minimum values of 1.00, 1.06, 0.61, and 0.79 cm^3 K mol^{-1} for **3.1** – **3.4** respectively. These were consistent with a non-interacting mononuclear system, which

[i] Spin-only $\chi T = [g^2S(S+1)]/8$; $S = {}^1/_2$, assuming $g = 2$

[ii] *L-S* $\chi T = [g^2J(J+1)]/8$; $S = {}^1/_2$ and $L = 2$ so $J = {}^5/_2$, Landé factor $g = {}^6/_5$ (whereby $g = {}^3/_2 + [S(S+1)-L(L+1)]/2J(J+1)$)

was confirmed by X-ray crystallographic analysis of **3.1** – **3.4** showing only long Ni···Ni distances (10.32 – 10.63 Å) between the two closest approaching molecule, precluding any intermolecular magnetic interactions.

Furthermore, the field dependence of the magnetisation (*M*) in applied dc fields between 0 to 7 T at temperature increments of 1.8, 3, 5, and 7 K was determined for compounds **3.1** – **3.4** (Figure 3.12). Each compound, and in particular **3.1**, showed a rapid increase in *M* at fields below 2 T. This was followed by a more gradual increase of M with increasing field, although the magnetisation did not reach saturation under the 7 T field. Lower-than-expected magnetisation values for **3.1** – **3.4** of 2.01, 1.82, 1.67, and 1.94 μ_B, in combination with the non-superimposition of the reduced magnetisation curves indicate the magnetic anisotropy intrinsic to the Ni(I) ion.

Table 3.5 Magnetic susceptibility (χT) values at 300 K (χT at 1.8 K in italics) and magnetisation saturations (M_S).

Compound	χT **(cm^3 K mol^{-1})**	M_S **(μ_B)**
[Ni(6Mes)$_2$]Br (**3.1**)	1.11 (*1.00*)	2.01
[Ni(6Xyl)$_2$]Br (**3.2**)	1.20 (*1.06*)	1.82
[Ni(7Mes)$_2$]Br (**3.3**)	1.24 (*0.61*)	1.67
[Ni(7Xyl)$_2$]Br (**3.4**)	1.27 (*0.79*)	1.94

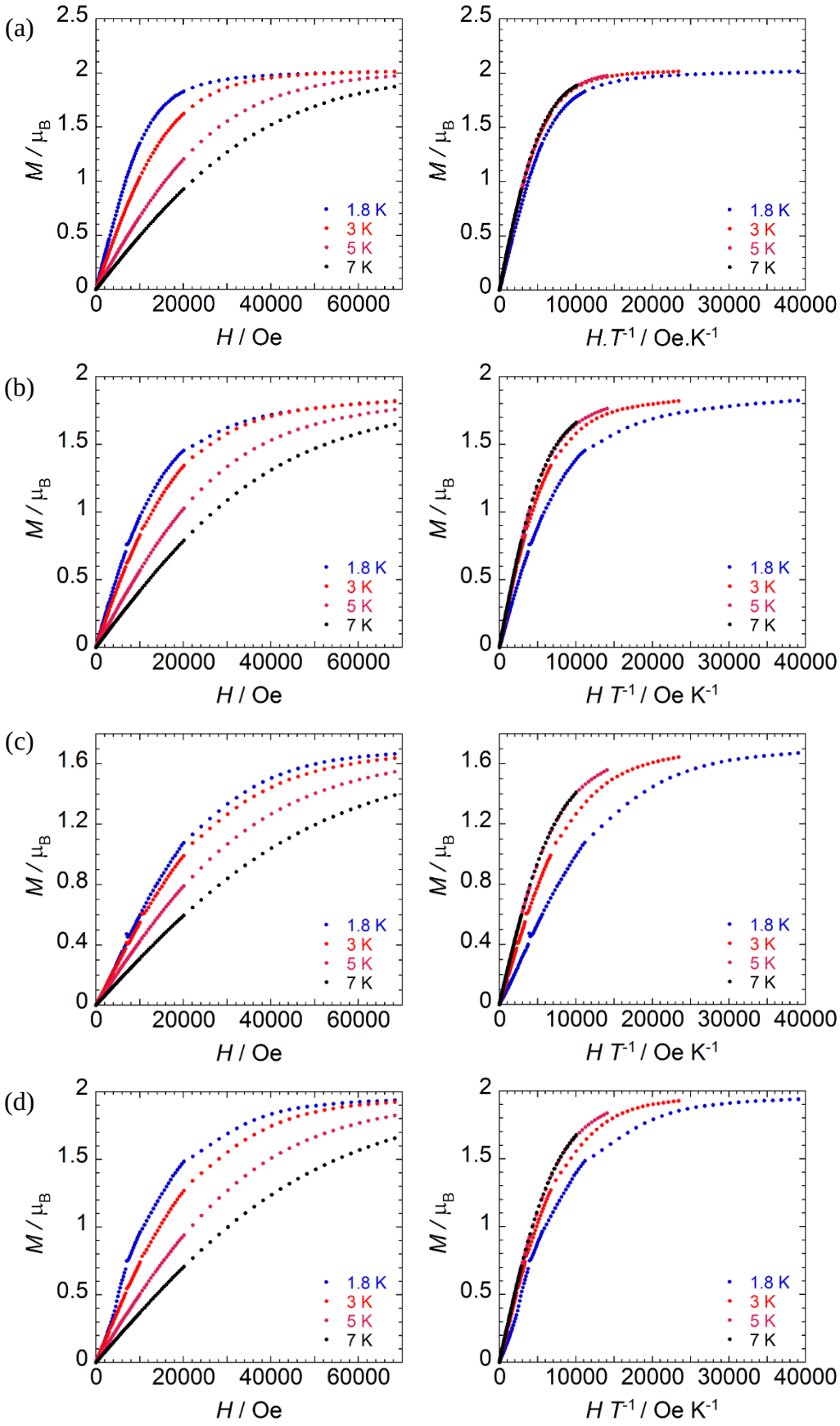

Figure 3.12 Field dependence of the magnetisation (*M vs. H*) (left) and reduced magnetisation (*M vs. H* T^{-1}) (right) for (a) **3.1**, (b) **3.2**, (c) **3.3**, and (d) **3.4**.

3.7.2 Dynamic Magnetic Properties

Measurement of the ac susceptibilities was performed in order to check the presence of any slow magnetic relaxation behaviour. No out-of-phase (χ'') signal was observed under a zero applied dc field, however, each compound exhibited χ'' signals under applied dc fields at 2 K (Figure 3.13, χ' curves in Appendix 7, Figure A7.1). The appearance of a χ'' signal when recording susceptibility measurements under applied fields implied the presence of a QTM mechanism causing rapid relaxation of signals when under zero applied field. The χ'' signal shows a peak maximum that shifts towards lower frequencies (v) with increasing dc field, with the lowest frequency reached with dc fields of *ca*. 600 Oe in **3.1** – **3.3** ((a) – (c), Figure 3.13). Compound **3.4** required application of a higher dc field before the χ'' signal was observed, with the lowest frequency reached when under a 1600 Oe field. This appeared to be an anomalous result, as **3.4** still showed frequency dependent signals at temperatures between 1.8 – 8 K when under the lower strength 600 Oe dc field ((d), Figure 3.14). Accordingly, the frequency dependence of the ac susceptibilities of all four Ni(I) compounds was studied under a 600 Oe dc field.

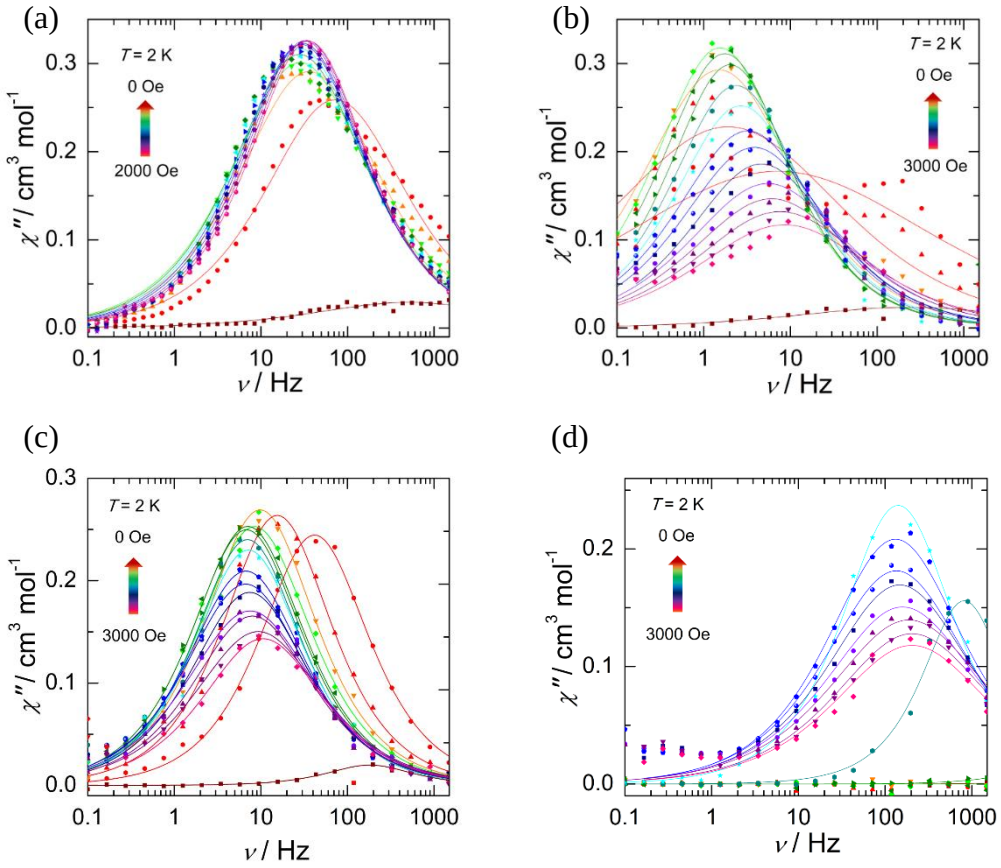

Figure 3.13 Frequency dependence of the out-of-phase (χ'') magnetic susceptibility of (a) **3.1**, (b) **3.2**, (c) **3.3**, and (d) **3.4** as a function of the applied dc field at 2 K. Solid lines represent generalised Debye fits at each field strength.

With the optimal 600 Oe applied dc field set, frequency dependent signals were observed across the temperature ranges 1.8 – 9 K (**3.1**), 1.8 – 12 K (**3.2**), and 1.8 – 8 K (**3.3** and **3.4**) (Figure 3.14). All compounds showed increasing χ'' signals with decreasing temperature and frequency, across the full temperature range, consistent with field-induced SIM behaviour.

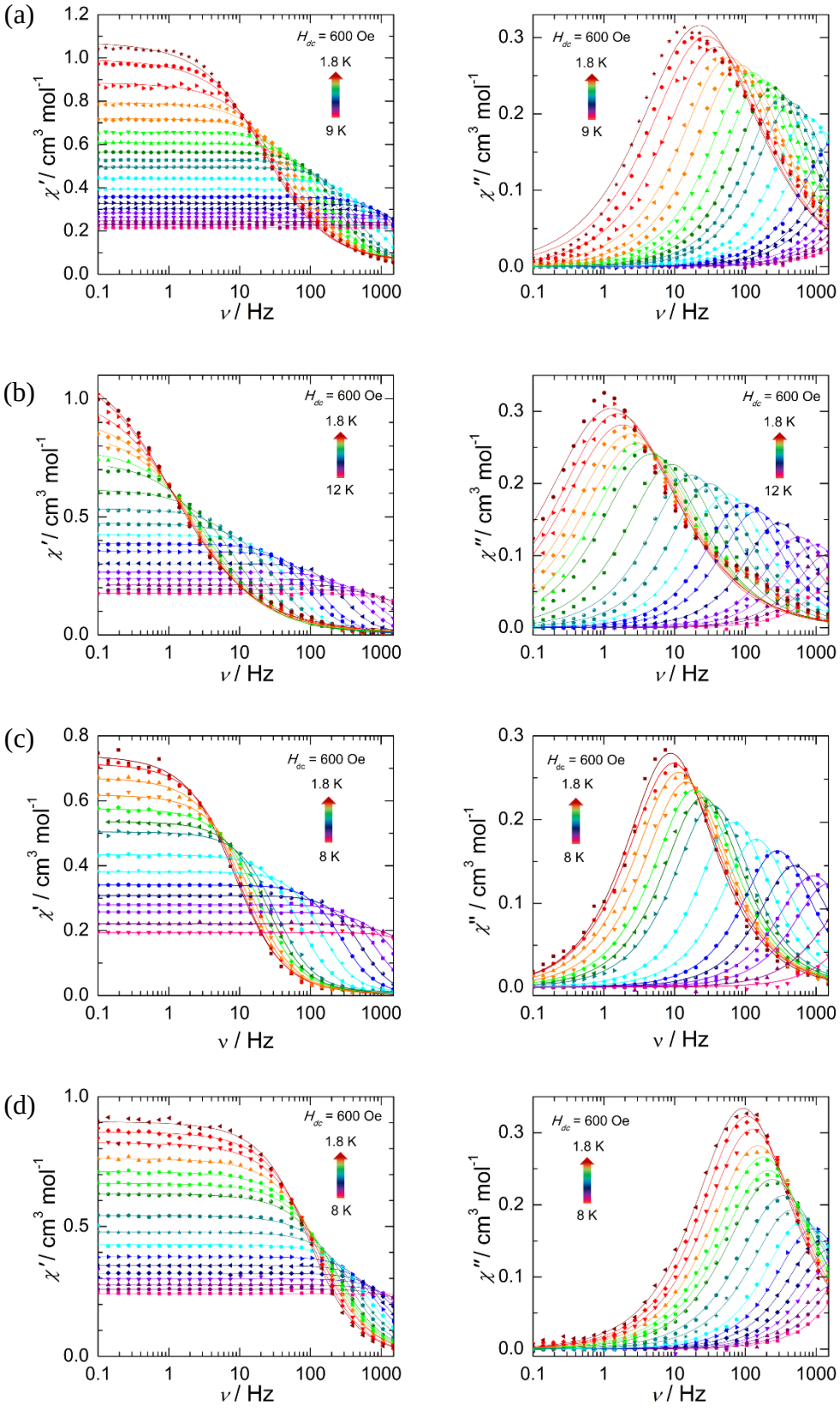

Figure 3.14 Frequency dependence of the in-phase (χ') and out-of-phase (χ'') magnetic susceptibility of (a) **3.1**, (b) **3.2**, (c) **3.3**, and (d) **3.4** as a function of temperature under a 600 Oe applied dc field. Solid lines represent generalised Debye fits at each temperature.

The frequency dependent data of the χ' and χ'' signals as a function of both the applied field (Figure 3.13) and the temperature (Figure 3.14) were fitted to the generalised Debye model as described in Equation 3.2, to give τ, α, χ_S, and χ_T values (where τ is the magnetisation relaxation time, α reflects the extent of the distribution of relaxation times, and χ_S and χ_T are the adiabatic and isothermal and adiabatic susceptibilities respectively).[23] The Debye model parameters determined for compounds **3.1** – **3.4** be found in Appendix 7, with a small range of α parameters ($\alpha < 0.4$) on the vast majority of the fitted data suggesting a reasonable distribution of the relaxation times.

Equation 3.2 χ'' and χ' Debye fits.

$$\chi''(\omega) = (\chi_T - \chi_S)\frac{(\omega\tau)^{1-\alpha}\cos\left(\frac{\pi\alpha}{2}\right)}{1 + 2(\omega\alpha)^{1-\alpha}\,sin\left(\frac{\pi\alpha}{2}\right) + (\omega\tau)^{2-2\alpha}}$$

$$\chi'(\omega) = \chi_S + (\chi_T - \chi_S)\frac{1 + (\omega\tau)^{1-\alpha}\sin\left(\frac{\pi\alpha}{2}\right)}{1 + 2(\omega\alpha)^{1-\alpha}\,sin\left(\frac{\pi\alpha}{2}\right) + (\omega\tau)^{2-2\alpha}}$$

Using the magnetic relaxation data for **3.1** – **3.4** collected under different dc fields at 2 K, dependence of τ on the field was analysed by means of fitting the plot of τ^{-1} *vs.* H (field strength in T rather than Oe) to the relaxation processes in Equation 3.3, whereby the two components denote the direct and QTM processes respectively (Figure 3.15). A constant (D) was also used, with the aim of improving the fits and describing the small contribution of the combination of Raman and Orbach processes. As shown in Figure 3.15, the experimental data could be fitted with reasonable parameters (Table 3.6).

Equation 3.3 Field dependent relaxation pathways for τ^{-1} *vs.* H plot.

$$\tau^{-1} = AH^4T + \frac{B_1}{1 + B_2H^2}$$

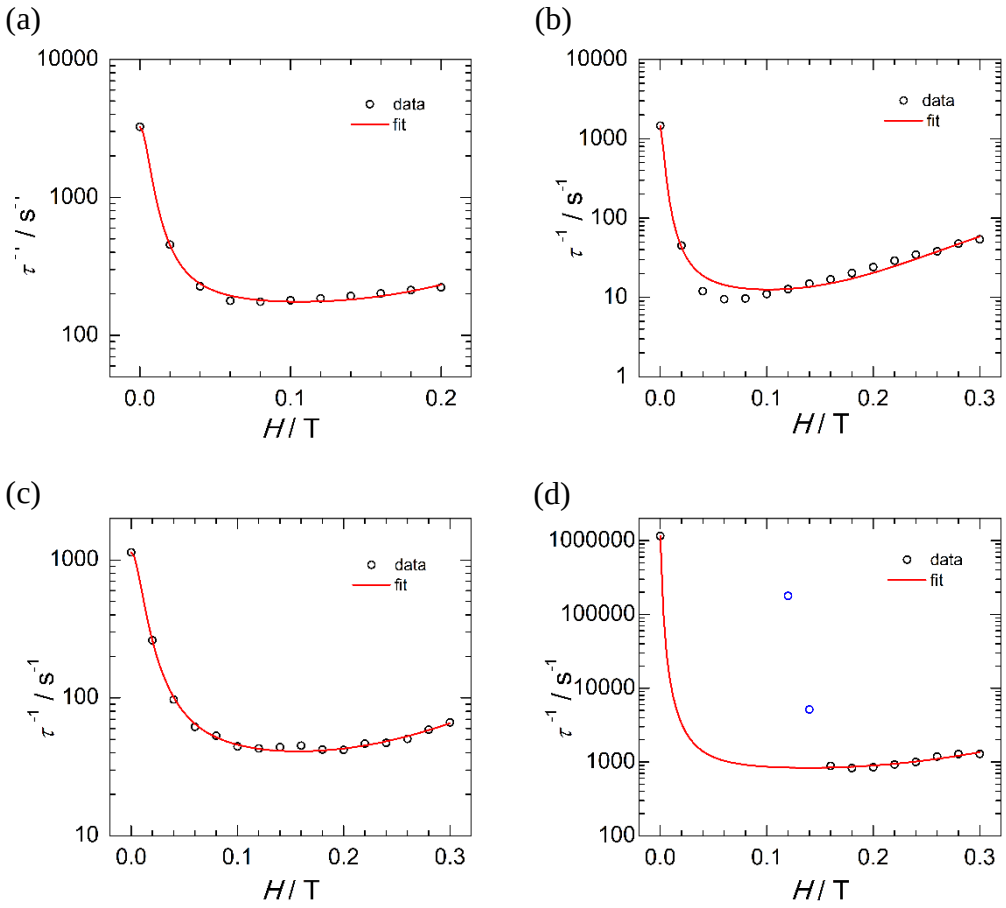

Figure 3.15 Field dependence of the magnetisation relaxation times (τ) of (a) **3.1**, (b) **3.2**, (c) **3.3**, and (d) **3.4** at 2 K. Solid red lines correspond to the best fits using direct and QTM relaxation mechanisms according to Equation 3.3. Blue data points were ignored during the fit.

Table 3.6 The parameters used for best fit of Equation 3.3 and Equation **3.4** for compounds **3.1** – **3.4**.

	A (s^{-1} T^{-4} K^{-1})	B_1 (s^{-1})	B_2 (T^{-2})	C (s^{-1})	n
3.1	2.23×10^4	3.09×10^3	2.40×10^4	3.20	4.85
3.2	2.95×10^3	1.45×10^3	1.11×10^5	0.10	4.96
3.3	1.86×10^3	1.10×10^3	9.70×10^3	0.25	5.90
3.4	3.66×10^4	1.16×10^6	1.12×10^6	43.01	3.01

Further insight into the relaxation dynamics of **3.1** – **3.4** were obtained through plotting τ^{-1} *vs.* T (at 600 Oe = 0.06 T) and modelling to the temperature dependent

relaxation processes featured in Equation 3.4; first and second components represent the direct and QTM processes again, while the third and fourth terms denote Raman and Orbach routes (Figure 3.16). By fixing the parameters of the direct and QTM processes obtained from the τ^{-1} *vs.* H plot (and set H to 0.06 T), fits to the Raman and Orbach relaxation mechanisms across the full temperature range yielded parameters shown in Table 3.6.

Equation 3.4 Temperature dependent relaxation pathways for τ^{-1} *vs.* T plot.

$$\tau^{-1} = AH^4T + \frac{B_1}{1 + B_2H^2} + CT^n + {\tau_0}^{-1} \exp\left(\frac{-U_{eff}}{k_BT}\right)$$

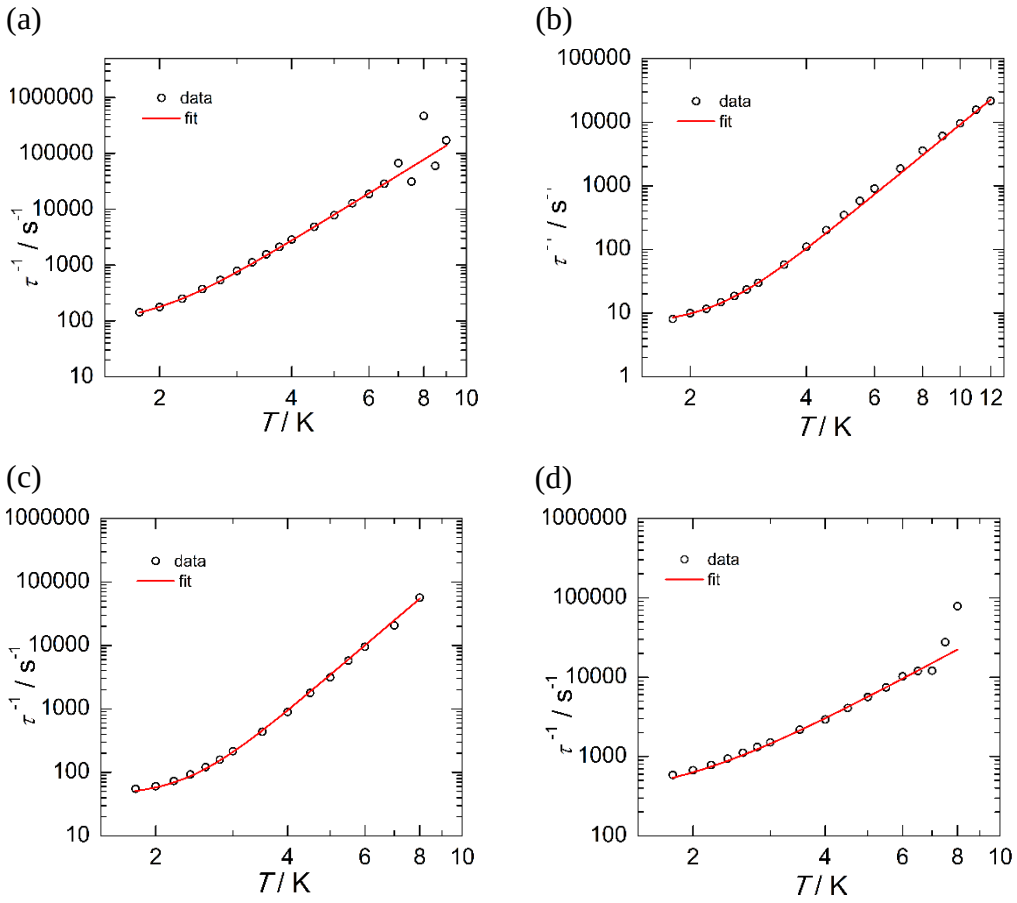

Figure 3.16 Temperature dependence of the magnetisation relaxation times (τ) of (a) **3.1**, (b) **3.2**, (c) **3.3**, and (d) **3.4** under a 600 Oe applied dc field. Solid red lines correspond to the best fits using direct, QTM, Raman, and Orbach relaxation mechanisms according to Equation 3.4.

Across all the compounds, the Raman process components (C and n) appeared to be well fitted. However, the Orbach process could not be fitted with reasonable parameters, due to a lack of exponential data points at the high temperature region. This is especially in light of plotting ln(τ) *vs.* T^{-1} for **3.1** – **3.4** (Figure 3.17), which was fitted with Arrhenius' law and gave estimated U_{eff} values in the range 42.2 – 98.1 K (29.3 – 68.5 cm^{-1}). Only the first few data points at high temperatures are part of the linear Arrhenius regime, before the other relaxation processes dominate and cause the observed deviation from linearity, so these values could be treated as the lower limit for U_{eff} as the variable-field FTIR and CASSCF calculations predicted an energy gap between the ground and first excited states *ca.* ten times larger (*cf.* FTIR: 643 cm^{-1}, CASSCF: 1045 cm^{-1}). While the barrier values for compounds **3.1** – **3.4** were rather modest (although they represent the only examples of Ni(I) SIMs), the presence of the spin-lattice relaxation processes caused fast magnetic relaxation. The phonon based Raman and direct relaxations are common amongst transition metal SIMs but, strictly speaking, the QTM mechanism should not be present in a Kramers ion (non-integer S value, *i.e.*, has an odd electron count) when in zero field. The field induced nature of the susceptibility signals, and absence of any χ'' signals at zero field for any of the Ni(I) compounds most likely arises from mixing between the degenerate ground state and thermally accessible excited states, thus leading to QTM and rapid magnetic relaxation.

Further computation and experimental work is ongoing into establishing if a relationship between the difference in the magnetic anisotropy and energies of the first excited states can explain the difference in relaxation times, or if it is all due to the difference in vibrational modes.

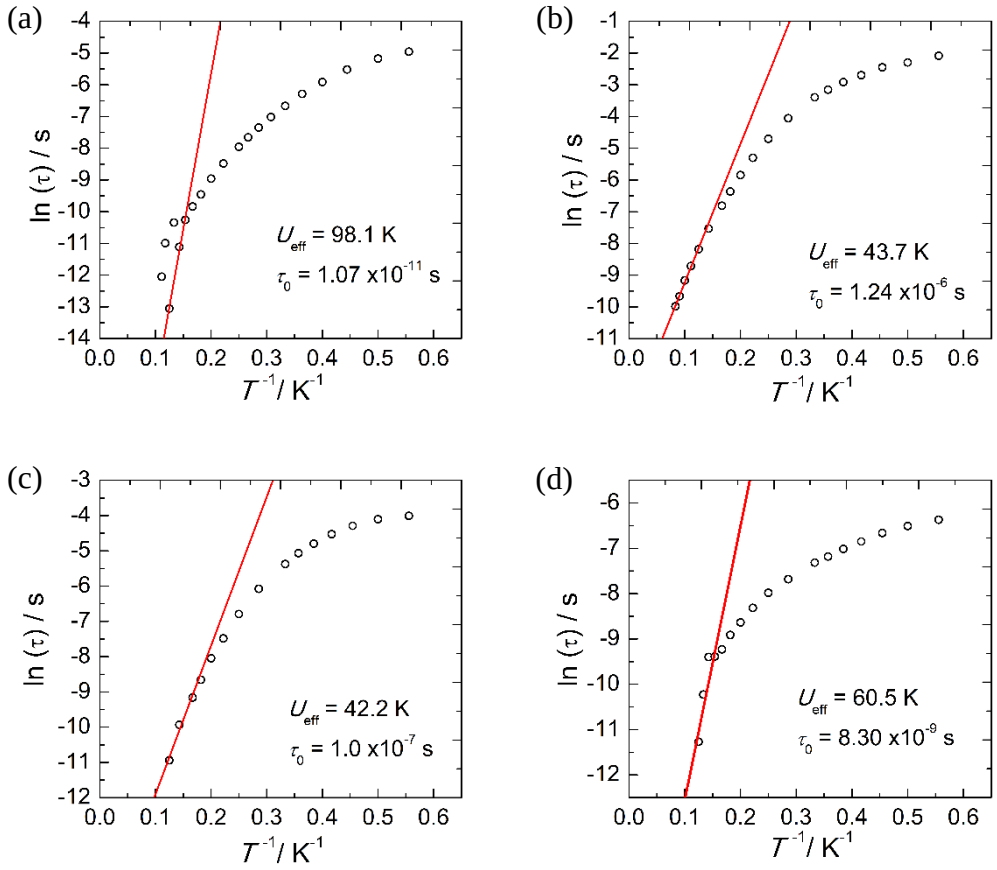

Figure 3.17 Relaxation times of the magnetisation ln(τ) *vs.* T^{-1} (Arrhenius plot using ac data) for (a) **3.1**, (b) **3.2**, (c) **3.3**, and (d) **3.4** under a 600 Oe applied dc field. Solid red lines correspond to linear fits using the parameters stated in the text.

3.8 Summary

A recent review by Power presented just 18 examples of two-coordinate Ni(I) species and work herein this chapter has shown the synthesis and characterisation of three more such species.[24] Synthesis of compounds **3.2** – **3.4** employed reactive three-coordinate Ni(I) precursors presented in Chapter 2, and EPR spectroscopy gave spectra with axial profiles with the $g_{\parallel}$ component signal a low fields (resulting in g values between 5.67 – 5.89) and a very broad $g_{\perp}$ component at high fields (g values between 0.541 – 0.631), and these values represent an unprecedented level of anisotropy for a transition metal system with a spin of S = ½. ^{1}H NMR spectra of the compounds showed paramagnetically shifted signals, and calculations of hyperfine parameters by DFT led to analysis of the contact shift and pseudocontact shift (PCS) contributions to the overall paramagnetic shift, which results in the wide chemical shift range observed for each Ni(I)

compound. Further analysis of the PCS allowed the anisotropy of the magnetic susceptibility to be quantified and used to explain the shielding/deshielding of the different ^{1}H NMR environments and thus the observed peaks.

X-ray crystallography revealed a near-linear geometry of the *bis*-NHC species analogous to that in compound **3.1**. CASSCF calculations on **3.1** – **3.4** performed as an extension on the original DFT work done for **3.1** revealed that all compounds had a low energy first excited state, meaning that the ground state is orbitally degenerate. The lone electron residing in the degenerate set of orbitals that make up the HOMO, in combination with the linear geometries, means that the orbital angular momentum is not fully quenched and causes sizable magnetic anisotropy and slow magnetic relaxation.

Static field magnetisation measurements gave room temperature χT values far higher than the calculated spin-only value for a d^9 ion, confirming the presence of unquenched orbital angular momentum. Introduction of an orbital contribution term to the calculated χT value gave a closer approximation to the experimental data. A comprehensive study of the ac magnetic susceptibilities revealed slow magnetic relaxation in compounds **3.1** – **3.4**. Fitting of the relaxation times derived from frequency dependence data as a function of field and temperature gave rise to reasonable parameters for QTM, direct and Raman processes which are responsible for the fast magnetic relaxation, while the linear Arrhenius plot revealed effective energy barriers in the range 29.3 – 68.5 cm^{-1}. Use of variable-field FTIR on compound **3.1** measured an electronic transition between ground and excited magnetic states at 643 cm^{-1}, suggesting that the Arrhenius derived U_{eff} values should be treated as the lower limit of the barrier.

3.9 References

1. W. A. Herrmann, G. Gerstberger and M. Spiegler, *Organometallics*, 1997, **16**, 2209-2212.
2. K. Matsubara, K. Ueno and Y. Shibata, *Organometallics*, 2006, **25**, 3422-3427.
3. R. C. Poulten, I. Lopez, A. Llobet, M. F. Mahon and M. K. Whittlesey, *Inorg. Chem.*, 2014, **53**, 7160-7169.
4. S. Miyazaki, Y. Koga, T. Matsumoto and K. Matsubara, *Chem. Commun.*, 2010, **46**, 1932-1934.
5. K. Zhang, M. Conda-Sheridan, S. R. Cooke and J. Louie, *Organometallics*, 2011, **30**, 2546-2552.
6. R. C. Poulten, M. J. Page, A. G. Algarra, J. J. Le Roy, I. López, E. Carter, A. Llobet, S. A. Macgregor, M. F. Mahon and D. M. Murphy, *J. Am. Chem. Soc.*, 2013, **135**, 13640-13643.
7. T. Troadec, S. Tan, C. J. Wedge, J. P. Rourke, P. R. Unwin and A. B. Chaplin, *Angew. Chem. Int. Ed.*, 2016, **55**, 3754-3757.
8. M. C. MacInnis, J. C. DeMott, E. M. Zolnhofer, J. Zhou, K. Meyer, R. P. Hughes and O. V. Ozerov, *Chem*, 2016, **1**, 902-920.
9. A. J. Arduengo, III, S. F. Gamper, J. C. Calabrese and F. Davidson, *J. Am. Chem. Soc.*, 1994, **116**, 4391-4394.
10. S. Caddick, F. G. N. Cloke, P. B. Hitchcock and A. K. D. Lewis, *Angew. Chem. Int. Ed.*, 2004, **43**, 5824-5827.
11. A. A. Danopoulos and D. Pugh, *Dalton Trans.*, 2008, 30-31.
12. K. Matsubara, S. Miyazaki, Y. Koga, Y. Nibu, T. Hashimura and T. Matsumoto, *Organometallics*, 2008, **27**, 6020-6024.
13. Y. Hoshimoto, Y. Hayashi, H. Suzuki, M. Ohashi and S. Ogoshi, *Organometallics*, 2014, **33**, 1276-1282.
14. Z. Cao, S. Xie, H. Fang and Z. Shi, *J. Am. Chem. Soc.*, 2018, **140**, 13575-13579.
15. P. P. Power, *Chem. Rev.*, 2012, **112**, 3482-3507.
16. A. L. Companion and M. A. Komarynsky, *J. Chem Educ.*, 1964, **41**, 257.
17. O. Kahn, *Molecular Magnetism*, Wiley, New York, 1993.
18. D. Gatteschi, R. Sessoli and J. Villain, *Molecular Nanomagnets*, Oxford University Press, Oxford, 2006.

19. J. M. Zadrozny, M. Atanasov, A. M. Bryan, C. Lin, B. D. Rekken, P. P. Power, F. Neese and J. R. Long, *Chem. Sci.*, 2013, **4**, 125-138.
20. J. M. Zadrozny, D. J. Xiao, M. Atanasov, G. J. Long, F. Grandjean, F. Neese and J. R. Long, *Nat. Chem.*, 2013, **5**, 577-581.
21. P. H. Rieger, *Electron Paramagnetic Resonance: Analysis and Interpretation*, RSC Publishing, Cambridge, 2007.
22. J. A. Weil, J. R. Bolton and J. E. Wertz, *Electron Paramagnetic Resonance: Elementary Theory and Practical Applications*, Wiley, New York, 1994.
23. S. M. J. Aubin, Z. Sun, L. Pardi, J. Krzystek, K. Folting, L. Brunel, A. L. Rheingold, G. Christou and D. N. Hendrickson, *Inorg. Chem.*, 1999, **38**, 5329-5340.
24. C. Lin and P. P. Power, *Chem. Soc. Rev.*, 2017, **46**, 5347-5399.

CHAPTER 4

4 SYNTHESIS OF TWO-COORDINATE HETEROLEPTIC [Ni(RE-NHC)(L)]X COMPOUNDS (L = NHC', PR_3; X = Br, BAr^F_4)

The reactivity of the three-coordinate Ni(RE-NHC)(PPh_3)Br compounds was not limited to the formation of homoleptic two-coordinate [Ni(RE-NHC)$_2$]Br species wherein the carbene ligands were identical. The next study was to attempt the synthesis and characterisation of a range of two-coordinate heteroleptic [Ni(RE-NHC)(L)]$^+$ compounds whereby L = NHC' or a tertiary phosphine. This would be achieved through:

- Synthesis of [Ni(RE-NHC)(NHC')]Br species in an effort to probe how varying the NHC ring size and N-substituents impacted on structure, spectroscopic properties, and magnetism.
- Following on from the halide abstraction reactions detailed in Chapter 2, studying the reactivity of Ni(RE-NHC)(PCy_3)Br compounds **2.20** – **2.23** with $NaBAr^F_4$ in an attempt to form [Ni(RE-NHC)(PR_3)]$^+$ compounds.
- Investigation of the influence on the geometry and magnetic properties when replacing an NHC ligand with a phosphine, for any successfully synthesised species.
- Ultimately, this work was an effort to access new SIMs and increase the number of reported two-coordinate Ni(I) compounds.

4.1 Synthesis and Characterisation of [Ni(RE-NHC)(NHC')]Br Compounds

4.1.1 Synthesis of [Ni(6Mes)(NHC')]Br Compounds 4.1 – 4.7

Much like the inclusion of other RE-NHCs in the synthesis of two-coordinate compounds in Chapter 2, the same synthetic route was adopted for the synthesis of a series of new heteroleptic [Ni(6Mes)(NHC')]Br species *via* the reaction of compound **2.1** with various free carbenes (Scheme 4.1). 6Xyl, 7Mes and 7Xyl were used as they had already proved to easily form two-coordinate Ni(I) species. 6Xyl-*p*-Br and 7Xyl-*p*-Br had also shown aptitude towards forming the desired linear compounds. Efforts with the five-

membered NHCs IMes and SIMes were also successful in affording new products, with the saturated carbene prepared from *in-situ* deprotonation of [SIMesH]Cl by $KN(SiMe_3)_2$. In all cases, overnight stirring in THF at room temperature formed new compounds **4.1** – **4.7** (Scheme 4.1), which were isolated as pale yellow/beige solids in yields of 40 – 80%.

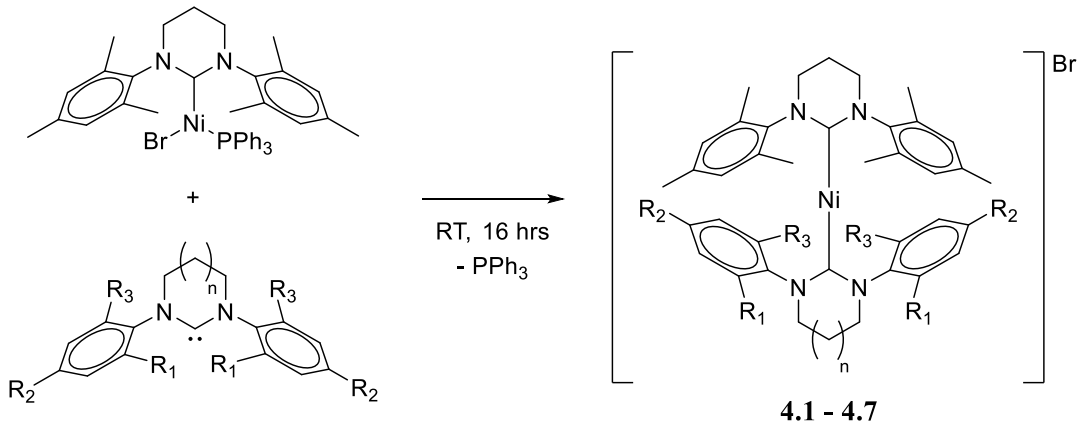

4.1: RE-NHC = 6Xyl, n = 1, R_1/R_3 = Me, R_2 = H
4.2: RE-NHC = 7Mes, n = 2, $R_1/R_2/R_3$ = Me
4.3: RE-NHC = 7Xyl, n = 2, R_1/R_3 = Me, R_2 = H
4.4: RE-NHC = 6Xyl-*p*-Br, n = 1, R_1/R_3 = Me, R_2 = Br
4.5: RE-NHC = 7Xyl-*p*-Br, n = 2, R_1/R_3 = Me, R_2 = Br
4.6: RE-NHC = IMes, n = 0, $R_1/R_2/R_3$ = Me
4.7: RE-NHC = SIMes, n = 0, $R_1/R_2/R_3$ = Me

Scheme 4.1 Synthesis of two-coordinate [Ni(6Mes)(RE-NHC')]Br compounds **4.1** – **4.7**.

Compounds **4.1** – **4.7** displayed paramagnetic ^{1}H NMR spectra, and much like for the homoleptic species, the signals could be integrated and assigned due to the wide spectral dispersion of the resonances. Carbene backbone proton resonances for all compounds were located in the range δ 40 to 57 ppm. **4.1** showed two broad signals at δ 53.4 (4H, NCH_2CH_2) and 51.0 ppm (8H, NCH_2), rather than the expected set of four peaks, due to the resonances for 6Mes and 6Xyl being coincident. Compound **4.2** displayed four signals (two for each RE-NHC) at δ 50.3 (4H, $NCH_2CH_{2(7Mes)}$), 47.9 (2H, $NCH_2CH_{2(6Mes)}$), 46.2 (4H, $NCH_{2(6Mes)}$), and 40.3 ppm (4H, $NCH_{2(7Mes)}$). It was possible to assign signals by comparison to the homoleptic derivatives **3.1** and **3.3**. **4.3** also displayed four signals, at δ 51.7 (4H, $NCH_2CH_{2(7Xyl)}$), 49.0 (2H, $NCH_2CH_{2(6Mes)}$), 47.3 (4H, $NCH_{2(6Mes)}$), and 41.2 ppm (4H, $NCH_{2(7Xyl)}$). One of the two *p*-Br functionalised carbene compounds, **4.4**, gave two pairs of resonances at δ 52.7 (2H, $NCH_2CH_{2(6Xyl\text{-}p\text{-}Br)}$), 52.5 (2H, $NCH_2CH_{2(6Mes)}$), 50.2 (4H, $NCH_{2(6Xyl\text{-}p\text{-}Br)}$), and 50.0 ppm (4H, $NCH_{2(6Mes)}$). The 7Xyl-*p*-Br analogue **4.5** exhibited signals at δ 51.8 (4H, $NCH_2CH_{2(7Xyl\text{-}p\text{-}Br)}$), 49.3 (2H,

NCH$_2$C$H_{2(6Mes)}$), 47.4 (4H, NC$H_{2(6Mes)}$), and 41.2 ppm (4H, NC$H_{2(7Xyl\text{-}p\text{-}Br)}$). Signals at δ 57.4 (2H, NC$H_{(IMes)}$), 49.7 (2H, NCH$_2$C$H_{2(6Mes)}$), and 44.0 ppm (4H, NC$H_{2(6Mes)}$) for **4.6**, and peaks at δ 57.2 (4H, NC$H_{2(SIMes)}$), 51.7 (2H, NCH$_2$C$H_{2(6Mes)}$), and 47.3 ppm (4H, NC$H_{2(6Mes)}$) for **4.7** could be assigned due to the different integrals for the backbone protons of the five-membered NHCs.

The N-aryl substituents were also assigned, with peaks in the range δ -7 to -23 ppm. Compound **4.1** showed a signal at δ -10.8 ppm (6H, *p*-CH_3) and a pair of broad peaks at δ -12.7 and -13.3 ppm (12H each, *o*-CH_3) for the N-aryl methyl protons, while resonances from the protons of the N-aryl rings were located upfield at δ -14.9 (2H, *p*-C$H_{aryl(6Xyl)}$), -20.5 (4H, *m*-C$H_{aryl(6Xyl)}$), and -21.3 ppm (4H, *m*-C$H_{aryl(6Mes)}$). The upfield region of the ^{1}H NMR spectrum of **4.2** contained three sets of two signals at δ -8.6 (6H, *p*-C$H_{3(7Mes)}$) and -9.0 ppm (6H, *p*-C$H_{3(6Mes)}$), δ -11.0 (12H, *o*-C$H_{3(7Mes)}$) and -11.8 ppm (12H, *o*-C$H_{3(6Mes)}$), and δ -16.9 (4H, *m*-C$H_{aryl(7Mes)}$) and -19.9 ppm (4H, *m*-C$H_{aryl(6Mes)}$). Compound **4.3** showed the same set of peaks for the N-aryl methyl protons with a peak at δ -9.4 ppm (6H, *p*-C$H_{3(6Mes)}$) and a broad peak due to overlapping of 6Mes and 6Xyl signals at δ -11.8 ppm (12H, *o*-C$H_{3(6Mes)}$, and 12H, *o*-C$H_{3(6Xyl)}$), while the resonances of the N-aryl ring protons were at δ -16.5 (2H, *p*-C$H_{aryl(7Xyl)}$), -17.7 (4H, *m*-C$H_{aryl(7Xyl)}$), and -20.0 ppm (4H, *m*-C$H_{aryl(6Mes)}$). Peaks at δ -10.4 (6H, *p*-C$H_{3(6Mes)}$), -11.4 (12H, *o*-C$H_{3(6Mes)}$), -13.2 (12H, *o*-C$H_{3(6Xyl\text{-}p\text{-}Br)}$), -19.8 (4H, *m*-C$H_{aryl(6Mes)}$), -21.1 ppm (4H, *m*-C$H_{aryl(6Xyl\text{-}p\text{-}Br)}$) for **4.4**, and signals at δ -9.3 (6H, *p*-C$H_{3(6Mes)}$), -10.7 (12H, *o*-C$H_{3(6Mes)}$), -12.2 (12H, *o*-C$H_{3(7Xyl\text{-}p\text{-}Br)}$), -18.1 (4H, *m*-C$H_{aryl(7Xyl\text{-}p\text{-}Br)}$), -19.6 ppm (4H, *m*-C$H_{aryl(6Mes)}$) for compound **4.5** completed the assignment of the *p*-Br species. The upfield regions of **4.6** and **4.7** were more tentatively assigned, due to both compounds having only mesityl N-substituents, and no homoleptic IMes or SIMes derivatives to compare ^{1}H NMR shifts with. Peaks were recorded at δ -6.9 (12H, *o*-C$H_{3(IMes)}$), -7.5 (6H, *p*-C$H_{3(6Mes)}$), -9.2 (6H, *p*-C$H_{3(IMes)}$), -10.1 (coincident of two peaks, 12H, *o*-C$H_{3(6Mes)}$, and 4H, *m*-C$H_{aryl(6Mes)}$), -22.8 ppm (4H, *m*-C$H_{aryl(IMes)}$) for compound **4.6**, while **4.7** displayed signals at δ -8.6 (12H, *o*-C$H_{3(SIMes)}$), -8.8 (6H, *p*-C$H_{3(SIMes)}$), -9.7 (6H, *p*-C$H_{3(6Mes)}$), -12.4 (12H, *o*-C$H_{3(6Mes)}$), -12.9 (4H, *m*-C$H_{aryl(6Mes)}$), -23.0 ppm (4H, *m*-C$H_{aryl(SIMes)}$).

The magnetic moments of **4.1** – **4.3** were recorded in CH_2Cl_2 at room temperature, resulting in values of 2.9 – 3.1 μ_B, representative of two unpaired electrons and thus comparable to the values for the homoleptic species in Chapter 3.

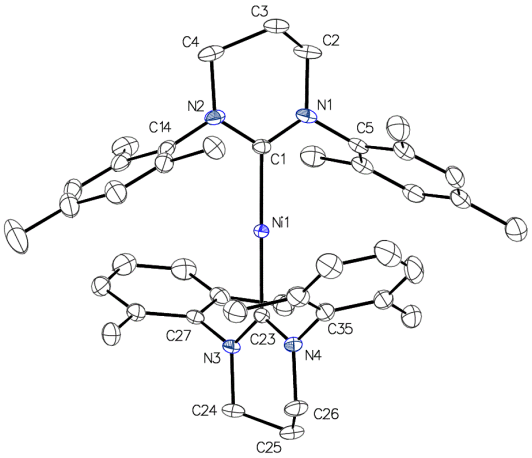

4.1

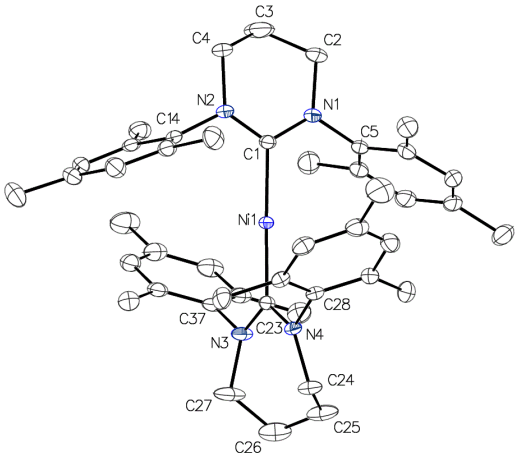

4.2

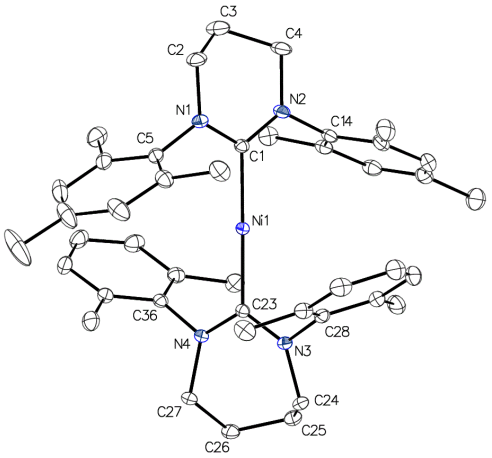

4.3

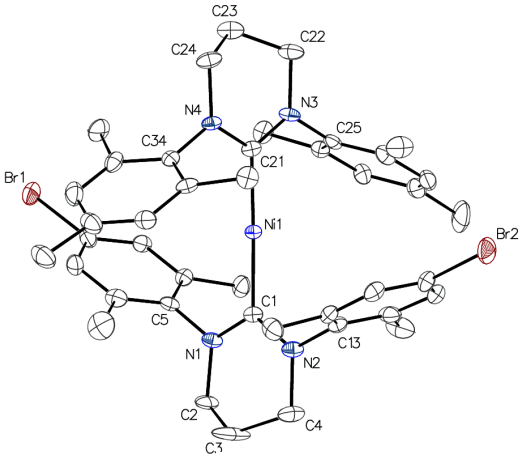

4.4

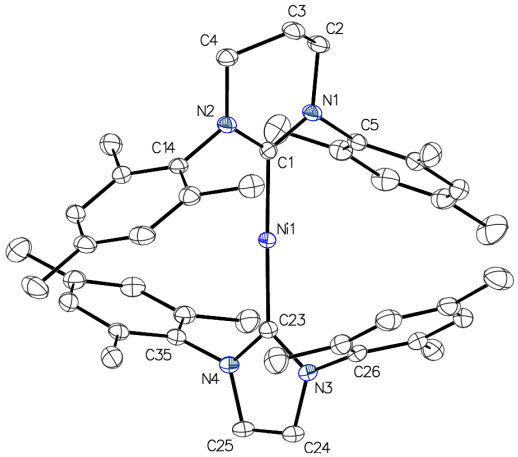

4.6

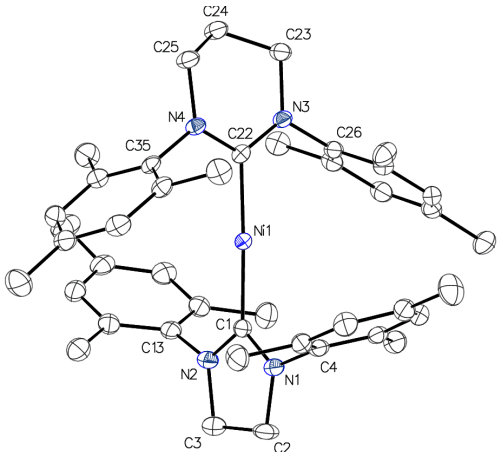

4.7

Figure 4.1 Molecular structures of the cations in **4.1** – **4.4** and **4.6** – **4.7**. Thermal ellipsoids are set at 30% probability. All hydrogen atoms have been omitted for clarity.

Recrystallisation of compounds **4.1** – **4.7** from CH_2Cl_2/hexane yielded, in all cases, crystals suitable for X-ray crystallography. The molecular structures of the cations in compounds **4.1** – **4.4** and **4.6** – **4.7** are shown in Figure 4.1,[i] with selected bond lengths and angles given in Table 4.1. All of the two-coordinate species showed C_{NHC}-Ni-C_{NHC} bond angles in the range 177.51(10) – 179.57(14)° (*cf.* 179.27(13)° for **3.1**). The Ni-C_{NHC} bond lengths in **4.1** – **4.4** were very similar across the quartet of compounds (1.941(4)/1.944(4), 1.952(4)/1.939(4), 1.951(2)/1.949(2), and 1.939(6)/1.925(6) Å respectively; note that values are given as Ni-C_{6Mes}/Ni-C_{NHC}'), showing that there are no significant changes upon replacing one 6Mes in **3.1** for another RE-NHC. Compound **4.5** displayed a significant difference between the two bond distances (1.961(4)/1.927(4) Å), potentially due to the electronics (better π-acceptor) and sterics (large bromide substituent) of the 7Xyl-*p*-Br carbene. The Ni-C_{NHC} distances in **4.6** and **4.7** (1.922(2)/1.911(2) and 1.926(3)/1.918(3) Å) reflect the presence of the 5-membered NHC, which are poorer π-acceptors than RE-NHCs. The internal N-C_{NHC}-N bond angles were in the expected ranges, where the seven-membered RE-NHCs had a slightly wider angle than their six-membered counterparts, while IMes and SIMes showed a significantly less obtuse bond angle. Torsion angles between the two planes of the NHCs were similar to those in the homoleptic Ni(I) series, with angles ranging from 66.4 – 80.9°.

Efforts to incorporate other RE-NHCs were unsuccessful for the N-aryl carbenes 6^{o}Tol, 7^{o}Tol and 6MesDAC, and N-alkyl carbenes 6^{i}Bu, 7^{i}Bu, 6^{n}Pent, and 7^{n}Pent. Just as for the attempts at making the homoleptic analogues with these carbenes, it seems that they do not feature the necessary steric and electronic properties to form the desired two-coordinate species. ^{1}H NMR spectra of reaction mixtures showed the unexpected appearance of signals for the two-coordinate homoleptic compound **3.1**. Upon either increasing the number of equiv. of free RE-NHCs or reacting the three-coordinate Ni(RE-NHC)(PPh_3)Br species (**2.3**, **2.6**, **2.9** – **2.13**) with free 6Mes, this still resulted in the formation of **3.1**. Hence, the RE-NHCs must have some labile character. As mentioned in Chapter 2, this species appears to readily form when the PPh_3 and Br groups of **2.1** are removed but not replaced by a suitably bulky ligand.

[i] The X-ray data set for compound **4.5** was of only poor quality. Although it was clear that the product formed was the desired heteroleptic species, structure parameters should be treated with caution.

Table 4.1 Selected bond lengths and angle for compounds **4.1** – **4.11**.

Compound	**Ni-C_{NHC} (Å)**	**N-C_{NHC}-N (°)**	**C-Ni-C (°)**	**Torsion angle (°)**
4.1	1.941(4)/1/944(4)	117.8(4)/117.9(4)	178.9(2)	75.4
4.2	1.952(4)/1.939(4)	117.5(4)/118.8(4)	178.56(19)	79.4
4.3	1.951(2)/1.949(2)	117.3(2)/119.2(2)	179.13(11)	66.4
4.4	1.939(6)/1.925(6)	117.0(6)/116.8(6)	178.6(2)	73.2
4.5	1.961(4)/1.927(4)	116.9(13)/118.0(13)	179.57(14)	75.6
4.6	1.922(2)/1.911(2)	118.4(2)/104.4(2)	177.53(10)	77.4
4.7	1.926(3)/1.918(3)	118.4(3)/108.5(3)	177.61(13)	80.9
4.8	1.949(5)/1.948(5)	116.3(4)/119.2(4)	179.6(2)	70.2
4.9[a]	1.950(2)	117.6(2)	179.34(13)	80.0
4.10	1.947(4)/1.952(4)	118.8(3)/117.6(3)	179.07(16)	73.8
4.11	1.916(3)/1.916(3)	119.7(3)/104.2(3)	179.39(15)	79.1

[a] Single values of Ni-C_{NHC} bond length and N-C_{NHC}-N bond angle given as the nickel metal centre was located on a symmetry site.

4.1.2 Synthesis of [Ni(RE-NHC)(NHC')]Br Compounds

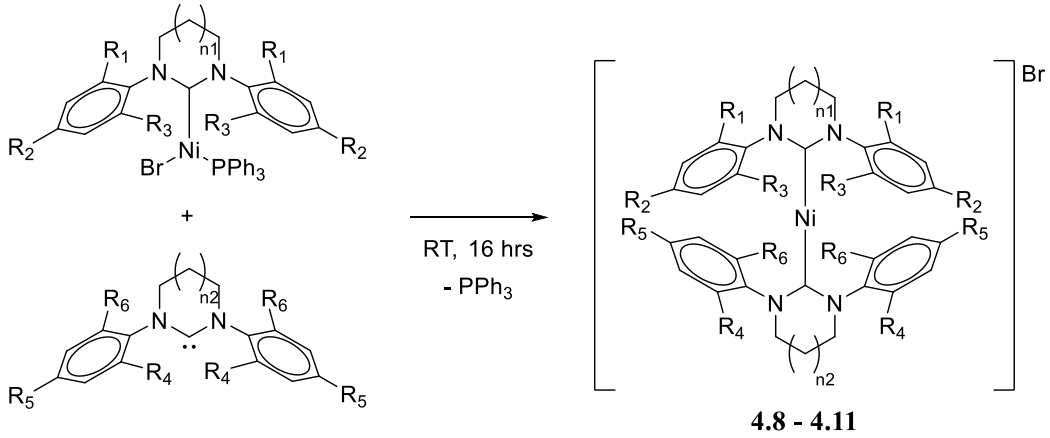

4.8: n_1 = 1, R_1/R_3 = Me, R_2 = H; n_2 = 2, $R_4/R_5/R_6$ = Me
4.9: n_1 = 1, R_1/R_3 = Me, R_2 = H; n_2 = 2, R_4/R_6 = Me, R_5 = H
4.10: n_1 = 2, $R_1/R_2/R_3$ = Me; n_2 = 2, R_4/R_6 = Me, R_5 = H
4.11: n_1 = 2, $R_1/R_2/R_3$ = Me; n_2 = 0, $R_4/R_5/R_6$ = Me

Scheme 4.2 Synthesis of two-coordinate [Ni(RE-NHC)(NHC')]Br compounds **4.8** – **4.11**.

To further increase the number of two-coordinate Ni(I) species, three-coordinate precursors other than **2.1** were used in conjunction with a range of NHCs. Thus, Ni(6Xyl)(PPh_3)Br and Ni(7Mes)(PPh_3)Br were reacted with free 7Mes, 7Xyl, and IMes to give compounds **4.8** – **4.11** (Scheme 4.2).

^{1}H NMR spectroscopy of **4.8** – **4.11** displayed the expected wide range of broad resonances. Assignment of the peaks was based on those for the homoleptic and heteroleptic species. Compound **4.8** displayed peaks for the backbone protons at δ 50.6 (4H, $NCH_2CH_{2(7Mes)}$), 48.2 (2H, $NCH_2CH_{2(6Xyl)}$), 47.0 (4H, $NCH_{2(6Xyl)}$), and 40.6 ppm (4H, $NCH_{2(7Mes)}$). The spectrum also featured upfield signals at δ -8.6 (6H, *p*-$CH_{3(7Mes)}$), -10.8 (12H, *o*-$CH_{3(6Xyl)}$), -11.0 (2H, *p*-$CH_{aryl(6Xyl)}$), -12.2 (12H, *o*-$CH_{3(7Mes)}$), -16.4 (4H, *m*-$CH_{aryl(7Mes)}$), and -20.2 ppm (4H, *m*-$CH_{aryl(6Xyl)}$) to complete the assignment. **4.9** displayed peaks at δ 52.3 (4H, $NCH_2CH_{2(7Xyl)}$), 49.5 (2H, $NCH_2CH_{2(6Xyl)}$), 48.1 (4H, $NCH_{2(7Xyl)}$), and 41.6 ppm (4H, $NCH_{2(7Xyl)}$), along with resonances at δ -11.7 (12H, *o*-$CH_{3(6Xyl)}$), -11.9 (2H, *p*-$CH_{aryl(6Xyl)}$), -12.2 (12H, *o*-$CH_{3(7Xyl)}$), -17.1 (2H, *p*-$CH_{aryl(7Xyl)}$), -17.4 (4H, *m*-$CH_{aryl(6Xyl)}$), and -20.4 ppm (4H, *m*-$CH_{aryl(7Xyl)}$) for the Xyl N-substituents. The *bis*-seven-membered RE-NHC compound **4.10** showed peaks for the backbone at δ 50.1 (4H, $NCH_2CH_{2(7Xyl)}$), 49.9 (4H, $NCH_2CH_{2(7Mes)}$), 39.3 (4H, $NCH_{2(7Xyl)}$), and 39.2 ppm (4H, $NCH_{2(7Mes)}$), with N-aryl substituent peaks at δ -8.4 (6H, *p*-$CH_{3(7Mes)}$), -10.9 (12H, *o*-$CH_{3(7Xyl)}$), -11.9 (12H, *o*-$CH_{3(7Mes)}$), -13.2 (2H, *p*-$CH_{aryl(7Xyl)}$), -17.5 (4H, *m*-

C$H_{aryl(7Xyl)}$), and -18.3 ppm (4H, *m*-C$H_{aryl(7Mes)}$). Finally, **4.11**, featuring the biggest difference in NHC ring size, showed the narrowest spectral width of all the heteroleptic compounds, with signals ranging from those for the backbones at δ 43.4 (2H, NC$H_{(IMes)}$), 35.2 (4H, $NCH_2CH_{2(7Mes)}$) and 31.1 ppm (4H, $NCH_{2(7Mes)}$), to the mesityl N-substituents at δ -3.0 (6H, *p*-C$H_{3(7Mes)}$), -3.6 (coincident of two peaks, 12H, *o*-C$H_{3(7Mes)}$, and 4H, *m*-C$H_{aryl(7Mes)}$), -3.7 ((6H, *p*-C$H_{3(IMes)}$), -4.6 (12H, *o*-C$H_{3(IMes)}$), -16.3 ppm (4H, *m*-C$H_{aryl(IMes)}$).

Eight further examples of [Ni(RE-NHC)(NHC')]Br compounds were prepared and characterised by ^{1}H NMR spectroscopy (Table 4.2), but no X-ray data was collected to definitively prove the two-coordinate nature of these species. The ^{1}H NMR data are given in Chapter 7 (section 7.9).

Table 4.2 Permutations of [Ni(RE-NHC)(NHC')]Br compounds formed. Compound numbers quoted are for examples characterised by X-ray diffraction, while tick marks denote examples characterised by ^{1}H NMR spectroscopy only.

NHC' / RE-NHC	6Xyl	7Mes	7Xyl	6Xyl-*p*-Br
7Mes	**4.8**	-	-	-
7Xyl	**4.9**	**4.10**	-	-
6Xyl-*p*-Br	✓	✓	✓	-
7Xyl-*p*-Br	✓	✓	-	-
IMes	✓	**4.11**	✓	✓

X-ray diffraction of crystals of compounds **4.8** – **4.11** afforded the molecular structures of the cationic components displayed in Figure 4.2. C_{NHC}-Ni-C_{NHC} bond angles varied between 179.07(16) – 179.6(2)°, Ni-C_{NHC} distances were very similar to those found for the previous heteroleptic species (range of 1.916(3) – 1.952(4) Å), and the torsion angles between the carbene planes were between 70.2 – 80.0° (Table 4.1). The difference in the N-C_{NHC}-N angles for **4.8** (116.3(4)/119.2(4)°) reflected the different ring sizes of the ligands, while **4.9** only displayed one N-C_{NHC}-N bond angle (117.6(2)°) due to the unit cell only containing half of the cation species as the nickel centre was located on a symmetry site, causing the carbenes to be disordered with each other in a 50:50 ratio.

4.10 gave similar bond angles to those found in compounds with two seven-membered RE-NHCs (*cf*. **3.4**: 118.28(15)°). The values for **4.11** were consistent with the significant difference in ring sizes (119.7(3) and 104.2(3)°).

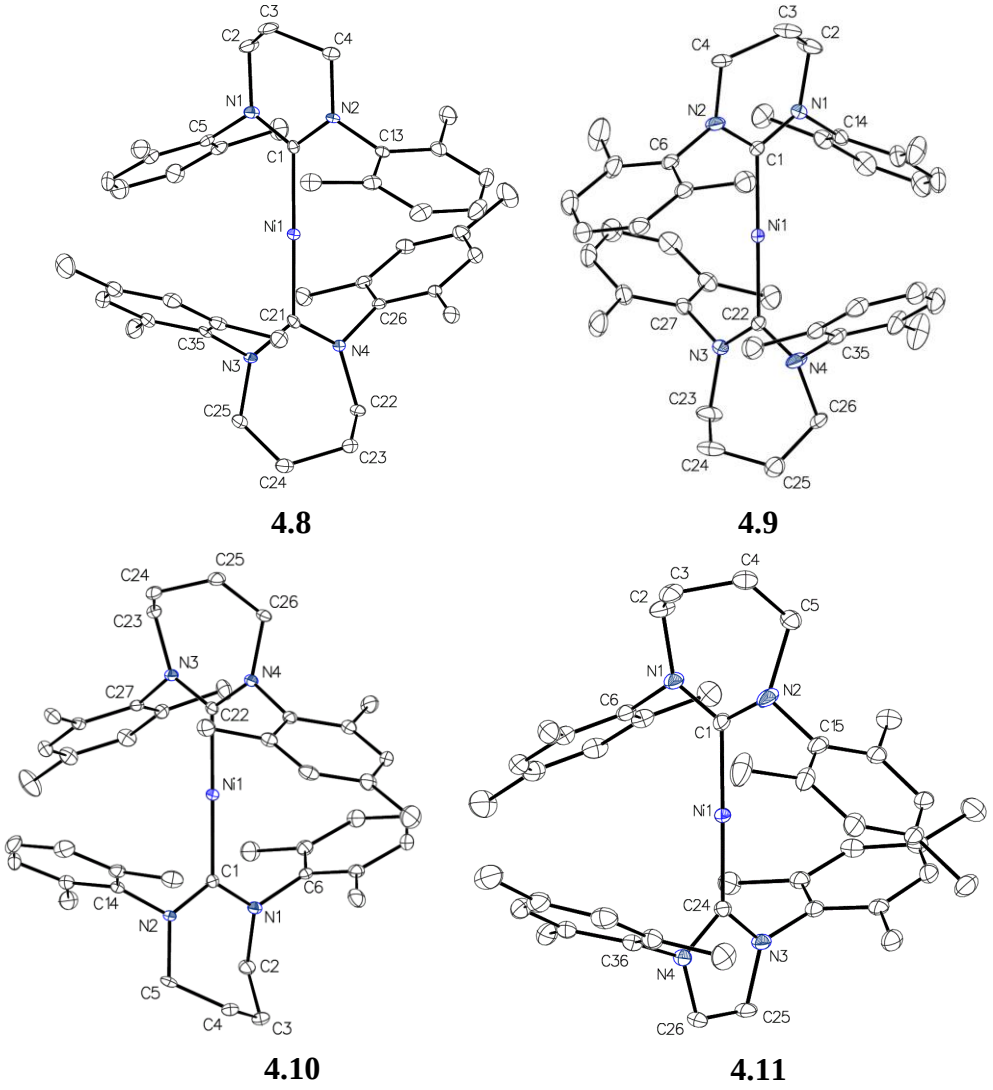

Figure 4.2 Molecular structures of the cations in **4.8** – **4.11**. Thermal ellipsoids are set at 30% probability. All hydrogen atoms have been omitted for clarity.

4.1.3 Magnetism of [Ni(RE-NHC)(NHC')]Br Compounds

SQUID measurements were carried out on [Ni(6Mes)(7Mes)]Br (**4.2**) and [Ni(6Mes)(IMes)]Br (**4.6**) to investigate how varying the NHC ring size and having two differing carbenes impacted on magnetic properties.

The dc magnetic susceptibility properties were measured on polycrystalline samples of **4.2** and **4.6** under a 1000 Oe static dc field in the temperature range 1.8 to

300 K (Figure 4.3), however, the measurements gave χT curves with an upturn at very low temperatures, suggestive of antiferromagnetic coupling between nickel centres. Repeating the measurements at 500 Oe, 5000 Oe, and 10000 Oe gave no such upturn and proved the 1000 Oe data to be anomalous. Room temperature molar magnetic susceptibility (χT) values of 1.04 and 1.45 cm^3 K mol^{-1} for compounds **4.2** and **4.6** respectively were taken from the 10000 Oe curves (Figure 4.3). While the room temperature values were larger than what was expected for an S = ½ system (0.375 cm^3 K mol^{-1}, assuming spin-only), it was consistent with the previously reported Ni(I) species **3.1** (1.11 cm^3 K mol^{-1}),[1] as well as the new two-coordinate compounds reported in Chapter 3. It can be reasoned that the room temperature χT values more closely resemble the expected value of a d^9 Ni(I) ion with unquenched orbital angular momentum (1.575 cm^3 K mol^{-1}). The temperature dependence of χT for each compound was measured, with values remaining fairly linear as the temperature decreased from 300 and 5 K, and a rapid drop below 5 K to minimum values of 0.93 and 1.24 cm^3 K mol^{-1} for **4.2** and **4.6**. This pattern is consistent with non-interaction between neighbouring Ni(I) ions. Indeed, the crystal structures of **4.2** and **4.6** revealed large Ni···Ni distances of 10.41 – 10.58 Å.

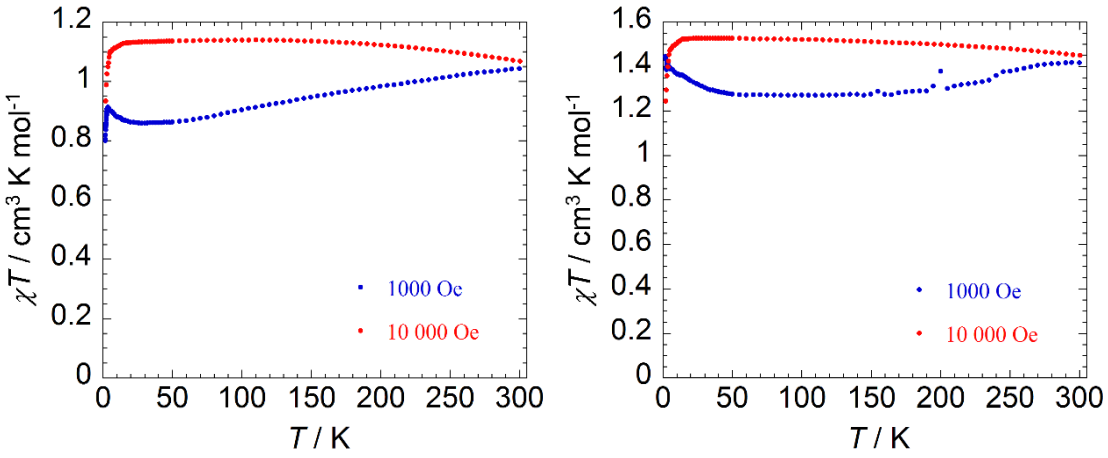

Figure 4.3 Temperature dependence of the χT product of compounds **4.2** (left) and **4.6** (right) under 1000 and 10000 Oe applied dc field (with χ being the molar magnetic susceptibility per molecule as defined by M/H).

The field dependence of magnetisation (M) in applied dc fields between 0 to 7 T at temperature increments of 1.8, 3, 5, and 7 K was probed for compounds **4.2** and **4.6** (Figure 4.4). Both compounds experienced rapid magnetisation at low field strengths

(< 2 T) before a more gradual increase in M as the applied field reached 7 T. The magnetisation did not reach complete saturation under the 7 T field at 1.8 K (only reaching values of 1.39 and 1.95 μ_B) and there was some separation between the reduced magnetisation curves (Figure 4.4). The static field magnetic properties of compounds **4.2** and **4.6** appear very similar to those of homoleptic two-coordinate species reported in Chapter 3 and showed the presence of magnetic anisotropy, a prerequisite for the Ni(I) ions having SIM behaviour.

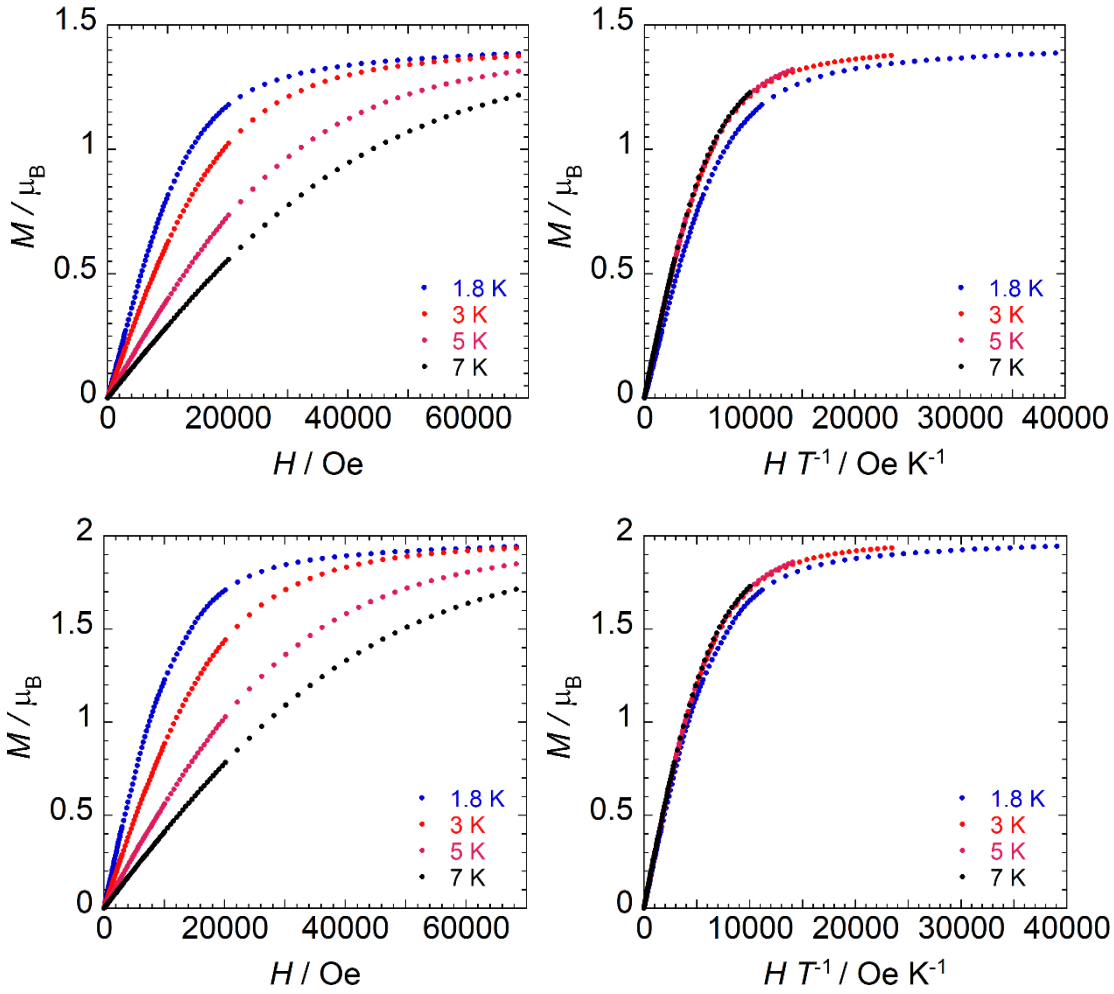

Figure 4.4 Field dependence of the magnetisation (*M vs. H*) and reduced magnetisation (*M vs. H* T^{-1}) for compounds **4.2** (top) and **4.6** (bottom).

Alternating current susceptibility measurements were performed to check for the presence of SIM behaviour. No out-of-phase (χ'') signal for either compound was observed with a zero applied dc field, but a frequency dependent signal appeared when under an applied dc field at 2 K (χ'' in Figure 4.5, χ' in Appendix 7, Figure A7.2). Just as

in Chapter 3, the appearance of signals under an external applied field implied that the QTM process was causing rapid relaxation of signals when under a zero applied field. Interestingly, the χ'' data of compound **4.2** revealed two peaks at fields of 600 Oe and above. The portion of the χ'' signal at higher frequencies (~ 10 Hz) appeared to remain at a constant frequency as the field strength increased, whereas the χ'' signal at lower frequencies (0.1 – 1 Hz) showed a shift of the peak maximum towards increasing frequencies as the field strength increased. This pattern has previously been shown to be a consequence of the direct process dominating the relaxation pathway at higher fields, and this was reflected in attempts to fit the τ^{-1} *vs.* H data with field dependent relaxation processes (QTM and direct) and only being able to determine reasonable parameters for the direct component (*vide infra*).[2] As the low frequency component maximum moves to increasing frequencies (or shorter relaxation times, as $\tau = \frac{1}{2\pi\nu}$) with increasing field strength, the magnitude of the high frequency signal only diminishes marginally. Conversely, recent work by Murugesu *et al*. featuring dinuclear Dy(III) species also displayed two frequency dependent peaks in the ac susceptibility data which, upon increasing dc field strength, showed complete suppression of the higher frequency signal.[3]

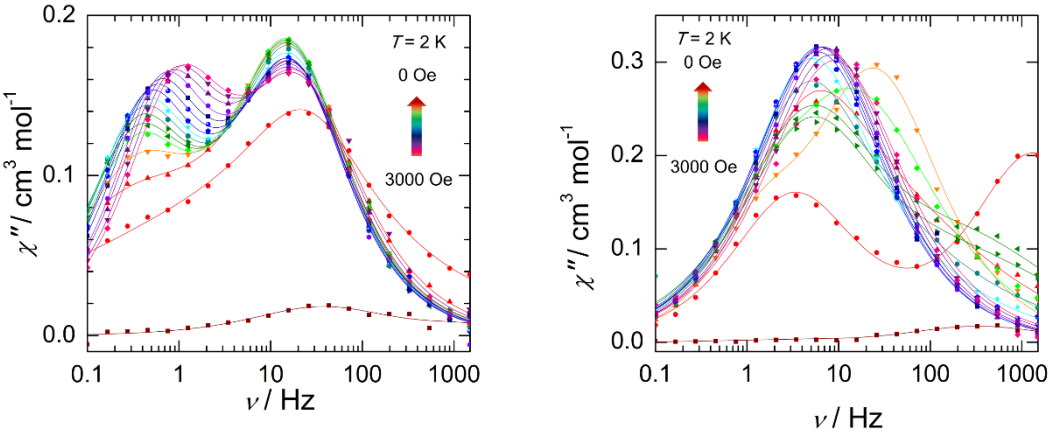

Figure 4.5 Frequency dependence of the out-of-phase (χ'') magnetic susceptibility of compounds **4.2** (left) and **4.6** (right) as a function of applied dc field at 2 K. Solid lines represent generalised double Debye fits at each field strength.

The χ'' data for compound **4.6** also showed some unusual behaviour, whereby the χ'' curve collected at 200 Oe showed two frequency dependent peaks, while the data collected at all other field strengths displayed no clear sign of the second peak. The

200 Oe measurement did not appear anomalous, as the χ'' signal showed two frequency dependent peaks across the temperature range of 1.8 to *ca*. 4 K (Appendix 7, Figure A7.4), and not just at 2 K (the temperature at which Figure 4.5 was collected).

The χ' and χ'' curves of both compounds were fitted to the generalised Debye model (as previously described in Chapter 3), and in the case of the χ'' signals, use of a double-set Debye fit was used to extract τ, α, χ_S, and χ_T parameters from both peaks. The Debye fits can be seen in Figure 4.5 as solid lines.

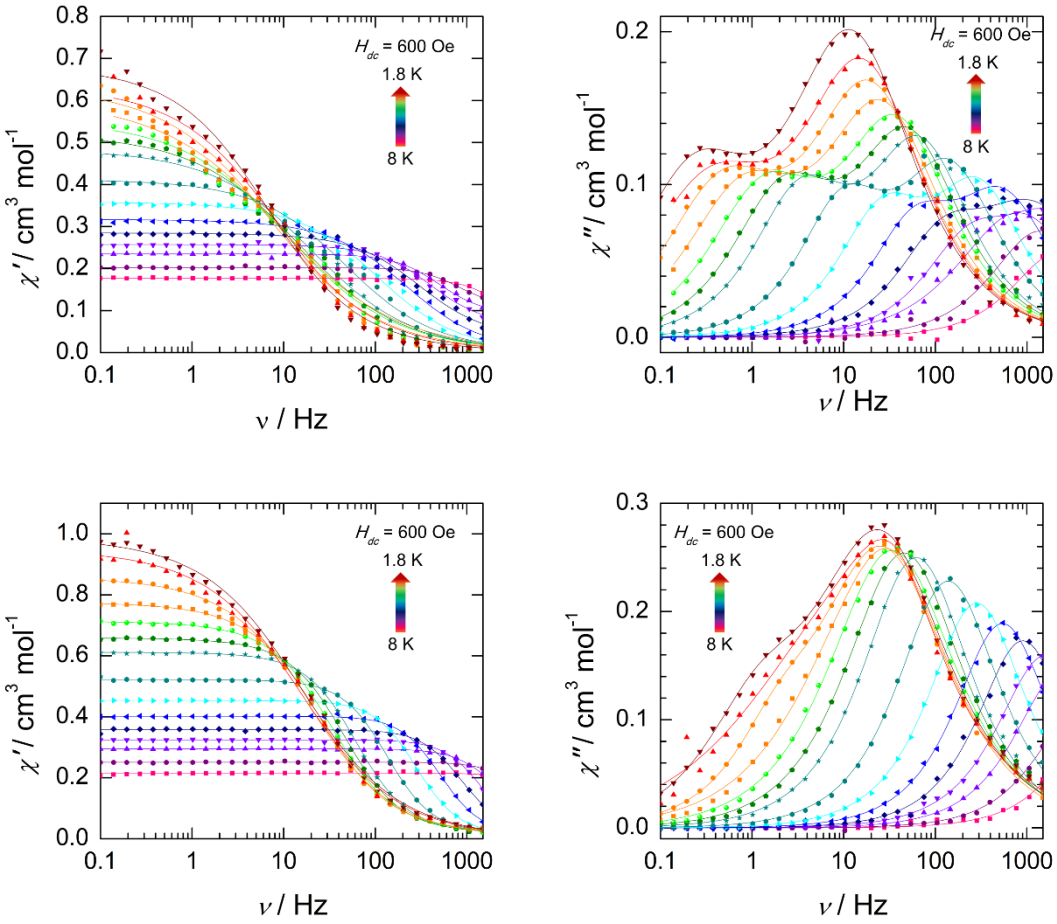

Figure 4.6 Frequency dependence of the in-phase (χ') and out-of-phase (χ'') magnetic susceptibility of compounds **4.2** (top) and **4.6** (bottom) as a function of temperature under a 600 Oe applied dc fields. Solid lines represent generalised double Debye fits at each temperature.

To elucidate the presence of any temperature dependent relaxation pathways, ac susceptibility measurements were performed on compounds **4.2** and **4.6** as a function of temperature (Figure 4.6). A dc field of 600 Oe was chosen for both compounds, as to

minimise the presence of the second frequency dependent peak and provide data sets that can be readily compared to the homoleptic species from Chapter 3. Additional ac susceptibility measurements were recorded at different field strengths (1200 and 3000 Oe for **4.2**, 200 Oe for **4.6**, all shown in Appendix 7, Figure A7.3). Measurements taken between 1.8 to 8 K showed increasing χ'' signals with decreasing temperature and frequency, diagnostic of field-induced SIM behaviour. As with the varied field data in Figure 4.5, use of single-set and double-set (where appropriate) Debye models were used to fit the χ' and χ'' curves respectively.

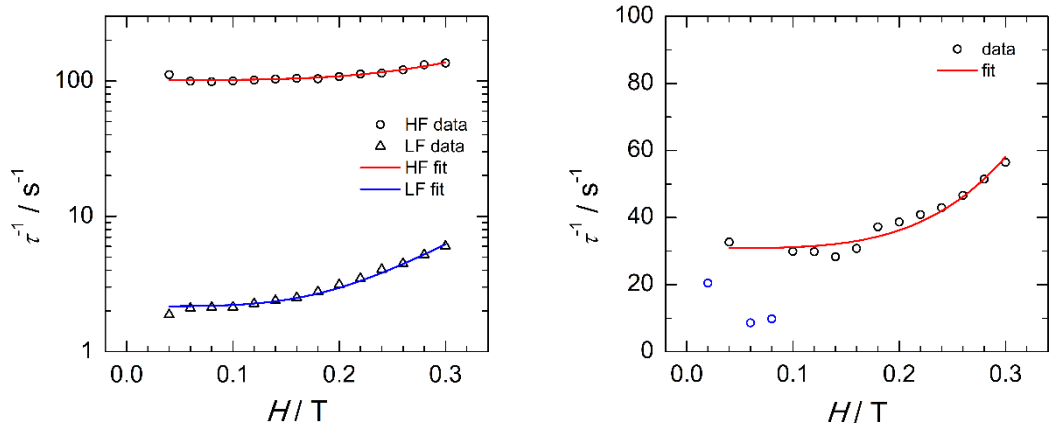

Figure 4.7 Field dependence of the magnetisation relaxation times (τ) of compounds **4.2** (left) and **4.6** (right) at 2 K. Solid red/blue lines correspond to the best fits using direct and QTM relaxation mechanisms according to Equation 3.3 (Chapter 3). Blue data points were ignored during the fit.

The relaxation times (τ) produced from the Debye model were subsequently used to determine parameters for both field and temperature dependent relaxation processes. For both compounds **4.2** and **4.6**, the plot of τ^{-1} *vs.* H was fitted with just the direct relaxation process (Equation 3.3), as the QTM did not produce any reasonable parameters (Figure 4.7). Direct process parameters for both the low and high frequency components of compound **4.2**, as well as **4.6**, can be found in Table 4.3. Notably, the low frequency component of compound **4.2** has a very slow relaxation time of 0.53 s under a small dc field of 400 Oe (0.04 T), and only reducing to 0.17 s as the field increased to 3000 Oe. The relaxation time is significantly longer than the values seen for compounds **3.1** – **3.4** (*cf.* **3.1**: 0.005 s at 1.8 K under 600 Oe). While there are no other Ni(I) examples in the

literature to compare to, a recent hexacoordinate Ni(II) species was recorded to have a slow relaxation of 1.3 s under a 8000 Oe field at 1.9 K.[4]

Table 4.3 Parameters used for best fit of Equation 3.3 and Equation **3.4** for **4.2** and **4.6**. Values in italics were obtained from fitting the low frequency (LF) data.

Compound	**A (s^{-1} T^{-4} K^{-1})**	**C (s^{-1})**	**n**
4.2	2.18×10^3	1.19	5.38
	2.50×10^2	*0.01*	(*7.19*)
4.6	1.68×10^3	0.62	5.62

The plots of τ^{-1} *vs.* *T* for compounds **4.2** and **4.6** were fitted with the temperature dependent relaxation pathways (Equations 4.1), incorporating the parameters obtained from the field dependent fits (Figure 4.8). The components for the Raman process were successfully fitted, giving parameters with a similar magnitude to those found for homoleptic compounds in Chapter 3. Once again, the Orbach mechanism could not be factored into the fits, indicating that the magnetic relaxation pathway occurring for compounds **4.2** and **4.6** was dominated by the direct and Raman processes.

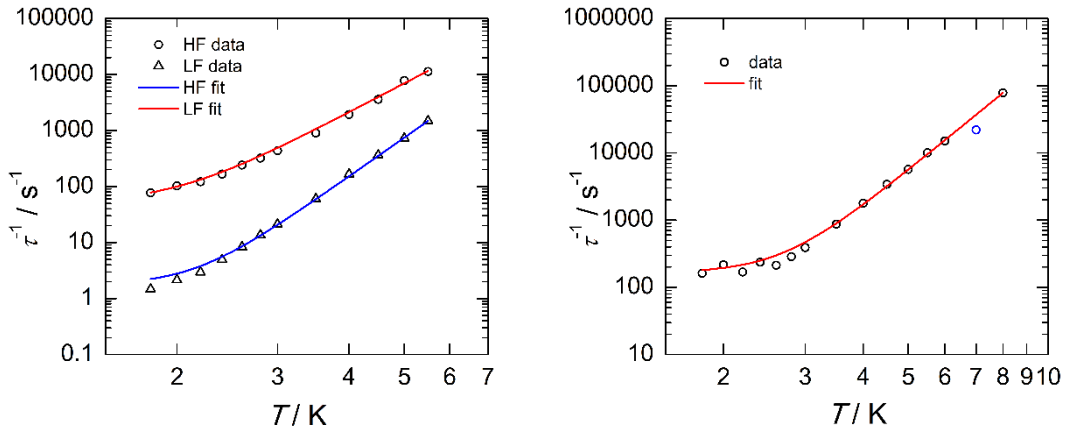

Figure 4.8 Temperature dependence of the magnetisation relaxation times (τ) of compounds **4.2** (left) and **4.6** (right) under a 600 Oe applied dc field. Solid red lines correspond to the best fits using direct, QTM, and Raman relaxation mechanisms according to Equation 3.4 (Chapter 3). Blue data points were ignored during the fit.

By rearranging the data to form a plot of ln(τ) *vs.* T^{-1}, the effective energy barrier to spin reversal could be estimated. Fitting of Arrhenius' law gave barrier and pre-exponential factor values of U_{eff} = 22.2 cm^{-1} (τ_0 = 2.19 × 10^{-6} s) for the low frequency component of **4.2**, U_{eff} = 17.2 cm^{-1} (τ_0 = 9.82 × 10^{-7} s) for the high frequency component, and U_{eff} = 24.4 cm^{-1} (τ_0 = 1.67 × 10^{-7} s) for **4.6**. The relaxation times deviate from the linear Arrhenius regime as the temperature decreases, showing that the direct and Raman processes dominate the relaxation pathways. Despite compound **4.2** showing significant slow relaxation at low temperature, this did not translate to the heteroleptic species having a remarkable spin reversal barrier. Additionally, having two different RE-NHCs appeared to cause the ac susceptibility data to produce two peaks, resulting in the relaxation process to be split into a low and a high frequency component.

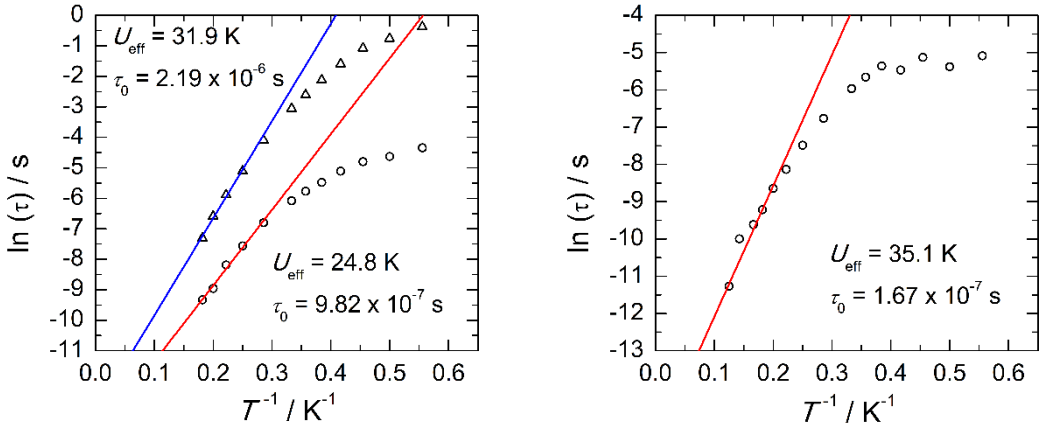

Figure 4.9 Relaxation time of the magnetisation ln(τ) *vs.* T^{-1} (Arrhenius plot using ac data) for compounds **4.2** (left) and **4.6** (right) under a 600 Oe applied dc field. Solid red lines correspond to linear fits.

4.2 Synthesis and Characterisation of [Ni(RE-NHC)(PCy$_3$)]BAr$^F{}_4$ Compounds

A recent publication featuring the species [Ni(P^{t}Bu$_3$)$_2$][Al(OC(CF$_3$)$_3$)$_4$] by Krossing *et al*. was the first example of a monomeric two-coordinate *bis*-phosphine Ni(I) compound.[5] Along with our *bis*-NHC species **3.1**, this further emphasises the paucity of two-coordinate nickel compounds featuring carbene and phosphine ligands. Reviewing the reactivity of three-coordinate species with halide abstracting agents in Chapter 2, but using the PCy$_3$ derivatives **2.20** – **2.23** also introduced in Chapter 2 as an entry point,

efforts to prepare mixed NHC-phosphine Ni(I) $[Ni(RE\text{-}NHC)(PR_3)]^+$ complexes as species that are intermediate between $[Ni(RE\text{-}NHC)_2]^+$ and $[Ni(PR_3)_2]^+$ were pursued.

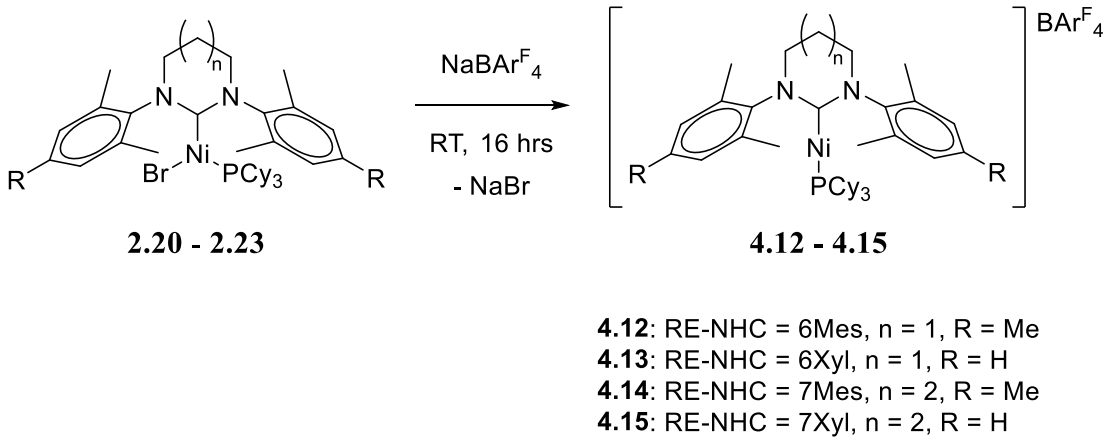

Scheme 4.3 Synthesis of two-coordinate $[Ni(RE\text{-}NHC)(PCy_3)]BAr^F_4$ compounds **4.12** – **4.15**.

As depicted in Scheme 4.3, the three-coordinate $Ni(RE\text{-}NHC)(PCy_3)Br$ compounds **2.20** – **2.23** were reacted $NaBAr^F_4$ in Et_2O overnight at room temperature. In all cases, reaction mixtures remained as pale yellow suspensions, (*cf.* the orange colour formed during the preparation of the bridging-bromide dimer **2.18**). Bromide extraction afforded the $[Ni(RE\text{-}NHC)(PCy_3)]BAr^F_4$ species **4.12** – **4.15**, which were readily isolated after filtration, as the compounds were very soluble in Et_2O due to the BAr^F_4 counterion, allowing easy separation from NaBr. Recrystallisation from Et_2O/pentane gave pale yellow crystalline material in isolated yields of 56 – 83%. In contrast to the *bis*-carbene species **3.1**, compounds **4.12** – **4.15** proved extremely sensitive to air and moisture, undergoing an instantaneous colour change to brown upon exposure of solutions to air. They did, however, display excellent stability when maintained under an inert atmosphere, with sealed NMR tubes of compound showing no sign of degradation by ^1H NMR spectroscopy after 5 days at 343 K.

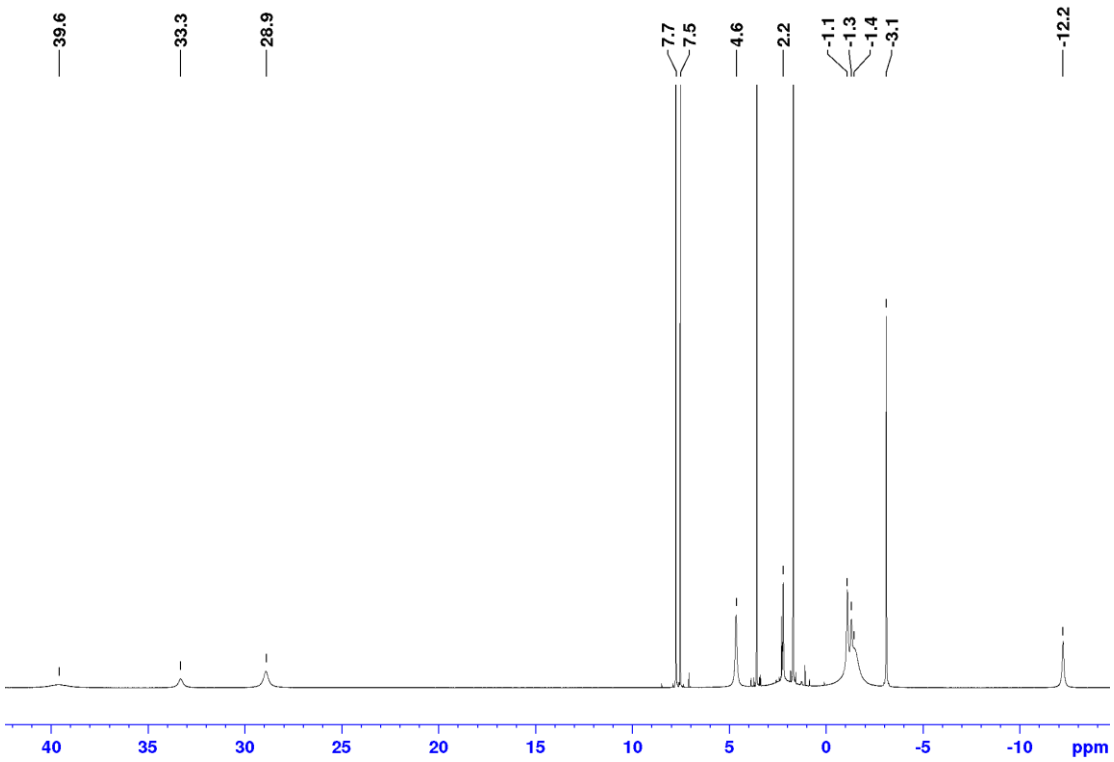

Figure 4.10 ^{1}H NMR spectrum (THF-d_8, 500 MHz, 298 K) of compound **4.12**.

The ^{1}H NMR spectra of **4.12** – **4.15** displayed broad paramagnetically shifted peaks in the range δ 41 to -17 ppm (spectrum of **4.12** shown Figure 4.10), with signals at δ 7.8 and 7.5 ppm for the aryl protons of the BAr^{F}_{4} counterion. Efforts to locate a signal for **4.12** in the $^{31}P\{^{1}H\}$ NMR spectrum through use of a 90° pulse sequence and reduction of the acquisition and delay times to the lowest possible values failed to produce any observable peak for the PCy_3 ligand, suggesting that the relaxation was too rapid to allow the detection of a signal. Room temperature solution magnetic moments for **4.12** – **4.15** were recorded *via* the Evans method in THF, with values of 2.5 – 2.6 μ_B respectively. These susceptibilities are slightly higher than those for the three-coordinate precursors (2.1 – 2.2 μ_B), but lower than the values recorded for *bis*-carbene compounds (2.9 – 3.3 μ_B), and thus indicative of the presence of magnetic anisotropy, albeit to a lower degree than the *bis*-NHC species.

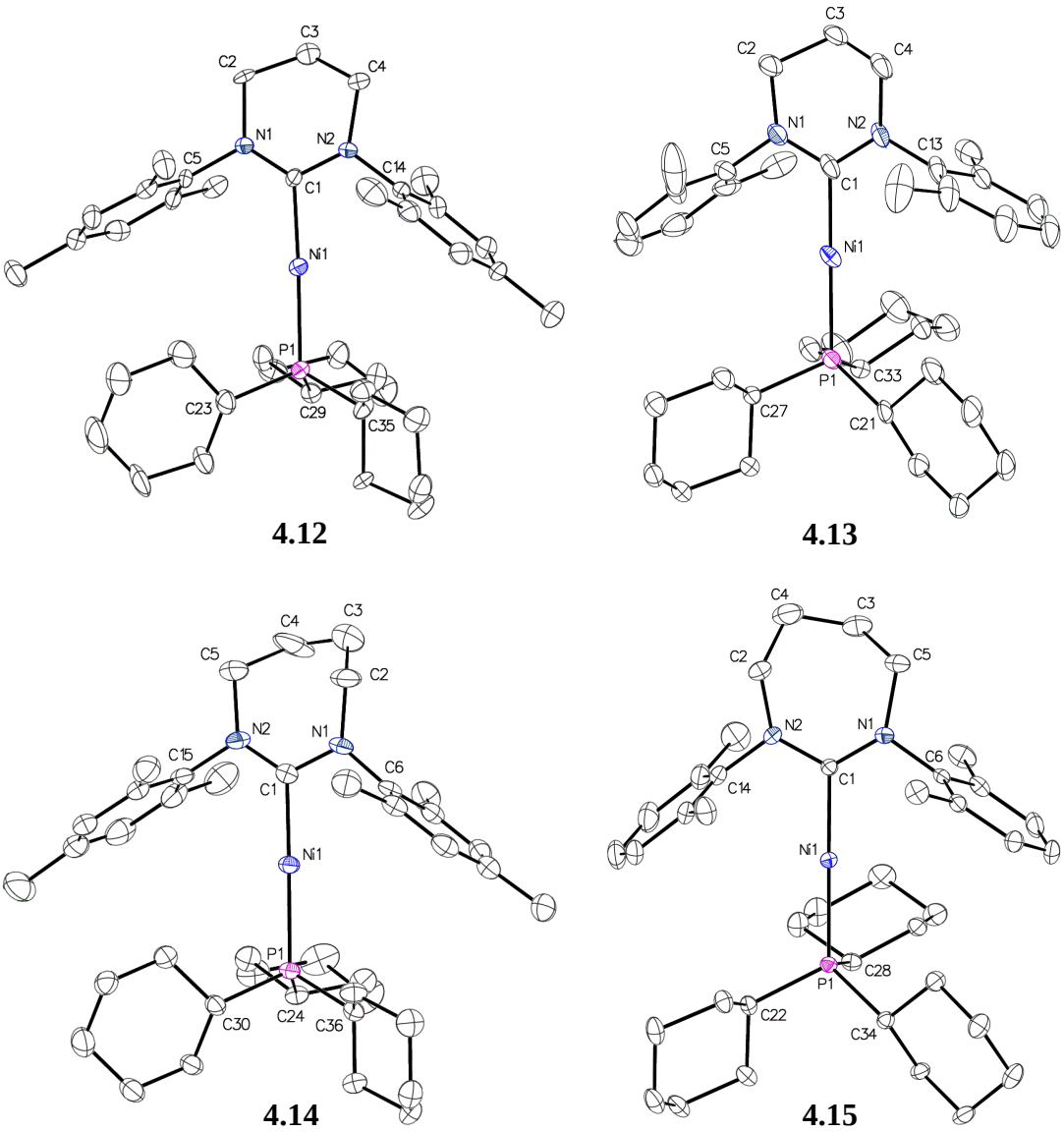

Figure 4.11 Molecular structures of the cations in **4.12** – **4.15**. Thermal ellipsoids are set at 30% probability. All hydrogen atoms have been omitted for clarity.

Crystallisation of **4.12** – **4.15** from Et_2O/pentane at room temperature formed pale yellow blocks, suitable for X-ray crystallography. Figure 4.11 shows the molecular structures of the cations in each case. Selected bond lengths and angles are given in Table 4.4. C_{NHC}-Ni-P bond angles of 173.30(8) – 175.60(12)° across the series of compounds indicates their near-linear geometries (*cf.* C_{NHC}-Ni-C_{NHC} angle = 179.27(13)° in **3.1**, and perfect 180° P-Ni-P angle in $[Ni(P^tBu_3)_2]^+$).[5] As with the two-coordinate *bis*-NHC compounds, no short contacts or stabilising C-H bond interactions were observed in any case. A comparison of the metrics reveals that the Ni-C_{NHC} bond lengths were fairly consistent throughout **4.12** – **4.15** (1.920(4) – 1.937(7) Å), but significantly reduced in

comparison to the three-coordinate precursor **2.20** (1.969(5)/1.987(10) Å). There was also a reduction in the Ni-P bond length (2.2219(19) Å in **4.12** *vs.* 2.2514(14)/2.2399(14) Å in **2.20**), while the N-C_{NHC}-N angle of the 6Mes carbene was notably wider (121.0(6)° for **4.12** *vs.* 116.4(4)/116.4(7)° for **2.20**). Thus, reduction in coordination number from three to two allows the ligands and N-aryl wing tips to "relax" and reside closer to the metal centre.

The Ni-P bond lengths of **4.12** – **4.15** (2.2204(10) – 2.2443(7) Å) were slightly shorter than those of Krossing's *bis*-phosphine species (2.250 Å),[5] but intermediate between those of other two-coordinate phosphine-containing (albeit neutral) Ni(I) complexes, amido species Ni(PR_3)(N($SiMe_3$)-2,6-(^{i}Pr)$_2$-C_6H_3) (R = ^{t}Bu, ^{i}Pr) and alkoxide complex Ni(P^{t}Bu$_3$)(η^5-(2,6-^{t}Bu$_2$-4-Me-C_6H_2O)), which feature Ni-P bond lengths in the range 2.1992(7) Å to 2.2333(4) Å.[6]

Table 4.4 Selected bond lengths and angles of compounds **4.12** – **4.15**.

Compound	Ni-C_{NHC} (Å)	Ni-P (Å)	N-C_{NHC}-N (°)	C_{NHC}-Ni-P (°)
4.12	1.937(7)	2.2219(19)	121.0(6)	173.9(2)
4.13	1.920(4)	2.2204(10)	118.7(4)	175.60(12)
4.14[a]	1.928(6)	2.2365(16)	121.9(6)	175.04(18)
	1.929(6)	2.2302(16)	121.6(5)	175.21(17)
4.15	1.933(2)	2.2443(7)	120.7(2)	173.30(8)

[a] Two independent molecules in the unit cell.

4.2.1 Magnetism of [Ni(RE-NHC)(PCy$_3$)]BAr$^F{}_4$

As with all the two-coordinate Ni(I) chemistry previously described, the presence of the unpaired electron in these d^9 compounds can lead to the opportunity for slow magnetic relaxation behaviour. Under a static dc field of 1000 Oe, the temperature dependence of the molar magnetic susceptibility of compounds **4.12** and **4.13** was investigated between 1.8 and 300 K (Figure 4.12). At low temperatures, the χT of both compounds (**4.12**: 0.59 cm^3 K mol^{-1}, **4.13**: 0.75 cm^3 K mol^{-1}) was greater than the expected value for a S = ½ system. As the temperature increased, the χT value went up linearly, indicative of temperature independent paramagnetism (TIP), whereby low-lying excited states couple with the magnetic ground state through the Zeeman perturbation.[7]

Efforts to apply a TIP term to correct for the deviation proved difficult, with several erroneous data points affecting the determination of room temperature χT values for **4.12** and **4.13**.

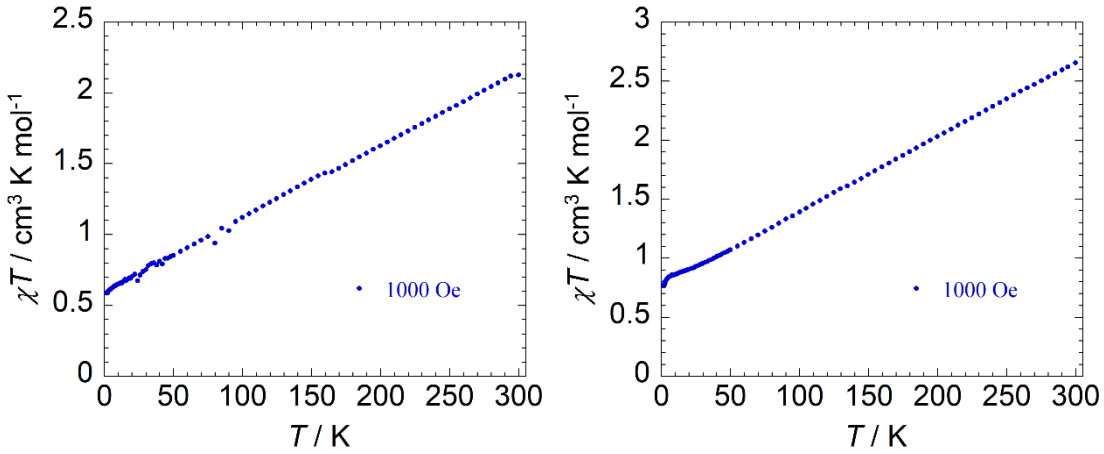

Figure 4.12 Temperature dependence of the χT product of compounds **4.12** (left) and **4.13** (right) under a 1000 Oe applied dc field (with χ being the molar magnetic susceptibility per molecule as defined by M/H).

The field dependent magnetisation measurements of **4.12** and **4.13** were carried out at 1.9, 3, 5, and 7 K (Figure 4.13). They showed a rapid increase in M at low field strengths, before slowly increasing to saturation values of 0.93 μ_B (**4.12**) and 0.85 μ_B (**4.13**) at 1.9 K under 7 T. These saturation values are significantly smaller than those of the $[Ni(RE\text{-}NHC)_2]^+$ species (*cf.* **3.1**: 2.01 μ_B), suggesting a lower level of magnetic anisotropy in the $[Ni(RE\text{-}NHC)(PCy_3)]^+$ compounds compared to the *bis*-NHC species. The reduced magnetisation curves are very nearly superimposed, reflecting the lack of significant magnetic anisotropy or orbital angular momentum in these compounds.

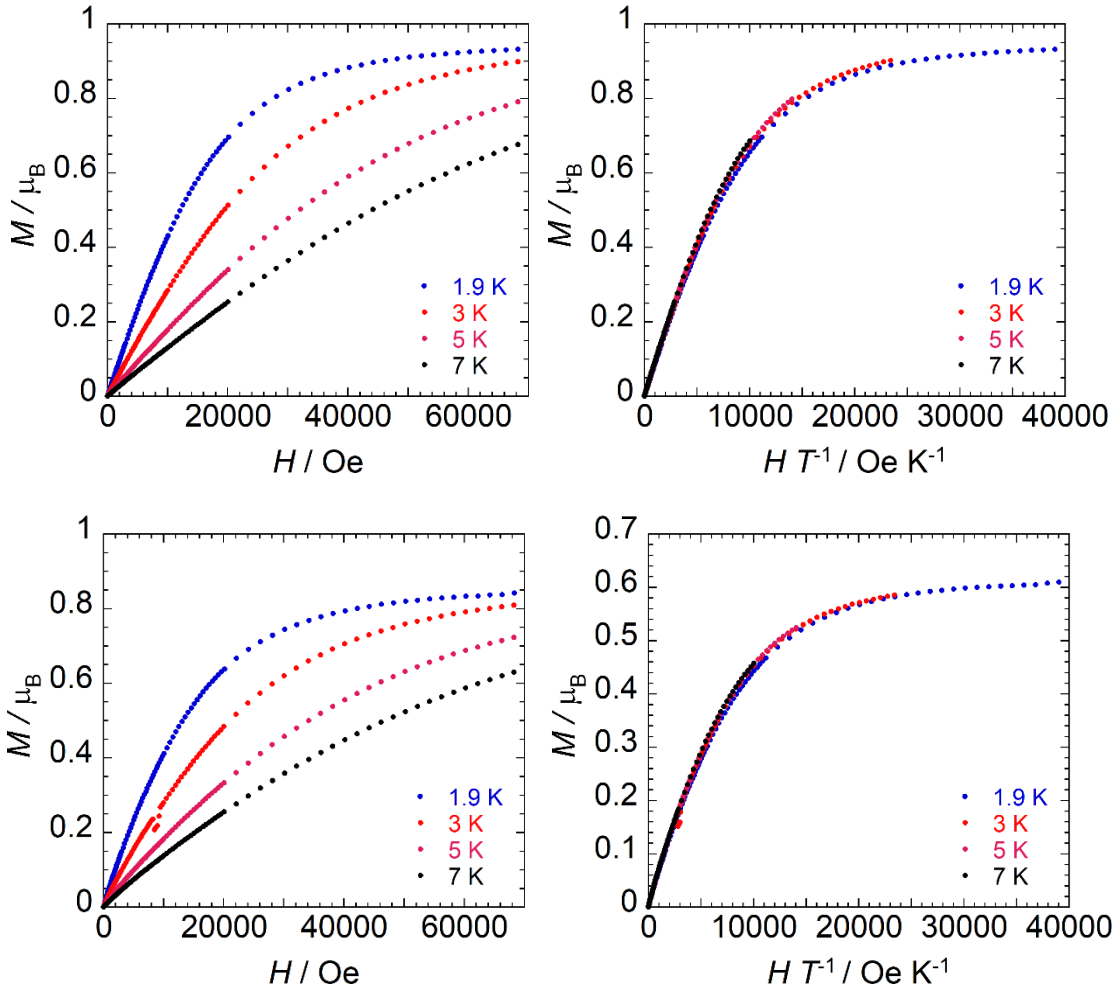

Figure 4.13 Field dependence of the magnetisation (*M vs. H*) and reduced magnetisation (*M vs. H* T^{-1}) for compound **4.12** (top) and **4.13** (bottom).

To investigate the relaxation dynamics, ac susceptibility measurements were carried out. No reasonable χ'' signal was observed for either **4.12** or **4.13** under zero applied dc field, just as with all previous Ni(I) species presented in this work. The frequency dependence of the ac susceptibility was measured as a function of applied dc field strength (0 to 5000 Oe) at 2 K and revealed one observed relaxation process across the entire field scope (χ'' in Figure 4.14, χ' in Appendix 7, Figure A7.5). The χ'' signal shows a peak maximum that shifts towards lower frequencies (ν) with increasing dc field, to a point (*ca.* 600 Oe), before shifting to higher frequencies. Hence, a small applied dc field of 600 Oe was selected to measure the frequency dependency as a function of temperature between 1.8 and 4 K (Figure 4.15), with χ'' signals decreasing with increasing temperature and frequency, showing the presence of SIM behaviour.

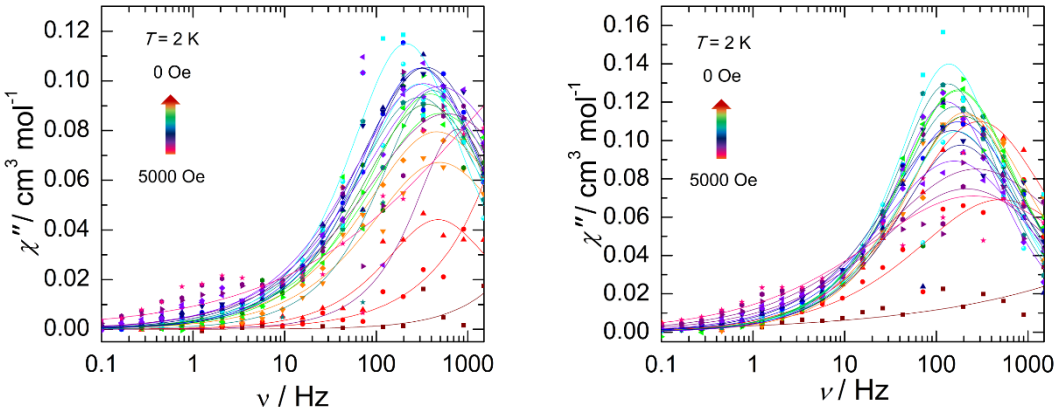

Figure 4.14 Frequency dependence of the out-of-phase (χ'') magnetic susceptibility of compounds **4.12** (left) and **4.13** (right) as a function of applied dc field at 2 K. Solid lines represent generalised Debye fits at each field strength.

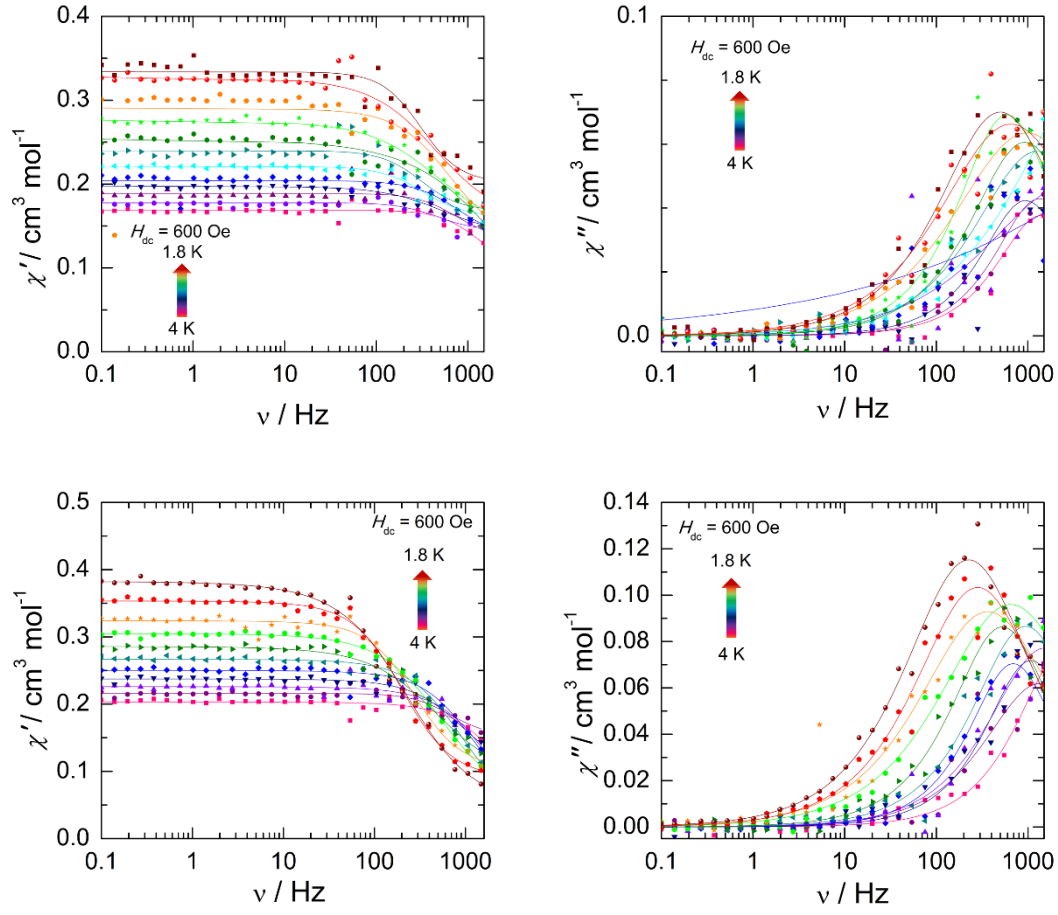

Figure 4.15 Frequency dependence of the in-phase (χ') and out-of-phase (χ'') magnetic susceptibility of compounds **4.12** (top) and **4.13** (bottom) as a function of temperature under a 600 Oe applied dc field. Solid lines represent generalised Debye fits at each temperature.

Use of the generalised Debye model to fit the frequency dependent data is shown as solid lines in both Figure 4.14 and Figure 4.15, although the presence of multiple anomalous data points in the χ' and χ'' curves for **4.12** and **4.13** results in the graphs appearing quite unclear. Regardless, attempts were made to use the extracted relaxation times to analyse the magnetic relaxation processes present in these compounds, although the results should be treated with caution due to the noisy data.

Plots of τ^{-1} *vs.* H at 2 K are shown in Figure 4.16, where best fits to the direct/QTM field dependent relaxation processes gave reasonable A, B_1, and B_2 parameters for **4.12** and **4.13** (Table 4.5). To determine whether direct/Raman/Orbach temperature dependent processes were present, τ^{-1} *vs.* T plots (at 600 Oe = 0.06 T) were fitted (Figure 4.17). From the magnitude of the fitted parameters, compound **4.12** appeared to be more dominated by the direct process, while **4.13** exhibits a more significant contribution from the QTM process. By fixing the parameters gained from the field dependent curves, the components of the Raman process could be reasonably well fitted for both compounds (Table 4.5), although the significant spread of data meant that several data points had to be masked from the fit. Orbach parameters were not included in the fitting, as no reasonable values could be obtained.

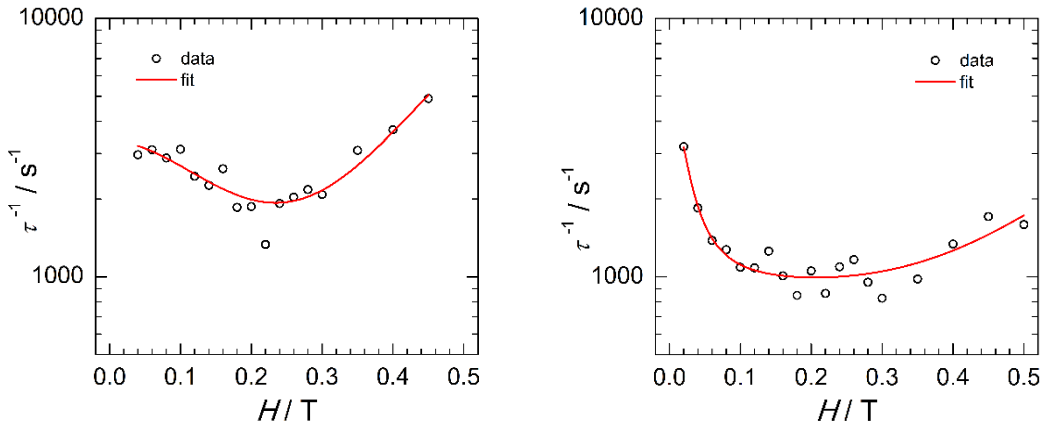

Figure 4.16 Field dependence of the magnetisation relaxation times (τ) of compounds **4.12** (left) and **4.13** (right) at 2 K. Solid red lines correspond to the best fits using direct and QTM relaxation mechanisms according to Equation 3.3 (Chapter 3).

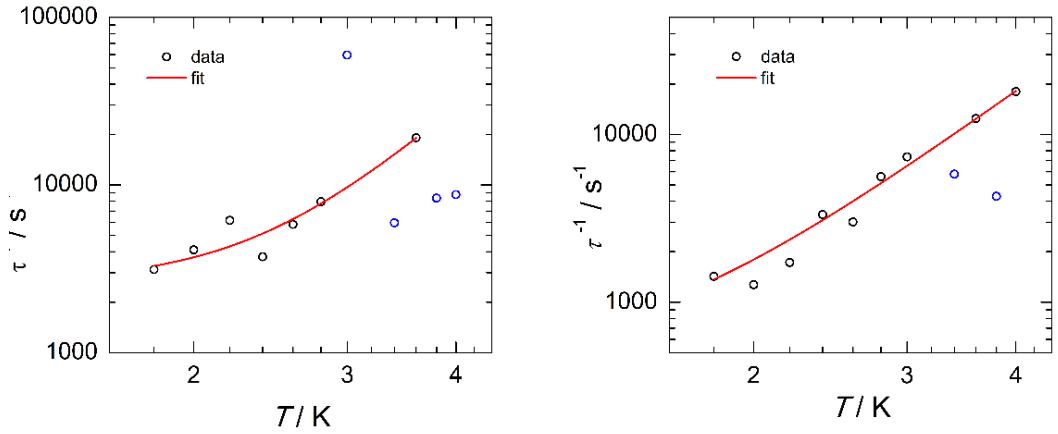

Figure 4.17 Temperature dependence of the magnetisation relaxation times (τ) of compounds **4.12** (left) and **4.13** (right) under a 600 Oe applied dc field. Solid red lines correspond to the best fits using direct, QTM, and Raman relaxation mechanisms according to Equation 3.4 (Chapter 3). Blue data points were ignored during the fit.

Table 4.5 Parameters used for best fit of Equation 3.3Equation 3.4 for **4.12** and **4.13**.

Compound	**A (s^{-1} T^{-4} K^{-1})**	**B_1 (s^{-1})**	**B_2 (T^{-2})**	**C (s^{-1})**	**n**
4.12	4.87×10^4	2.61×10^3	34.32	43.05	4.64
4.13	6.37×10^3	4.18×10^3	2.13×10^3	97.29	3.75

To estimate effective energy barrier values, relaxation times from the frequency dependence as a function of temperature data χ'' signals were used to plot ln(τ) *vs.* T^{-1}, and subsequently fitted with the Arrhenius law (Figure 4.18). Effective energy barrier and preexponential factor values of U_{eff} = 4.0 cm^{-1} (τ_0 = 1.47×10^{-5} s) for **4.12**, and U_{eff} = 7.5 cm^{-1} (τ_0 = 3.98×10^{-6} s) for **4.13** were obtained from the linear fit, although they should be only treated as estimates due to the vast spread of data. Based on the magnetism results for **4.12** and **4.13**, substitution of one of the RE-NHCs in $[Ni(RE\text{-}NHC)_2]^+$ to form $[Ni(RE\text{-}NHC)(PCy_3)]^+$ species does not lead to an improvement of the magnetic properties of Ni(I) ions, although with the caveat of a noisy dataset.

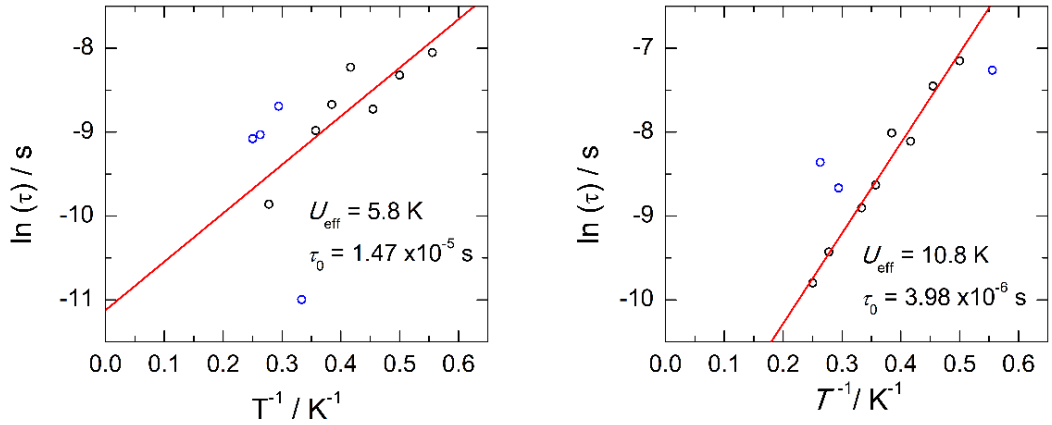

Figure 4.18 Relaxation time of the magnetisation ln(τ) *vs.* T^{-1} (Arrhenius plot using ac data) for compounds **4.12** (left) and **4.13** (right) under a 600 Oe applied dc field. Solid red lines correspond to linear fits. Blue data points were ignored during the fit.

4.3 Reactivity of [Ni(RE-NHC)(PCy$_3$)]BAr$^F_4$ Compounds

4.3.1 Substitution of the PCy$_3$ Ligand with Phosphines and NHCs

To probe the reactivity of the Ni(I) phosphine-NHC compounds, a reaction between **4.15** and 5 equiv. of P^{t}Bu$_3$ led to the substitution of PCy$_3$ at room temperature, affording the new two-coordinate species [Ni(7Xyl)(P^{t}Bu$_3$)]BAr$^F_4$ **4.16** (Scheme 4.4). The reaction was monitored *via* ^{31}P{^{1}H} NMR spectroscopy, whereby the appearance of the signal of free PCy$_3$ at *ca.* δ 8 ppm emerged rapidly, and continued to grow over 24 hrs. The organometallic product was isolated by evacuation of solvent, removal of excess P^{t}Bu$_3$ and released PCy$_3$ with pentane, and finally crystallisation from Et$_2$O/pentane, giving a pale-yellow solid in 42% isolated yield. The ^{1}H NMR spectrum of **4.16** displayed a new set of paramagnetic peaks between δ 32 to -19 ppm, but once again, no signal in the ^{31}P{^{1}H} NMR spectra. A room temperature solution magnetic moment of 2.2 μ$_B$ was recorded in THF (Evans method).

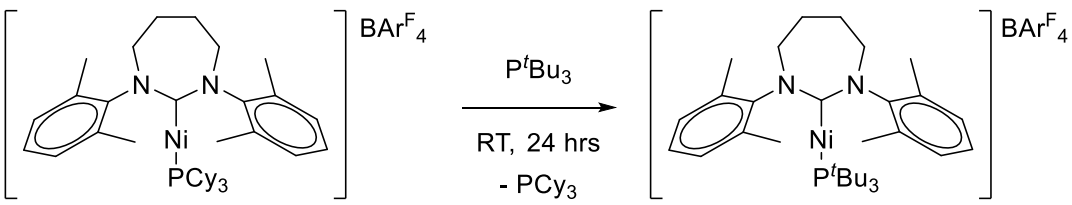

Scheme 4.4 Reaction of compound **4.15** with excess P^{t}Bu$_3$ to form **4.16**.

An X-ray study of **4.16** revealed a linear geometry (Figure 4.19), with a C-Ni-P bond angle of 177.91(7)°. This increase in bond angle relative to the PCy_3 analogue **4.15** (173.30(8)°) suggests that the greater steric bulk of P^tBu_3 forces the more linear geometry.[i] Bond lengths and the carbene N-C_{NHC}-N angle were unchanged (Table 4.6).

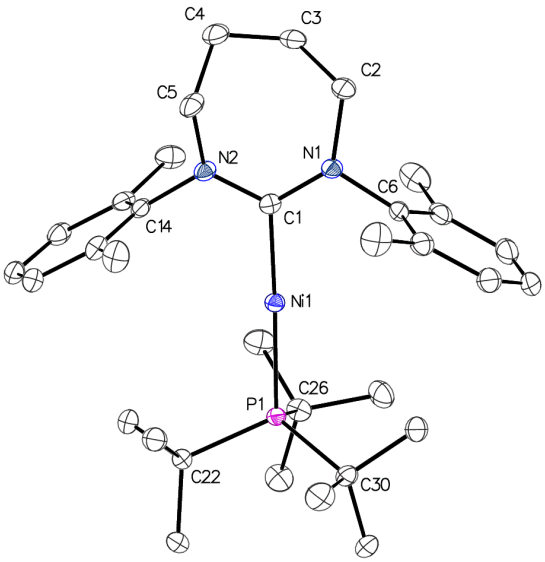

Figure 4.19 Molecule structure of the cation in compound **4.16**. Thermal ellipsoids are set at 30% probability. All hydrogen atoms have been omitted for clarity.

Following the successful substitution of the PCy_3 in $[Ni(7Xyl)(PCy_3)]^+$ with P^tBu_3, the reactivity between a range of tertiary phosphines and $[Ni(RE\text{-}NHC)(PCy_3)]^+$ species was investigated. Excess amounts of PPh_3, $P(o\text{-tol})_3$, $P(C_6F_5)_3$ and P^iPr_3 in combination with a range of $[Ni(RE\text{-}NHC)(PCy_3)]BAr^F{}_4$ compounds failed to yield any new products, at either room or elevated temperatures. Reactions were monitored by both ^1H and $^{31}P\{^1H\}$ NMR spectroscopy, with successful substitution deemed to have occurred if new ^1H paramagnetic peaks appeared and the ^{31}P signal for free PCy_3 emerged. The hypothetical PPh_3 substitution product had effectively already been synthesised and isolated in the form of the dimeric species **2.18**, and therefore the lack of reaction with PPh_3 was not surprising. The lack of reactivity with $P(o\text{-tol})_3$ and $P(C_6F_5)_3$ was most likely due to steric and electronic reasons respectively. P^iPr_3 showed promising signs of

[i] Tolman cone angles: PCy_3 = 179°, P^tBu_3 = 182°.[8]

substituting PCy_3 in **4.14** at room temperature, but the reaction failed to go to completion, preventing any new product from being separated from the starting material.

Table 4.6 Selected bond lengths and angles in compounds **4.15** and **4.16**.

Compound	Ni-C_{NHC} (Å)	Ni-P (Å)	N-C_{NHC}-N (°)	C_{NHC}-Ni-P (°)
4.15	1.933(2)	2.2443(7)	120.7(2)	173.30(8)
4.16	1.932(2)	2.2455(6)	120.0(2)	177.91(7)

As well as trying to substitute PCy_3 for phosphines, the possibility of using NHCs to form $[Ni(RE\text{-}NHC)(RE\text{-}NHC')]^+$ compounds *via* a different route to that shown previously was investigated. The reaction of **4.12** with one equiv. of 6Mes showed $[Ni(6Mes)_2]BAr^F{}_4$ was formed cleanly after only 30 min at room temperature (*cf.* 16 hr reaction time between $Ni(6Mes)(PPh_3)Br$ and 6Mes). This was perhaps an unremarkable result, as the homoleptic species has previously been shown to form readily under a variety of conditions. A more challenging trial of the synthetic route was examined by treatment of **4.12** with the diamidocarbene 6MesDAC. However, after 5 days at room temperature, no new products were formed.

4.3.2 EPR Spectroscopy of [Ni(RE-NHC)(PR$_3$)]BAr$^F{}_4$ Compounds 4.12 – 4.16

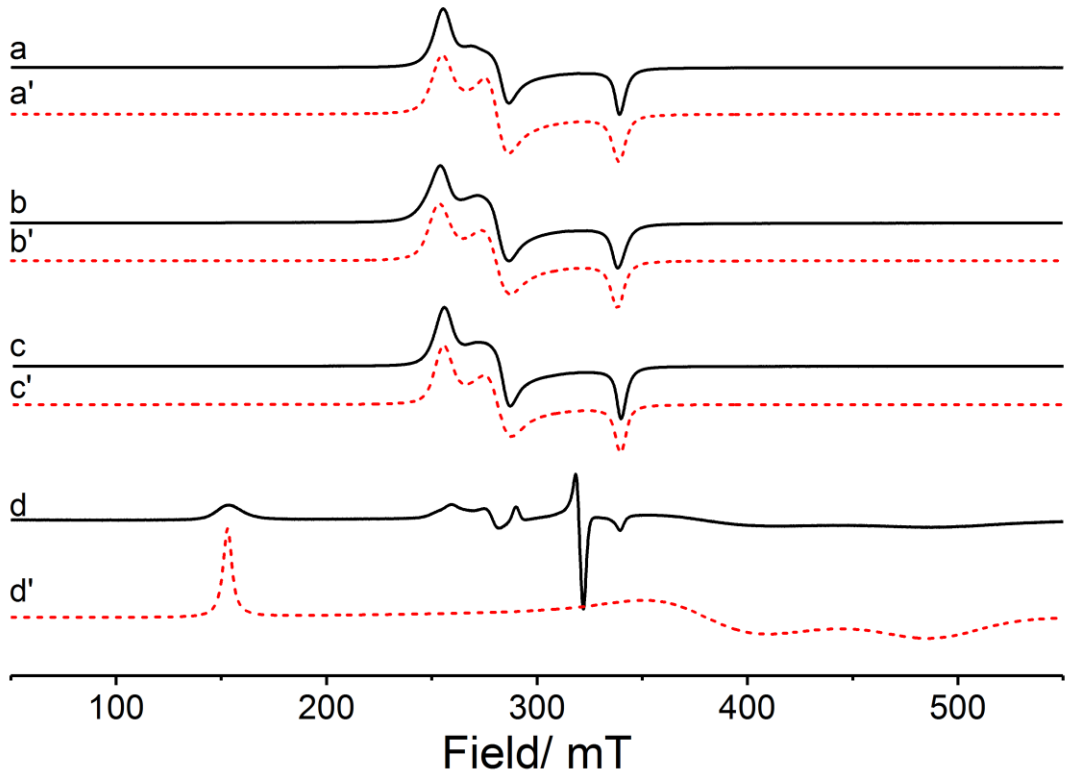

Figure 4.20 Experimental (black line) and simulated (red line) X-band CW EPR spectra (THF/toluene, 120 K) of compounds **4.12** (a), **4.14** (b), **4.13** (c), and **4.16** (d).

X-band EPR spectra of compounds **4.12** – **4.14** and **4.16** were recorded in frozen solutions of THF/toluene at 120 K (Figure 4.20). PCy_3 derivatives **4.12** – **4.14** gave rhombic spectra as typically associated with three-coordinate Ni(I) species. This likely reflects the formation of THF-bound species, as supported by the fact that the simulated spectra of $[Ni(RE\text{-}NHC)(PCy_3)(THF)]^+$ species closely match the experimental data. The spectrum of the P^{t}Bu$_3$ analogue **4.16** (Figure 4.20, (d)) proved to be an interesting case, with what appeared to be a mixture of two- and three-coordinate species present. There were significant signals that appeared to correspond to the three-coordinate THF-bound species, matching the spectra recorded for the PCy_3 derivatives. There was also an appearance of a signal at low fields (~ 150 mT), reminiscent of such a signal observed for the two-coordinate *bis*-NHC compounds in Chapter 3. However, no associated signal could be seen in the high field region, perhaps due to the fact that the NHC-phosphine system has lower magnetic anisotropy than the *bis*-NHC complexes. Spin Hamiltonian parameters of **4.12** – **4.14** and **4.16** are shown in Table 4.7, and efforts into calculating the *g* values for **4.16** through CASSCF to rationalise the observed spectrum are ongoing.

Table 4.7 Spin Hamiltonian parameters for compounds **4.12** – **4.14** and **4.16.**

Compound	g_1	g_2	g_3
4.12	2.0025	2.415	2.665
4.13	2.001	2.415	2.663
4.14	2.0047	2.415	2.676
4.16	1.388	1.783	4.425

4.3.3 Electrochemistry of [Ni(RE-NHC)(PR$_3$)]BAr$^F_4$ Compounds 4.12 – 4.16

The redox potentials of compounds **4.12** – **4.16** were compared by measurement of the cyclic voltammograms at a 3 mm diameter glassy carbon electrode in THF with [^{n}Bu$_4$N]PF$_6$ electrolyte.[i] Each compound showed independent and irreversible oxidation and reduction waves, with peak potentials relative to the reversible potential for decamethylferrocene Fe(III/II) redox system displayed in Table 4.8. Compounds **4.12**, **4.13** and **4.15** showed similar redox potentials, while the lower oxidation potential for **4.16** (0.44 V *vs.* FeCp*$_2^{+/0}$) compared to **4.15** (0.58 V *vs.* FeCp*$_2^{+/0}$) suggested that the P^{t}Bu$_3$ ligand was more electron donating than PCy$_3$ (Figure 4.21).[ii] There was an associated shift in the reduction potential, therefore this trend may reflect contributions other than purely electronic (*e.g.*, interaction with solvent). An anodic pre-wave for compounds **4.12** – **4.15** possibly indicated a slow preceding chemical step that was consuming the current from the main oxidation peak. It remains unclear what the nature of the nickel compound is after undergoing the electron transfer process. Further studies with both electrochemical techniques and chemical redox agents could show what Ni(0) and Ni(II) species are forming and whether the compounds remain two-coordinate or undergo ligand rearrangement to form new organometallic complexes.

[i] Efforts to probe the effect of changing the electrolyte to [^{n}Bu$_4$N]BAr$^F_4$ occurred, however, synthesis of electrolyte pure enough to use was unsuccessful. ^{1}H NMR spectra of the synthesised electrolyte appeared clean and matched literature values in CDCl$_3$,[9] but the voltammogram of the electrolyte showed some redox chemistry of the starting material used ([^{n}Bu$_4$N]Br).

[ii] Note that the Tolman electronic parameter (TEP), used as a measure of the donor strength of defined by the carbonyl stretching frequency in Ni(PR$_3$)(CO)$_3$ complexes, describes PCy$_3$ and P^{t}Bu$_3$ having very similar νCO values (2056.4 and 2056.1 cm^{-1} respectively) and thus very similar donor strength.[10]

Table 4.8 Redox potentials (3 mm diameter glassy carbon, scan rate 0.05 V s^{-1}, 2 mM) for compounds **4.12** – **4.16** in THF *vs*. $FeCp^*_2{}^{+/0}$.

Compound	E_p^{ox} ***vs*. FeCp*$_2^{+/0}$ (V)**	E_p^{red} ***vs*. FeCp*$_2^{+/0}$ (V)**	$\Delta E_p^{ox,red}$ **(V)**
4.12	0.59	-1.51	2.10
4.13	0.71	-1.36	2.07
4.14	0.59	-1.58	2.17
4.15	0.58	-1.45	2.03
4.16	0.44	-1.82	2.26

Table 4.9 Peak current values for compounds **4.12** – **4.16** with varying scan rates.

Compound	**0.01 V s^{-1}**		**0.02 V s^{-1}**		**0.05 V s^{-1}**	
	I_p^{ox} (µA)	I_p^{red} (µA)	I_p^{ox} (µA)	I_p^{red} (µA)	I_p^{ox} (µA)	I_p^{red} (µA)
4.12	2.25	-1.66	3.98	-5.17	9.68	-13.01
4.13	1.44	-2.14	2.69	-6.84	2.61	-12.41
4.14	3.81	-4.04	7.12	-9.93	12.46	-18.67
4.15	1.89	-2.41	2.83	-4.13	6.19	-8.33
4.16	3.56	-3.58	5.87	-8.70	-	-13.70

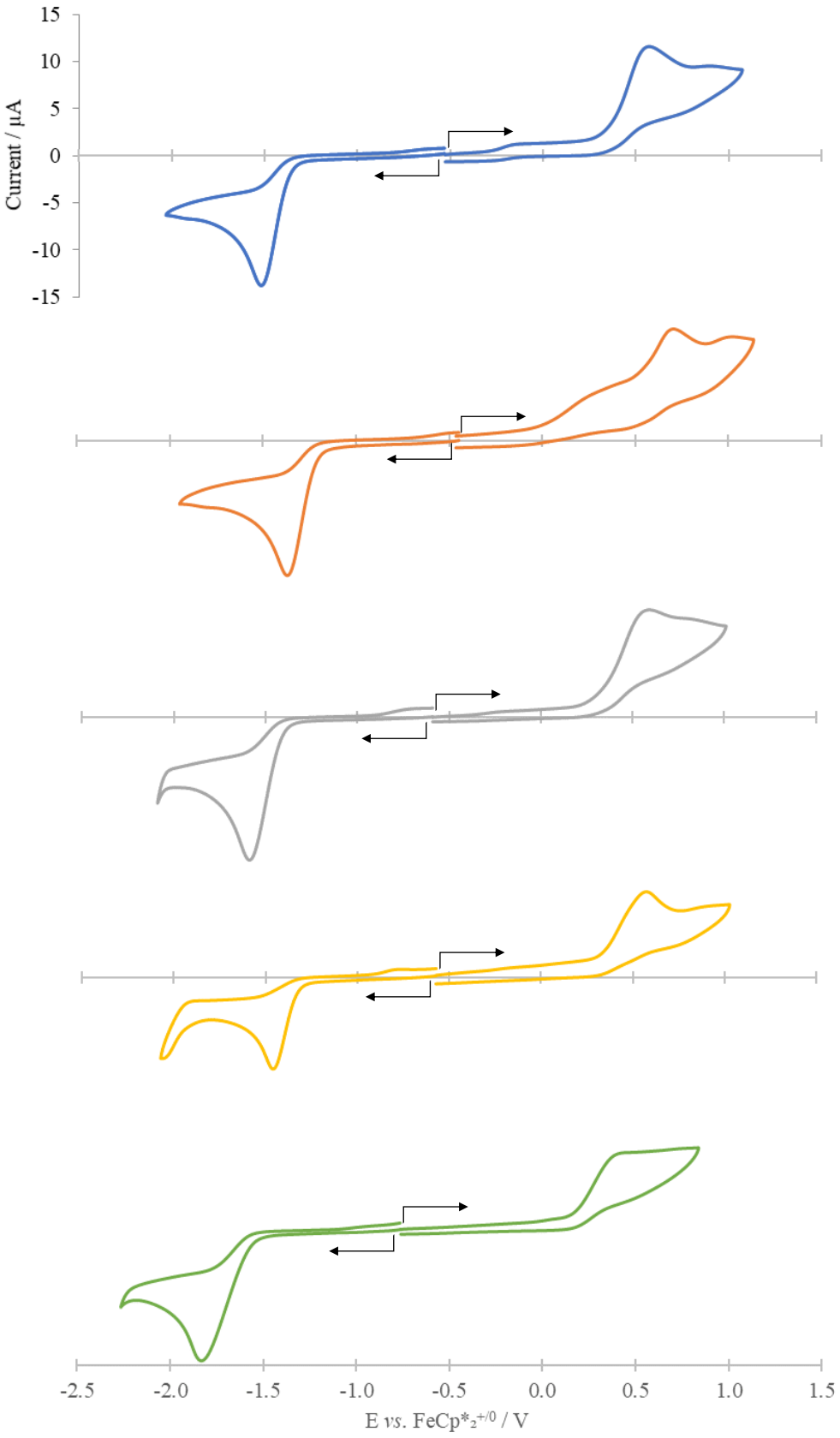

Figure 4.21 Cyclic voltammograms of compounds **4.12** – **4.16** *vs.* FeCp*$_2^{+/0}$ in THF (scan rate 0.05 V s^{-1}, 2 mM) (● **4.12**, ● **4.13**, ● **4.14**, ● **4.15**, ● **4.16**). Arrow indicates initial scanning direction.

When varying the scan rate (0.01, 0.02, 0.05 V s^{-1}), the peak potential value remained consistent, and the peak current (height) appeared to be dependent on the scan rate (Table 4.9). Plotting peak current *vs*. square root of scan rate confirmed this linear relationship (Appendix 5), and therefore allowed the use of the Randles-Sevcik equation to estimate diffusion coefficients (*D*) for compounds **4.12** – **4.16** (Equations 4.1). Assuming a one electron redox process generated average *D* values of 0.24, 0.20, 0.46, 0.09, and 0.26 × 10^{-9} m^2 s^{-1} for compounds **4.12** to **4.16** respectively. Use of the Wilke-Chang equation (Equations 4.1) to calculate an approximate diffusion coefficient of the two-coordinate species in THF gave a value of 0.67 × 10^{-9} m^2 s^{-1}. The fact that the experimentally observed values are of the same magnitude as the approximation validates that the system was diffusion controlled and that it involves a one electron process. Although the *D* values vary slightly across the set, one would expect the molecular volumes to be fairly similar across the range of the five compounds, and so the variation is most likely due to slight differences in concentration.

Equations 4.1 and 4.2 Randles-Sevcik and Wilke-Chang equations.[i, ii]

$$D = 1.38 \times 10^{-11}\, {I_p}^2\, A^{-2}\, C^{-2}\, \upsilon^{-1}$$

$$D = 7.4 \times 10^{-8}\, \frac{\sqrt{M}\, T}{\eta\, V^{0.6}}$$

4.3.4 Reactivity of [Ni(RE-NHC)(PR_3)]$BAr^F{}_4$ Compounds with Small Molecules

4.3.4.1 CO, N_2, H_2

Given the observed reactivity of [Ni(RE-NHC)(PCy_3)]$^+$ species with P^tBu_3, and the extreme sensitivity towards air and moisture, the reactivity of **4.12** – **4.16** with other small molecules was probed. No colour change and no change to the ^{1}H NMR spectrum occurred when either **4.13** was exposed to 1 atm of H_2, or **4.15** to N_2, at both room temperature and at 343 K. Upon exposure of **4.13** – **4.16** to CO (1 atm) in Et_2O, an instantaneous colour change from pale yellow to bright green occurred. Having previously described the synthesis of [Ni(6Mes)(PPh_3)(CO)]$^+$ (*via* the THF solvate **2.17**

[i] Rearranged from $I_p = 0.4463nFAC(nFvD/RT)^{1/2}$: I_p = peak current, n = # of electrons, F = Faraday's constant, A = area of electrode, C = concentration, v = scan rate, D = diffusion coefficient, R = gas constant, T = temperature.

[ii] M = molar mass of solvent, T = temperature, η = viscosity of solvent, V = molar volume of compound.

and the bromide-bridged dimer **2.18**) which featured a colour change to green, it seemed that $[Ni(RE\text{-}NHC)(PCy_3)]^+$ compounds could be used as precursors to $[Ni(RE\text{-}NHC)(PCy_3)(CO)]^+$ species (Scheme 4.5). Isolation of each carbonyl species **4.17** – **4.20** as green crystals from Et_2O/pentane, with **4.19** isolated in 79% yield. **4.19** displayed a paramagnetic ^1H NMR spectrum and a solution magnetic susceptibility measurement of 1.5 μ_B in THF (*cf.* Ni(I)-CO species **2.19**: 1.8 μ_B). Treatment of a THF solution of **4.20** with isotopically labelled ^{13}CO (1 atm) generated a carbonyl resonance in the $^{13}C\{^1H\}$ NMR spectrum at δ 198.7 ppm. As in the case with compound **2.19**, the appearance of this peak was indicative of reversible CO coordination at the Ni(I) centre.

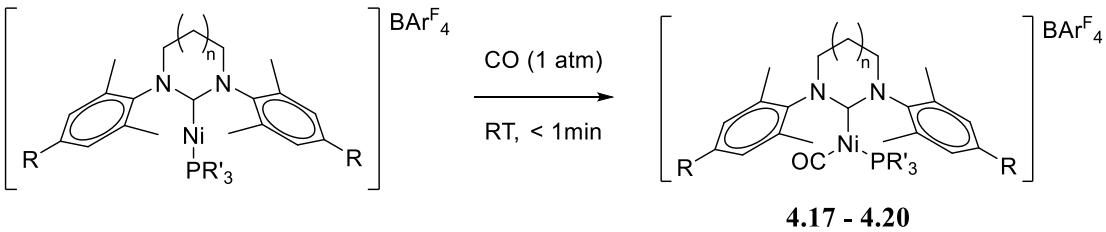

Scheme 4.5 Synthesis of compounds **4.17** – **4.20** by exposure of $[Ni(RE\text{-}NHC)(PR_3)]BAr^F_4$ species to CO.

IR spectroscopy of **4.17** – **4.20** confirmed formation of the Ni(I)-CO species, with carbonyl stretching bands for the PCy_3 analogues appearing at 2027 – 2028 cm^{-1} (Appendix 4). The P^tBu_3 derivative **4.20** showed a CO stretch at a slightly lower frequency (2023 cm^{-1}), consistent with a more electron-donating phosphine (*cf.* data in Table 4.8).

The 7Xyl compounds **4.19** and **4.20** were characterised by X-ray crystallography (Figure 4.22). As with the previous three-coordinate cationic nickel carbonyl species **2.19**, both structures showed a distorted T-shape. The C_{NHC}-Ni-P bond angles of 155.88(7)° and 157.23(8)° respectively were intermediate between those in **2.19** (151.93(9)°) and the THF-bound T-shaped species **2.17** (158.59(6)°). Ni-CO bond lengths (**4.19**: 1.793(3), **4.20**: 1.812(3) Å) were comparable with other reported examples.[11-17]

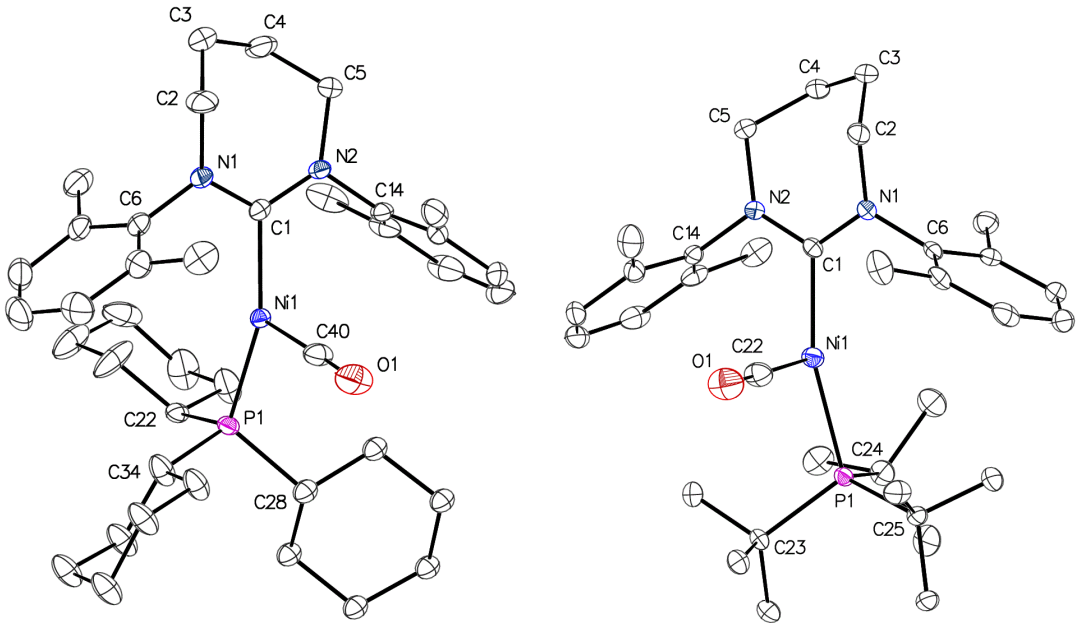

Figure 4.22 Molecular structures of the cations in **4.19** and **4.20**. Thermal ellipsoids are set at 30% probability. All hydrogen atoms have been omitted for clarity.

4.3.4.2 MeI and p-FC$_6$H$_4$I

Given the interest in the use of low-coordinate Ni(I) species in cross coupling chemistry,[18, 19] the reactivity of [Ni(RE-NHC)(PR$_3$)]$^+$ compounds towards simple alkyl and aryl halides was explored (Scheme 4.6). There is a paucity of examples of isolation of Ni(III) species arising from stoichiometric addition to Ni(I), with one recently reported reaction between the *bis*-amido Ni(I) anion [Ni{N(SiMe$_3$)(C$_6$H$_3$(^{i}Pr)$_2$)}$_2$]$^-$ and MeI leading to formation of a Ni(III)-methyl species.[20, 21] Other Ni(III)-alkyl/aryl species have been isolated with the tetradentate ligands [P(C$_6$H$_3$-2-S)$_3$]$^{3-}$ and [N(^{t}Bu){CH$_2$(C$_5$H$_3$N)CH$_2$}$_2$N(^{t}Bu)],[22, 23] in *bis*-halide Ni{C$_6$H$_3$(CH$_2$NMe$_2$)$_2$}X$_2$ compounds,[24, 25] and in the reaction between a Ni-cyclam macrocycle and alkyl radicals.[26]

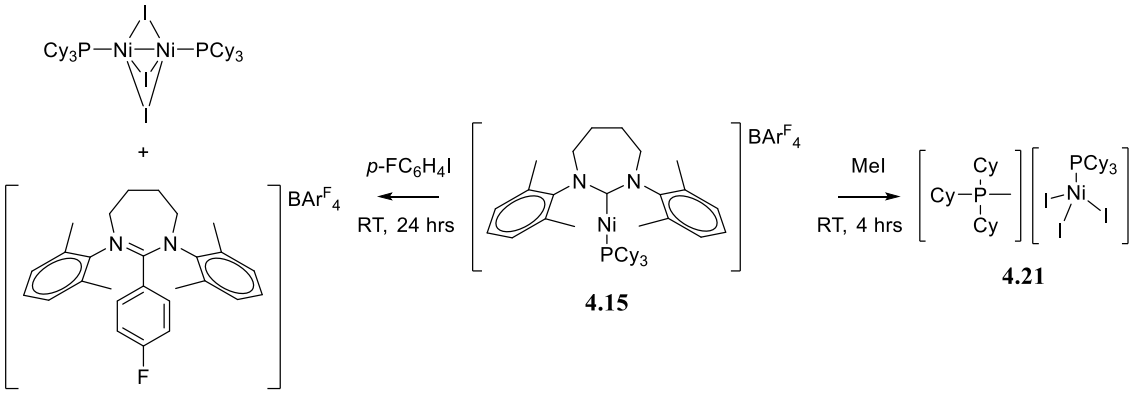

4.22, 4.23 **4.15** **4.21**

Scheme 4.6 Synthesis of compounds **4.21** – **4.23** *via* the reaction between **4.15** and MeI (right), and between **4.15** and p-FC_6H_4I (left).

At room temperature, **4.15** and 2 equiv. of MeI produced a colour change from pale yellow to very dark green, before a further change to red within 4 hrs, assumed to result from a degradation process. Red crystals isolated from Et_2O/pentane were shown to be a phosphonium cation $[PCy_3Me]^+$ **4.21** paired with the nickelate $[Ni(PCy_3)I_3]^-$ counterion (Appendix 1, Figure A1.2).[27] The fate of the 7Xyl ligand was not established, although, presumably the carbene was methylated to form a diazepinium salt with an accompanying BAr^F_4 counterion.

The reaction of **4.15** with *p*-FC_6H_4I also resulted in a colour change from yellow to dark green, although no further colour changes were then observed. X-ray crystallography of dark green needles isolated from the reaction mixture were shown to be the dimeric, formally mixed Ni(I)/Ni(II) species $[\{Ni(PCy_3)\}_2(\mu\text{-}I)_3]$ **4.22** , featuring statistically different Ni-P bond distances (2.2646(7) Å and 2.2708(7) Å) (Figure 4.23). Mixed-valent nickel species featuring a Ni-Ni bond are rare in the literature, with one recently reported example by Peng containing a Ni(II)-Ni(I)-Ni(II) moiety with Ni-Ni distances of 2.403(2) Å and 2.377(2) Å, slightly shorter than the Ni-Ni bond in **4.22** (2.4585(5) Å).[28] Colourless crystals also formed during recrystallisation. These were revealed by X-ray diffraction to be the salt $[7Xyl{\cdot}C_6H_4F]BAr^F_4$ **4.23**, resulting from arylation of the carbene.

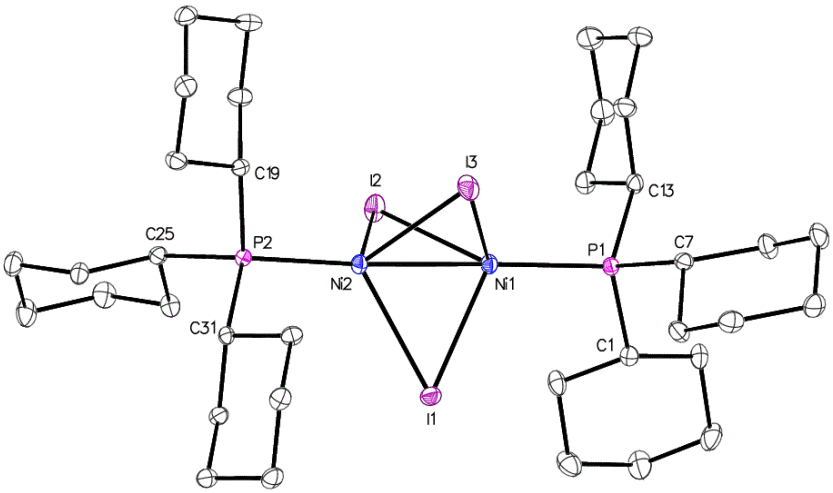

Figure 4.23 Molecular structure of compound **4.22**. Thermal ellipsoids are set at 30% probability. All hydrogen atoms have been omitted for clarity.

4.4 Summary

Following on from the preparation of two-coordinate compounds **3.1** – **3.6** in Chapter 3 whereby both ligands were identical, addition of a second (different) carbene to three-coordinate precursor Ni(6Mes)(PPh_3)Br **2.1** led to the formation of seven new [Ni(6Mes)(NHC')]Br compounds **4.1** – **4.7**. Changing the starting nickel-containing compound from 6Mes derivative **2.1** to 6Xyl and 7Mes derivatives gave rise to four more isolated [Ni(RE-NHC)(NHC')]Br species **4.8** – **4.11**. As with the homoleptic examples in Chapter 3, compounds **4.1** – **4.11** all showed broad ^{1}H NMR peaks across a wide chemical shift range, allowing assignment of all proton environments. X-ray structures of **4.1** – **4.11** revealed near-linear geometries.

Magnetic moment measurements supported the presence of two unpaired electrons and also indicated that these heteroleptic compounds displayed properties of single ion magnets. Static field properties of [Ni(6Mes)(7Mes)]Br **4.2** and [Ni(6Mes)(IMes)]Br **4.6** suggested a similar level of magnetic anisotropy compared to the original two-coordinate species **3.1**, and dynamic ac susceptibility measurements revealed two peaks (low and high frequency) in the out-of-phase (χ'') curves across all fields for **4.2**, and at low fields (< 400 Oe) in **4.6**. Use of a double-set generalised Debye model determined the field and temperature relaxation process parameters of **4.2** and **4.6**, and the low frequency component of **4.2** exhibited a very slow relaxation time of 0.53 s at 1.8 K under a 400 Oe dc field. The magnetic relaxation was deemed to go *via* a

combination of the direct and Raman processes, and the Arrhenius plot gave estimated energy barriers to spin reversal in the range 24.8 – 35.1 cm^{-1}.

As well as the formation of *bis*-NHC two-coordinate compounds, a range of near-linear $[Ni(RE\text{-}NHC)(PCy_3)]^+$ species **4.12** – **4.15** were formed *via* the removal of the bromide ligand from $Ni(RE\text{-}NHC)(PCy_3)Br$ precursors with $NaBAr^F{}_4$. Substitution of the PCy_3 in **4.15** with P^tBu_3 gave rise to $[Ni(7Xyl)(P^tBu_3)]^+$ **4.16**. Compounds **4.12** – **4.16** were characterised by paramagnetic ^1H NMR and EPR spectroscopy, X-ray diffraction, and electrochemistry. EPR spectra of **4.12** – **4.14** showed rhombic *g* profiles, consistent with three-coordinate Ni(I) species and thus suggestive of solvent coordination to nickel. The appearance of the spectra for compound **4.16** was different and suggested a two- and three-coordinate species, whereby the steric bulk of P^tBu_3 appeared to prevent complete solvation of the two-coordinate species. Cyclic voltammetry measurements of **4.12** – **4.16** showed irreversible oxidation and reduction waves with peak potentials measured relative to decamethylferrocene. Varying the scan rate of the voltammetry displayed a dependent change of the peak current. Linear plots of peak current *vs*. the square root of the scan rate indicated a one electron redox process, allowing the use of the Randles-Sevcik equation to determine diffusion coefficients for compounds **4.12** – **4.16**.

$[Ni(RE\text{-}NHC)(PR_3)]^+$ compounds reversibly reacted with CO to give the Ni(I) carbonyl species **4.17** – **4.20**, which were structurally and spectroscopically characterised. Further reactivity of the two-coordinate compounds was explored, in an attempt to form a new Ni(III) species *via* the oxidative addition of aryl- and alkyl-halides. However, stable oxidative addition products could not be isolated, but instead the salt $[PCy_3Me][Ni(PCy_3)I_3]$ **4.21**, and mixed valence dimer $[\{Ni(PCy_3)\}_2(\mu\text{-}I)_3]$ **4.22** were generated and structurally characterised.

In light of the overall aims of the thesis, a major finding was that SQUID measurements of **4.12** and **4.13** revealed SIM properties. The room temperature χT values were larger than expected for Ni(I), although not as large as the values seen for *bis*-NHC Ni(I) compounds. Susceptibility measurements confirmed the field-induced SIM behaviour, but several erroneous data points hindered efforts to accurately fit the relaxation times for field and temperature dependent process parameters. Arrhenius plots containing very noisy data estimated effective energy barriers of 4.0 – 7.5 cm^{-1}. Although values should be treated with caution, they did imply that the substitution of one RE-NHC ligand with a PCy_3 caused a reduction in the magnetic anisotropy of the Ni(I) centre, thus lowering the magnetic relaxation times and U_{eff} values.

4.5 References

1. R. C. Poulten, M. J. Page, A. G. Algarra, J. J. Le Roy, I. López, E. Carter, A. Llobet, S. A. Macgregor, M. F. Mahon and D. M. Murphy, *J. Am. Chem. Soc.*, 2013, **135**, 13640-13643.
2. S. T. Liddle and J. van Slageren, *Chem. Soc. Rev.*, 2015, **44**, 6655-6669.
3. D. Errulat, R. Marin, D. A. Gálico, K. L. M. Harriman, A. Pialat, B. Gabidullin, F. Iikawa, O. D. D. Couto, J. O. Moilanen, E. Hemmer, F. A. Sigoli and M. Murugesu, *ACS Cent. Sci.*, 2019, **5**, 1187-1198.
4. J. Titiš, V. Chrenková, C. Rajnák, J. Moncol, D. Valigura and R. Boča, *Dalton Trans.*, 2019, **48**, 11647-11650.
5. M. M. Schwab, D. Himmel, S. Kacprzak, V. Radtke, D. Kratzert, P. Weis, M. Wernet, A. Peter, Z. Yassine, D. Schmitz, E. Scheidt, W. Scherer, S. Weber, W. Feuerstein, F. Breher, A. Higelin and I. Krossing, *Chem. Eur. J.*, 2018, **24**, 918-927.
6. M. I. Lipschutz and T. D. Tilley, *Organometallics*, 2014, **33**, 5566-5570.
7. O. Kahn, *Molecular Magnetism*, Wiley, New York, 1993.
8. C. A. Tolman, *J. Am. Chem. Soc.*, 1970, **92**, 2956-2965.
9. T. Ono, M. Ohta and K. Sada, *ACS Macro Lett.*, 2012, **1**, 1270-1273.
10. C. A. Tolman, *Chem. Rev.*, 1977, **77**, 313-348.
11. N. A. Eckert, A. Dinescu, T. R. Cundari and P. L. Holland, *Inorg. Chem.*, 2005, **44**, 7702-7704.
12. P. Stavropoulos, M. Carrie, M. C. Muetterties and R. H. Holm, *J. Am. Chem. Soc.*, 1990, **112**, 5385-5387.
13. P. J. Schebler, B. S. Mandimutsira, C. G. Riordan, L. M. Liable-Sands, C. D. Incarvito and A. L. Rheingold, *J. Am. Chem. Soc.*, 2001, **123**, 331-332.
14. M. J. Ingleson, B. C. Fullmer, D. T. Buschhorn, H. Fan, M. Pink, J. C. Huffman and K. G. Caulton, *Inorg. Chem.*, 2008, **47**, 407-409.
15. B. Horn, S. Pfirrmann, C. Limberg, C. Herwig, B. Braun, S. Mebs and R. Metzinger, *Z. Anorg. Allg. Chem.*, 2011, **637**, 1169-1174.
16. C. Yoo, S. Oh, J. Kim and Y. Lee, *Chem. Sci.*, 2014, **5**, 3853-3858.
17. M. Abubekerov, L. Y. M. Eymann, T. L. Gianetti and J. Arnold, *Dalton Trans.*, 2016, **45**, 14581-14590.

18. K. Zhang, M. Conda-Sheridan, S. R. Cooke and J. Louie, *Organometallics*, 2011, **30**, 2546-2552.
19. K. Matsubara, Y. Fukahori, T. Inatomi, S. Tazaki, Y. Yamada, Y. Koga, S. Kanegawa and T. Nakamura, *Organometallics*, 2016, **35**, 3281-3287.
20. M. I. Lipschutz, X. Yang, R. Chatterjee and T. D. Tilley, *J. Am. Chem. Soc.*, 2013, **135**, 15298-15301.
21. M. I. Lipschutz and T. D. Tilley, *Angew. Chem. Int. Ed.*, 2014, **53**, 7290-7294.
22. C. Lee, C. Chen, F. Liao, C. Hu and G. Lee, *J. Am. Chem. Soc.*, 2010, **132**, 9256-9258.
23. B. Zheng, F. Tang, J. Luo, J. W. Schultz, N. P. Rath and L. M. Mirica, *J. Am. Chem. Soc.*, 2014, **136**, 6499-6504.
24. D. M. Grove, G. Van Koten, R. Zoet, N. W. Murrall and A. J. Welch, *J. Am. Chem. Soc.*, 1983, **105**, 1379-1380.
25. D. M. Grove, G. Van Koten, P. Mul, A. A. H. Van der Zeijden, J. Terheijden, M. C. Zoutberg and C. H. Stam, *Organometallics*, 1986, **5**, 322-326.
26. D. G. Kelley, A. Marchaj, A. Bakac and J. H. Espenson, *J. Am. Chem. Soc.*, 1991, **113**, 7583-7587.
27. A. Morvillo and A. Turco, *J. Organomet. Chem.*, 1981, **208**, 103-113.
28. C. Hsieh, T. Liu, Y. Song, G. Lee, B. Jin, T. Lin and S. Peng, *Dalton Trans.*, 2019, **48**, 9912-9915.

CHAPTER 5

5 CATALYTIC HYDROPHOSPHINATION OF ALKYNES

Some of the work in this chapter has been published previously in:

W. J. M. Blackaby, S. E. Neale, C. J. Isaac, S. Sabater, S. A. Macgregor and M. K. Whittlesey, *ChemCatChem*, 2019, **11**, 1893-1897

5.1 Background

5.1.1 P-C and P-H Oxidative Addition to Nickel Under Stoichiometric Conditions

Our group previously reported the synthesis of the three-coordinate Ni(0) compound Ni(6Mes)(PPh_3)$_2$ and showed multiple examples of substituting one labile triphenylphosphine ligand with alkyne, alkene, ketone or aldehyde.[1] During attempts to substitute the phosphine ligands with further NHC ligands, the reaction with IMe_4 led to the activation of a P-C bond in PPh_3 to form the four-coordinate Ni(II) phosphido aryl compound Ni(IMe_4)$_2$(PPh_2)(Ph) **5.1**. Very few examples of terminal nickel phosphido species have been reported in the literature,[2-6] and isolation of a terminal phosphido compound from a formal P-C oxidative addition across a single metal centre had not been reported prior to this example. Given the fact that the 6Mes and one of the PPh_3 ligands was lost during this transformation, compound **5.1** could be formed more atom efficiently by direct reaction of Ni(COD)$_2$, IMe_4 and PPh_3 (Scheme 5.1). Efforts to make a nickel phosphido hydride species *via* oxidative addition of diphenylphosphine (PPh_2H) and phenylphosphine ($PPhH_2$) in combination with IMe_4 led to the corresponding *bis*-phosphido compounds Ni(IMe_4)$_2$(PPh_2)$_2$ **5.2** and Ni(IMe_4)$_2$($PPhH$)$_2$ **5.3** respectively (Scheme 5.1). The P-H oxidative addition products were seen in NMR spectra recorded at the start of each reaction, though could not be isolated due to their conversion to **5.2** and **5.3** by a process that remains under investigation.

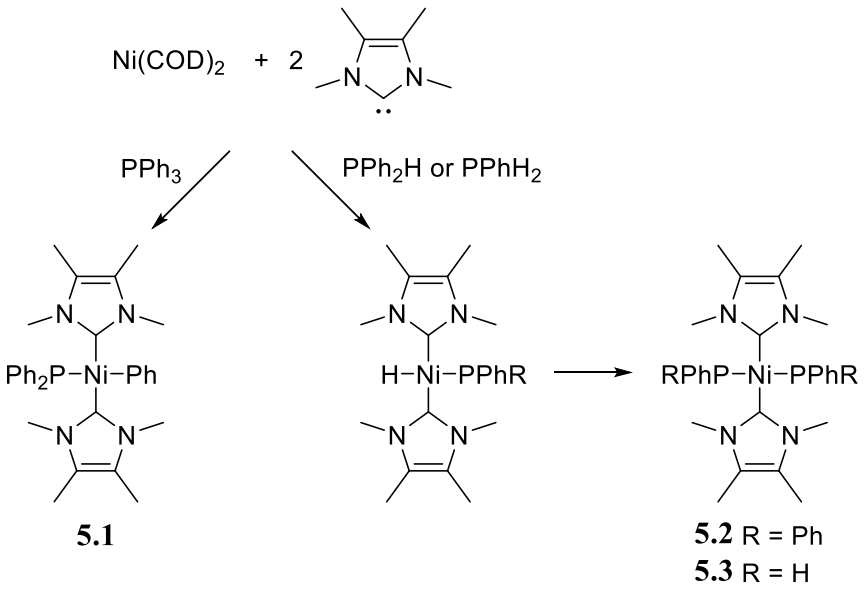

Scheme 5.1 P-C/P-H activation reactions with $Ni(COD)_2$, IMe_4 and phosphines.

The scope of NHCs and tertiary phosphines that would also undergo such Ni-NHC mediated transformations was then investigated further. IEt_2Me_2 was used to form $Ni(IEt_2Me_2)_2(PPh_2)(Ph)$ **5.4**. The reaction required heating to 343 K, whereas **5.1** could be formed at room temperature. The molecular structure of **5.4** showed the same square-planar geometry around the nickel as in **5.1**, with the observed lengthening of Ni-P and Ni-C_{Ph} bonds (Ni-P of 2.2851(8) Å in **5.4** compared to 2.2520(5) Å in **5.1**, and Ni-C_{Ph} of 1.960(3) Å in **5.4** compared to 1.937(1) Å in **5.1**) most likely due to the increased steric bulk from the N-ethyl groups relative to only methyl groups.

With the even bulkier NHC $I^iPr_2Me_2$, the reaction failed to proceed cleanly at either room temperature or 343 K, with the $^{31}P\{^1H\}$ NMR spectrum showing many phosphorus containing products. There is precedence for $Ni(COD)_2$ and ^{i}Pr containing NHCs to perform unwanted side reactions, with Radius showing Ni(0) and I^iPr_2 formed the dimeric species $\{Ni(I^iPr_2)_2\}_2(COD)$.[7] The formation of a similar product with $I^iPr_2Me_2$ may explain why reaction with PPh_3 did not yield any clean P-C activation chemistry.

P-C bond activation was also observed when using substituted tertiary phosphines. The use of tri(*p*-tolyl)phosphine with $Ni(COD)_2$ and IMe_4 to form $Ni(IMe_4)_2(P(p\text{-tol})_2)(p\text{-tol})$ was confirmed spectroscopically. Again, the reaction needed heating to 343 K to go to completion. Efforts to use the more electron-withdrawing example of tri(*p*-fluorophenyl)phosphine proved difficult, with full consumption of the

starting phosphine determined spectroscopically. However, the presence of many new phosphorus containing products did not allow assignment of any P-C activated species.

In light of the P-C and P-H oxidative addition to nickel under stoichiometric conditions, catalytic hydrophosphination of alkynes and alkenes was explored.

5.2 Catalytic Hydrophosphination of Alkynes with Nickel

Metal catalysed hydrophosphination of alkynes provides a straightforward method to making useful phosphines.[8-11] This has been explored previously using a wide variety of transition metal complexes based on iron,[12] cobalt,[13] nickel,[14, 15] zirconium,[16] ruthenium,[17] rhodium,[18] palladium,[14] as well as lanthanides.[19, 20] In particular, the work by Oro and co-workers[18] looking at rhodium-NHC catalysed double hydrophosphination of alkynes in part inspired the work reported herein.

Of particular interest was the *in-situ* formation of the Ni(II) phosphido hydride species $Ni(IMe_4)_2(PPh_2)(H)$ (before transformation to **5.2**), and its possible reaction with an alkyne or alkene. Coordination of the unsaturated species to the nickel, followed by a reductive elimination step, and finally oxidative addition of more PPh_2H to reform the phosphido hydride species would complete a hypothetical catalytic cycle. With this in mind, investigation started with the addition of PPh_2H to phenylacetylene (PhC≡CH, alkyne substituent **R** = Ph) in a molar ratio of 1.2:1 catalysed by a mixture of 5 mol% $Ni(COD)_2$ and 15 mol% IMe_4 in THF at room temperature (Scheme 5.2).

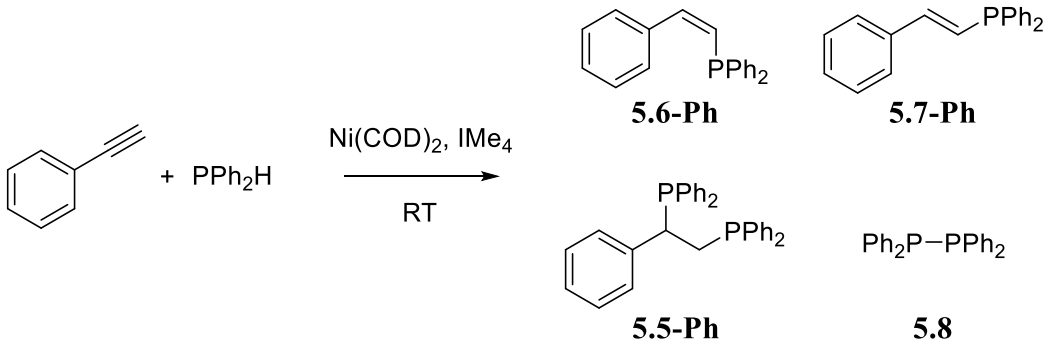

Scheme 5.2 Ni/IMe_4 catalysed hydrophosphination of PhC≡CH with PPh_2H.

The reaction was monitored by inverse-gated $^{31}P\{^1H\}$ NMR spectroscopy and after 24 hrs showed 97% conversion of PPh_2H. The main product from the reaction was the double addition product **5.5-Ph**, with *Z*- and *E*-anti-Markovnikov products **5.6-Ph** and

5.7-Ph also prominent in the mixture. There was also a small amount of dehydrocoupled product tetraphenylbiphosphine **5.8**. Figure 5.1 shows an example $^{31}P\{^{1}H\}$ NMR spectrum illustrating the formation of products **5.5-Ph** – **5.7-Ph** and **5.8**.

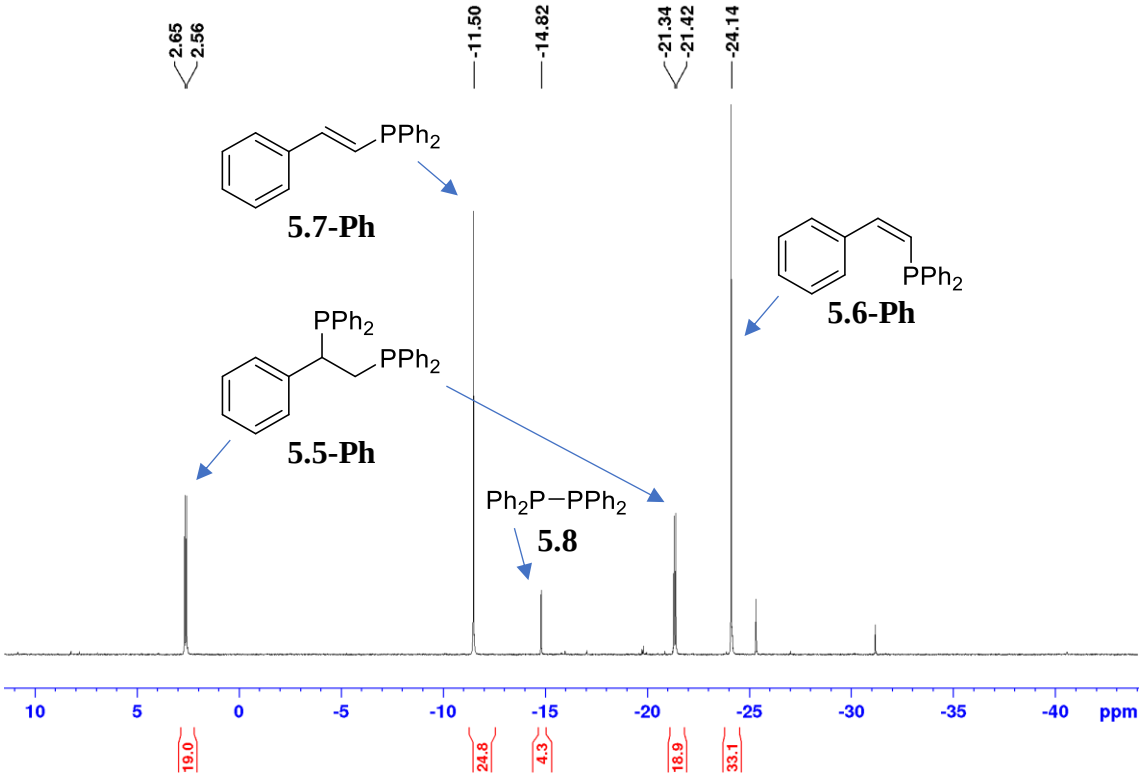

Figure 5.1 Inverse-gated $^{31}P\{^{1}H\}$ NMR spectrum (THF-d_8, 202 MHz, 298 K) of Ni/IMe$_4$ catalysed hydrophosphination of PhC≡CH with PPh$_2$H.

A screening of different solvents and reaction temperatures was conducted in an effort to maximise the conversion to the desired double addition product **5.5-Ph**. The screen revealed the best conditions for Ni/IMe$_4$ catalysed hydrophosphination to be 1.2 equiv. of PPh$_2$H to PhC≡CH with a catalyst loading of 5 mol% Ni(COD)$_2$ and 15 mol% IMe$_4$ in benzene at 343 K. Following on from the optimisation, the scope of this transformation was investigated for several types of alkynes, covering a wide range of substrates such as aromatic, aliphatic, heteroatom containing, and internal alkynes. The results are summarised in Table 5.1.

Table 5.1 Ni/IMe_4 catalysed hydrophosphination of alkynes with PPh_2H.[a]

Entry	Alkyne	Conversion (%)[b]	5.5-R as (%) of all products	5.6-R/5.7-R as (%) of all products	5.6-R:5.7-R ratio
1	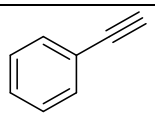	100	52	37	0.9 : 1
2	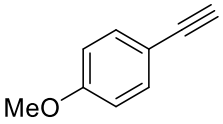	93	67	23	0.6 : 1
3	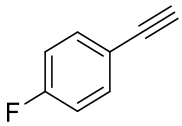	100	46	35	1.2 : 1
4	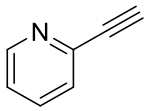	97	0	76	0.2 : 1
5	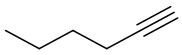	79	0	89	0.5 : 1
6	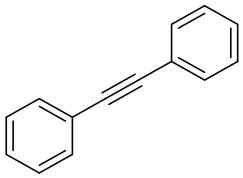	82	0	82	-[c]
7	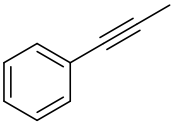	89	0	36	7.5 : 1

[a] Conditions: $Ni(COD)_2$ (0.015 mmol), IMe_4 (0.045 mmol), alkyne (0.29 mmol) and PPh_2H (0.35 mmol), benzene (0.5 mL), 343 K, 24 hrs. [b] Based on phosphine consumption quantified by integration of inverse-gated $^{31}P\{^1H\}$ NMR spectra. [c] Only **5.7-Ph$_2$** formed.

All entries showed excellent conversion of the starting materials, and while the double addition product **5.5-R** could only be accessed by *p*-substituted phenylacetylenes, they were formed in good yields (entries 1 – 3). The single addition products **5.6-R** and **5.7-R** were also present, in a ratio of 0.9:1 for PhC≡CH (entry 1), 0.6:1 for *p*-MeO-PhC≡CH (entry 2), and 1.2:1 for *p*-F-PhC≡CH (entry 3). The *ortho*-2-pyridyl-substituted alkyne (entry 4) and 1-hexyne (entry 5) displayed selectivity towards the *E*- isomer **5.7-R**, with particular note being the high conversion and lack of side products for the

aliphatic alkyne. PhC≡CPh exclusively formed the *E*-anti-Markovnikov product in good yield, whereas PhC≡CMe gave mostly the *Z*- isomer but with lots of other unassignable products.

5.3 N-heterocyclic Carbene Non-Innocence in the Catalytic Hydrophosphination of Alkynes[21]

5.3.1 Control Reaction with IMe$_4$

During the efforts to maximise conversion and selectivity of Ni/IMe$_4$ catalysed hydrophosphination, the influence of the different components within the catalytic system was studied through testing of blank runs. While the absence of both Ni(COD)$_2$ and IMe$_4$ did not yield any hydrophosphination products as expected, Ni(COD)$_2$ by itself was too unstable to perform any catalysis. Remarkably, catalytic amounts (10 mol%) of IMe$_4$ demonstrated hydrophosphination in the absence of any nickel, with high conversion and selectivity towards *Z*-anti-Markovnikov product **5.6-Ph** (Scheme 5.3). The *E*- isomer **5.7-Ph** was also present, but no double addition product **5.5-Ph** was observed. This showed that although it was remarkable for an NHC to perform this transformation, the nickel centre was required to go to the double hydrophosphination product **5.5-Ph**. To prove that only monohydrophosphination could occur, a catalytic run with 2.4 equiv. of PPh$_2$H to PhC≡CH only showed **5.6-Ph** and **5.7-Ph** after 48 hrs.

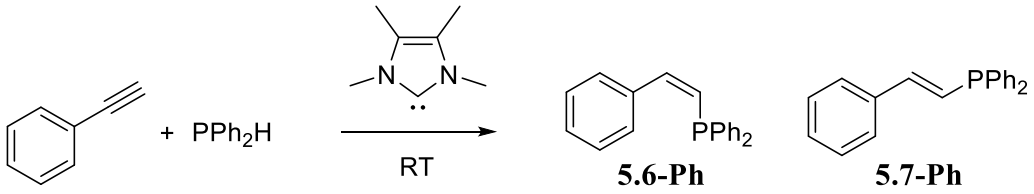

5.6-Ph **5.7-Ph**

Scheme 5.3 IMe$_4$ catalysed hydrophosphination of PhC≡CH with PPh$_2$H.

In light of these exciting results with just the NHC present, the effect of solvent and other reaction variables was investigated. The results are reported in Table 5.2.

Table 5.2 IMe_4 catalysed hydrophosphination of PhC≡CH with PPh_2H.[a]

Entry	Solvent	Conversion (%)[b]	5.6-Ph/5.7-Ph products as (%) of all products	5.6-Ph/5.7-Ph ratio
1	THF	81	90	2.8 : 1
2[c]	Toluene	72	86	2.0 : 1
3	Benzene	46	87	2.3 : 1
4	Cyclohexane	55	83	2.2 : 1
5[d]	THF	63	89	3.1 : 1
6[e]	THF	65	90	3.0 : 1

[a] Conditions: IMe_4 (0.04 mmol), PhC≡CH (0.40 mmol) and PPh_2H (0.44 mmol), solvent (0.5 mL), 298 K, 24 hrs. [b] Based on phosphine consumption quantified by integration of inverse-gated $^{31}P\{^1H\}$ NMR spectra. [c] 95 hr reaction. [d] Reaction tube not stirred or shaken. [e] Performed with exclusion of light.

All conditions showed preferred selectivity towards **5.6-Ph**, with THF (entry 1) yielding the highest conversion of PPh_2H and least amount of side products. The reaction left without agitation (entry 5) showed only a slight decrease in activity. Running the reaction in the dark (entry 6) had no effect, suggesting no possibility that photochemically generated radicals could lead to any catalysis. This was shown to be the case in work reported by Lindner[22] who used primary phosphines to photochemically hydrophosphinate vinyl ethers. The work was extended to include secondary phosphines transforming a range of vinyl and allyl derivatives photochemcially.[23] Tzschach,[24] Oshima,[25] and Ogawa[26] described work wherein light induced homolytic cleavage of the P-P bond in tetraphenylbiphosphine **5.8** led to the functionalisation of PhC≡CH. Efforts to use the known radical trap (bromomethyl)cyclopropane to confirm this theory led to immediate precipitation of a bright yellow solid, thus halting any hydrophosphination from occurring. It was inconclusive as to whether the reaction actually involved any radicals, or if one of the reagents was too sensitive to the radical trap used.

5.3.2 Screening of NHCs as Catalysts

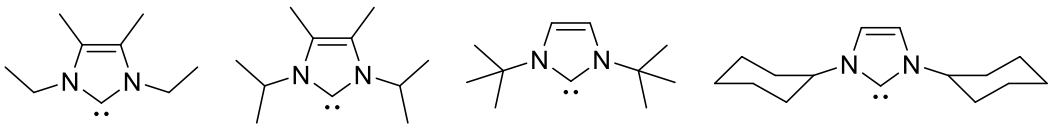

Figure 5.2 Structures and abbreviations of the N-alkyl NHCs screened.

With conditions selected to give reproducible catalytic results for IMe_4, a range of N-alkyl and N-aryl substituted NHCs were trialled for hydrophosphination with the model system of PhC≡CH and PPh_2H (N-alkyl NHCs given in Figure 5.2). The results of the catalyst screening are shown in Table 5.3. The N-alkyl substituted NHCs (entries 1 – 5) showed excellent conversions of PPh_2H and, with the exception of IEt_2Me_2 (entry 2), displayed similarly high selectivity towards formation of **5.6-Ph**, along with a paucity of unwanted side products. N-aryl substituted NHCs (entries 6 and 7) proved to be poor catalysts under the chosen conditions. The ring-expanded NHC and DAC examples (entries 8 and 9) also gave poor results. With IMe_4, the conversion and selectivity were similar whether Ni(0) was involved or not, baring the generation of the double addition product when involving $Ni(COD)_2$.

The percentage buried volume ($\%V_{bur}$) of the NHCs involved with this catalysis, currently considered to be the best way to determine the steric profile of carbenes, are shown in Table 5.3.[27-32] There is no correlation between PPh_2H conversion and the carbene sterics when represented by $\%V_{bur}$, which is consistent with DFT calculations reported later in section 5.3.6. The difference in reactivity appears to be related to whether the catalysts have alkyl or aryl N-substituents, and so could be influenced by electronics (*vide infra*).

Table 5.3 NHC catalysed hydrophosphination of PhC≡CH with PPh_2H,[a] and percentage buried volume ($\%V_{bur}$) of each NHC.[b]

Entry	Catalyst	Conversion (%)[c]	5.6-Ph/5.7-Ph products as (%) of all products	5.6-Ph:5.7-Ph ratio	$\%V_{bur}$
1	IMe_4	81	90	2.8 : 1	26.1
2	IEt_2Me_2	92	74	0.9 : 1	-
3	$I^iPr_2Me_2$	85	93	2.0 : 1	38.5
4	I^tBu	89	100	3.5 : 1	39.6
5	ICy	92	100	2.6 : 1	27.4
6[d]	IMes	14	71	-[e]	36.5
7[d]	IPr	0	-	-	44.5
8[d]	6Mes	9	100	-[e]	42.2
9[d]	6MesDAC	0	-	-	41.8[f]

[a] Conditions: Catalyst (0.04 mmol), PhC≡CH (0.40 mmol) and PPh_2H (0.44 mmol), THF (0.5 mL), 298 K, 16 hrs. [b] Determined for [AuCl(NHC)] compounds with Au-NHC bond length set to 2.00 Å. [c] Based on phosphine consumption quantified by integration of inverse-gated $^{31}P\{^1H\}$ NMR spectra. [d] 18 hr reaction. [e] Only **5.6-Ph** formed. [f] Determined for $[Cu(6MesDAC)_2]PF_6$ with Cu-NHC bond length set to 1.90 Å.

5.3.3 Alkyne and Phosphine Screening

Varying the nature of the alkyne or secondary phosphine was investigated to elucidate more details about the role of the NHC in catalytic hydrophosphination. 10 mol% I^tBu (Figure 5.2) was selected as the catalyst for the alkyne screening, on the grounds of the conversion of starting material and lack of side products formed with PhC≡CH (Table 5.3). As with the Ni-NHC catalysed hydrophosphination in Table 5.1, a range of alkynes including aromatic, aliphatic, heteroatom containing, and internal substrates was probed (Table 5.4). The presence of the electron-donating *p*-MeO group (entry 2) resulted in good conversion and no side products, while significantly increasing the **5.6-R**:**5.7-R** ratio. Both electron-withdrawing *p*-F and *p*-CF_3 groups (entries 3 and 4)

gave excellent conversions of phosphine but exhibited different product selectivity; the *p*-F group gave an increased **5.6-R**:**5.7-R** ratio whereas the *p*-CF_3 substituent exclusively formed the *E*-anti-Markovnikov product **5.7-*p*-CF_3Ph** (details *vide infra*). The *ortho*-2-pyridyl-substituted alkyne (entry 5) also showed the same reversal in regioselectivity, while no hydrophosphination was observed for the challenging aliphatic 1-hexyne (entry 6). Internal alkynes (entries 7 and 8) showed some reactivity. PhC≡CPh displayed similar selectivity to that of PhC≡CH, while PhC≡CMe afforded predominantly dehydrocoupled product **5.8** together with minor amounts of both **5.6-PhMe** and **5.7-PhMe**. A small range of alkene substrates were also screened, albeit with IMe_4 as the catalyst, with the results summarised in Appendix 8.

Table 5.4 I^{t}Bu catalysed hydrophosphination of alkynes with PPh_2H.[a]

Entry	Alkyne	Conversion (%)[b]	5.6-R/5.7-R products as (%) of all products	5.6-R:5.7-R ratio
1	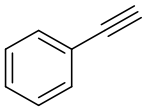	97	100	3.6 : 1
2	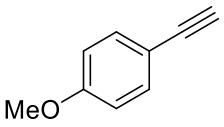	71	100	35.1 : 1
3	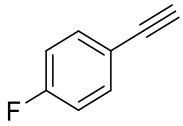	100	92	9.3 : 1
4	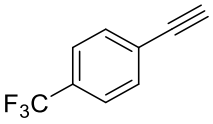	96	65	-[c]
5	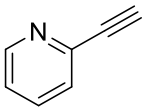	99	92	0.01 : 1
6	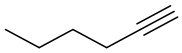	6	0	-[d]
7	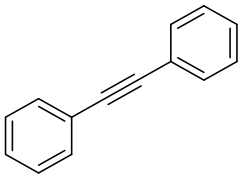	53	95	3.1 : 1
8	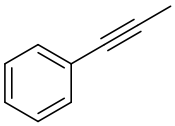	24	51	0.6 : 1

[a] Conditions: I^{t}Bu (0.04 mmol), alkyne (0.40 mmol) and PPh_2H (0.44 mmol), THF (0.5 mL), 298 K, 24 hrs. [b] Based on phosphine consumption quantified by integration of inverse-gated $^{31}P\{^1H\}$ NMR spectra. [c] Only **5.7-*p*-CF$_3$Ph** formed. [d] Only **5.8** formed.

To try and ascertain further details about the catalysis, the electronic properties of the secondary phosphine substrate were also varied. A range of substituted phosphine oxides were reduced with pinacolborane (HBPin) to form clean free phosphines under mild conditions (Scheme 5.4).[33] Following a simple work-up involving the quenching of

any remaining HBPin with ^{i}PrOH and filtration through an alumina plug, the phosphines were then used for IMe_4 catalysed hydrophosphination of PhC≡CH.[i]

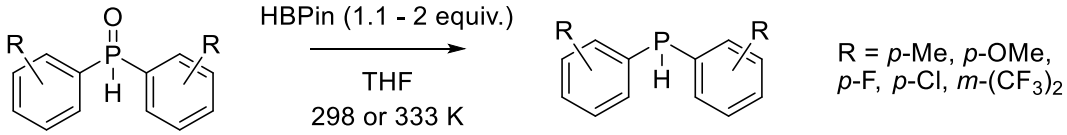

Scheme 5.4 Substituted secondary phosphine reduction with HBPin in THF.

Due to limited amounts of material, each catalytic run was performed only once. Thus, while the results should be treated with some caution, they still show some interesting patterns (Table 5.5). The presence of a *p*-Me group (entry 2) brought about a slight decrease in conversion compared to PPh_2H (entry 1), while the more strongly donating *p*-MeO group (entry 3) further decreases the conversion, and both show a lower selectivity towards **5.6-R**. Conversely, the electron-withdrawing *p*-F substituted phosphine (entry 4) leads to similar conversion and product selectivity to entry 1. The next phosphine, with *p*-Cl groups (entry 5), initially showed good activity after 1.5 hrs, however the conversion plateaued apparently due to a side reaction between IMe_4 and the chlorinated substrate, with N-alkyl NHCs known to decompose in chlorinated solvents.[34] The final phosphine contained both electronic and steric considerations, with two electron-withdrawing *m*-CF_3 groups (entry 6). This substrate was essentially inactive, with a very low conversion. A small proportion of products were the desired alkenyl-phosphines, and only the *Z*-anti-Markovnikov isomer **5.6-Ph(*m*-$(CF_3)_2$Ph)** was formed. The lack of result may be due to the increased steric bulk not allowing the NHC to access the P-H bond as easily as in the *p*-substituted substrates.

[i] Note the use of IMe_4, and not I^{t}Bu which was used for alkyne screening. Though not the most active catalyst (Table 5.3), any impact from the different electronics of the substituted secondary phosphines should be clear.

Table 5.5 IMe_4 catalysed hydrophosphination of PhC≡CH with substituted diphenylphosphines (P**R'**$_2$H, **R'** = substituted aryl group).[a]

Entry	Phosphine	Conversion (%)[b]	5.6-Ph(*R'*)/5.7-Ph(*R'*) products as (%) of all products	5.6-Ph(*R'*): 5.7-Ph(*R'*) ratio
1	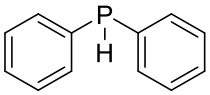	81	90	2.8 : 1
2	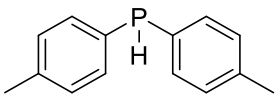	70	84	1.7 : 1
3	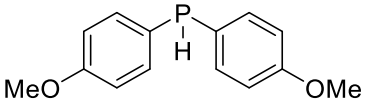	64	83	1.8 : 1
4	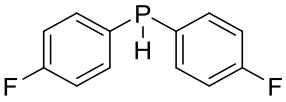	86	80	3.6 : 1
5[c]	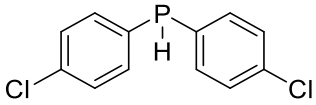	51	96	6.1 : 1
6[c]	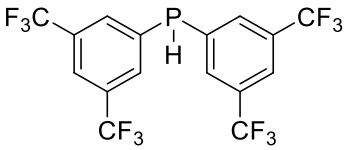	19	37	-[d]

[a] Conditions: IMe_4 (10 mol%), PhC≡CH (1 equiv.) and substituted diphenylphosphine (1.1 equiv.), THF (0.5 mL), 298 K, 18 hrs. [b] Based on phosphine consumption quantified by integration of inverse-gated $^{31}P\{^1H\}$ NMR spectra. [c] 1.5 hr reaction. [d] Only **5.6-Ph(*m*-*(CF$_3$)$_2$Ph*)** formed.

5.3.4 Stoichiometric Reactions between NHCs and Substrates

To probe how the NHC mediated catalysis, stoichiometric reactions between NHCs and substrates were carried out. Test reactions employed both IMe_4 and I^{t}Bu.

5.3.4.1 IMe_4 + PPh_2H

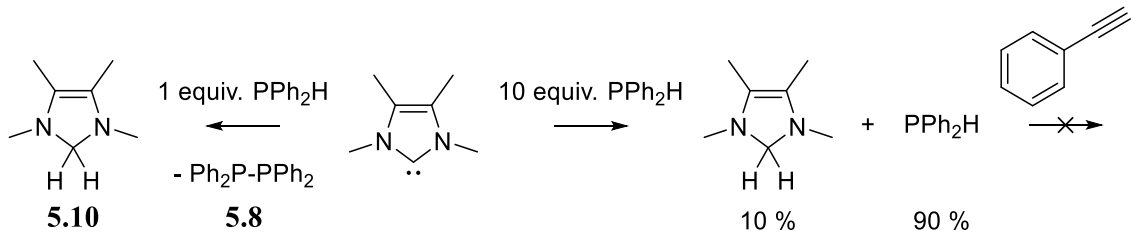

Scheme 5.5 Reactivity of IMe_4 with PPh_2H.

A 1:1 reaction between IMe_4 and PPh_2H showed the clean formation of dehydrocoupled product tetraphenylbiphosphine **5.8** and aminal product **5.10** (Scheme 5.5) after 72 hrs at room temperature. The latter was characterised by a signal in the ^1H NMR spectrum at δ 3.56 ppm for the animal CH_2 group,[35] along with an upfield shift of the wing tip and backbone methyl groups from δ 3.44 and 2.02 ppm in IMe_4 to δ 2.30 and 1.59 ppm respectively. The $^{13}C\{^1H\}$ NMR spectrum showed a resonance at δ 81.6 ppm for the CH_2 group, along with peaks at δ 124.0, 38.0 and 9.6 ppm for the carbons within the backbone, and the wing tip and backbone methyl groups.

Efforts to determine if IMe_4 could catalytically dehydrocouple PPh_2H to form **5.8** was examined with a 1:10 ratio reaction (Scheme 5.5), however only 10% of **5.8** was observed which corresponded to the full 10 mol% catalytic loading of IMe_4 converting to **5.10**. The formation of **5.10** was fast as within 10 min all of the IMe_4 was consumed. The aminal compound **5.10** was also catalytically inactive towards hydrophosphination; when alkyne substrate was added to the reaction, no products were formed.

5.3.4.2 IMe_4 + $PhC{\equiv}CH$

IMe_4 and PhC≡CH (1:10 ratio) appeared to demonstrate the oxidative addition of the terminal C-H bond across the carbenic carbon to form species **5.11**, with the appearance of a new resonance in the ^1H NMR spectrum at δ 3.76 ppm assigned to C_{IMe4}-H (Figure 5.3). Also, after 10 min at room temperature, the ^{13}C carbenic carbon signal of IMe_4 at δ 213.9 ppm was replaced by a new peak at δ 82.5 ppm to reflect the change in valency. Addition of PPh_2H to the reaction mixture led to the rapid formation of hydrophosphination products. This could mean either that **5.11** was an active catalyst for hydrophosphination, or that the formation of product **5.11** was reversible and IMe_4 was performing the catalysis. Efforts to isolate **5.11** were thwarted by decomposition of the

compound in solution within a few hrs. The reversibility of the formation of **5.11** was probed by the addition of excess PhC≡CD to convert all IMe_4 to the oxidative addition product (confirmed by disappeared free IMe_4 peaks at δ 3.44 and 2.02 ppm and emergence of new signals at δ 2.44 and 1.63 ppm for wing tip and backbone methyl groups respectively), before addition of PhC≡CH generated the diagnostic chemical shift at δ 3.76 ppm.

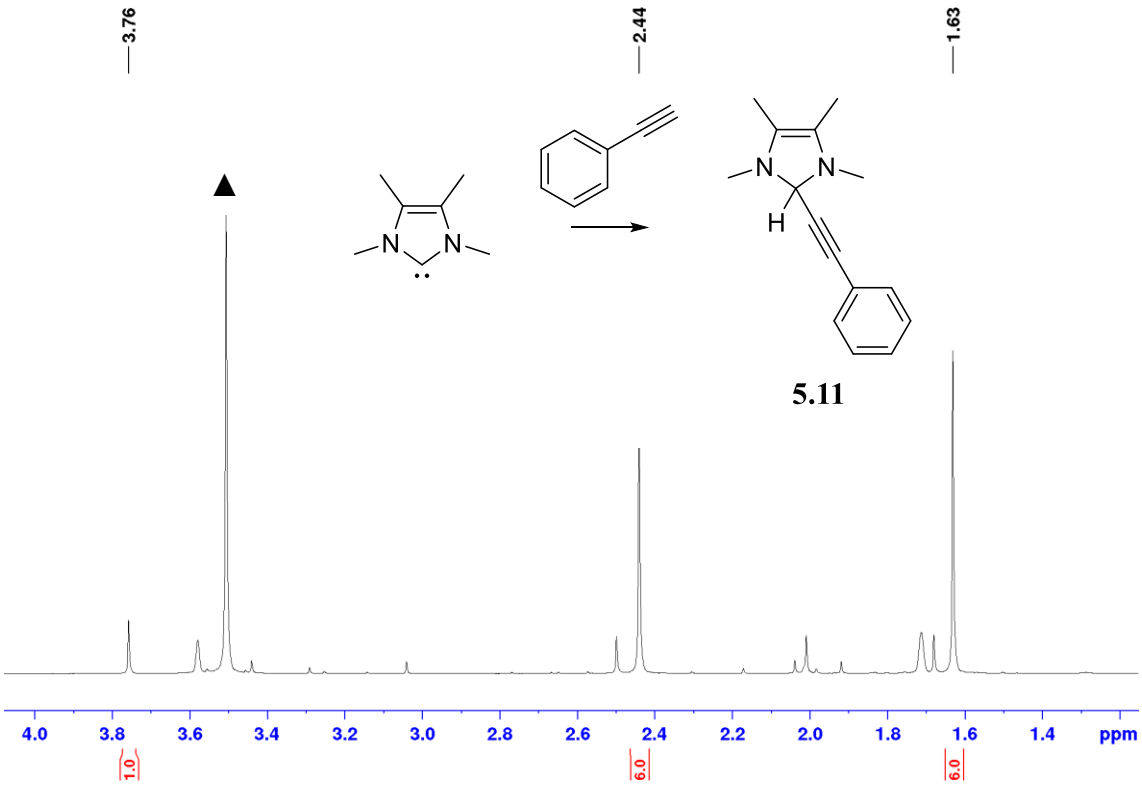

Figure 5.3 ^{1}H NMR spectrum (THF-d_8, 500 MHz, 298 K) of crude reaction mixture of IMe_4 and 10 equiv. of PhC≡CH to form **5.11** (▲ = PhC≡CH).

5.3.4.3 I^{t}Bu + PPh$_2$H

The reaction of a 1:10 molar ratio of I^{t}Bu and PPh_2H was much slower than in the case of IMe_4 as, after 24 hrs at room temperature, only 6% of **5.8** was formed (*cf.* 10% of **5.8** formed in 10 min for IMe_4 + PPh_2H). However, it still showed the presence of the dehydrocoupling process (to give **5.12**) rather than an addition of the P-H bond across the carbenic centre. Signals in the ^{1}H NMR spectrum (Figure 5.4) at δ 4.20 ppm corresponded to the new CH_2 group, and peaks at δ 5.44 and 1.06 ppm for the backbone protons and *tert*-butyl wing tips completed the assignment.[36]

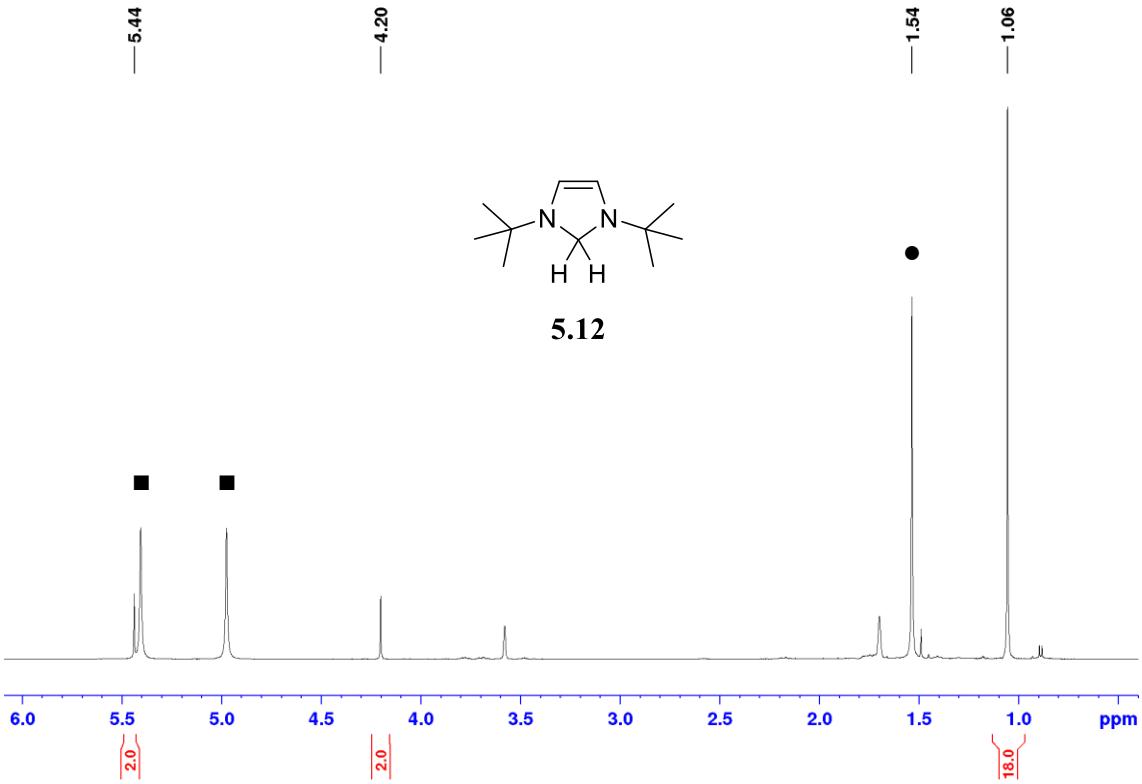

Figure 5.4 ^{1}H NMR spectrum (THF-d_8, 500 MHz, 298 K) of reaction between I^{t}Bu and 10 equiv. of PPh_2H to form **5.12** (■ = PPh_2H, ● = free I^{t}Bu).

5.3.4.4 I^{t}Bu + PhC≡CH

No reaction was observed between I^{t}Bu and 10 equiv. of PhC≡CH, most likely due to the steric clash between bulky *tert*-butyl groups and the alkyne. Subsequent addition of PPh_2H led to hydrophosphination catalysis with the same conversion and selectivity seen during the earlier screening process (Table 5.4), showing that while no oxidative addition process happened, no decomposition of the catalyst occurred either.

5.3.5 Determination of Electronic Properties of NHCs

The electronics of a ligand are described by the σ- and π-donation as well as π-accepting capabilities, which are inherently defined by the frontier orbitals of the ligands (HOMO and LUMO). The HOMO determines the electron-donor strength, with higher HOMO energy leading to stronger electron-donation. Conversely, the LUMO characterises the electron-accepting strength of a ligand, such that a lower energy LUMO will result in a better π-acceptor.

A recent review by Huynh[37] reveals that carbonyl based methods, Ni(0) based Tolman's electronic parameter (TEP)[38] and related Rh(I) and Ir(I) versions first developed by Lappert[39] and Crabtree[40] (Figure 5.5), show little differentiation in the electronics of the NHCs used in this study (Table 5.6). These methods use IR spectroscopy to measure the stretching frequency of CO bonds. A stronger donor would increase the electron density on the metal, leading to more backdonation to the anti-bonding π^* orbital of the CO, weakening the triple bond which would correspond to a lower stretching frequency. The IR spectroscopy based methods only detect the net donor strength of a ligand (the ligand itself can partake in electron-backdonation), and so are unable to distinguish between σ-donor and π-acceptor contributions.[37] The only notable results were 6Mes and 6MesDAC (Table 5.6, entries 8 and 9). The former has a wider N-C-N angle due to ring expansion, leading to a higher energy HOMO and thus greater electron-donating ability (lower wavenumber), whereas the latter contains two electron-withdrawing CO double bonds in the backbone making it particularly electron-poor.

Recent contributions to quantifying electronic properties have also come from using multinuclear spectroscopy. Huynh's electronic parameter (HEP) measures the ^{13}C shift of $^{i}Pr_2$-bimy in *trans*-[Pd(NHC)($^{i}Pr_2$-bimy)Br_2] compounds (Figure 5.5).[41, 42] The Lewis acidic metal centre negates backdonation to a ligand, so primarily displays the σ-donor ability of the NHC. A stronger σ-donor causes weakening of the Pd-$C_{iPr2\text{-}bimy}$ bond due to the *trans* influence. As the bond weakens the ^{13}C chemical shift moves more downfield because the $^{i}Pr_2$-bimy carbenic carbon lone pair is available to donate into the vacant p_π orbital, leading to deshielding of the carbenic carbon.[43] Table 5.6 shows that ICy (entry 5) has greater σ-donation compared to IMes and IPr (entries 6 and 7), which agrees with alkyl groups being more electron-donating than aryl. HEP has the limitation of underestimating the donating ability of very bulky N-substituents, where the increased steric bulk causes less efficient metal coordination, reducing the electronic contribution. This can be seen with the use of I^{t}Bu (entry 4), which one would expect to have a higher HEP value due to the electron-donating *tert*-butyl groups.

Other methods have used main group elements phosphorus and selenium to form adducts, phosphinidenes[44] and selenoureas[45] respectively, and use ^{31}P or ^{77}Se NMR spectroscopy to measure the chemical shift of the adduct (Figure 5.5). Bertrand proposed the use of NHC-phosphinidene adducts to evaluate the π-accepting properties of the NHC, based on the concept of backdonation from the phosphorus lone pair into the vacant carbene p_π orbital leads to a more deshielded phosphorus nucleus and a more downfield

chemical shift in the ^{31}P NMR spectrum.[44] IMes and IPr (Table 5.6, entries 6 and 7) have similar values due to their comparable structures (unsaturated backbone, aryl N-substituents). IMe_4 (entry 1) has a much more upfield chemical shift, due to the carbene having mainly σ-donation and very little π-accepting capabilities as the methyl groups provide no stabilisation of the LUMO. Conversely, 6MesDAC (entry 9) has a very downfield signal due to the electron-withdrawing carbonyl backbone stabilising and lowering the energy of the LUMO.

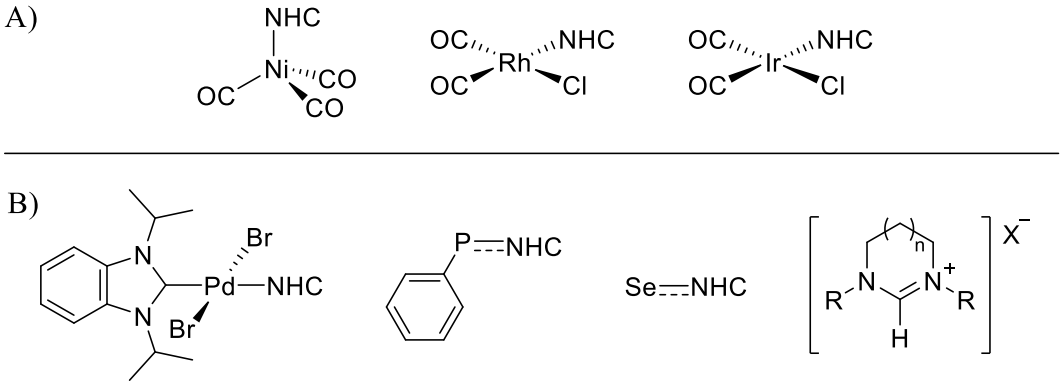

Figure 5.5 Structures of compounds used for A) carbonyl based measurements of electronic properties; $Ni(CO)_3(NHC)$ used for TEP (left), *cis*-$[Rh(NHC)(CO)_2Cl]$ (centre), *cis*-$[Ir(NHC)(CO)_2Cl]$ (right), and B) multinuclear NMR spectroscopy based measurements of electronic properties; *trans*-$[Pd(NHC)(^{i}Pr_2\text{-bimy})Br_2]$ used for HEP (far left), phosphinidene adduct (left), selenourea adduct (right), and protonated carbene salt (far right).[37]

A less challenging synthetic route was proposed by Ganter,[45] where deprotonation of carbene salts in presence of elemental selenium led to the formation of selenoureas (Figure 5.5). The same concept as Bertrand's work applies, where stronger π-acceptors cause deshielding of the selenium nucleus, inducing a downfield shift of the adduct product peak in the ^{77}Se NMR spectrum. Table 5.6 shows that 6MesDAC (entry 9) exhibits the same extreme downfield chemical shift seen for ^{31}P NMR. 6Mes (entry 8) also shows relatively high π-accepting capabilities, because ring-expanded NHCs have a narrower HOMO-LUMO gap which makes them both better σ-donors and π-acceptors. IMes and IPr (entries 6 and 7) show more mild downfield shifts, and ICy (entry 5) has the most upfield chemical shift of the NHCs selected. $I^{t}Bu$ (entry 4) displays a downfield chemical shift that suggests excellent π-accepting abilities, quite unlike ICy, IMe_4 or

I^{i}Pr$_2$Me$_2$. This has been suggested to be due to an increase in steric bulk compared to the other N-alkyl NHCs, however this would lead to less efficient coordination to the selenium, so poorer orbital overlap and lower probability of backdonation. Another reason could be due to the expectation of a tertiary alkyl substituted NHC being such a strong σ-donor, leading to a subsequent increase of π-backbonding, however this is also unsatisfactory as this effect should also be seen for ICy or I^{i}Pr$_2$Me$_2$, albeit milder.

A further method proposed by Ganter and Nolan uses ^{1}H NMR spectroscopy to measure the $^1J_{CH}$ coupling constant of the salts, which are often used as precursors in NHC synthesis (Figure 5.5).[46, 47] The size of the coupling constant between the iminium carbon and attached proton can reveal the σ-donating ability of the NHC. This is based on the hybridisation of the carbon atom, and a correlation between *J* value and the fraction of *s* character within that hybridised orbital (given as $^1J_{CH} = 500 \cdot s$).[43, 46-49] As the *s* character in the orbital increases (0.25 in sp^3 to 0.5 in *sp*), the orbital becomes a poorer σ-donor. The relationship between *J* and *s* means that as *s* increases, so will the value of *J*. Larger *J* values will then correspond to poorer σ-donation from the NHCs. Table 5.6 shows that [6MesH]$^+$ (entry 8) has the lowest $^1J_{CH}$ coupling constant and is the strongest σ-donor, in agreement with all of the previous evidence. [IMesH]$^+$ and [IPrH]$^+$ (entries 6 and 7) displayed milder σ-donor capabilities, while [ICyH]$^+$ and [I^{t}BuH]$^+$ have slightly lower *J* values, reflecting the increase in donor strength expected for N-alkyl substituted NHCs (albeit the first time this had been seen for I^{t}Bu, due to steric/chemical incompatibilities in the other methods).

In conclusion, a new exciting catalytic transformation using only NHCs was shown, though no satisfactory connection between electronic properties and catalytic activity could be found. Along with the earlier finding of no strict relationship between NHC sterics and catalysis (section 5.3.2), the two effects must combine to contribute to the observed reactivity.

Table 5.6 TEP, averaged CO stretch wavenumbers, HEP, ^{31}P NMR, ^{77}Se NMR and $^{1}J_{CH}$ coupling constant values for selected NHC compounds.[37]

Entry	NHC	TEP (cm^{-1})	Rh(I) (cm^{-1})	Ir(I) (cm^{-1})	HEP (ppm)	Phosphinidene adduct (ppm)	Selenourea adduct acetone/chloroform (ppm)		$^{1}J_{CH}$ coupling in [NHC·H]X (Hz)
1	IMe_4	-	-	-	-	-53.5	3	-	-
2	IEt_2Me_2	-	-	-	-	-	-	-	-
3	$I^iPr_2Me_2$	-	2036	-	-	-	-	18	-
4	I^tBu	-	2036	2023	177.6	-	197	183	219.2
5	ICy	2050	-	2023	181.2	-	-4	-22	220.2
6	IMes	2051	2039	2023	177.2	-23.0	35	27	225.2
7	IPr	2052	2038	2024	177.5	-18.9	87	90	223.7
8	6Mes	-	2029	-	-	-	271	-	199.8
9	6MesDAC	-	2046	2031	-	83.0	847	-	-

5.3.6 DFT Calculations

DFT calculations on the I^{t}Bu/PPh$_2$H/PhC≡CH system were undertaken by Prof. Stuart Macgregor and Sam Neale from Heriot-Watt University, to try and probe the mechanism of NHC catalysed hydrophosphination. Figure 5.6 displays the initial formation of the carbene-phosphine adduct **I** at +6.0 kcal/mol, from which deprotonation of PPh$_2$H by the NHC occurs through **TS(I-II)** at +18.1 kcal/mol. This forms an ion-pair, [I^{t}BuH][PPh$_2$] **II** at +4.9 kcal/mol, which can access P-C bond formation *via* **TS(II-III)** at +17.9 kcal/mol to give **III**, the product of carbene insertion into the P-H bond (or addition of the P-H bond across the carbene), at +9.1 kcal/mol. No direct pathway for this transformation could be computed and, at least for this combination of substrates, the insertion product **III** is thermodynamically less favoured than the ion-pair **II**. Both the ion-pair **II** and insertion product **III** are thermodynamically uphill from free I^{t}Bu and PPh$_2$H, consistent with their non-observation experimentally (section 5.3.4.3). However, the computational work showed that they are kinetically accessible.

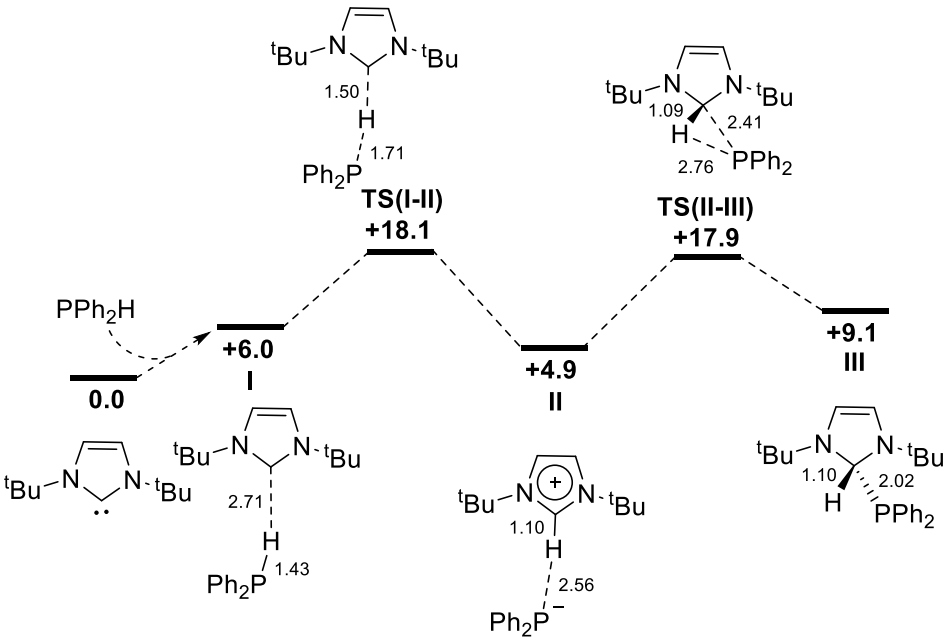

Figure 5.6 Computed free energy reaction profile for P-H activation of PPh$_2$H with I^{t}Bu (kcal/mol, computed at the M052X-D3(THF)/def2-TZVP//TPSS(THF)DZP level). Selected distances are shown in Å.

The computed pathways for the reaction with PhC≡CH to form the *Z*- and *E*-anti-Markovnikov products **5.6-Ph** and **5.7-Ph** are shown in Figure 5.7. Initial nucleophilic attack of the $[PPh_2]^-$ in ion-pair **II** at the terminal end of the alkyne occurs *via* **TS(II-IV)** at +23.2 kcal/mol, as shown in both Figure 5.7 and Figure 5.8. The attack at the *β*-carbon (adjacent to the phenyl ring) and formation of the Markovnikov product involves a much less accessible transition state at +29.4 kcal/mol. The phosphide attack forms a new ion-pair, **IV** at +9.3 kcal/mol, comprising of a *Z*-alkenyl anion and $[I^tBuH]^+$. Formation of **5.6-Ph** then requires movement of the imidazolium to position the I^tBu-H bond adjacent to the alkenyl anion lone pair; this is most simply modelled by dissociation to a THF solvent-separated ion-pair at +15.7 kcal/mol which then recombines to make **Va** at +4.6 kcal/mol. Proton transfer within **Va** readily occurs to form **5.6-Ph** and free I^tBu at -25.5 kcal/mol. Alternatively, isomerisation of **IV** can occur *via* an allenyl transition state structure **TS(IV-Vb)** at +15.3 kcal/mol as shown in Figure 5.8. This would generate the ion-pair **Vb** at +5.2 kcal/mol, with proton transfer to form the *E*- isomer **5.7-Ph** and free I^tBu at -28.1 kcal/mol. Efforts to characterise an alternative pathway involving nucleophilic attack of the phosphorus lone pair in the neutral carbene insertion species **III** were unsuccessful, with all computed structures reverting to the ion-pair **II**. The computed profiles show hydrophosphination to be strongly exergonic (ΔG = 25.5 and 28.1 kcal/mol for **5.6-Ph** and **5.7-Ph** respectively) and have a reasonable overall barrier of 23.2 kcal/mol in which phosphide nucleophilic attack is rate-limiting.

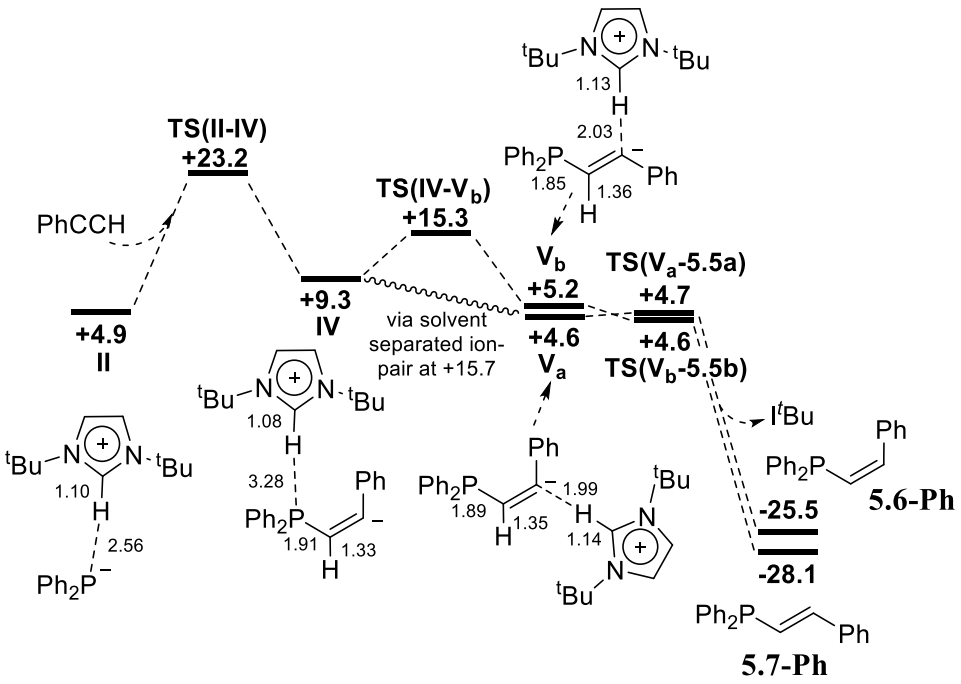

Figure 5.7 Computed free energy reaction profiles for formation of *Z*- and *E*-anti-Markovnikov products (**5.6-Ph** and **5.7-Ph**) *via* reaction of ion-pair **II** with PhC≡CH (kcal/mol, computed at the M052X-D3(THF)/def2-TZVP//TPSS(THF)DZP level). Selected distances are shown in Å.

The geometry of **TS(II-IV)** (Figure 5.8) shows developing sp^2 character at both alkyne carbons, and during this process (and ultimately in intermediate **IV**) a formal negative charge developing on that *β*-carbon can be stabilised *via* delocalisation around the adjacent phenyl ring. This accounts for the lack of hydrophosphination seen with 1-hexyne (Table 5.4, entry 6), and the transition state computed using 1-propyne as a model aliphatic alkyne is much higher in energy at +31.5 kcal/mol. With the internal alkyne PhC≡CMe (Table 5.4, entry 8), an overall barrier of 29.0 kcal/mol was computed, consistent with the much lower activity of this substrate compared to PhC≡CH and presumably reflecting the greater steric bulk associated with attack at an internal alkyne carbon. Based on these computed profiles, the **5.6-R**:**5.7-R** ratio of the hydrophosphination products will be determined by the rates of the different rearrangements of intermediate **IV**. While formation of **Vb** is well defined *via* the allenyl species **TS(IV-Vb)** at +15.3 kcal/mol (Figure 5.8), it is less straightforward to assess the generation of **Va**. It was earlier described to proceed *via* a THF solvent-separated ion-pair at +15.7 kcal/mol, but other possibilities can be considered, including rearrangement within the ion-pair, or addition of a second, external $[I^tBuH]^+$ directly to the alkenyl

carbon. As such, 15.7 kcal/mol should be considered as an upper limit for this rearrangement barrier. The two routes leading to **5.6-Ph** and **5.7-Ph** are therefore likely to be competitive, and indeed experimentally both isomers are observed in most substrates (Scheme 5.3).

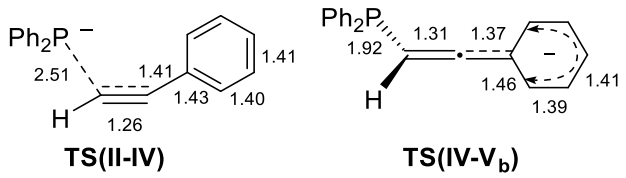

TS(II-IV) **TS(IV-V$_b$)**

Figure 5.8 Computed geometries for key transition states **TS(II-IV)** and **TS(IV-Vb)**. Selected distances are shown in Å and spectator imidazolium cations have been omitted for clarity.

Recomputing these rearrangements with *p*-F and *p*-MeO substituted phenylacetylenes show that the solvent-separated ion-pair becomes more accessible than the isomerisation *via* **TS(IV-Vb)**. For *p*-F-PhC≡CH the ion-pair is 1.1 kcal/mol more stable (ion-pair at +15.3 kcal/mol; isomerisation at +16.4 kcal/mol), while for *p*-MeO-PhC≡CH the difference increases to 2.0 kcal/mol (ion-pair at +19.2 kcal/mol; isomerisation at +21.2 kcal/mol).[50] Formation of **Va** (and hence the *Z*- isomer) therefore becomes more favoured with these substituted alkynes, reflecting the higher **5.6-R**:**5.7-R** ratios observed experimentally (Table 5.4). Natural bond orbital (NBO) charge calculations on **TS(IV-Vb)** indicate an increase in negative charge in the aryl substituent that appears to be poorly accommodated by *+M* substituents. In contrast, *+I* substituents would be expected to facilitate isomerisation and lead to lower **5.6-R**:**5.7-R** ratios. This was confirmed with calculations on *p*-CF_3-PhC≡CH for which the isomerisation transition state was computed to lie 5.1 kcal/mol below the solvent-separated ion-pair indicating the *E*- isomer should be preferred.[50] Efforts to model these pathways for *ortho*-2-pyridyl-substituted phenylacetylene (for which the *E*- isomer is also strongly favoured; Table 5.4, entry 5) were complicated by the presence of H-bonding to the free pyridyl nitrogen. This was subsequently shown experimentally with the I^{t}Bu catalysed hydrophosphination of *p*-CF_3-PhC≡CH giving exclusively the *E*- isomer (Table 5.4, entry 4).

Hydrophosphination with the simple dialkylphosphine dimethylphosphine (PMe_2H) with PhC≡CH was also modelled. As with PPh_2H, insertion of I^{t}Bu into the P-

H bond involves a two-step process *via* an ion-pair (*cf*. Figure 5.6). However, in this case the carbene insertion product (**III$_{Me}$** at +7.0 kcal/mol) was now significantly more stable than the preceding ion-pair (**II$_{Me}$** at +22.2 kcal/mol). Onward reaction of **II$_{Me}$** with PhC≡CH entailed a high energy transition state at +35.1 kcal/mol. This reflects the lack of reactivity observed experimentally when using 10 mol% I^{t}Bu with di-*tert*-butylphosphine (P^{t}Bu$_2$H) and PhC≡CH (Appendix 8), and correlates with the much higher *p*K$_a$ of dialkyl- versus diarylphosphines.[51]

The catalytic hydrophosphination has similarities to NHC catalysed conjugate addition reactions in which the NHC acts as a general base to activate alcohols, amines, and ketones.[52-54] While examples of base catalysed hydrophosphination have previously been shown, these typically use more explicit bases such as KO^{t}Bu or KN(SiMe$_3$)$_2$.[55-60]

5.3.7 Use of CAACs as Catalysts for Alkene and Alkyne Hydrophosphination

A small range of CAACs (Figure 5.9) were kindly donated by the Bertrand group to see if changing the *σ*-donating and *π*-accepting capabilities of the catalyst impact on the hydrophosphination catalysis or whether unwanted reactivity with the substrates prevails. The same experimental methods as mentioned in section 5.3.5 reflect the changes in electronic characteristics compared to NHCs. For example, the TEP value of ^{Menthyl}CAAC was recorded at 2042 cm^{-1} (*cf*. ICy at 2050 cm^{-1}), while the Ir(I)-carbonyl data showed a value of 2013 cm^{-1} (*cf*. I^{t}Bu at 2023 cm^{-1}).[37] The significantly lower frequencies are indicative of greater *σ*-donation (greater backbonding into CO *π** orbital, weakening the carbonyl bond). The *π*-accepting abilities are also borne out by the phosphinidene and selenourea adduct data. The phosphinidene adduct formed with ^{Menthyl}CAAC had a ^{31}P NMR chemical shift at δ 56.2 ppm (*cf*. the most *π*-accepting NHC – 6MesDAC at δ 83.0 ppm),[37] while the ^{77}Se NMR signal for the selenourea adduct of ^{Et2}CAAC was recorded at δ 482 ppm (in acetone; *cf*. 6MesDAC δ at 847 ppm).[61] The positive values for both ^{31}P and ^{77}Se NMR show increased deshielding of the NMR active nuclei due to greater backdonation from the adduct into the empty p_π orbital of the CAAC.

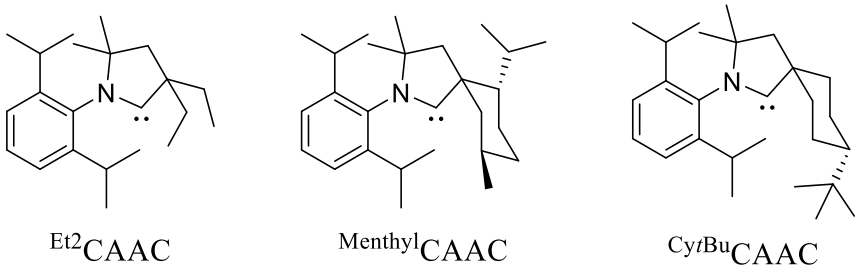

Figure 5.9 Structures and abbreviations of the CAACs screened.

The results of the hydrophosphination of PhC≡CH with PPh_2H using 10 mol% of the three CAACs as catalysts are displayed in Table 5.7. The diethyl substituted CAAC (entry 1) displayed no catalysis, rather only a side reaction between the CAAC and phosphine. A known transformation between the dimethyl substituted CAAC and PPh_2H gave the oxidative addition of the P-H bond across the carbenic centre (Scheme 1.8),[62] and the NMR spectra for entry 1 appear to result from an analogous species. A 1:1 reaction between ^{Et2}CAAC and PPh_2H showed rapid formation of a diagnostic doublet in the ^{1}H NMR spectrum at δ 4.88 ppm ($^2J_{HP}$ = 4.5 Hz) and another doublet in the $^{13}C\{^1H\}$ NMR spectrum at δ 74.2 ppm ($^1J_{CP}$ = 8.4 Hz) corresponding to the oxidative addition product (compound **5.13**, data in section 7.12.1.4). The presence of bulkier menthyl and *tert*-butylcyclohexyl substituents (entries 2 and 3) led to hydrophosphination rather than oxidative addition, affording full conversion of the phosphine within 1 hr and good selectivity for the *Z*- isomer **5.6-Ph** as seen for the NHCs (Table 5.3). Further studies with a wider range of CAACs are currently ongoing.

Table 5.7 CAAC catalysed hydrophosphination of PhC≡CH with PPh_2H.[a]

Entry	Catalyst	Conversion (%)[b]	5.6-Ph/5.7-Ph products as (%) of all products	5.6-Ph:5.7-Ph ratio
1	^{Et2}CAAC	6	0	-[c]
2[d]	^{Menthyl}CAAC	100	93	2.3 : 1
3[d]	^{CytBu}CAAC	100	93	2.4 : 1

[a] Conditions: Catalyst (0.04 mmol), PhC≡CH (0.40 mmol) and PPh_2H (0.44 mmol), THF (0.5 mL), 298 K, 18 hrs. [b] Based on phosphine consumption quantified by integration of inverse-gated $^{31}P\{^1H\}$ NMR spectra. [c] Only P-H oxidative addition product formed. [d] 1 hr reaction.

Though no CAAC catalysed hydrophosphination of other alkynes was investigated, a small alkene screen (as with IMe_4) was performed with ^{Menthyl}CAAC (Table 5.8). Styrene (entry 1) showed transformation to the anti-Markovnikov hydrophosphination product $PhCH_2CH_2PPh_2$ within 1 hr at room temperature. The challenging aliphatic alkenes 3,3-dimethyl-1-butene and 1-hexene (entries 2 and 3) gave no hydrophosphination products, but rather a side reaction between the CAAC and phosphine, analogous to the oxidative addition of the P-H bond seen with ^{Et2}CAAC. As with the catalyst screening, further investigations into substrate scope and stoichiometric reactivity are ongoing.

Table 5.8 ^{Menthyl}CAAC catalysed hydrophosphination of alkenes with PPh_2H.[a]

Entry	Alkene	Conversion to $PhCH_2CH_2PPh_2$ (%)[b]	Hydrophosphination product (%) of all products
1	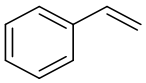	100	92
2[c]	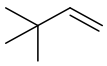	7	0[d]
3[c]	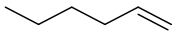	7	0[d]

[a] Conditions: ^{Menthyl}CAAC (0.04 mmol), alkene (0.40 mmol) and PPh_2H (0.44 mmol), THF (0.5 mL), 298 K, 2 hrs. [b] Based on phosphine consumption quantified by integration of inverse-gated $^{31}P\{^1H\}$ NMR spectra. [c] 24 hr reaction. [d] Only P-H oxidative addition product formed.

The activity of bulky CAACs towards hydrophosphination was much improved compared to NHCs (full conversion of PPh_2H within 1 hr, compared to 24 hrs when using I^{t}Bu). This led to efforts to push the catalysis towards the double hydrophosphination product **5.5-Ph** seen for transition metal catalysts (Scheme 5.2). A 10 mol% loading of ^{Menthyl}CAAC with PhC≡CH and 2 equiv. of PPh_2H gave the formation of **5.6-Ph** and **5.7-Ph**, the desired double addition product **5.5-Ph**, dehydrocoupled product **5.8**, and the Markovnikov internal addition product **5.9-Ph** (Scheme 5.6). The catalysis required a longer time scale, with the double addition product becoming the major species after 44 hrs at room temperature.

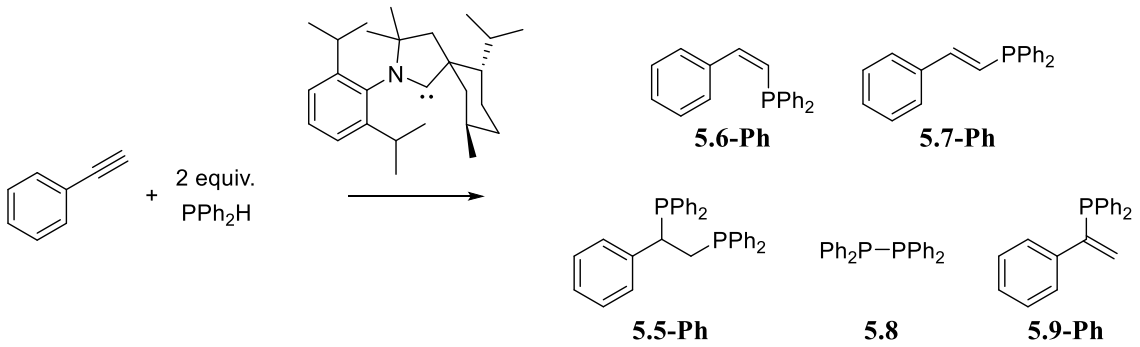

Scheme 5.6 ^{Menthyl}CAAC catalysed hydrophosphination of PhC≡CH with PPh_2H.

5.4 Summary

In conclusion, during studies of hydrophosphination catalysed by Ni-NHC compounds, blank experiments showed that N-alkyl substituted NHCs could themselves perform catalysis in the absence of any nickel with excellent conversions. A range of alkyne and phosphine substrates was screened, showing that the impact of differing electronics helped or hindered the catalysis. Stoichiometric reactions between NHCs and PPh_2H showed the formation of the catalytically inactive aminal products **5.10** and **5.12**, while the reaction with PhC≡CH formed the short-lived acetylide hydride adduct **5.11**.

DFT calculations produced support for a mechanism in which initial P-H activation proceeded *via* deprotonation, *i.e.*, with the NHC acting as a Brønsted base. The onward reaction with PhC≡CH involved the rate-limiting nucleophilic attack of the resulting ion-pair phosphide anion at the more accessible terminal alkyne carbon, with the regioselectivity being determined by the rearrangement of the resultant alkenyl anion. The mechanism accounts for the scope of the reaction which favours relatively acidic aryl phosphines, as well as aryl-substituted alkynes in which charge delocalisation around the aryl ring provides additional stabilisation of the alkenyl anion intermediate. The computational work also shows that the catalytic alkyne hydrophosphination does not rely on E-H bond oxidative addition of the type often targeted in main group catalysis.[63-66]

The use of CAACs as catalysts for hydrophosphination revealed that due to the increased σ-donor and π-acceptor capabilities, there was a competing P-H bond oxidative addition process occurring. As a result, in the case of smaller CAACs, no catalysis was seen. Bulkier CAACs showed more preference for the catalytic pathway and some formation of the double hydrophosphination product **5.5-Ph**, though they displayed

limited activity during substrate screening. The fact that CAACs show differing reactivity depending on the alkyl substituents has led to further experimental and computational investigations, which are ongoing.[67]

5.5 References

1. S. Sabater, M. J. Page, M. F. Mahon and M. K. Whittlesey, *Organometallics*, 2017, **36**, 1776-1783.
2. H. Schäfer, *Z. Anorg. Allg. Chem*, 1979, **459**, 157-169.
3. H. Schäfer and D. Binder, *Z. Anorg. Allg. Chem*, 1987, **546**, 55-78.
4. R. Melenkivitz, D. J. Mindiola and G. L. Hillhouse, *J. Am. Chem. Soc.*, 2002, **124**, 3846-3847.
5. Y. S. Ganushevich, V. A. Miluykov, F. M. Polyancev, S. K. Latypov, P. Lonnecke, E. Hey-Hawkins, D. G. Yakhvarov and O. G. Sinyashin, *Organometallics*, 2013, **32**, 3914-3919.
6. J. A. Kessler and V. M. Iluc, *Dalton Trans.*, 2017, **46**, 12125-12131.
7. T. Schaub and U. Radius, *Chem. Eur. J.*, 2005, **11**, 5024-5030.
8. F. Alonso, I. P. Beletskaya and M. Yus, *Chem. Rev.*, 2004, **104**, 3079-3159.
9. D. Zhao and R. Wang, *Chem. Soc. Rev.*, 2012, **41**, 2095-2108.
10. L. Rosenberg, *ACS Catal.*, 2013, **3**, 2845-2855.
11. V. Koshti, S. Gaikwad and S. H. Chikkali, *Coord. Chem. Rev.*, 2014, **265**, 52-73.
12. K. J. Gallagher and R. L. Webster, *Chem. Commun.*, 2014, **50**, 12109-12111.
13. J. Rajpurohit, P. Kumar, P. Shukla, M. Shanmugam and M. Shanmugam, *Organometallics*, 2018, **37**, 2297-2304.
14. M. A. Kazankova, I. V. Efimova, A. N. Kochetkov, V. V. Afanas'ev, I. P. Beletskaya and P. H. Dixneuf, *Synlett*, 2001, **4**, 497-500.
15. A. D. Sadow, I. Haller, L. Fadini and A. Togni, *J. Am. Chem. Soc.*, 2004, **126**, 14704-14705.
16. M. B. Ghebreab, C. A. Bange and R. Waterman, *J. Am. Chem. Soc.*, 2014, **136**, 9240-9243.
17. F. Jerome, F. Monnier, H. Lawicka, S. Derien and P. H. Dixneuf, *Chem. Commun.*, 2003, 696-697.
18. A. Di Giuseppe, R. De Luca, R. Castarlenas, J. J. Perez-Torrente, M. Crucianelli and L. A. Oro, *Chem. Commun.*, 2016, **52**, 5554-5557.
19. K. Takaki, G. Koshoji, K. Komeyama, M. Takeda, T. Shishido, A. Kitani and K. Takehira, *J. Org. Chem.*, 2003, **68**, 6554-6565.
20. A. M. Kawaoka and T. J. Marks, *J. Am. Chem. Soc.*, 2005, **127**, 6311-6324.

21. W. J. M. Blackaby, S. E. Neale, C. J. Isaac, S. Sabater, S. A. Macgregor and M. K. Whittlesey, *ChemCatChem*, 2019, **11**, 1893-1897.
22. E. Lindner, M. Schmid, P. Wegner, C. Nachtigal, M. Steimann and R. Fawzi, *Inorg. Chim. Acta*, 1999, **296**, 103-113.
23. M. V. Jimenez, J. J. Perez-Torrente, M. I. Bartolome and L. A. Oro, *Synthesis*, 2009, **11**, 1916-1922.
24. A. Tzschach and S. Baensch, *J. Prakt. Chem.*, 1971, **313**, 254-258.
25. A. Sato, H. Yorimitsu and K. Oshima, *Angew. Chem. Int. Ed.*, 2005, **44**, 1694-1696.
26. S. Kawaguchi, S. Nagata, T. Shirai, K. Tsuchii, A. Nomoto and A. Ogawa, *Tetrahedron Lett.*, 2006, **47**, 3919-3922.
27. A. C. Hillier, W. J. Sommer, B. S. Yong, J. L. Petersen, L. Cavallo and S. P. Nolan, *Organometallics*, 2003, **22**, 4322-4326.
28. A. Poater, B. Cosenza, A. Correa, S. Giudice, F. Ragone, V. Scarano and L. Cavallo, *Eur. J. Inorg. Chem.*, 2009, 1759-1766.
29. H. Clavier and S. P. Nolan, *Chem. Commun.*, 2010, **46**, 841-861.
30. A. Gómez-Suárez, D. J. Nelson and S. P. Nolan, *Chem. Commun.*, 2017, **53**, 2650-2660.
31. J. J. Dunsford, K. J. Cavell and B. M. Kariuki, *Organometallics*, 2012, **31**, 4118-4121.
32. L. R. Collins, T. M. Rookes, M. F. Mahon, I. M. Riddlestone and M. K. Whittlesey, *Organometallics*, 2014, **33**, 5882-5887.
33. C. B. Provis-Evans, E. A. C. Emanuelsson and R. L. Webster, *Adv. Synth. Catal.*, 2018, **360**, 3999-4004.
34. T. Schaub, U. Radius, A. Brucks, M. P. Choules, M. T. Olsen and T. B. Rauchfuss, *Inorg. Synth.*, 2010, **35**, 78-83.
35. D. Franz and S. Inoue, *Chem. Asian J.*, 2014, **9**, 2083-2087.
36. A. Jana, C. Schulzke and H. W. Roesky, *J. Am. Chem. Soc.*, 2009, **131**, 4600-4601.
37. H. V. Huynh, *Chem. Rev.*, 2018, **118**, 9457-9492.
38. C. A. Tolman, *J. Am. Chem. Soc.*, 1970, **92**, 2953-2956.
39. M. J. Doyle, M. F. Lappert, P. L. Pye and P. Terreros, *J. Chem. Soc., Dalton Trans.*, 1984, 2355-2364.

40. A. R. Chianese, X. Li, M. C. Janzen, J. W. Faller and R. H. Crabtree, *Organometallics*, 2003, **22**, 1663-1667.
41. H. V. Huynh, Y. Han, R. Jothibasu and J. A. Yang, *Organometallics*, 2009, **28**, 5395-5404.
42. Q. Teng and H. V. Huynh, *Dalton Trans.*, 2017, **46**, 614-627.
43. D. Tapu, D. A. Dixon and C. Roe, *Chem. Rev.*, 2009, **109**, 3385-3407.
44. O. Back, M. Henry-Ellinger, C. D. Martin, D. Martin and G. Bertrand, *Angew. Chem. Int. Ed.*, 2013, **52**, 2939-2943.
45. A. Liske, K. Verlinden, H. Buhl, K. Schaper and C. Ganter, *Organometallics*, 2013, **32**, 5269-5272.
46. K. Verlinden, H. Buhl, W. Frank and C. Ganter, *Eur. J. Inorg. Chem.*, 2015, 2416-2425.
47. G. Meng, L. Kakalis, S. P. Nolan and M. Szostak, *Tetrahedron Lett.*, 2019, **60**, 378-381.
48. H. A. Bent, *Chem. Rev.*, 1961, **61**, 275-311.
49. H. Günther, *NMR Spectroscopy: Basic Principles, Concepts and Applications in Chemistry*, Wiley, Weinheim, 3rd edn., 2013.
50. See Supporting Information in reference 21.
51. J. Li, L. Liu, Y. Fu and Q. Guo, *Tetrahedron*, 2006, **62**, 4453-4462.
52. S. J. Ryan, L. Candish and D. W. Lupton, *Chem. Soc. Rev.*, 2013, **42**, 4906-4917.
53. D. M. Flanigan, F. Romanov-Michailidis, N. A. White and T. Rovis, *Chem. Rev.*, 2015, **115**, 9307-9387.
54. N. Wang, J. Xu and J. K. Lee, *Org. Biomol. Chem.*, 2018, **16**, 8230-8244.
55. J. L. Bookham and D. M. Smithies, *J. Organomet. Chem.*, 1999, **577**, 305-315.
56. T. Bunlaksananusorn and P. Knochel, *Tetrahedron Lett.*, 2002, **43**, 5817-5819.
57. O. Delacroix and A. C. Gaumont, *Curr. Org. Chem.*, 2005, **9**, 1851-1882.
58. A. Perrier, V. Comte, C. Moïse, P. Richard and P. Le Gendre, *Eur. J. Org. Chem.*, 2010, 1562-1568.
59. N. T. Coles, M. F. Mahon and R. L. Webster, *Chem. Commun.*, 2018, **54**, 10443-10446.
60. S. N. Arbuzova, N. K. Gusarova and B. A. Trofimov, *Arkivoc*, 2006, 12-36.
61. E. Tomás-Mendivil, M. M. Hansmann, C. M. Weinstein, R. Jazzar, M. Melaimi and G. Bertrand, *J. Am. Chem. Soc.*, 2017, **139**, 7753-7756.

62. G. D. Frey, J. D. Masuda, B. Donnadieu and G. Bertrand, *Angew. Chem. Int. Ed.*, 2010, **49**, 9444-9447.
63. P. P. Power, *Nature*, 2010, **463**, 171.
64. K. Revunova and G. I. Nikonov, *Dalton Trans.*, 2015, **44**, 840-866.
65. C. Weetman and S. Inoue, *ChemCatChem*, 2018, **10**, 4213-4228.
66. T. Chu and G. I. Nikonov, *Chem. Rev.*, 2018, **118**, 3608-3680.
67. D. R. Tolentino, S. E. Neale, C. J. Isaac, S. A. Macgregor, M. K. Whittlesey, R. Jazzar and G. Bertrand, *J. Am. Chem. Soc.*, 2019, **141**, 9823-9826.

CHAPTER 6

6 FUTURE WORK

Based on the observation that $[Ni(RE\text{-}NHC)(PCy_3)]^+$ species **4.12** – **4.14** gave EPR spectra that were suggestive of the three-coordinate THF-bound analogue, and the spectrum of $[Ni(7Xyl)(P^tBu_3)]^+$ (**4.16**) displayed a mixture of two- and three-coordinate complexes, increasing the steric bulk of the ligands could prevent the coordination of solvent entirely and allow the collection of spectra of purely two-coordinate species. First would be to form the P^tBu_3 derivate using $[Ni(7Mes)(PCy_3)]^+$, which features bulkier N-mesityl substituents. The bulk could be further increased by introducing diisopropylphenyl (DIPP) groups, which would involve synthesising the three-coordinate precursor compound. An alternative route could be to try collecting EPR data in the other solvents which are less likely to coordinate to the metal centre, *i.e.*, 2-MeTHF or Et_2O would be good initial candidates.

The introduction of a second Ni(I) ion to the *bis*-NHC system with the aim of inducing exchange coupling between the metal centres could lead to some interesting magnetic properties and behaviour. Using a ditopic NHC ligand, for example the quinone based species reported by Bielawski *et al.* (Figure 6.1) would maintain the framework of two NHCs coordinated to each Ni(I) centre, while also involving a π-system that could allow the unpaired electrons to "communicate" with each other.[1]

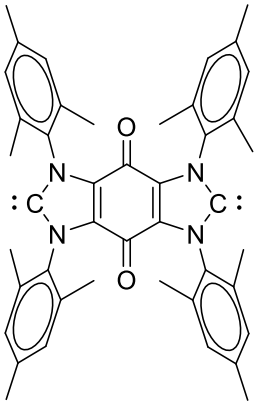

Figure 6.1 Example of a ditopic NHC ligand.

Replacement of the RE-NHCs in any of the two- or three-coordinate Ni(I) species with other carbene ligands such as CAACs, ring-expanded CAACS (RE-CAACs), or bicyclic CAACs (BiCAACs) (Figure 6.2) could be of interest, to determine if similar electronic structures and magnetic anisotropy would be present in such Ni(I) species. A

small range of mono- and *bis*-CAAC nickel complexes have been reported, however, all examples are either Ni(0) or Ni(II).[2-10] As shown in Chapter 1, Roesky *et al*. made two- and three-coordinate Fe(I) compounds Fe(^{Me2}CAAC)$_2$Cl **xiii** and [Fe(^{Me2}CAAC)$_2$]B(C_6F_5)$_4$ **xliv** which exhibited slow magnetic relaxation.[11] The report also presents the EPR spectrum of **xiii** with an axial *g* profile, whereas the spectrum of the two-coordinate derivate **xliv** had significantly less axiality. The authors issued a warning that the bonding of the CAAC to the metal centre in the two-coordinate species was causing a reduction in axiality, and hence impacted on the magnetic properties. Our *bis*-NHC Ni(I) species also display highly axial EPR spectrum, and so it would be interesting to see if a similar effect would be present in such a nickel *bis*-CAAC example.

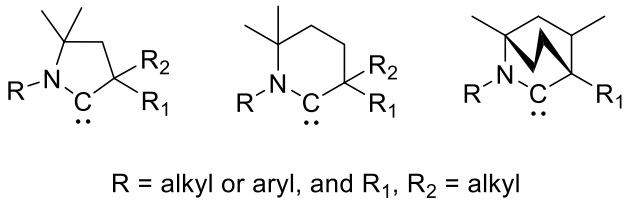

Figure 6.2 Structures of CAACs, RE-CAACs, and BiCAACs.

Synthesis and structural characterisation of *bis*-NHC Pd(I) complexes, likely from either the reduction or oxidation of palladium precursors bearing the desired ligands, would be of interest. The linear *bis*-phosphine species [Pd(P^{t}Bu$_3$)$_2$]$^+$ has recently been reported as the first unsupported Pd(I) two-coordinate species, formed *via* the oxidation of the Pd(0) precursor Pd(P^{t}Bu$_3$)$_2$.[12, 13] The challenge would be to make the analogous RE-NHC complex, while preventing additional stabilisation of the low-coordinate species by C-H activation of the carbene ligand. The heavier congener would have more diffuse 4*d* orbitals, which can potentially result in greater spin-orbit coupling, highly anisotropic *g* values, and large zero-field splitting parameters, which are all requisites for SIM behaviour.[14]

6.1 References

1. A. Tennyson, R. Ono, T. Hudnall, D. Khramov, J. A. Er, J. Kamplain, V. Lynch, J. Sessler and C. Bielawski, *Chem. Eur. J.*, 2010, **16**, 304-315.
2. U. S. D. Paul and U. Radius, *Organometallics*, 2017, **36**, 1398-1407.
3. M. Henrion, B. de P. Cardoso, V. Cesar, M. J. Chetcuti and V. Ritleng, *Organometallics*, 2017, **36**, 1113-1121.
4. U. S. D. Paul, C. Sieck, M. Haehnel, K. Hammond, T. B. Marder and U. Radius, *Chem. Eur. J.*, 2016, **22**, 11005-11014
5. K. C. Mondal, S. Roy, B. Maity, D. Koley and H. W. Roesky, *Inorg. Chem.*, 2016, **55**, 163-169.
6. B. Dittrich, C. M. Wandtke, A. Meents, K. Proepper, K. C. Mondal, P. P. Samuel, S. K. Amin, A. P Singh, H. W. Roesky and N. S. Sidhu, *ChemPhysChem*, 2015, **16**, 412-419.
7. K. C. Mondal, P. P. Samuel, Y. Li, H. W. Roesky, S. Roy, L. Ackermann, N. S. Sidhu, G. M. Sheldrick, E. Carl, S. Demeshko, S. De, P. Parameswaran, L. Ungur, L. F. Chibotaru and D. M. Andrada, *Eur. J. Inorg. Chem.*, 2014, **5**, 818-823.
8. S. Pelties and R. Wolf, *Z. Anorg. Allg. Chem.*, 2013, **639**, 2581-2585.
9. A. El-Hellani, J. Monot, S. Tang, R. Guillot, S. Bour and V. Gandon, *Inorg. Chem.*, 2013, **52**, 11493-11502.
10. D. G. Gusev, *Organometallics*, 2009, **28**, 6458-6461.
11. P. P. Samuel, K. C. Mondal, N. Amin Sk, H. W. Roesky, E. Carl, R. Neufald, D. Stalke, S. Demchenko, F. Meyer and L. Ungur, *J. Am. Chem. Soc.*, 2014, **136**, 11964-11971.
12. T. Troadec, S. Tan, C. J. Wedge, J. P. Rourke, P. R. Unwin and A. B. Chaplin, *Angew. Chem. Int. Ed.*, 2016, **55**, 3754-3757.
13. M. C. MacInnis, J. C. DeMott, E. M. Zolnhofer, J. Zhou, K. Meyer, R. P. Hughes and O. V. Ozerov, *Chem*, 2016, **1**, 902-920.
14. X. Wang, C. Avendano and K. R. Dunbar, *Chem. Soc. Rev.*, 2011, **40**, 3213-3238.

CHAPTER 7

7 EXPERIMENTAL

7.1 General Procedures

All air sensitive compounds and syntheses were handled and carried out under argon using standard Schlenk and glovebox techniques, with dried and degassed solvents. As most of the compounds involved were also water sensitive, all glassware was oven dried overnight at 413 K and then flame-dried before use. Solvents were purified using an MBraun solvent purification system (hexane, pentane, CH_2Cl_2, Et_2O, toluene), distilled from sodium benzophenone ketyl (C_6H_6, THF), from calcium hydride (CH_3CN, C_6H_5F), or from activated magnesium and iodine (MeOH, EtOH, ^{i}PrOH). Deuterated solvents (Sigma Aldrich) were vacuum transferred from potassium (C_6D_6, THF-d_8, toluene-d_8) or calcium hydride ($CDCl_3$, CD_2Cl_2). DMSO-d_6 was used as received. All solvents were stored over activated 4 Å molecular sieves following degassing. All reagents needed for iminium salt synthesis were used as received. $Ni(COD)_2$ (Strem Chemicals), $KN(SiMe_3)_2$, $Ni(PPh_3)_2Br_2$, $Ni(dme)Br_2$, PCy_3, P^tBu_3, MeI, 4-fluoroiodobenzene (all Sigma Aldrich), and $TlPF_6$ (Alfa Aeser) were stored under argon in a glovebox and at 238 K if necessary. $NaBAr^F{}_4$ was synthesised by a modified literature preparation and stored under argon.[1] Literature methods were used to prepare [SIMesH]Cl,[2] IMe_4,[3] IEt_2Me_2,[3] $I^iPr_2Me_2$,[3] I^tBu,[4] ICy,[5] IMes,[6] IPr,[7] ^{Et2}CAAC,[8] and ^{Menthyl}CAAC.[9] $^{Cyt Bu}$CAAC was kindly donated by Rodolphe Jazzar. All liquid reagents used for hydrophosphination catalysis were stored over activated 4 Å molecular sieves following degassing.

7.2 Characterisation Techniques

NMR data was collected on Bruker Avance 400 and 500 MHz spectrometers and referenced to the resonances of the residual solvent chemical shifts as follows (^{1}H, ^{13}C): $CDCl_3$ (δ 7.26, 77.16), C_6D_6 (δ 7.16, 128.06), CD_2Cl_2 (δ 5.32, 53.84), THF-d_8 (δ 3.58, 67.21), DMSO-d_6 (δ 2.50, 39.52), toluene-d_8 (δ 2.08, 20.43).[10] ^{31}P{^{1}H} NMR spectra were externally referenced to 85% H_3PO_4 (δ 0.0), ^{11}B{^{1}H} NMR spectra to 15% $BF_3{\cdot}OEt_2$ (δ 0.0) and ^{19}F{^{1}H} NMR spectra to neat $CFCl_3$ (δ 0.0). Evans solution magnetic susceptibility measurements were recorded on a 500 MHz NMR spectrometer at 298 K.

IR spectra was recorded on a Nicolet Nexus FTIR spectrometer as either KBr discs or in the quoted solvent.

X-ray crystal structures were recorded on Agilent Technologies SuperNova or Xcalibur diffractometers at 150 K, with structural solutions and refinements performed using SHELXS-97[12] and SHELXL-97[12] respectively.

Mass spectrometry was recorded on a Bruker MicrOTOF electrospray time-of-flight mass spectrometer (ESI-TOF) coupled to an Agilent High Performance Liquid Chromatography (HPLC). Samples were prepared to a concentration of 10 μg/mL in CH_3CN.

X-band (9.5 GHz) CW EPR data was collected on Bruker EMX and E500 spectrometers using a 10 inch magnet (ER 073) with 12 kW powers supply (ER 083) at Cardiff University, with samples prepared as reported in previous literature.[13]

SQUID data was collected on a Quantum Design magnetometer at the University of Ottawa, as previously reported.[14]

Cyclic voltammetry was recorded using the Emstatblue potentiostat (Alvatek UK) to measure remotely under glovebox (MBraun) conditions with THF solvent and 20 mM tetrabutylammonium hexafluorophosphate ($[^nBu_4N]PF_6$) as supporting electrolyte. The working electrode was a 3 mm diameter glassy carbon electrode, the counter and reference electrodes were graphite rods. Voltammograms were recorded across multiple scan rates (0.01 Vs^{-1}, 0.02 Vs^{-1}, and 0.05 Vs^{-1}) in both cathodic and anodic directions, before re-recording at 0.05 Vs^{-1} with added decamethylferrocene ($FeCp^*_2$) to determine potential values relative to the $FeCp^*_2{}^{+/0}$ redox couple.

Elemental analysis was performed by Elemental Microanalysis Limited, Okehampton.

7.3 Preparation of Ring-Expanded N-heterocyclic Carbene (RE-NHC) Precursors

All RE-NHC precursors (pyrimidinium and diazepinium salts) containing aryl or alkyl (^{i}Bu, ^{n}Pent, Cy) *N*-substituents were synthesised *via* the formamidine route adapted from work by Cavell,[15] Kariuki,[16] and Lavigne.[17] The remaining RE-NHC precursors with alkyl (Et, ^{i}Pr, ^{t}Bu, ^{i}Bu) *N*-substituents were synthesised *via* the diamine microwave route used by Delaude.[18] All syntheses were carried out under aerobic conditions, except for 6MesDAC·HCl, which needed to be synthesised under argon.

It is worth noting that the halide salts were unsuitable for deprotonation (section 7.4.1) due to decomposition, and so the halide was exchanged for either BF_4 or PF_6 anions.[15]

7.3.1 Preparation of 1,3-bis(2,4,6-trimethylphenyl)-3,4,5,6-tetrahydropyrimidin-1-ium tetrafluoroborate ([6MesH]BF_4)

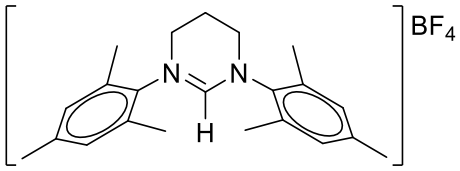

7.3.1.1 Preparation of N,N'-bis(2,4,6-trimethylphenyl)formamidine

2,4,6-Trimethylaniline (25.0 g, 185.0 mmol), triethyl orthoformate (13.7 g, 92.5 mmol) and glacial acetic acid (0.3 g, 5.0 mmol) were charged to a distillation apparatus and heated at 393 K for 2 hrs. After all the EtOH generated was distilled off, the resulting pale orange solid was cooled to room temperature and washed with Et_2O (2 × 30 mL), leaving a white precipitate which was dried on a Buchner funnel. Yield: 22.8 g (88%).

7.3.1.2 Preparation of 1,3-bis(2,4,6-trimethylphenyl)-3,4,5,6-tetrahydropyrimidin-1-ium tetrafluoroborate ([6MesH]BF_4)

N,N'-*bis*(2,4,6-trimethylphenyl)formamidine (14.0 g, 50.0 mmol), $BrCH_2CH_2CH_2Br$ (10.1 g, 50.0 mmol) and K_2CO_3 (3.5 g, 25.0 mmol) were dissolved in CH_3CN (250 mL) within a 500 mL round bottom flask and refluxed for 16 hrs. The solvent was removed on a rotary evaporator and the resulting residue was extracted into CH_2Cl_2 (30 mL) and filtered to remove inorganic salts. Addition of Et_2O (30 mL) resulted in a white precipitate which was isolated, washed with cold Et_2O (2 × 30 mL), and dried *in vacuo*. Yield: 16.7 g (83%).

The entire batch of pyrimidinium bromide salt (16.7 g, 41.6 mmol) was dissolved in $(CH3)_2CO$ (150 mL) and added to a flask containing $NaBF_4$ (5.0 g, 45.8 mmol) in H_2O (50 mL). After 1 hr of stirring, all the volatiles were removed *via* a rotary evaporator and the resulting slurry was extracted into CH_2Cl_2 (100 mL) and washed with H_2O (3 × 80 mL) *via* a separating funnel. The CH_2Cl_2 portion was dried over $MgSO_4$ for 2 hrs and filtered before the solution was concentrated down to ca. 10 mL. Et_2O (30 mL) was added to form a white precipitate which was isolated, further washed with cold Et_2O (2 × 30 mL)

and dried under vacuum. Yield: 12.2 g (72%). ^{1}H NMR ($CDCl_3$, 500 MHz, 298 K): δ 7.49 (s, 1H, NC*H*N), 6.95 (s, 4H, *m*-CH_{aryl}), 3.92 (t, $^{3}J_{HH}$ = 5.7 Hz, 4H, NCH_2CH$_2$), 2.57 (quin, $^{3}J_{HH}$ = 5.7 Hz, 2H, NCH$_2$CH_2), 2.30 (s, 12H, *o*-CH_3), 2.28 (s, 6H, *p*-CH_3). ^{13}C{^{1}H} NMR ($CDCl_3$, 125 MHz, 298 K): δ 154.1 (s, N*C*HN), 140.7 (s, C_{aryl}), 136.5 (s, C_{aryl}), 134.5 (s, C_{aryl}), 130.3 (s, *m*-*C*H$_{aryl}$), 46.5 (s, N*C*H$_2$CH$_2$), 21.2 (s, *p*-*C*H$_3$), 19.4 (s, NCH$_2$*C*H$_2$), 17.6 (s, *o*-*C*H$_3$). ESI-MS calcd. (found) for [M^+ – BF_4] $(C_{22}H_{29}N_2)^+$: *m/z* 321.2331 (321.2349).

7.3.2 Preparation of 1,3-bis(2,6-dimethylphenyl)-3,4,5,6-tetrahydropyrimidin-1-ium tetrafluoroborate ([6XylH]BF$_4$)

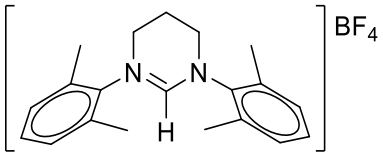

7.3.2.1 Preparation of N,N'-bis(2,6-dimethylphenyl)formamidine

Following the method as for N,N'-*bis*(2,4,6-trimethylphenyl)formamidine (section 7.3.1.1), but using 2,6-dimethylaniline (20.0 g, 165.0 mmol), triethyl orthoformate (12.2 g, 82.5 mmol) and glacial acetic acid (0.3 g, 5.0 mmol) to form the desired white solid product. Yield: 12.4 g (60%).

7.3.2.2 Preparation of 1,3-bis(2,6-dimethylphenyl)-3,4,5,6-tetrahydropyrimidin-1-ium tetrafluoroborate ([6XylH]BF$_4$)

Following the same method as for [6MesH]BF_4 (section 7.3.1.2), but using N,N'-*bis*(2,6-dimethylphenyl)formamidine (10.1 g, 40.0 mmol), BrCH$_2$CH$_2$CH$_2$Br (8.1 g, 40.0 mmol) and K_2CO_3 (2.8 g, 20.0 mmol) in CH_3CN (250 mL) to form [6XylH]Br. Yield: 9.6 g (64%).

Identical anion exchange conditions were used to those that were employed for [6MesH]BF_4 (section 7.3.1.2), but with [6XylH]Br (9.6 g, 25.7 mmol) and $NaBF_4$ (3.4 g, 30.9 mmol) in (CH3)$_2$CO/H_2O to yield [6XylH]BF_4 as a white solid. Yield: 7.7 g (79%). ^{1}H NMR ($CDCl_3$, 500 MHz, 298 K): δ 7.54 (s, 1H, NC*H*N), 7.28 (t, $^{3}J_{HH}$ = 7.6 Hz, 2H, *p*-CH_{aryl}), 7.23 (d, $^{3}J_{HH}$ = 7.6 Hz, 4H, *m*-CH_{aryl}), 4.02 (t, $^{3}J_{HH}$ = 5.7 Hz, 4H, NCH_2CH$_2$), 2.62 (quin, $^{3}J_{HH}$ = 5.7 Hz, 2H, NCH$_2$CH_2), 2.39 (s, 12H, *o*-CH_3). ^{13}C{^{1}H} NMR ($CDCl_3$, 125 MHz, 298 K): δ 153.9 (s, N*C*HN), 138.9 (s, C_{aryl}), 135.0 (s, C_{aryl}), 130.7 (s, *p*-*C*H$_{aryl}$),

129.8 (s, *m*-*C*CH_{aryl}), 46.5 (s, N*C*H_2CH_2), 19.5 (s, NCH_2*C*H_2), 17.8 (s, *o*-*C*H_3). ESI-MS calcd. (found) for $[M^+ - BF_4]$ $(C_{20}H_{25}N_2)^+$: *m/z* 293.2018 (293.2025).

7.3.3 Preparation of 1,3-bis(2-methylphenyl)-3,4,5,6-tetrahydropyrimidin-1-ium tetrafluoroborate ([6^{o}TolH]BF_4)

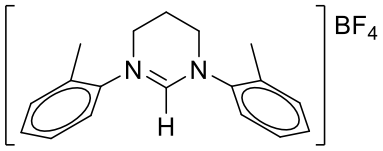

7.3.3.1 Preparation of N,N'-bis(2-methylphenyl)formamidine

Following the method as for N,N'-*bis*(2,4,6-trimethylphenyl)formamidine (section 7.3.1.1), but using 2-methylaniline (19.8 g, 185.0 mmol), triethyl orthoformate (13.7 g, 92.5 mmol) and glacial acetic acid (0.3 g, 5.0 mmol) to form the desired white solid product. Yield: 17.4 g (84%).

7.3.3.2 Preparation of 1,3-bis(2-methylphenyl)-3,4,5,6-tetrahydropyrimidin-1-ium tetrafluoroborate ([6^{o}TolH]BF_4)

Following the same method as for [6MesH]BF_4 (section 7.3.1.2), but using N,N'-*bis*(2-methylphenyl)formamidine (17.4 g, 77.6 mmol), $BrCH_2CH_2CH_2Br$ (15.7 g, 77.6 mmol) and K_2CO_3 (5.4 g, 38.8 mmol) in CH_3CN (250 mL) to form [6^{o}TolH]Br. Yield: 14.0 g (52%).

Identical anion exchange conditions to those that were used for [6MesH]BF_4 (section 7.3.1.2) were employed, but with [6^{o}TolH]Br (14.0 g, 40.5 mmol) and $NaBF_4$ (5.3 g, 48.6 mmol) to yield [6^{o}TolH]BF_4 as a white solid. Yield: 7.4 g (52%). ^{1}H NMR ($CDCl_3$, 500 MHz, 298 K): δ 7.67 (m, 2H, *o*-C*H*$_{aryl}$), 7.61 (s, 1H, NC*H*N), 7.29 – 7.35 (m, 6H, *m,p*-C*H*$_{aryl}$), 3.96 (t, $^3J_{HH}$ = 5.7 Hz, 4H, NC*H*$_2$$CH_2$), 2.51 (quin, $^3J_{HH}$ = 5.7 Hz, 2H, NCH_2C*H*$_2$), 2.36 (s, 6H, *o*-C*H*$_3$). ^{13}C{^{1}H} NMR ($CDCl_3$, 125 MHz, 298 K): δ 153.5 (s, N*C*HN), 140.2 (s, *C*$_{aryl}$), 133.4 (s, *C*$_{aryl}$), 131.7 (s, *C*H$_{aryl}$), 130.5 (s, *C*H$_{aryl}$), 128.4 (s, *C*H$_{aryl}$), 127.7 (s, *C*H$_{aryl}$), 47.1 (s, N*C*H_2CH_2), 19.6 (s, NCH_2*C*H_2), 17.5 (s, *o*-*C*H_3). ESI-MS calcd. (found) for $[M^+ - BF_4]$ $(C_{18}H_{21}N_2)^+$: *m/z* 265.1705 (265.1714).

7.3.4 Preparation of 1,3-bis(3,5-dimethylphenyl)-3,4,5,6-tetrahydropyrimidin-1-ium tetrafluoroborate ([6^{m}XylH]BF$_4$)

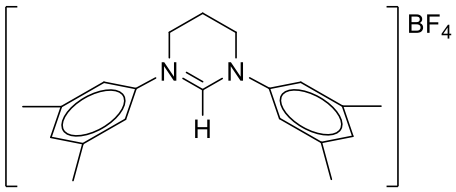

7.3.4.1 Preparation of N,N'-bis(3,5-dimethylphenyl)formamidine

Following the method as for N,N'-*bis*(2,4,6-trimethylphenyl)formamidine (section 7.3.1.1), but using 3,5-dimethylaniline (10.0 g, 82.5 mmol), triethyl orthoformate (6.1 g, 41.3 mmol) and glacial acetic acid (0.2 g, 2.5 mmol) to form the desired yellow solid product. Yield: 9.6 g (92%).

7.3.4.2 Preparation of 1,3-bis(3,5-dimethylphenyl)-3,4,5,6-tetrahydropyrimidin-1-ium tetrafluoroborate ([6^{m}XylH]BF$_4$)

Following the same method as for [6MesH]BF$_4$ (section 7.3.1.2), but using N,N'-*bis*(3,5-dimethylphenyl)formamidine (5.0 g, 20.0 mmol), BrCH$_2$CH$_2$CH$_2$Br (4.0 g, 20.0 mmol) and K$_2$CO$_3$ (1.4 g, 10.0 mmol) in CH$_3$CN (150 mL) to form [6^{m}XylH]Br. Yield: 1.2 g (16%).

Identical anion exchange conditions were used to those that were employed for [6MesH]BF$_4$ (section 7.3.1.2), but with [6^{m}XylH]Br (1.2 g, 3.2 mmol) and NaBF$_4$ (0.4 g, 3.9 mmol) to yield [6^{m}XylH]BF$_4$ as a white solid. Yield: 0.5 g (41%). ^{1}H NMR (CDCl$_3$, 500 MHz, 298 K): δ 7.69 (s, 1H, NC*H*N), 7.07 (s, 4H, *o*-C*H*$_{aryl}$), 7.02 (s, 2H, *p*-C*H*$_{aryl}$), 4.03 (t, $^3J_{HH}$ = 5.8 Hz, 4H, NC*H*$_2$CH$_2$), 2.47 (quin, $^3J_{HH}$ = 5.8 Hz, 2H, NCH$_2$C*H*$_2$), 2.34 (s, 12H, *m*-C*H*$_3$). ^{13}C{^{1}H} NMR (CDCl$_3$, 125 MHz, 298 K): δ 151.1 (s, N*C*HN), 141.6 (s, *i*-*C*$_{aryl}$), 140.5 (s, *m*-*C*$_{aryl}$), 131.0 (s, *p*-*C*H$_{aryl}$), 121.0 (s, *o*-*C*H$_{aryl}$), 46.8 (s, N*C*H$_2$CH$_2$), 21.3 (s, *m*-*C*H$_3$), 19.4 (s, NCH$_2$*C*H$_2$).

7.3.5 Preparation of 1,3-bis(4-bromo-2,6-dimethylphenyl)-3,4,5,6-tetrahydropyrimidin-1-ium tetrafluoroborate ([6Xyl-p-BrH]BF_4)

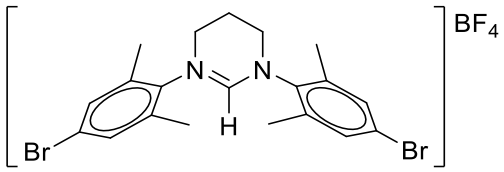

7.3.5.1 Preparation of N,N'-bis(4-bromo-2,6-dimethylphenyl)formamidine

Following the method as for N,N'-*bis*(2,4,6-trimethylphenyl)formamidine (section 7.3.1.1), but using 4-bromo-2,6-dimethylaniline (12.0 g, 60.0 mmol), triethyl orthoformate (4.4 g, 30.0 mmol) and glacial acetic acid (0.2 g, 2.5 mmol) refluxed for 16 hrs to form the desired off-white solid product. Yield: 9.3 g (76%).

7.3.5.2 Preparation of 1,3-bis(4-bromo-2,6-dimethylphenyl)-3,4,5,6-tetrahydropyrimidin-1-ium tetrafluoroborate ([6Xyl-p-BrH]BF_4)

Following the same method as for [6MesH]BF_4 (section 7.3.1.2), but using N,N'-*bis*(4-bromo-2,6-dimethylphenyl)formamidine (3.1 g, 7.5 mmol), $BrCH_2CH_2CH_2Br$ (1.5 g, 7.5 mmol) and K_2CO_3 (0.5 g, 3.8 mmol) in CH_3CN (150 mL) to form [6Xyl-*p*-BrH]Br. Yield: 1.2 g (30%).

Identical anion exchange conditions to those that were used for [6MesH]BF_4 (section 7.3.1.2) were employed, but with [6Xyl-*p*-BrH]Br (1.2 g, 2.3 mmol) and $NaBF_4$ (0.3 g, 2.7 mmol) in $(CH3)_2CO/H_2O$ to yield [6Xyl-*p*-BrH]BF_4 as a white solid. Yield: 0.9 g (73%). ^{1}H NMR ($CDCl_3$, 500 MHz, 298 K): δ 7.62 (s, 1H, NC*H*N), 7.34 (s, 4H, *m*-C*H*$_{aryl}$), 3.97 (t, $^3J_{HH}$ = 5.6 Hz, 4H, NC*H*$_2$CH$_2$), 2.56 (quin, $^3J_{HH}$ = 5.6 Hz, 2H, NCH$_2$C*H*$_2$), 2.35 (s, 12H, *o*-C*H*$_3$). ^{13}C{^{1}H} NMR ($CDCl_3$, 125 MHz, 298 K): δ 154.1 (s, N*C*HN), 137.9 (s, *i*-*C*$_{aryl}$), 137.1 (s, *o*-*C*$_{aryl}$), 132.7 (s, *m*-*C*H$_{aryl}$), 124.6 (s, *p*-*C*$_{aryl}$), 46.5 (s, N*C*H$_2$CH$_2$), 19.4 (s, NCH$_2$*C*H$_2$), 17.7 (s, *o*-*C*H$_3$).

7.3.6 Preparation of 1,3-bis(2,4,6-trimethylphenyl)-4,5,6,7-tetrahydro-[1,3]-diazepin-1-ium tetrafluoroborate ([7MesH]BF_4)

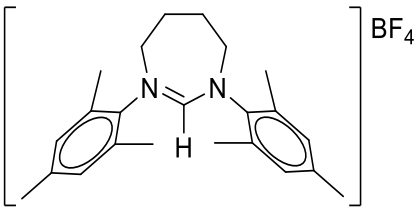

N,N'-*bis*(2,4,6-trimethylphenyl)formamidine (section 7.3.1.1) (22.4 g, 80.0 mmol), $ICH_2CH_2CH_2CH_2I$ (26.0 g, 84.0 mmol) and K_2CO_3 (11.1 g, 80.0 mmol) were dissolved in CH_3CN (250 mL) within a 500 mL round bottom flask and refluxed for 16 hrs. The solvent was removed using a rotary evaporator and the resulting residue was extracted into CH_2Cl_2 (30 mL) and filtered to remove inorganic salts. Addition of Et_2O (30 mL) resulted in a white precipitate which was isolated, washed with cold Et_2O (2 × 30 mL), and dried *in vacuo*. Yield: 30.9 g (84%).

The entire batch of iodide salt (30.9 g, 66.8 mmol) was dissolved in $(CH3)_2CO$ (150 mL) and added to a flask containing $NaBF_4$ (8.8 g, 80.2 mmol) in H_2O (50 mL). After 1 hr of stirring, all the volatiles were removed *via* a rotary evaporator and the resulting slurry was extracted into CH_2Cl_2 (100 mL) and washed with H_2O (3 × 80 mL) *via* a separating funnel. The CH_2Cl_2 portion was dried over $MgSO_4$ for 2 hrs and filtered before the solution was concentrated down to ca. 10 mL. Et_2O (30 mL) was added to form a white precipitate which was isolated and further washed with cold Et_2O (2 × 30 mL) and dried under vacuum. Yield: 20.3 g (72%). ^{1}H NMR ($CDCl_3$, 500 MHz, 298 K): δ 7.21 (s, 1H, NC*H*N), 6.94 (s, 4H, *m*-CH_{aryl}), 4.36 (t, $^3J_{HH}$ = 5.5 Hz, 4H, NC$H_2$$CH_2$), 2.50 (t, $^3J_{HH}$ = 5.5 Hz, 4H, NCH_2CH_2), 2.37 (s, 12H, *o*-CH_3), 2.26 (s, 6H, *p*-CH_3). ^{13}C{^{1}H} NMR ($CDCl_3$, 125 MHz, 298 K): δ 158.3 (s, N*C*HN), 140.5 (s, *C*$_{aryl}$), 139.5 (s, *C*$_{aryl}$), 133.8 (s, *C*$_{aryl}$), 130.4 (s, *m*-*C*H$_{aryl}$), 54.9 (s, N*C*$H_2$$CH_2$), 25.3 (s, NCH_2CH_2), 21.0 (s, *p*-*C*H_3), 18.2 (s, *o*-*C*H_3). ESI-MS calcd. (found) for [M^+ – BF_4] $(C_{23}H_{31}N_2)^+$: *m/z* 335.2487 (335.2499).

7.3.7 Preparation of 1,3-bis(2,6-dimethylphenyl)-4,5,6,7-tetrahydro-[1,3]-diazepin-1-ium tetrafluoroborate ([7XylH]BF$_4$)

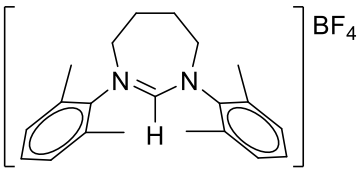

Following the same method as for [7MesH]BF_4 (section 7.3.6), but using N,N'-*bis*(2,6-dimethylphenyl)formamidine (12.6 g, 50.0 mmol), $ICH_2CH_2CH_2CH_2I$ (16.3 g, 52.5 mmol) and K_2CO_3 (6.9 g, 50.0 mmol) in CH_3CN (250 mL) to form [7XylH]I. Yield: 15.7 g (72%).

Identical anion exchange conditions were used to those that were employed for [7MesH]BF_4 (section 7.3.6), but with [7XylH]I (15.7 g, 36.1 mmol) and $NaBF_4$ (4.8 g, 43.4 mmol) in $(CH3)_2CO/H_2O$ to yield [7XylH]BF_4 as a white solid. Yield: 12.3 g (86%). ^{1}H NMR ($CDCl_3$, 500 MHz, 298 K): δ 7.28 (s, 1H, NC*H*N), 7.23 (m, 2H, *p*-CH_{aryl}), 7.15 (m, 4H, *m*-CH_{aryl}), 4.39 (t, $^3J_{HH}$ = 5.4 Hz, 4H, NCH_2CH$_2$), 2.55 (t, $^3J_{HH}$ = 5.4 Hz, 4H, NCH$_2$CH_2), 2.43 (s, 12H, *o*-CH_3). ^{13}C{^{1}H} NMR ($CDCl_3$, 125 MHz, 298 K): δ 158.2 (s, N*C*HN), 141.8 (s, *C*$_{aryl}$), 134.2 (s, *C*$_{aryl}$), 130.4 (s, *p*-*C*H$_{aryl}$), 129.9 (s, *m*-*C*H$_{aryl}$), 54.9 (s, N*C*H$_2$CH$_2$), 25.4 (s, NCH$_2$*C*H$_2$), 18.3 (s, *o*-*C*H$_3$). ESI-MS calcd. (found) for [M^+ – BF_4] $(C_{21}H_{27}N_2)^+$: *m/z* 307.2174 (307.2186).

7.3.8 Preparation of 1,3-bis(2-methylphenyl)-4,5,6,7-tetrahydro-[1,3]-diazepin-1-ium tetrafluoroborate ([7^{o}TolH]BF$_4$)

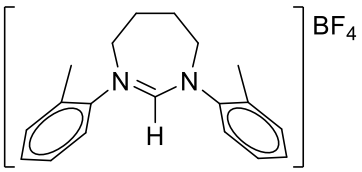

Following the same method as for [7MesH]BF_4 (section 7.3.6), but using N,N'-*bis*(2-methylphenyl)formamidine (15.9 g, 65.0 mmol), $ICH_2CH_2CH_2CH_2I$ (21.2 g, 68.3 mmol) and K_2CO_3 (9.0 g, 65.0 mmol) in CH_3CN (250 mL) and refluxed for 48 hrs to form [7^{o}TolH]I. Yield: 20.8 g (79%).

Identical anion exchange conditions to those that were used to form [7MesH]BF_4 (section 7.3.6) were employed, but with [7^{o}TolH]I (20.8 g, 51.2 mmol) and $NaBF_4$ (6.7 g, 61.4 mmol) to yield [7^{o}TolH]BF_4 as a white solid. Yield: 14.6 g (78%). ^{1}H NMR (CD_2Cl_2, 500 MHz, 298 K): δ 7.67 (m, 2H, *o*-CH_{aryl}), 7.43 (s, 1H, NC*H*N), 7.26 – 7.34 (m, 6H,

m,p-C*H*$_{aryl}$), 4.41 (br s, 4H, NC*H*$_2$CH$_2$), 2.47 (m, 4H, NCH$_2$C*H*$_2$), 2.43 (s, 6H, *o*-C*H*$_3$). ^{13}C{^{1}H} NMR ($CDCl_3$, 125 MHz, 298 K): δ 157.7 (s, N*C*HN), 143.0 (s, *C*$_{aryl}$), 132.9 (s, *C*$_{aryl}$), 131.8 (s, *C*H$_{aryl}$), 130.3 (s, *C*H$_{aryl}$), 128.5 (s, *C*H$_{aryl}$), 127.7 (s, *C*H$_{aryl}$), 55.6 (s, N*C*H$_2$CH$_2$), 25.5 (s, NCH$_2$*C*H$_2$), 17.9 (s, *o*-*C*H$_3$). ESI-MS calcd. (found) for [M$^+$ – BF_4] ($C_{19}H_{23}N_2$)$^+$: *m/z* 279.1861 (279.1874).

7.3.9 Preparation of 1,3-bis(3,5-dimethylphenyl)-4,5,6,7-tetrahydro-[1,3]-diazepin-1-ium tetrafluoroborate ([7^{m}XylH]BF$_4$)

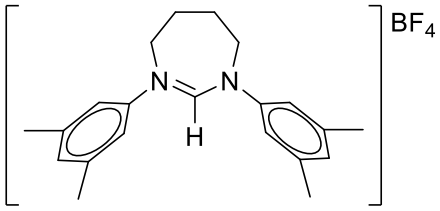

Following the same method as for [7MesH]BF_4 (section 7.3.6), but using N,N'-*bis*(3,5-dimethylphenyl)formamidine (5.0 g, 20.0 mmol), $ICH_2CH_2CH_2CH_2I$ (6.5 g, 21.0 mmol) and K_2CO_3 (1.4 g, 10.0 mmol) in CH_3CN (250 mL) to form [7^{m}XylH]I. Yield: 4.1 g (47%).

Identical anion exchange conditions were used to those that were employed for [7MesH]BF_4 (section 7.3.6), but with [7^{m}XylH]I (4.1 g, 9.4 mmol) and $NaBF_4$ (1.2 g, 11.3 mmol) in $(CH3)_2CO/H_2O$ to yield [7^{m}XylH]BF_4 as a bright yellow solid. Yield: 1.7 g (46%). ^{1}H NMR ($CDCl_3$, 500 MHz, 298 K: δ 7.60 (s, 1H, NC*H*N), 7.14 (s, 4H, *o*-C*H*$_{aryl}$), 7.01 (s, 2H, *p*-C*H*$_{aryl}$), 4.46 (m, 4H, NC*H*$_2$CH$_2$), 2.37 (m, 4H, NCH$_2$C*H*$_2$), 2.32 (s, 12H, *m*-C*H*$_3$). ^{13}C{^{1}H} NMR ($CDCl_3$, 125 MHz, 298 K): δ 155.9 (s, N*C*HN), 143.7 (s, *i*-*C*$_{aryl}$), 140.6 (s, *m*-*C*$_{aryl}$), 131.2 (s, *p*-*C*H$_{aryl}$), 122.2 (s, *o*-*C*H$_{aryl}$), 54.8 (s, N*C*H$_2$CH$_2$), 25.2 (s, NCH$_2$*C*H$_2$), 21.3 (s, *m*-*C*H$_3$). ESI-MS calcd. (found) for [M$^+$ – BF_4] ($C_{21}H_{27}N_2$)$^+$: *m/z* 307.2174 (307.2194).

7.3.10 Preparation of 1,3-bis(4-bromo-2,6-dimethylphenyl)-4,5,6,7-tetrahydro-[1,3]-diazepin-1-ium tetrafluoroborate ([7Xyl-p-BrH]BF$_4$)

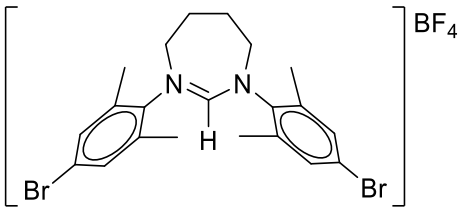

Following the same method as for [7MesH]BF_4 (section 7.3.6), but using N,N'-*bis*(4-bromo-2,6-dimethylphenyl)formamidine (2.1 g, 5.0 mmol), $ICH_2CH_2CH_2CH_2I$ (1.6 g, 5.3 mmol) and K_2CO_3 (0.3 g, 2.5 mmol) in CH_3CN (150 mL) to form [7Xyl-*p*-BrH]I. Yield: 2.6 g (88%).

Identical anion exchange conditions to those that were used for [7MesH]BF_4 (section 7.3.6) were employed, but with [7Xyl-*p*-BrH]I (2.6 g, 4.4 mmol) and $NaBF_4$ (0.6 g, 5.3 mmol) in $(CH3)_2CO/H_2O$ to yield [7Xyl-*p*-BrH]BF_4 as an off-white solid. Yield: 1.7 g (70%). ^{1}H NMR ($CDCl_3$, 500 MHz, 298 K): δ 7.37 (s, 1H, NC*H*N), 7.32 (s, 4H, *m*-CH_{aryl}), 4.41 (t, $^3J_{HH}$ = 5.4 Hz, 4H, NCH_2CH$_2$), 2.52 (t, $^3J_{HH}$ = 5.4 Hz, 4H, NCH$_2$CH_2), 2.42 (s, 12H, *o*-CH_3). ^{13}C{^{1}H} NMR ($CDCl_3$, 125 MHz, 298 K): δ 158.4 (s, N*C*HN), 140.7 (s, *i*-C_{aryl}), 136.4 (s, *o*-C_{aryl}), 132.7 (s, *m*-*C*H$_{aryl}$), 124.2 (s, *p*-C_{aryl}), 55.0 (s, N*C*H$_2$CH$_2$), 25.3 (s, NCH$_2$*C*H$_2$), 18.3 (s, *o*-*C*H$_3$). ESI-MS calcd. (found) for [M^+ – BF_4] $(C_{21}H_{25}N_2Br_2)^+$: *m/z* 465.0384 (465.0376).

7.3.11 Preparation of 2-chloro-1,3-dimesityl-5,5-dimethyl-4,6-dioxohexahydropyrimidine (6MesDAC·HCl)

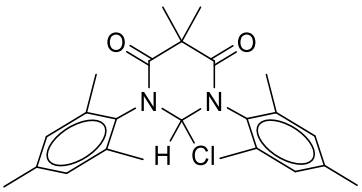

N,N'-*bis*(2,4,6-trimethylphenyl)formamidine (4.0 g, 14.3 mmol) and triethylamine (3.0 mL, 21.5 mmol) were dissolved in CH_2Cl_2/hexane (1:2, v/v, 30 mL) and cooled to 273 K. Dimethylmalonyl chloride (2.0 mL, 15.1 mmol) was carefully added to the stirred solution to form an off-white suspension. After 30 min, the suspension was filtered through celite, and the celite washed with CH_2Cl_2/hexane (1:2, v/v, 30 mL). The filtrates were combined and reduced *in vacuo* to leave the desired white solid. Yield: 2.8 g (48%). ^{1}H NMR ($CDCl_3$, 500 MHz, 298 K): δ 6.96 (s, 4H, *m*-CH_{aryl}), 6.93 (s, 1H,

NC*H*ClN), 2.31 (s, 12H, *o*-C*H*$_3$), 2.29 (s, 6H, *p*-C*H*$_3$), 1.79 (s, 6H, C(C*H*$_3$)$_2$). ^{13}C{^{1}H} NMR ($CDCl_3$, 125 MHz, 298 K): δ 170.9 (s, N*C*O), 139.1 (s, C_{aryl}), 136.1 (s, C_{aryl}), 132.4 (s, C_{aryl}), 130.3 (s, *m*-*C*H$_{aryl}$), 90.7 (s, N*C*HClN), 48.4 (s, *C*(CH$_3$)$_2$), 23.7 (s, C(*C*H$_3$)$_2$), 21.1 (s, *p*-*C*H$_3$), 19.3 (s, *o*-*C*H$_3$). ESI-MS calcd. (found) for [M^+ – Cl + H_2O] $(C_{24}H_{29}N_2O_2H_2O)^+$: *m/z* 395.2335 (377.2327).

7.3.12 Preparation of 1,3-diethyl-3,4,5,6-tetrahydropyrimidin-1-ium hexafluorophosphate ([6EtH]PF$_6$)

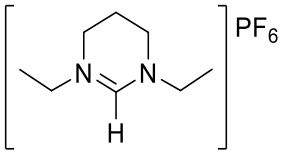

N,N'-diethyl-1,3-propanediamine (0.3 mL, 2.0 mmol), triethyl orthoformate (2.0 mL, 12.0 mmol) and NH_4PF_6 (0.3 g, 2.0 mmol) were dissolved in EtOH (6 mL) before being charged to two separate microwave vials. The vials were irradiated for 5 min at 393 K with 25 W microwave power. After cooling, the EtOH solution was diluted with Et_2O (10 mL) to form a white precipitate which was isolated *via* Buchner filtration. Yield: 0.4 g (70%). NMR shows two isomers in a 46:54 ratio. *Isomer 1*: ^{1}H NMR ($CDCl_3$, 500 MHz, 298 K): δ 7.80 (s, 1H, NC*H*N), 3.52 (q, $^3J_{HH}$ = 7.3 Hz, 4H, C*H*$_2$CH$_3$), 3.37 (t, $^3J_{HH}$ = 6.0 Hz, 4H, NC*H*$_2$CH$_2$), 2.15 (quin, $^3J_{HH}$ = 6.0 Hz, 2H, NCH$_2$C*H*$_2$), 1.31 (t, $^3J_{HH}$ = 7.3 Hz, 6H, CH$_2$C*H*$_3$). ^{13}C{^{1}H} NMR ($CDCl_3$, 125 MHz, 298 K): δ 152.0 (s, N*C*HN), 50.7 (s, *C*H$_2$CH$_3$), 42.3 (s, N*C*H$_2$CH$_2$), 18.8 (s, NCH$_2$*C*H$_2$), 13.0 (s, CH$_2$*C*H$_3$). *Isomer 2*: ^{1}H NMR ($CDCl_3$, 500 MHz, 298 K): δ 7.69 (s, 1H, NC*H*N), 3.46 (q, $^3J_{HH}$ = 7.3 Hz, 4H, C*H*$_2$CH$_3$), 3.36 (t, $^3J_{HH}$ = 6.0 Hz, 4H, NC*H*$_2$CH$_2$), 2.10 (quin, $^3J_{HH}$ = 6.0 Hz, 2H, NCH$_2$C*H*$_2$), 1.26 (t, $^3J_{HH}$ = 7.3 Hz, 6H, CH$_2$C*H*$_3$). ^{13}C{^{1}H} NMR ($CDCl_3$, 125 MHz, 298 K): δ 151.5 (s, N*C*HN), 50.4 (s, *C*H$_2$CH$_3$), 42.2 (s, N*C*H$_2$CH$_2$), 18.7 (s, NCH$_2$*C*H$_2$), 12.9 (s, CH$_2$*C*H$_3$). ESI-MS calcd. (found) for [M^+ – PF_6] $(C_8H_{17}N_2)^+$: *m/z* 141.1392 (141.1392).

7.3.13 Preparation of 1,3-diisopropyl-3,4,5,6-tetrahydropyrimidin-1-ium hexafluorophosphate ([6^{i}PrH]PF$_6$)

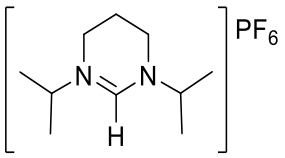

Following the method as for [6EtH]PF_6 (section 7.3.12), but using N,N'-diisopropyl-1,3-propanediamine (0.4 mL, 2.0 mmol), triethyl orthoformate (2.0 mL, 12.0 mmol) and NH_4PF_6 (0.3 g, 2.0 mmol) to form [6^{i}PrH]PF_6 as a white precipitate. Yield: 0.5 g (73%). ^{1}H NMR ($CDCl_3$, 500 MHz, 298 K): δ 7.85 (s, 1H, NC*H*N), 3.93 (sept, $^3J_{HH}$ = 6.7 Hz, 2H, C*H*$(CH_3)_2$), 3.45 (t, $^3J_{HH}$ = 5.8 Hz, 4H, NC*H*$_2$$CH_2$), 2.09 (quin, $^3J_{HH}$ = 5.8 Hz, 2H, NCH_2C*H*$_2$), 1.21 (d, $^3J_{HH}$ = 6.7 Hz, 12H, CH(C*H*$_3$)$_2$). ^{13}C{^{1}H} NMR ($CDCl_3$, 125 MHz, 298 K): δ 150.4 (s, N*C*HN), 57.3 (s, *C*H$(CH_3)_2$), 38.8 (s, N*C*$H_2$$CH_2$), 20.1 (s, CH(*C*$H_3$)$_2$), 19.1 (s, NCH_2*C*H_2). ESI-MS calcd. (found) for [M^+ – PF_6] $(C_{10}H_{21}N_2)^+$: *m/z* 169.1705 (169.1703).

7.3.14 Preparation of 1,3-di-tert-butyl-3,4,5,6-tetrahydropyrimidin-1-ium tetrafluoroborate ([6^{t}BuH]BF$_4$)

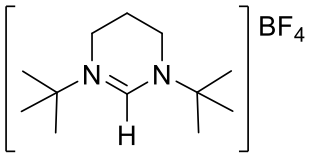

7.3.14.1 Preparation of N,N'-di-tert-butyl-1,3-propanediamine

Tert-butylamine (18.3 g, 250.0 mmol) and $BrCH_2CH_2CH_2Br$ (10.1 g, 50.0 mmol) were charged to a 250 mL round bottom flask along with H_2O (2 mL) and refluxed for 16 hrs. After allowing to cool, a mixture of NaOH (6.0 g, 150.0 mmol) in H_2O (200 mL) and Et_2O (50 mL) was used to separate the product from any unreacted amine starting material. The ether layer was collected while the H_2O layer was washed with more Et_2O (3 × 50 mL) before drying the combined organic portions over NaOH for 2 hrs. The solution was filtered and the volatiles removed on a rotary evaporator to form the product as a pale orange oil. Yield: 6.3 g (69%).

7.3.14.2 Preparation of 1,3-di-tert-butyl-3,4,5,6-tetrahydropyrimidin-1-ium tetrafluoroborate ([6^{t}BuH]BF$_4$)

Following the method as for [6EtH]PF$_6$ (section 7.3.12), but using N,N'-di-*tert*-butyl-1,3-propanediamine (0.7 g, 3.8 mmol), triethyl orthoformate (1.0 mL, 6.0 mmol) and NH_4BF_4 (0.4 g, 3.8 mmol) to form [6^{t}BuH]BF$_4$ as a white precipitate. Yield: 0.5 g (43%). ^{1}H NMR ($CDCl_3$, 500 MHz, 298 K): δ 7.85 (s, 1H, NC*H*N), 3.45 (t, $^3J_{HH}$ = 5.8 Hz, 4H, NC*H*$_2$CH$_2$), 2.07 (quin, $^3J_{HH}$ = 5.8 Hz, 2H, NCH$_2$C*H*$_2$), 1.45 (s, 18H, C(C*H*$_3$)$_3$). ^{13}C{^{1}H} NMR ($CDCl_3$, 125 MHz, 298 K): δ 146.6 (s, N*C*HN), 61.2 (s, *C*(CH$_3$)$_3$), 39.6 (s, NCH$_2$CH$_2$), 27.4 (s, C(*C*H$_3$)$_3$), 19.7 (s, NCH$_2$*C*H$_2$). ESI-MS calcd. (found) for [M$^+$ – BF$_4$] (C$_{12}$H$_{25}$N$_2$)$^+$: *m/z* 197.2018 (197.2017).

7.3.15 Preparation of 1,3-diisobutyl-3,4,5,6-tetrahydropyrimidin-1-ium tetrafluoroborate ([6^{i}BuH]BF$_4$)

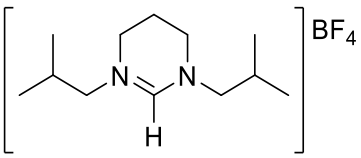

7.3.15.1 Preparation of N,N'-diisobutyl-1,3-propanediamine

Isobutylamine (18.3 g, 250.0 mmol) and BrCH$_2$CH$_2$CH$_2$Br (10.1 g, 50.0 mmol) were charged to a 250 mL round bottom flask along with H$_2$O (2 mL) and refluxed for 16 hrs. After allowing to cool, a mixture of NaOH (6.0 g, 150.0 mmol) in H$_2$O (200 mL) and Et$_2$O (50 mL) was used to separate the product from any unreacted amine starting material. The ether layer was collected while the H$_2$O layer was washed with more Et$_2$O (3 × 50 mL) before drying the combined organic portions over NaOH for 2 hrs. The solution was filtered and the volatiles removed on a rotary evaporator to form the product as an orange oil. Yield: 3.2 g (35%).

7.3.15.2 Preparation of 1,3-diisobutyl-3,4,5,6-tetrahydropyrimidin-1-ium tetrafluoroborate ([6^{i}BuH]BF$_4$)

Following the method as for [6EtH]PF$_6$ (section 7.3.12), but using N,N'-diisobutyl-1,3-propanediamine (0.7 g, 3.8 mmol), triethyl orthoformate (1.0 mL, 6.0 mmol) and NH_4BF_4 (0.4 g, 3.8 mmol) to form [6^{i}BuH]BF$_4$ as a pale orange precipitate. Yield: 0.4 g (37%). ^{1}H NMR ($CDCl_3$, 500 MHz, 298 K): δ 7.98 (s, 1H,

NC*H*N), 3.38 (t, $^{3}J_{HH}$ = 5.8 Hz, 4H, NCH_2CH$_2$), 3.30 (d, $^{3}J_{HH}$ = 7.6 Hz, 4H, NCH_2), 2.15 (quin, $^{3}J_{HH}$ = 5.8 Hz, 2H, NCH$_2$CH_2), 1.99 (sept, $^{3}J_{HH}$ = 6.8 Hz, 2H, C*H*(CH$_3$)$_2$), 0.92 (d, $^{3}J_{HH}$ = 6.8 Hz, 12H, CH(CH_3)$_2$). ^{13}C{^{1}H} NMR (CDCl$_3$, 125 MHz, 298 K): δ 153.4 (s, N*C*HN), 62.6 (s, N*C*H$_2$), 43.2 (s, N*C*H$_2$CH$_2$), 26.4 (s, *C*H(CH$_3$)$_2$), 19.3 (s, CH(*C*H$_3$)$_2$), 18.9 (s, NCH$_2$*C*H$_2$).

7.3.16 Preparation of 1,3-diisobutyl-3,4,5,6-tetrahydropyrimidin-1-ium hexafluorophosphate ([6^{i}BuH]PF$_6$)

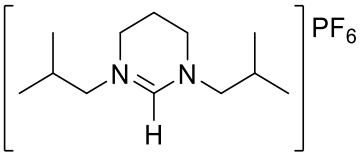

7.3.16.1 Preparation of N,N'-bis(isobutyl)formamidine

Isobutylamine (4.4 g, 60.0 mmol), triethyl orthoformate (4.5 g, 30.0 mmol) and glacial acetic acid (1.8 g, 30.0 mmol) were charged to a 250 mL round bottom flask (**CAUTION** – fumes on addition of acid) and distilled at 413 K for 16 hrs. After cooling, the flask was left under vacuum until a pale orange oil formed. This acetic acid salt was neutralised with a mixture of NaOH (1.3 g, 33.0 mmol) in H_2O (10 mL) and Et_2O (10 mL) stirred for 2 hrs, before collection of the ether layer and washing of the H_2O layer with extra Et_2O (3 × 10 mL). The combined organic portions were dried over $MgSO_4$ for 2 hrs, filtered, and reduced to dryness on a rotary evaporator. Yield: 2.2 g (46%).

7.3.16.2 Preparation of 1,3-diisobutyl-3,4,5,6-tetrahydropyrimidin-1-ium hexafluorophosphate ([6^{i}BuH]PF$_6$)

N,N'-*bis*(isobutyl)formamidine (2.2 g, 14.0 mmol), BrCH$_2$CH$_2$CH$_2$Br (3.1 g, 15.4 mmol) and K_2CO_3 (1.0 g, 7.0 mmol) were dissolved in CH_3CN (150 mL) within a 250 mL round bottom flask and refluxed for 16 hrs. After cooling, the solvent was removed on a rotary evaporator and the resulting residue extracted into CH_2Cl_2 (10 mL) and filtered to remove inorganic salts. Addition of Et_2O (20 mL) to the filtrate resulted in the formation of an oily residue, which was isolated by pumping the flask down to dryness. Yield: 2.0 g (52%).

All the oil was used in the anion exchange step. [6^{i}BuH]Br (2.0 g, 7.2 mmol) was dissolved in (CH3)$_2$CO (30 mL) and added to a flask containing KPF_6 (1.6 g, 8.7 mmol)

in H_2O (30 mL). After stirring for 1 hr, all volatiles were removed *via* a rotary evaporator and the resulting residue extracted into CH_2Cl_2 (50 mL) and washed with H_2O (3 × 30 mL) *via* a separating funnel. The CH_2Cl_2 portion was dried over $MgSO_4$ for 2 hrs and then filtered, before the solution was concentrated down to ca. 10 mL. Et_2O (30 mL) was added to form a white precipitate which was isolated, further washed with cold Et_2O (2 × 30 mL) and dried under vacuum. Yield: 0.6 g (23%). ^{1}H NMR (DMSO-d_6, 500 MHz, 298 K): δ 8.31 (s, 1H, NC*H*N), 3.35 (t, $^3J_{HH}$ = 5.8 Hz, 4H, NCH_2CH$_2$), 3.21 (d, $^3J_{HH}$ = 7.5 Hz, 4H, NCH_2), 1.98 (m, 4H, coincidence of NCH$_2$CH_2 and C*H*(CH$_3$)$_2$ signals), 0.86 (d, $^3J_{HH}$ = 6.7 Hz, 12H, CH(CH_3)$_2$). ^{13}C{^{1}H} NMR (DMSO-d_6, 125 MHz, 298 K): δ 152.9 (s, N*C*HN), 61.3 (s, N*C*H$_2$), 42.5 (s, NCH$_2$CH$_2$), 25.6 (s, *C*H(CH$_3$)$_2$), 19.1 (s, CH(*C*H$_3$)$_2$), 18.3 (s, NCH$_2$*C*H$_2$). ESI-MS calcd. (found) for [M$^+$ – PF$_6$] (C$_{12}$H$_{25}$N$_2$)$^+$: *m/z* 197.2018 (197.2019).

7.3.17 Preparation of 1,3-dineopentyl-3,4,5,6-tetrahydropyrimidin-1-ium tetrafluoroborate ([6^{n}PentH]BF$_4$)

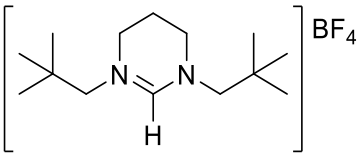

7.3.17.1 Preparation of N,N'-bis(neopentyl)formamidine

Following the method as for N,N'-*bis*(isobutyl)formamidine (section 7.3.16.1), but using neopentylamine (5.2 g, 60.0 mmol), triethyl orthoformate (4.4 g, 30.0 mmol) and glacial acetic acid (1.8 g, 30.0 mmol) to form the desired off-white solid product. Yield: 4.7 g (85%).

7.3.17.2 Preparation of 1,3-dineopentyl-3,4,5,6-tetrahydropyrimidin-1-ium tetrafluoroborate ([6^{n}PentH]BF$_4$)

Following the same method as for [6^{i}BuH]PF$_6$ (section 7.3.16.2), but using N,N'-*bis*(neopentyl)formamidine (1.4 g, 7.5 mmol), BrCH$_2$CH$_2$CH$_2$Br (1.8 g, 9.0 mmol) and K_2CO_3 (0.5 g, 3.8 mmol) in CH_3CN (150 mL) to form [6^{n}PentH]Br. Yield: 1.3 g (57%). Identical anion exchange conditions to those that were used for [6^{i}BuH]PF$_6$ (section 7.3.16.2) were employed, but with [6^{n}PentH]Br (2.0 g, 6.6 mmol) and $NaBF_4$ (0.9 g, 7.9 mmol) to yield [6^{n}PentH]BF$_4$ as a white solid. Yield: 0.8 g (40%). ^{1}H NMR ($CDCl_3$,

500 MHz, 298 K): δ 7.83 (s, 1H, NC*H*N), 3.51 (t, $^{3}J_{HH}$ = 5.7 Hz, 4H, NC*H*$_2$CH$_2$), 3.36 (s, 4H, NC*H*$_2$), 2.14 (quin, $^{3}J_{HH}$ = 5.7 Hz, 2H, NCH$_2$C*H*$_2$), 1.00 (s, 18H, C(C*H*$_3$)$_3$). ^{13}C{^{1}H} NMR ($CDCl_3$, 125 MHz, 298 K): δ 155.8 (s, N*C*HN), 67.4 (s, N*C*H$_2$), 46.5 (s, N*C*H$_2$CH$_2$), 33.4 (s, *C*(CH$_3$)$_3$), 27.7 (s, C(*C*H$_3$)$_3$), 19.1 (s, NCH$_2$*C*H$_2$). ESI-MS calcd. (found) for [M^+ – BF_4] $(C_{14}H_{29}N_2)^+$: *m/z* 225.2331 (225.2334).

7.3.18 Preparation of 1,3-dicyclohexyl-3,4,5,6-tetrahydropyrimidin-1-ium hexafluorophosphate ([6CyH]PF$_6$)

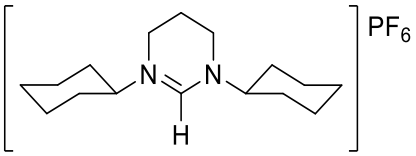

7.3.18.1 Preparation of N,N'-bis(cyclohexyl)formamidine

Cyclohexylamine (6.0 g, 60.0 mmol), triethyl orthoformate (4.5 g, 30.0 mmol) and glacial acetic acid (0.2 g, 3.0 mmol) were charged to a 100 mL round bottom flask (**CAUTION** – fumes on addition of acid) and distilled at 413 K for 2 hrs. Upon cooling to room temperature, an off-white solid formed, which was isolated and washed with Et_2O (2 × 10 mL). Yield: 0.9 g (9%).

7.3.18.2 Preparation of 1,3-dicyclohexyl-3,4,5,6-tetrahydropyrimidin-1-ium hexafluorophosphate ([6CyH]PF$_6$)

Following the same method as for [6^{i}BuH]PF_6 (section 7.3.16.2), but using N,N'-*bis*(cyclohexyl)formamidine (0.9 g, 4.3 mmol), BrCH$_2$CH$_2$CH$_2$Br (1.0 g, 4.8 mmol) and K_2CO_3 (0.3 g, 2.2 mmol) in CH_3CN (150 mL) to form [6CyH]Br as an off-white precipitate, which upon isolating on a Buchner funnel, became sticky. Yield: 0.8 g (56%).

Identical anion exchange conditions were used to those that were employed for [6^{i}BuH]PF_6 (section 7.3.16.2), but with [6CyH]Br (0.8 g, 2.4 mmol) and KPF_6 (0.5 g, 2.9 mmol) in $(CH3)_2CO/H_2O$ to yield [6CyH]PF_6 as a white solid. Yield: 0.8 g (85%). ^{1}H NMR (DMSO-*d*$_6$, 500 MHz, 298 K): δ 8.22 (s, NC*H*N), 3.42 (m, NC*H*), 3.34 (t, $^{3}J_{HH}$ = 5.7 Hz, NC*H*$_2$CH$_2$), 1.91 (quin, $^{3}J_{HH}$ = 5.7 Hz, NCH$_2$C*H*$_2$), 1.79 (br d, Cy), 1.49 – 1.62 (m, Cy), 1.20 – 1.37 (m, Cy), 1.08 – 1.13 (m, Cy). ^{13}C{^{1}H} NMR (DMSO-*d*$_6$, 125 MHz, 298 K): δ 150.8 (s, N*C*HN), 63.2 (s, N*C*H), 40.0 (s, N*C*H$_2$CH$_2$), 29.9 (s, *C*H$_2$), 24.8 (s,

CH_2), 24.6 (s, CH_2), 18.9 (s, NCH_2CH_2). ESI-MS calcd. (found) for $[M^+ - PF_6]$ $(C_{16}H_{29}N_2)^+$: *m/z* 249.2331 (249.2333).

7.3.19 Preparation of 1,3-diisobutyl-4,5,6,7-tetrahydro-[1,3]-diazepin-1-ium tetrafluoroborate ([7^{i}BuH]BF$_4$)

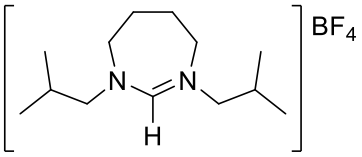

Following the same method as for [6^{i}BuH]PF_6 (section 7.3.16.2), but using N,N'-*bis*(isobutyl)formamidine (4.7 g, 30.0 mmol), $ICH_2CH_2CH_2CH_2I$ (9.8 g, 31.5 mmol) and K_2CO_3 (2.1 g, 15.0 mmol) in CH_3CN (150 mL) to form [7^{i}BuH]I as an off-white precipitate. Yield: 8.4 g (83%).

Identical anion exchange conditions to those that were used for [6^{i}BuH]PF_6 (section 7.3.16.2) were employed, but with [7^{i}BuH]I (12.6 g, 37.2 mmol) and $NaBF_4$ (4.9 g, 44.7 mmol) to form [7^{i}BuH]BF_4 as a white precipitate. Yield: 9.0 g (81%). ^{1}H NMR ($CDCl_3$, 500 MHz, 298 K): δ 8.02 (s, 1H, NC*H*N), 3.70 (t, $^3J_{HH}$ = 5.4 Hz, 4H, NCH_2CH_2), 3.33 (d, $^3J_{HH}$ = 7.5 Hz, 4H, NCH_2), 2.12 (t, $^3J_{HH}$ = 5.4 Hz, 4H, NCH_2CH_2), 1.97 (sept, $^3J_{HH}$ = 6.8 Hz, 2H, $CH(CH_3)_2$ signals), 0.92 (d, $^3J_{HH}$ = 6.8 Hz, 12H, $CH(CH_3)_2$). ^{13}C{^{1}H} NMR ($CDCl_3$, 125 MHz, 298 K): δ 158.3 (s, N*C*HN), 65.2 (s, NCH_2), 50.0 (s, NCH_2CH_2), 27.1 (s, $CH(CH_3)_2$), 25.0 (s, NCH_2CH_2), 19.4 (s, $CH(CH_3)_2$). ESI-MS calcd. (found) for $[M^+ - BF_4]$ $(C_{13}H_{27}N_2)^+$: *m/z* 211.2174 (211.2215).

7.3.20 Preparation of 1,3-dineopentyl-4,5,6,7-tetrahydro-[1,3]-diazepin-1-ium tetrafluoroborate ([7^{n}PentH]BF$_4$)

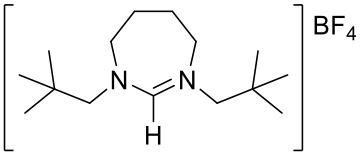

Following the same method as for [6^{i}BuH]PF_6 (section 7.3.16.2), but using N,N'-*bis*(neopentyl)formamidine (4.6 g, 25.0 mmol), $ICH_2CH_2CH_2CH_2I$ (8.1 g, 26.3 mmol) and K_2CO_3 (1.7 g, 12.5 mmol) in CH_3CN (100 mL) to form [7^{n}PentH]I as an off-white precipitate. Yield: 5.6 g (61%).

Identical anion exchange conditions were used to those that were employed for [6^{i}BuH]PF_6 (section 7.3.16.2), but with [7^{n}PentH]I (5.6 g, 15.3 mmol) and $NaBF_4$ (2.0 g,

18.3 mmol) in $(CH3)_2CO/H_2O$ to form [7^nPentH]BF_4 as a white precipitate. Yield: 3.8 g (75%). ^{1}H NMR ($CDCl_3$, 500 MHz, 298 K): δ 8.02 (s, 1H, NC*H*N), 3.81 (t, $^3J_{HH}$ = 5.5 Hz, 4H, NC*H*$_2$CH$_2$), 3.44 (s, 4H, NC*H*$_2$), 2.18 (m, $^3J_{HH}$ = 5.5 Hz, 4H, NCH$_2$C*H*$_2$), 1.00 (s, 18H, C(C*H*$_3$)$_3$). ^{13}C{^{1}H} NMR ($CDCl_3$, 125 MHz, 298 K): δ 160.6 (s, N*C*HN), 69.9 (s, NCH$_2$), 52.9 (s, N*C*H$_2$CH$_2$), 33.3 (s, *C*(CH$_3$)$_3$), 27.6 (s, C(*C*H$_3$)$_3$), 25.1 (s, NCH$_2$*C*H$_2$). ESI-MS calcd. (found) for [M^+ – BF_4] $(C_{15}H_{31}N_2)^+$: *m/z* 239.2487 (239.2539).

7.4 Isolation of Free RE-NHCs

All reactions were performed using standard Schlenk line techniques under an argon atmosphere. The reaction conditions were similar to those used by Cavell and co-workers, using the appropriate pyrimidinium/diazepinium tetrafluoroborate salt and $KN(SiMe_3)_2$ in C_6H_6.[15] Again, the exception to this was with the diamidocarbene species 6MesDAC where the base was changed to $NaN(SiMe_3)_2$. No alkyl RE-NHCs were successfully isolated due to their oily nature.

7.4.1 General Procedure for Preparation of Free RE-NHCs

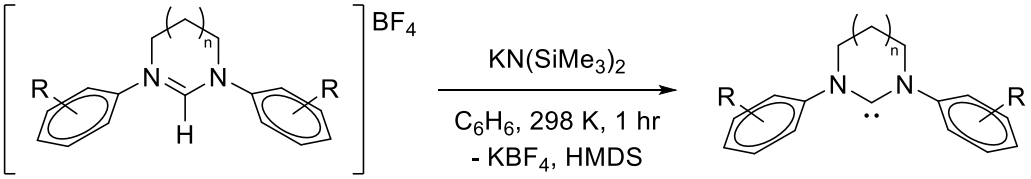

7.4.1.1 Preparation of 6Mes (1,3-bis(2,4,6-trimethylphenyl)-3,4,5,6-tetrahydropyrimid-2-ylidene)

A flame-dried Schlenk flask was charged with [6MesH]BF_4 (6.0 g, 14.7 mmol) and $KN(SiMe_3)_2$ (3.0 g, 15.0 mmol) in C_6H_6 (60 mL) and stirred for 1 hr. Solvent was removed under reduced pressure, the resulting off-white coloured residue was extracted into Et_2O (60 mL) and filtered through celite pre-wetted with Et_2O. The solution was concentrated and left at 243 K overnight to yield white crystalline solid which was isolated, washed with cold Et_2O (2 × 30 mL), and dried *in vacuo*. Yield: 2.70 g (57%). ^{1}H NMR (C_6D_6, 500 MHz, 298 K): δ 6.85 (s, 4H, *m*-C*H*$_{aryl}$), 2.76 (t, $^3J_{HH}$ = 5.9 Hz, 4H, NC*H*$_2$), 2.31 (s, 12H, *o*-C*H*$_3$), 2.17 (s, 6H, *p*-C*H*$_3$), 1.68 (m, 2H, NCH$_2$C*H*$_2$).

7.4.1.2 Preparation of 6Xyl (1,3-bis(2,6-dimethylphenyl)-3,4,5,6-tetrahydropyrimid-2-ylidene)

Method as for 6Mes (section 7.4.1.1), but using [6XylH]BF_4 (3.0 g, 7.9 mmol) and $KN(SiMe_3)_2$ (1.7 g, 8.5 mmol) in C_6H_6 (60 mL) to generate 6Xyl. Yield: 1.7 g (73%). ^{1}H NMR (C_6D_6, 500 MHz, 298 K): δ 7.05 (s, 6H, *m,p*-CH_{aryl}), 2.69 (t, $^3J_{HH}$ = 5.8 Hz, 4H, NCH_2), 2.29 (s, 12H, *o*-CH_3), 1.63 (quin, $^3J_{HH}$ = 5.8 Hz, 2H, NCH_2CH_2).

7.4.1.3 Preparation of 6^{o}Tol (1,3-bis(2-methylphenyl)-3,4,5,6-tetrahydropyrimid-2-ylidene)

Method as for 6Mes (section 7.4.1.1), but using [6^{o}TolH]BF_4 (3.0 g, 8.5 mmol) and $KN(SiMe_3)_2$ (1.8 g, 9.0 mmol) in C_6H_6 (60 mL) to generate 6^{o}Tol. Yield: 1.1 g (48%). ^{1}H NMR (C_6D_6, 500 MHz, 298 K): δ 7.25 (m, 2H, *o*-CH_{aryl}), 7.02 – 7.12 (m, 6H, *m,p*-CH_{aryl}), 2.88 (t, $^3J_{HH}$ = 5.9 Hz, 4H, NCH_2), 2.33 (s, 6H, *o*-CH_3), 1.59 (m, 2H, NCH_2CH_2).

7.4.1.4 Preparation of 6^{m}Xyl (1,3-bis(3,5-dimethylphenyl)-3,4,5,6-tetrahydropyrimid-2-ylidene)

Method as for 6Mes (section 7.4.1.1), but using [6^{m}Xyl]BF_4 (0.4 g, 1.1 mmol) and $KN(SiMe_3)_2$ (0.2 g, 1.1 mmol) in C_6H_6 (30 mL) to generate 6^{m}Xyl. Yield: 0.1 g (34%). ^{1}H NMR (C_6D_6, 500 MHz, 298 K): δ 6.52 (s, 4H, *o*-CH_{aryl}), 6.46 (s, 2H, *p*-CH_{aryl}), 3.23 (br m, 4H, NCH_2), 2.25 (s, 12H, *m*-CH_3), 1.89 (br m, 2H, NCH_2CH_2).

7.4.1.5 Preparation of 6Xyl-p-Br (1,3-bis(4-bromo-2,6-dimethylphenyl)-3,4,5,6-tetrahydropyrimid-2-ylidene)

Method as for 6Mes (section 7.4.1.1), but using [6Xyl-*p*-BrH]BF_4 (2.3 g, 4.3 mmol) and $KN(SiMe_3)_2$ (0.9 g, 4.5 mmol) in C_6H_6 (60 mL) to generate 6Xyl-*p*-Br. Yield: 0.7 g (37%). ^{1}H NMR (C_6D_6, 500 MHz, 298 K): δ 7.16 (s, 4H, *m*-CH_{aryl}), 2.49 (t, $^3J_{HH}$ = 5.7 Hz, 4H, NCH_2), 2.02 (s, 12H, *o*-CH_3), 1.49 (quin, $^3J_{HH}$ = 5.7 Hz, 2H, NCH_2CH_2).

7.4.1.6 Preparation of 7Mes (1,3-bis(2,4,6-trimethylphenyl)-4,5,6,7-tetrahydro-[1,3]-diazepin-2-ylidene)

Method as for 6Mes (section 7.4.1.1), but using [7MesH]BF_4 (3.0 g, 7.1 mmol) and $KN(SiMe_3)_2$ (1.6 g, 8.0 mmol) in C_6H_6 (60 mL) to generate 7Mes. Yield: 1.2 g (50%). ^{1}H NMR (C_6D_6, 500 MHz, 298 K): δ 6.84 (s, 4H, *m*-C*H*$_{aryl}$), 3.35 (br s, 4H, NC*H*$_2$), 2.35 (s, 12H, *o*-C*H*$_3$), 2.19 (s, 6H, *p*-C*H*$_3$), 1.75 (br s, 4H, NCH_2CH_2).

7.4.1.7 Preparation of 7Xyl (1,3-bis(2,6-dimethylphenyl)-4,5,6,7-tetrahydro-[1,3]-diazepin-2-ylidene)

Method as for 6Mes (section 7.4.1.1), but using [7XylH]BF_4 (3.0 g, 7.6 mmol) and $KN(SiMe_3)_2$ (1.7 g, 8.5 mmol) in C_6H_6 (60 mL) to generate 7Xyl. Yield: 1.4 g (61%). ^{1}H NMR (C_6D_6, 500 MHz, 298 K): δ 7.04 (m, 6H, *m,p*-C*H*$_{aryl}$), 3.30 (m, 4H, NC*H*$_2$), 2.33 (s, 12H, *o*-C*H*$_3$), 1.71 (m, 4H, NCH_2CH_2).

7.4.1.8 Preparation of 7^{o}Tol (1,3-bis(2-methylphenyl)-4,5,6,7-tetrahydro-[1,3]-diazepin-2-ylidene)

Method as for 6Mes (section 7.4.1.1), but using [7^{o}TolH]BF_4 (3.0 g, 8.1 mmol) and $KN(SiMe_3)_2$ (1.8 g, 9.0 mmol) in C_6H_6 (60 mL) to generate 7^{o}Tol. Yield: 1.9 g (83%). ^{1}H NMR (C_6D_6, 500 MHz, 298 K): δ 7.25 – 7.30 (m, 2H, *o*-C*H*$_{aryl}$), 6.94 – 7.13 (m, 6H, *m,p*-C*H*$_{aryl}$), 3.45 (br s, 4H, NC*H*$_2$), 2.33 (s, 6H, *o*-C*H*$_3$), 1.68 (m, 4H, NCH_2CH_2).

7.4.1.9 Preparation of 7Xyl-p-Br (1,3-bis(4-bromo-2,6-dimethylphenyl)-4,5,6,7-tetrahydro-[1,3]-diazepin-2-ylidene)

Method as for 6Mes (section 7.4.1.1), but using [7Xyl-*p*-BrH]BF_4 (3.5 g, 6.7 mmol) and $KN(SiMe_3)_2$ (1.5 g, 7.5 mmol) in C_6H_6 (60 mL) to generate 7Xyl-*p*-Br. Yield: 0.9 g (32%). ^{1}H NMR (C_6D_6, 500 MHz, 298 K): δ 7.16 (s, 4H, *m*-C*H*$_{aryl}$), 3.08 (m, 4H, NC*H*$_2$), 2.06 (s, 12H, *o*-C*H*$_3$), 1.58 (m, 4H, NCH_2CH_2).

7.4.1.10 Preparation of 6MesDAC 1,3-bis(2,4,6-trimethylphenyl)-4,6-diketo-5,5-dimethylpyrimidin-2-ylidene

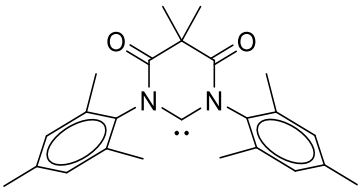

A flame-dried Schlenk flask was charged with [6MesDAC·HCl] (2.8 g, 6.8 mmol) and $NaN(SiMe_3)_2$ (1.3 g, 7.1 mmol) in C_6H_6 (60 mL) and the suspension stirred for 1 hr before filtering through celite. The solvent was removed using reduced pressure and the resulting off-white residue washed with hexane (3 × 30 mL) and dried *in vacuo*. Yield: 2.1 g (81%). ^{1}H NMR (C_6D_6, 500 MHz, 298 K): δ 6.79 (s, 4H, *m*-CH_{aryl}), 2.12 (s, 18H, *o,p*-CH_3), 1.50 (s, 6H, CCH_3).

7.5 Synthesis of Ni(RE-NHC)(PPh_3)Br Compounds

7.5.1 Synthesis of Ni(6Mes)(PPh_3)Br (2.1)

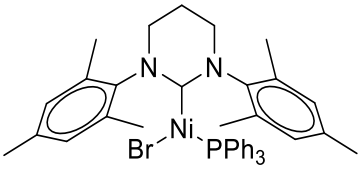

6Mes (640 mg, 2.00 mmol), $Ni(COD)_2$ (275 mg, 1.00 mmol) and $Ni(PPh_3)_2Br_2$ (743 mg, 1.00 mmol) were dissolved in THF (30 mL) in a J. Young's ampoule to form a dark yellow solution. After 1 hr the solution was pumped down to dryness, washed with Et_2O (2 × 10 mL) and the resulting solid recrystallised from THF/hexane at room temperature to yield analytically pure compound. Yield: 1.21 g (84%). ^{1}H NMR (C_6D_6, 500 MHz, 298 K): δ 30.2 (br s), 16.1 (br s), 10.8 (s), 9.6 (br s), 8.8 (br s), 7.7 (br s), 4.0 (s), 1.9 (s), 0.7 (br s), -1.2 (br s), -16.8 (br s). Anal. calcd. (found) for $C_{40}H_{43}N_2BrNiP$ (%): C 66.60 (66.45), H 6.01 (6.16), N 3.88 (3.95). Solution magnetic moment (Evans method, C_6H_6): 2.1 μ_B.

7.5.2 Synthesis of Ni(6Xyl)(PPh$_3$)Br (2.2)

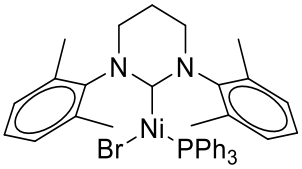

Method as for **2.1** (section 7.5.1), but with 6Xyl (300 mg, 1.03 mmol), Ni(COD)$_2$ (141 mg, 0.51 mmol) and Ni(PPh$_3$)$_2$Br$_2$ (381 mg, 0.51 mmol). Analytically pure product was achieved upon recrystallisation from THF/hexane. Yield: 530 mg (71%). ^{1}H NMR (C$_6$D$_6$, 500 MHz, 298 K): δ 29.4 (br s), 16.3 (br s), 10.8 (s), 9.8 (br s), 8.5 (br s), 8.1 (br s), 2.2 (br s), 1.9 (br s), 0.7 (br s), -1.1 (br s), -17.1 (br s). Anal. calcd. (found) for C$_{38}$H$_{39}$N$_2$BrNiP (%): C 65.83 (65.50), H 5.67 (5.50), N 4.04 (4.05). Solution magnetic moment (Evans method, C$_6$H$_6$): 2.0 μ$_B$.

7.5.3 Synthesis of Ni(6^{o}Tol)(PPh$_3$)Br (2.3)

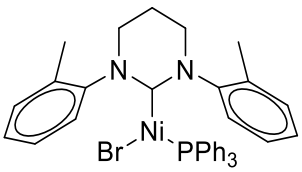

Method as for **2.1** (section 7.5.1), but with 6^{o}Tol (250 mg, 0.95 mmol), Ni(COD)$_2$ (130 mg, 0.47 mmol) and Ni(PPh$_3$)$_2$Br$_2$ (351 mg, 0.47 mmol). Analytically pure product was achieved upon recrystallisation from C$_6$H$_6$/hexane. Yield: 202 mg (32%). ^{1}H NMR (C$_6$D$_6$, 500 MHz, 298 K): δ 31.5 (br s), 18.4 (br s), 11.1 (br m), 9.2 (br s), 8.9 (br m), 7.7 (br s), 7.5 (br s), 5.5 (br s), 4.8 (br s), 1.3 (br m), 1.0 (br m), -0.1 (br s), -0.5 (br s), -11.2 (br s), -19.4 (br s). Anal. calcd. (found) for C$_{36}$H$_{35}$N$_2$BrNiP (%): C 65.00 (64.81), H 5.30 (5.21), N 4.21 (4.35). Solution magnetic moment (Evans method, C$_6$H$_6$): 1.8 μ$_B$.

7.5.4 Synthesis of Ni(6Xyl-p-Br)(PPh$_3$)Br (2.4)

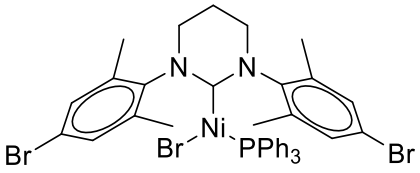

Method as for **2.1** (section 7.5.1), but with 6Xyl-*p*-Br (100 mg, 0.22 mmol), Ni(COD)$_2$ (31 mg, 0.11 mmol) and Ni(PPh$_3$)$_2$Br$_2$ (83 mg, 0.11 mmol). Multiple efforts to

isolate clean product were hindered by decomposition to leave a dull yellow/grey powder after all work-ups, even in a dry ice/$(CH3)_2CO$ bath at 195 K. The following yield and ^1H NMR data are of crude reaction mixtures. Yield: 132 mg (70%). ^1H NMR (C_6D_6, 500 MHz, 298 K): δ 28.6 (br s), 16.0 (br s), 11.0 (br s), 9.9 (br s), 8.2 (br s), 1.9 (br s), 0.4 (br s), -0.9 (br s), 1.0 (br s), -17.6 (br s).

7.5.5 Synthesis of Ni(7Mes)(PPh$_3$)Br (2.5)

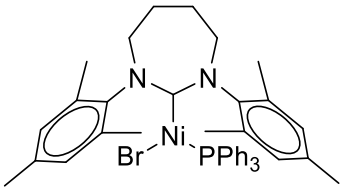

Method as for **2.1** (section 7.5.1), but with 7Mes (100 mg, 0.30 mmol), $Ni(COD)_2$ (41 mg, 0.15 mmol) and $Ni(PPh_3)_2Br_2$ (111 mg, 0.15 mmol), recrystallised from THF/hexane to form a bright yellow solid. Yield: 148 mg (67%). ^1H NMR (C_6D_6, 500 MHz, 298 K): δ 12.3 (br s), 10.6 (br s), 10.0 (br s), 8.6 (br s), 8.1 (br s), 4.5 (s), 3.3 (br s), 2.9 (m), 2.8 (s), 2.5 (s), 2.4 (br s), 1.8 (br s), 0.9 (br s), -1.3 (br s). Anal. calcd. (found) for $C_{41}H_{45}N_2BrNiP$ (%): C 66.96 (67.22), H 6.17 (6.26), N 3.81 (3.41). Solution magnetic moment (Evans method, C_6H_6): 1.8 μ_B.

7.5.6 Synthesis of Ni(7Xyl)(PPh$_3$)Br (2.6)

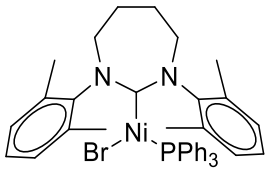

Method as for **2.1** (section 7.5.1), but with 7Xyl (250 mg, 0.82 mmol), $Ni(COD)_2$ (112 mg, 0.41 mmol) and $Ni(PPh_3)_2Br_2$ (303 mg, 0.41 mmol). Analytically pure product was achieved upon recrystallisation from C_6H_6/hexane. Yield: 377 mg (65%). ^1H NMR (C_6D_6, 500 MHz, 298 K): δ 11.7 (br s), 10.6 (br s), 10.1 (br s), 8.5 (br s), 7.9 (br s), 3.5 (br s), 2.8 (s), 2.4 – 2.3 (br m), 1.0 (br s), -1.2 (br s). Anal. calcd. (found) for $C_{39}H_{41}N_2BrNiP{\cdot}0.5C_6H_6$ (%): C 67.59 (67.80), H 5.94 (5.76), N 3.75 (3.61). Solution magnetic moment (Evans method, C_6H_6): 1.9 μ_B.

7.5.7 Synthesis of Ni(7^{o}Tol)(PPh$_3$)Br (2.7)

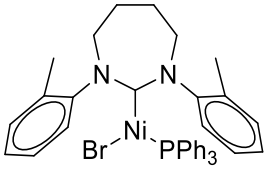

Method as for **2.1** (section 7.5.1), but with 7^{o}Tol (250 mg, 0.90 mmol), Ni(COD)$_2$ (124 mg, 0.45 mmol) and Ni(PPh$_3$)$_2$Br$_2$ (334 mg, 0.45 mmol). Analytically pure product was achieved upon recrystallisation from C_6H_6/hexane. Yield: 234 mg (38%). ^{1}H NMR (C_6D_6, 500 MHz, 298 K): δ 11.0 (br s), 9.4 (br s), 7.9 (br s), 4.4 (br s), 2.4 (s), 0.2 (br s), -2.5 (br s). Anal. calcd. (found) for $C_{37}H_{37}N_2BrNiP$ (%): C 65.42 (65.38), H 5.49 (5.39), N 4.12 (4.02). Solution magnetic moment (Evans method, C_6H_6): 1.7 μ_B.

7.5.8 Synthesis of Ni(7Xyl-p-Br)(PPh$_3$)Br (2.8)

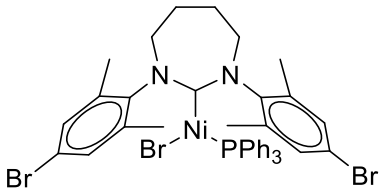

Method as for **2.1** (section 7.5.1), but with 7Xyl-*p*-Br (76 mg, 0.16 mmol), Ni(COD)$_2$ (23 mg, 0.08 mmol) and Ni(PPh$_3$)$_2$Br$_2$ (61 mg, 0.08 mmol). Just as for compound **2.7** (section 7.5.4), multiple efforts to isolate clean product were hindered by decomposition to leave a dull yellow/grey powder after all work-ups, even in a dry ice/(CH3)$_2$CO bath at 195 K. The following yield and ^{1}H NMR data are of crude reaction mixtures. Yield: 115 mg (81%). ^{1}H NMR (C_6D_6, 500 MHz, 298 K): δ 18.9 (br s), 10.8 (br s), 10.5 (br s), 7.8 (br s), 5.6 (br s), 2.6 (br s), 2.2 (br s), 0.9 (br 2), -1.2 (br s), -4.8 (br s).

7.5.9 Synthesis of Ni(6MesDAC)(PPh$_3$)Br (2.9)

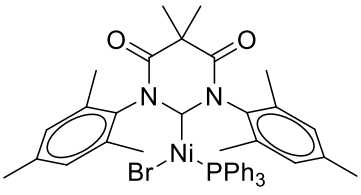

Method as for **2.1** (section 7.5.1), but with 6MesDAC (137 mg, 0.36 mmol), Ni(COD)$_2$ (50 mg, 0.18 mmol) and Ni(PPh$_3$)$_2$Br$_2$ (135 mg, 0.18 mmol), recrystallised from C_6H_6/hexane to form a dark brown solid. Yield: 233 mg (82%). ^{1}H NMR (C_6D_6, 500 MHz, 298 K): δ 10.4 (br s), 9.0 (br s), 8.4 (br s), 4.4 (br s), 3.7 (br s), 2.4 (s), 2.4 (s),

1.2 (s), -0.8 (br s). Anal. calcd. (found) for $C_{42}H_{43}N_2BrNiO_2P$ (%): C 64.89 (65.02), H 5.58 (5.44), N 3.60 (3.78). Solution magnetic moment (Evans method, C_6H_6): 1.3 μ_B.

7.5.10 Synthesis of Ni(6Et)$_2$Br$_2$ (2.10)

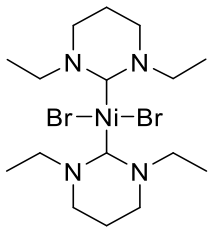

A THF (2 mL) suspension of [6EtH]PF_6 (10 mg, 0.03 mmol) and $KN(SiMe_3)_2$ (7 mg, 0.03 mmol) in a J. Young's NMR tube was shaken for 1 hr at room temperature, before shaking was stopped to allow the precipitate to settle. A second NMR tube was charged with $Ni(COD)_2$ (5 mg, 0.02 mmol) and $Ni(PPh_3)_2Br_2$ (13 mg, 0.02 mmol) and cooled in an ice bath to prevent the $Ni(COD)_2$ decomposing. The THF solution was transferred to the second NMR tube *via* filter cannula. Once all the THF had transferred across, the now orange solution was shaken for a further 2 hrs at room temperature. All the volatiles were then removed under vacuum and the yellow/orange residue washed with hexane (2 × 2 mL). Orange blocks formed from crystallisation in THF/hexane, shown to be the Ni(II) compound **2.10** rather than the mono-carbene Ni(I) product.

7.5.11 Synthesis of Ni(6^{i}Pr)$_2$Br$_2$ (2.11)

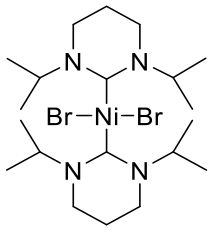

Method as for **2.10** (section 7.5.13), but with [6^{i}PrH]PF_6 (12 mg, 0.04 mmol) and $KN(SiMe_3)_2$ (8 mg, 0.04 mmol) in THF (0.5 mL) followed by $Ni(COD)_2$ (5 mg, 0.02 mmol) and $Ni(PPh_3)_2Br_2$ (14 mg, 0.02 mmol). Orange blocks formed from crystallisation in THF/hexane, shown to be the Ni(II) compound **2.11** rather than the mono-carbene Ni(I) product.

7.5.12 Synthesis of Ni(6^{t}Bu)'Br (2.12)

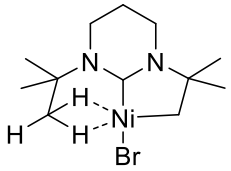

Method as for **2.10** (section 7.5.13), but with [6^{t}BuH]BF_4 (15 mg, 0.05 mmol) and $KN(SiMe_3)_2$ (11 mg, 0.05 mmol) in THF (5 mL) followed by $Ni(COD)_2$ (8 mg, 0.03 mmol) and $Ni(PPh_3)_2Br_2$ (20 mg, 0.03 mmol). Compound **2.12** crystallised as one large orange block. Yield: 3 mg (18%). ^{1}H NMR (C_6D_6, 500 MHz, 298 K): δ 2.51 (s, 2H, NiC*H*$_2$), 2.00 (m, 4H, NC*H*$_2$), 0.91 (s, 6H, NC(C*H*$_3$)$_2$), 0.86 (m, 2H, NCH_2CH_2), 0.54 (s, 9H, NC(C*H*$_3$)$_3$). Anal. calcd. (found) for $C_{12}H_{23}N_2BrNi$ (%): C 43.16 (42.92), H 6.94 (6.48), N 8.39 (8.56).

7.5.13 Synthesis of Ni(6^{i}Bu)(PPh$_3$)Br (2.13)

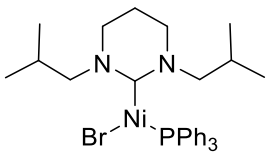

A THF (30 mL) suspension of [6^{i}BuH]BF_4 (284 mg, 1.00 mmol) and $KN(SiMe_3)_2$ (200 mg, 1.00 mmol) in a Schlenk flask was stirred for 1 hr at room temperature, before stirring was stopped to allow precipitate to settle. A second Schlenk flask was charged with $Ni(COD)_2$ (138 mg, 0.50 mmol) and $Ni(PPh_3)_2Br_2$ (372 mg, 0.50 mmol) and cooled in an ice bath to prevent the $Ni(COD)_2$ decomposing. The THF solution was transferred to the second Schlenk flask *via* filter cannula. Once all the THF had transferred across, the now orange solution was stirred for a further 2 hrs at room temperature. All the volatiles were then removed under vacuum and the yellow/orange residue washed with hexane (2 × 30 mL). Clean compound was recrystallised from C_6H_6/hexane as yellow blocks. Yield: 220 mg (37%). ^{1}H NMR (C_6D_6, 500 MHz, 298 K): δ 18.1 (br s), 10.8 (br s), 9.3 (br s), 5.5 (br s), 3.1 (br s), 2.5 (br s), 1.7 (br s), -0.1 (br s), -4.0 (br s).

7.5.14 Synthesis of Ni(6^{n}Pent)(PPh$_3$)Br (2.14)

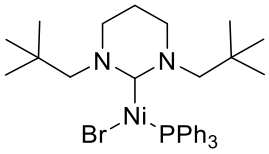

Method as for **2.13** (section 7.5.13), but with [6^{n}PentH]BF$_4$ (312 mg, 1.00 mmol) and KN(SiMe$_3$)$_2$ (210 mg, 1.05 mmol) in THF (30 mL) followed by Ni(COD)$_2$ (138 mg, 0.50 mmol) and Ni(PPh$_3$)$_2$Br$_2$ (372 mg, 0.50 mmol). The resultant yellow residue was recrystallised from C$_6$H$_6$/hexane, where two different forms of crystals always co-crystallised. Compound **2.14** crystallised as yellow blocks, whereas a Ni(II) side product Ni(6^{n}Pent)$_2$Br$_2$ (Appendix 1) crystallised as dark orange blocks. Yield of both products: 537 mg (86%). ^{1}H NMR (C$_6$D$_6$, 500 MHz, 298 K): δ 23.7 (br s), 10.9 (br s), 5.8 (br s), 2.4 (br s), 1.0 (br s), -0.8 (br s), -5.2 (br s), -18.3 (br s). Anal. calcd. (found) for C$_{32}$H$_{43}$N$_2$BrNiP (%): C 61.47 (61.42), H 6.93 (6.90), N 4.48 (4.32). Solution magnetic moment (Evans method, THF): 1.6 μ$_B$.

7.5.15 Synthesis of Ni(7^{i}Bu)(PPh$_3$)Br (2.15)

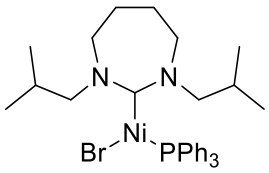

Method as for **2.13** (section 7.5.13), but with [7^{i}BuH]BF$_4$ (149 mg, 0.50 mmol) and KN(SiMe$_3$)$_2$ (100 mg, 0.50 mmol) in THF (30 mL) followed by Ni(COD)$_2$ (69 mg, 0.25 mmol) and Ni(PPh$_3$)$_2$Br$_2$ (186 mg, 0.25 mmol). Efforts to isolate compound **2.15** only gave dark orange blocks of a Ni(II) side product Ni(7^{i}Bu)$_2$Br$_2$ (Appendix 1). Yield: 110 mg (36%). ^{1}H NMR (C$_6$D$_6$, 500 MHz, 298 K): δ 10.8 (br s), 9.6 (br s), 5.3 (br s), 5.1 (br s), 4.9 (br s), 3.2 (br s), 2.8 (br s), 1.9 (br s), 1.3 (br s).

7.5.16 Synthesis of Ni(7^{n}Pent)(PPh$_3$)Br (2.16)

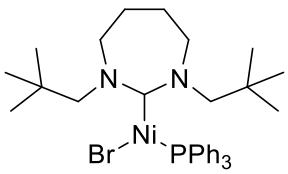

Method as for **2.13** (section 7.5.13), but with [7^{n}PentH]BF$_4$ (237 mg, 0.73 mmol) and KN(SiMe$_3$)$_2$ (145 mg, 0.73 mmol) in THF (30 mL) followed by Ni(COD)$_2$ (100 mg,

0.36 mmol) and $Ni(PPh_3)_2Br_2$ (270 mg, 0.36 mmol). Compound **2.16** crystallised as yellow blocks, whereas a Ni(II) side product $Ni(7^nPent)_2Br_2$ (Appendix 1) crystallised as dark orange blocks. Yield of both products: 133 mg (26%). ^{1}H NMR (C_6D_6, 500 MHz, 298 K): δ 10.9 (br s), 5.5 (br s), 4.8 (br s), 3.0 (br s), 2.3 (br s), 1.3 (br s), 1.1 (br s), 0.7 (br s).

7.6 Reactivity of Ni(6Mes)(PPh$_3$)Br

7.6.1 Synthesis of [Ni(6Mes)(PPh$_3$)(THF)]PF$_6$ (2.17)

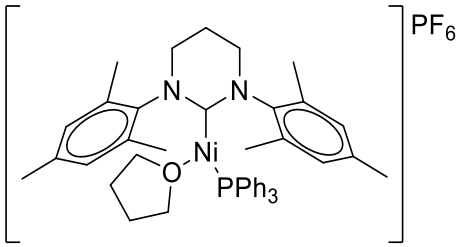

A THF (20 mL) solution of $TlPF_6$ (95 mg, 0.27 mmol) was added to a J. Young's ampoule of **2.1** (163 mg, 0.023 mmol) and the suspension stirred for 2 hrs. Insoluble material was filtered off, the THF solution concentrated and hexane (20 mL) was added to form a beige precipitate. The solid was isolated by cannula filtration, recrystallised from THF/hexane, and dried *in vacuo*. Yield: 138 mg (85%). ^{1}H NMR (THF-d_8, 500 MHz, 298 K): δ 16.9 (br s), 9.9 (br s), 6.1 (br s), 5.3 (br s), 3.1 (br s). Anal. calcd. (found) for $C_{44}H_{51}N_2F_6NiOP_2$ (%): C 61.56 (61.39), H 5.99 (5.85), N 3.26 (3.18). Solution magnetic moment (Evans method, THF): 2.2 μ_B.

7.6.2 Synthesis of [{Ni(6Mes)(PPh$_3$)}$_2$(μ-Br)]BAr$^F_4$ (2.18)

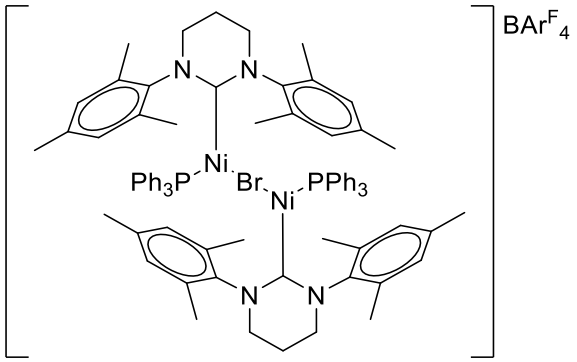

Compound **2.1** (100 mg, 0.14 mmol) and $NaBAr^F_4$ (130 mg, 0.15 mmol) were dissolved in Et_2O (10 mL) and the solution stirred for 16 hrs in a J. Young's resealable ampoule. The solution was concentrated to ca. 2 mL, filtered and layered with pentane

(10 mL) to form large orange crystals suitable for X-ray diffraction. Yield: 125 mg (81%). Anal. calcd. (found) for $C_{112}H_{98}N_4BBrF_{24}Ni_2P_2$ (%): C 60.43 (60.07), H 4.44 (4.68), N 2.52 (2.36). Solution magnetic moment (Evans method, Et_2O): 2.5 μ_B. Solid state magnetic moment (Gouy balance): 2.4 μ_B.

7.6.3 Synthesis of [Ni(6Mes)(PPh$_3$)(CO)]PF$_6$ (2.19)

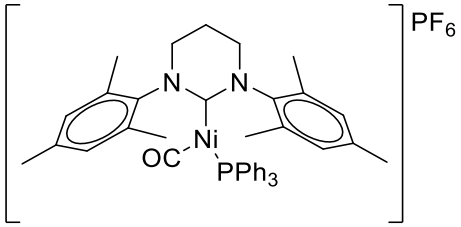

To a stirred, degassed THF solution (0.5 mL) of **2.17** (20 mg, 0.02 mmol), 1 atm of CO was added. An immediate colour change from pale yellow to green occurred, and after 1 min the solution was reduced to dryness to prevent further reaction. The residue was extracted into THF (0.5 mL), filtered and layered with hexane (2 mL) to produce green crystals. Yield: 15 mg (79%). ^{1}H NMR (500 MHz, THF-d_8, 298 K): δ 16.9 (br s), 10.7 (br s), 9.9 (br s), 8.4 (s), 7.7 (br s), 7.1 (s), 6.5 (br s), 5.3 (br s), 4.9 (br s), 3.9 (br s), 3.4 (br s), 2.6 (br s), 2.4 (br s), 2.3 (br s), 2.1 (br s). IR (THF): ν_{CO} = 2035 cm^{-1}. IR (KBr): ν_{CO} = 2030 cm^{-1}. Anal. calcd. (found) for $C_{41}H_{43}N_2F_6NiOP$ (%): C 60.47 (60.45), H 5.32 (5.58), N 3.44 (2.96). Solution magnetic moment (Evans method, THF): 1.8 μ_B

7.7 Synthesis of Ni(RE-NHC)(PCy$_3$)Br Compounds

7.7.1 Synthesis of Ni(6Mes)(PCy$_3$)Br (2.20)

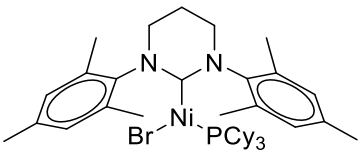

A flame-dried Schlenk flask was charged with 6Mes (200 mg, 0.62 mmol), PCy_3 (176 mg, 0.62 mmol), $Ni(COD)_2$ (86 mg, 0.32 mmol) and $Ni(dme)Br_2$ (96 mg, 0.32 mmol) before addition of C_6H_6 (30 mL). The reaction mixture was stirred for 1 hr at room temperature before cannula filtration into a second Schlenk flask. The C_6H_6 filtrate was pumped down to dryness under reduced pressure to leave a brown residue. Hexane (30 mL) was added to the residue and stirred vigorously for 30 min to form a fine beige powder. The product was isolated by removal of hexane washings with a cannula filter.

Analytically pure compound was obtained from recrystallisation in minimal C_6H_6 layered with hexane to yield pale-yellow crystals. Yield: 347 mg (75%). ^{1}H NMR (C_6D_6, 500 MHz, 298 K): δ 35.5 (br s), 22.5 (br s), 10.6 (br s), 10.2 (br s), 8.3 (br s), 4.7 (br s), 4.3 (s), 4.1 (br s), 3.7 (s), 1.8 (br s), -1.3 (br s). Solution magnetic moment (Evans method, THF): 2.1 μ_B.

7.7.2 Synthesis of Ni(6Xyl)(PCy$_3$)Br (2.21)

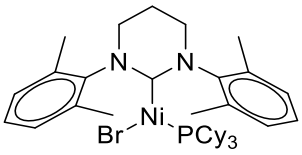

Method as for **2.20** (section 7.7.1), but using 6Xyl (100 mg, 0.34 mmol), PCy_3 (96 mg, 0.34 mmol), $Ni(COD)_2$ (47 mg, 0.17 mmol) and $Ni(dme)Br_2$ (53 mg, 0.17 mmol) in C_6H_6 (30 mL). Yield: 132 mg (54%). ^{1}H NMR (C_6D_6, 500 MHz, 298 K): δ 31.9 (br s), 20.0 (br s), 10.3 (br s), 9.6 (s), 8.7 (br s), 4.4 (br s), 3.6 (s), 2.1 (s), 1.9 (s), 1.7 (s), -1.9 (br s). Anal. calcd. (found) for $C_{38}H_{57}N_2BrNiP$ (%): C 64.15 (64.26), H 8.08 (7.88), N 3.94 (4.37). Solution magnetic moment (Evans method, THF): 2.1 μ_B.

7.7.3 Synthesis of Ni(7Mes)(PCy$_3$)Br (2.22)

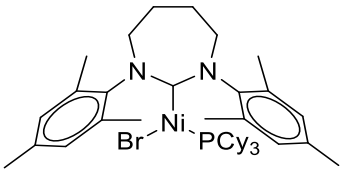

Method as for **2.20** (section 7.7.1), but using 7Mes (395 mg, 1.18 mmol), PCy_3 (332 mg, 1.18 mmol), $Ni(COD)_2$ (163 mg, 0.59 mmol) and $Ni(dme)Br_2$ (183 mg, 0.59 mmol). Yield: 250 mg (28%). ^{1}H NMR (C_6D_6, 500 MHz, 298 K): δ 28.5 (br s), 11.7 (br s), 11.0 (br s), 10.5 (br s), 8.5 (br s), 7.8 (br s), 6.8 (s), 4.6 (s), 4.2 (br s), 3.5 (br s), 3.2 (br s), 2.3 (s), 2.1 (s), 1.5 (br m), 1.1 (br m), -2.4 (br s). Solution magnetic moment (Evans method, THF): 2.2 μ_B.

7.7.4 Synthesis of Ni(7Xyl)(PCy$_3$)Br (2.23)

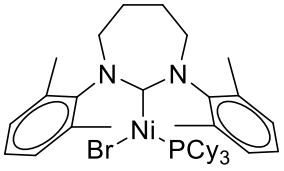

Method as for **2.20** (section 7.7.1), but using 7Xyl (389 mg, 1.27 mmol), PCy_3 (369 mg, 1.27 mmol), $Ni(COD)_2$ (174 mg, 0.63 mmol) and $Ni(dme)Br_2$ (194 mg, 0.63 mmol). Yield: 560 mg (61%). ^{1}H NMR (C_6D_6, 500 MHz, 298 K): δ 25.6 (br s), 12.0 (br s), 11.5 (br s), 10.7 (br s), 9.6 (br s), 8.7 (br s), 7.4 (br s), 4.3 (br s), 3.5 (br s), 2.2 (br s), 1.9 (br s), 1.6 (br s), 1.2 (br s), -2.9 (br s). Anal. calcd. (found) for $C_{39}H_{59}N_2BrNiP$ (%): C 64.57 (64.70), H 8.20 (8.18), N 3.86 (4.02). Solution magnetic moment (Evans method, THF): 2.2 μ_B.

7.8 Synthesis of Homoleptic [Ni(RE-NHC)$_2$]Br Compounds

7.8.1 Synthesis of [Ni(6Mes)$_2$]Br (3.1)

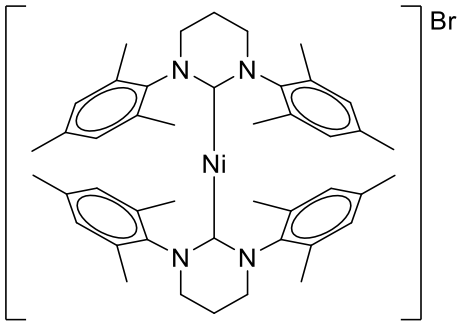

A flame-dried Schlenk flask was charged with compound **2.1** (250 mg, 0.37 mmol) and 6Mes (167 mg, 0.52 mmol) in THF (30 mL) and the contents stirred for 16 hrs to form an off-white suspension. The precipitate was isolated by cannula filtration, washed with Et_2O (2 × 10 mL), and dried under reduced pressure. Recrystallisation from CH_2Cl_2/hexane at room temperature yielded off-white crystals. Yield: 218 mg (81%). ^{1}H NMR (CD_2Cl_2, 500 MHz, 298 K): δ 52.7 (br s), 50.1 (br s), -10.6 (s), -12.8 (br s), -20.7 (s). Anal. calcd. (found) for $C_{44}H_{56}N_4BrNi$ (%): C 67.79 (67.86), H 7.24 (7.24), N 7.19 (6.98). Solution magnetic moment (Evans method, CH_2Cl_2): 3.3 μ_B.

7.8.2 Synthesis of [Ni(6Xyl)$_2$]Br (3.2)

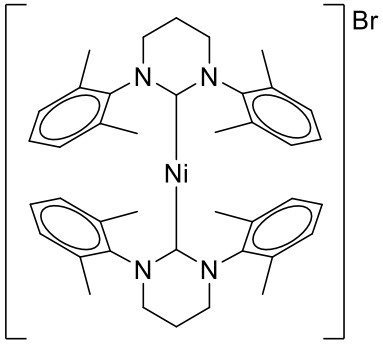

Method as for **3.1** (section 7.8.1), but using compound **2.2** (96 mg, 0.14 mmol) and 6Xyl (64 mg, 0.22 mmol) in THF (20 mL). Recrystallisation from CH_2Cl_2/hexane at room temperature yielded off-white crystals. Yield: 54 mg (54%). ^{1}H NMR (CD_2Cl_2, 500 MHz, 298 K): δ 54.4 (br s), 52.1 (br s), -13.3 (br s), -15.6 (s), -21.3 (s). Anal. calcd. (found) for $C_{40}H_{48}N_4BrNi$ (%): C 66.41 (66.62), H 6.69 (6.70), N 7.74 (7.54). Solution magnetic moment (Evans method, CH_2Cl_2): 3.3 μ_B.

7.8.3 Synthesis of [Ni(7Mes)$_2$]Br (3.3)

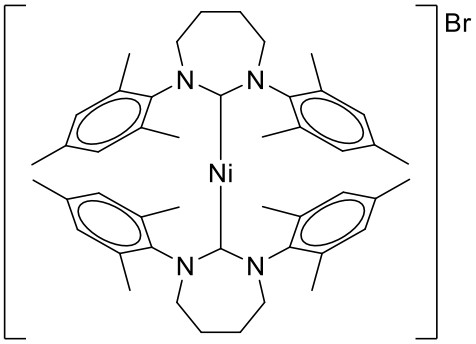

Method as for **3.1** (section 7.8.1), but using compound **2.5** (200 mg, 0.34 mmol) and 7Mes (171 mg, 0.51 mmol) in THF (30 mL). Recrystallisation from CH_2Cl_2/hexane at room temperature yielded yellow crystals. Yield: 181 mg (66%). ^{1}H NMR (CD_2Cl_2, 500 MHz, 298 K): δ 49.2 (br s), 38.7 (br s), -8.3 (s), -11.2 (br s), -17.7 (s). Acceptable element analysis could not be determined even after multiple attempts. Solution magnetic moment (Evans method, CH_2Cl_2): 3.0 μ_B.

7.8.4 Synthesis of [Ni(7Xyl)$_2$]Br (3.4)

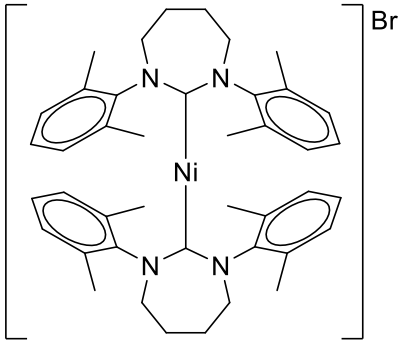

Method as for **3.1** (section 7.8.1), but using compound **2.6** (200 mg, 0.35 mmol) and 7Xyl (162 mg, 0.53 mmol) in THF (30 mL). Recrystallisation from CH_2Cl_2/hexane at room temperature yielded yellow crystals. Yield: 205 mg (77%). ^{1}H NMR (CD_2Cl_2, 500 MHz, 298 K): δ 51.1 (br s), 40.0 (br s), -11.8 (br s), -14.1 (s), -18.2 (s). Anal. calcd. (found) for $C_{42}H_{52}N_4BrNi$ (%): C 67.13 (67.39), H 6.97 (6.82), N 7.46 (7.31). Solution magnetic moment (Evans method, CH_2Cl_2): 3.1 μ_B.

7.8.5 Synthesis of [Ni(6Xyl-p-Br)$_2$]Br (3.5)

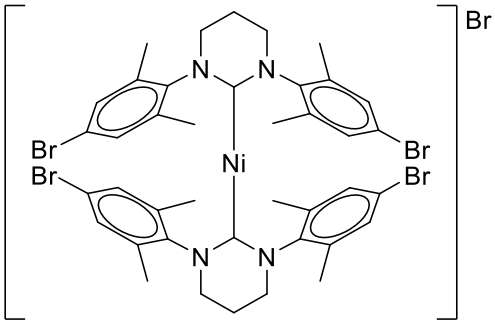

A flame-dried Schlenk flask was charged with [6Xyl-*p*-BrH]BF_4 (89 mg, 0.15 mmol) and $KN(SiMe_3)_2$ (30 mg, 0.15 mmol) in THF (15 mL) and the contents stirred for 1 hr to form an off-white suspension. After the precipitate was allowed to settle, the THF filtrate was decanted away into a second flame-dried Schlenk flask that contained compound **2.4** (85 mg, 0.10 mmol). The mixture of *in-situ* generated 6Xyl-*p*-Br and **2.4** was stirred for 2 hrs, forming a dark yellow suspension. The precipitate was isolated by cannula filtration, washed with Et_2O (2 × 10 mL) and dried under reduced pressure. Multiple attempts at recrystallisation from CH_2Cl_2/hexane at both 238 K and room temperature did not yield material suitable for X-ray diffraction, mainly just powder and oily residues. Yield: 107 mg (103% - must contain starting material). ^{1}H NMR (CD_2Cl_2, 500 MHz, 298 K): δ 53.1 (br s), 50.7 (br s), -12.0 (br s), -20.3 (br s).

7.8.6 Synthesis of [Ni(7Xyl-p-Br)$_2$]Br (3.6)

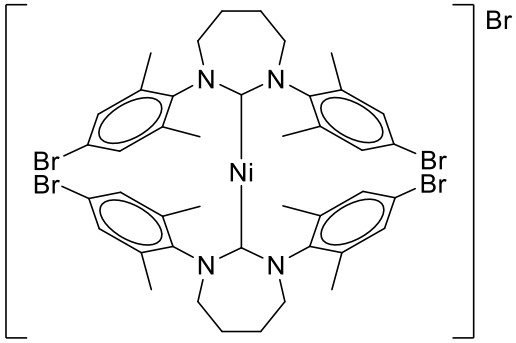

Method as for **3.5** (section 7.8.5), but using [7Xyl-*p*-BrH]BF_4 (65 mg, 0.12 mmol) and $KN(SiMe_3)_2$ (24 mg, 0.12 mmol) in THF, followed by compound **2.8** (68 mg, 0.08 mmol). Efforts to obtain material suitable for X-ray diffraction only gave powder and oily residues. ^{1}H NMR (CD_2Cl_2, 500 MHz, 298 K): δ 50.4 (br s), 39.6 (br s), -10.7 (br s), -17.8 (br s).

7.9 Synthesis of Heteroleptic [Ni(RE-NHC)(NHC')]Br Compounds

7.9.1 Synthesis of [Ni(6Mes)(6Xyl)]Br (4.1)

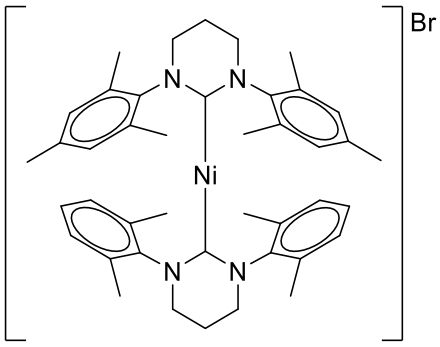

Method as for **3.1** (section 7.8.1), but using compound **2.1** (250 mg, 0.35 mmol) and 6Xyl (152 mg, 0.52 mmol) in THF (30 mL). Recrystallisation from CH_2Cl_2/hexane at room temperature yielded pale-yellow crystals. Yield: 208 mg (80%). ^{1}H NMR (CD_2Cl_2, 500 MHz, 298 K): δ 53.4 (br s), 51.0 (br s), 50.8 (br s), -10.8 (br s), -12.7 (br s), -13.3 (br s), -14.9 (br s), -20.5 (br s), -21.3 (br s). Anal. calcd. (found) for $C_{42}H_{52}N_4BrNi$ (%): C 67.13 (66.76), H 6.97 (6.83), N 7.46 (7.57). Solution magnetic moment (Evans method, CH_2Cl_2): 3.0 μ_B

7.9.2 Synthesis of [Ni(6Mes)(7Mes)]Br (4.2)

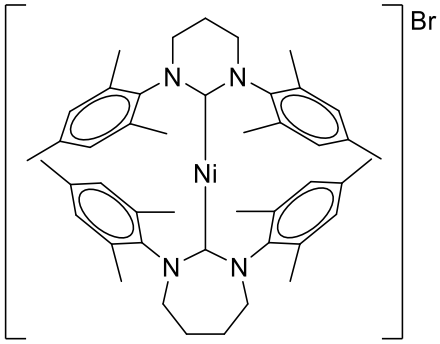

Method as for **3.1** (section 7.8.1), but using compound **2.1** (250 mg, 0.35 mmol) and 7Mes (173 mg, 0.52 mmol) in THF (30 mL). Recrystallisation from CH_2Cl_2/hexane at room temperature yielded yellow crystals. Yield: 198 mg (72%). ^{1}H NMR (CD_2Cl_2, 500 MHz, 298 K): δ 50.3 (br s), 47.9 (br s), 46.2 (br s), 40.3 (br s), -8.6 (s), -9.0 (s), -11.0 (br s), -11.8 (br s), -16.9 (br s), -19.9 (br s). Anal. calcd. (found) for $C_{45}H_{58}N_4BrNi$ (%): C 68.11 (68.21), H 7.37 (7.29), N 7.06 (6.97). Solution magnetic moment (Evans method, CH_2Cl_2): 2.9 μ_B

7.9.3 Synthesis of [Ni(6Mes)(7Xyl)]Br (4.3)

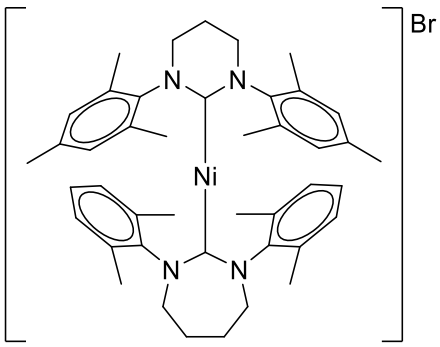

Method as for **3.1** (section 7.8.1), but using compound **2.1** (250 mg, 0.35 mmol) and 7Xyl (159 mg, 0.52 mmol) in THF (30 mL). Recrystallisation from CH_2Cl_2/hexane at room temperature yielded yellow crystals. Yield: 105 mg (40%). ^{1}H NMR (CD_2Cl_2, 500 MHz, 298 K): δ 51.7 (br s), 49.0 (br s), 47.3 (br s), 41.2 (br s), -9.4 (s), -11.8 (br s), -16.5 (br s), -17.7 (br s), -20.0 (br s). Anal. calcd. (found) for $C_{43}H_{54}N_4BrNi$ (%): C 67.47 (67.87), H 7.11 (7.03), N 7.32 (7.30). Solution magnetic moment (Evans method, CH_2Cl_2): 3.1 μ_B

7.9.4 Synthesis of [Ni(6Mes)(6Xyl-p-Br)]Br (4.4)

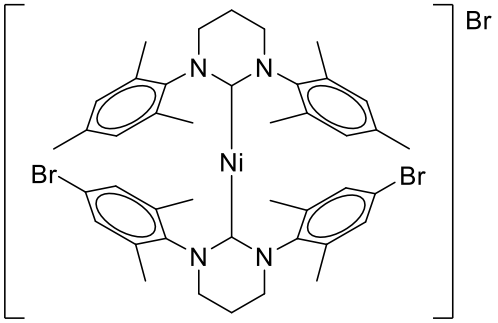

Method as for **3.5** (section 7.8.5), but using [6Xyl-*p*-BrH]BF_4 (216 mg, 0.41 mmol) and $KN(SiMe_3)_2$ (81 mg, 0.41 mmol) in THF, followed by compound **2.1** (196 mg, 0.27 mmol). Recrystallisation from CH_2Cl_2/hexane at 238 K yielded pale-yellow crystals. Yield: 177 mg (72%). ^{1}H NMR (CD_2Cl_2, 500 MHz, 298 K): δ 52.7 (br s), 52.5 (br s), 50.2 (br s), 50.0 (br s), -10.4 (s), -11.4 (br s), -13.2 (br s), -19.8 (br s), -21.1 (br s). Anal. calcd. (found) for $C_{42}H_{52}N_4Br_3Ni \cdot C_2H_4Cl_4$ (%): C 48.88 (49.29), H 5.22 (5.04), N 5.18 (5.38).

7.9.5 Synthesis of [Ni(6Mes)(7Xyl-p-Br)]Br (4.5)

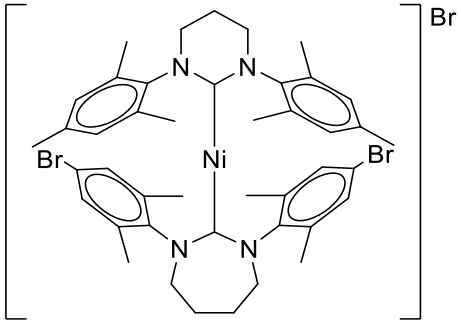

Method as for **3.5** (section 7.8.5), but using [7Xyl-*p*-BrH]BF_4 (115 mg, 0.21 mmol) and $KN(SiMe_3)_2$ (41 mg, 0.21 mmol) in THF, followed by compound **2.1** (100 mg, 0.14 mmol). Recrystallisation from CH_2Cl_2/hexane at room temperature yielded pale-yellow crystals. Yield: 52 mg (41%). ^{1}H NMR (CD_2Cl_2, 500 MHz, 298 K): δ 51.8 (br s), 49.3 (br s), 47.4 (br s), 41.2 (br s), -9.3 (s), -10.7 (br s), -12.2 (br s), -18.1 (br s), -19.6 (br s).

7.9.6 Synthesis of [Ni(6Mes)(IMes)]Br (4.6)

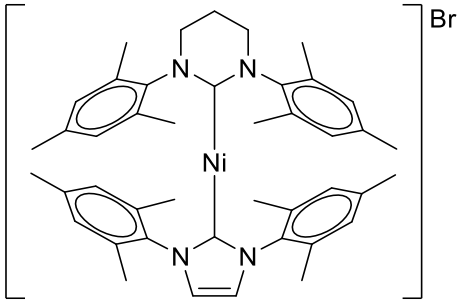

Method as for **3.1** (section 7.8.1), but using compound **2.1** (250 mg, 0.35 mmol) and IMes (158 mg, 0.52 mmol) in THF (20 mL). Recrystallisation from CH_2Cl_2/hexane at 238 K yielded off-white crystals. Yield: 121 mg (46%). ^{1}H NMR (CD_2Cl_2, 500 MHz, 298 K): δ 57.4 (br s), 49.7 (br s), 44.0 (br s), -6.9 (br s), -7.5 (s), -9.2 (s), -10.1 (br s), -22.8 (br s).

7.9.7 Synthesis of [Ni(6Mes)(SIMes)]Br (4.7)

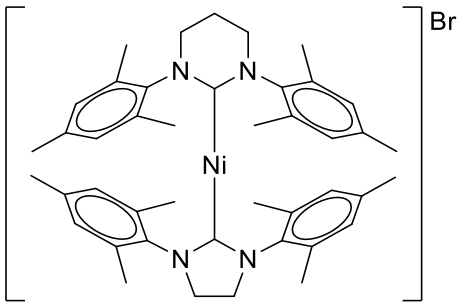

Method as for **3.5** (section 7.8.5), but using [SIMesH]Cl (15 mg, 0.04 mmol) and $KN(SiMe_3)_2$ (9 mg, 0.04 mmol) in THF, followed by compound **2.1** (21 mg, 0.03 mmol). Recrystallisation from CH_2Cl_2/hexane at 238 K yielded off-white crystals. Yield: 7 mg (31%). ^{1}H NMR (CD_2Cl_2, 500 MHz, 298 K): δ 57.2 (br s), 51.7 (br s), 47.3 (br s), -8.6 (br s), -8.8 (s), -9.7 (s), -12.4 (br s), -12.9 (br s), -23.0 (br s).

7.9.8 Synthesis of [Ni(6Xyl)(7Mes)]Br (4.8)

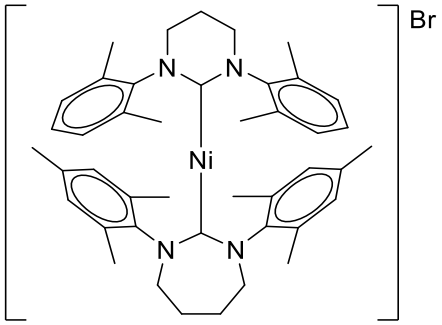

Method as for **3.1** (section 7.8.1), but using compound **2.2** (250 mg, 0.36 mmol) and 7Mes (181 mg, 0.54 mmol) in THF (30 mL). Recrystallisation from CH_2Cl_2/hexane at room temperature yielded pale-yellow crystals. Yield: 161 mg (58%). ^{1}H NMR (CD_2Cl_2, 500 MHz, 298 K): δ 50.6 (br s), 48.2 (br s), 47.0 (br s), 40.6 (br s), -8.6 (s), -10.8 (br s), -11.0 (br s), -12.2 (br s), -16.4 (br s), -20.2 (br s).

7.9.9 Synthesis of [Ni(6Xyl)(7Xyl)]Br (4.9)

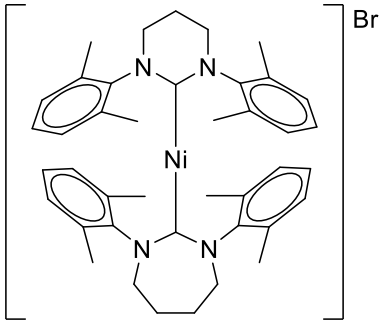

Method as for **3.1** (section 7.8.1), but using compound **2.6** (250 mg, 0.35 mmol) and 6Xyl (155 mg, 0.53 mmol) in THF (30 mL). Recrystallisation from CH_2Cl_2/hexane at room temperature yielded pale-yellow crystals. Yield: 199 mg (76%). ^{1}H NMR (CD_2Cl_2, 500 MHz, 298 K): δ 52.3 (br s), 49.5 (br s), 48.1 (br s), 41.6 (br s), -11.7 (br s), -11.9 (br s), -12.2 (br s), -17.1 (br s), -17.4 (br s), -20.4 (br s).

7.9.10 Synthesis of [Ni(7Mes)(7Xyl)]Br (4.10)

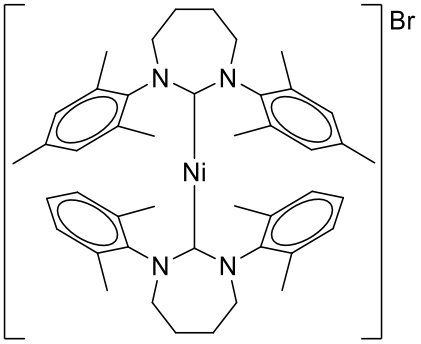

Method as for **3.1** (section 7.8.1), but using compound **2.5** (250 mg, 0.34 mmol) and 7Xyl (156 mg, 0.51 mmol) in THF (30 mL). Recrystallisation from CH_2Cl_2/hexane at room temperature yielded yellow crystals. Yield: 133 mg (50%). ^{1}H NMR (CD_2Cl_2, 500 MHz, 298 K): δ 50.1 (br s), 49.9 (br s), 39.3 (br s), 39.2 (br s), -8.4 (s), -10.9 (br s), -11.9 (br s), -13.2 (s), -17.5 (br s), -18.3 (br s).

7.9.11 Synthesis of [Ni(7Mes)(IMes)]Br (4.11)

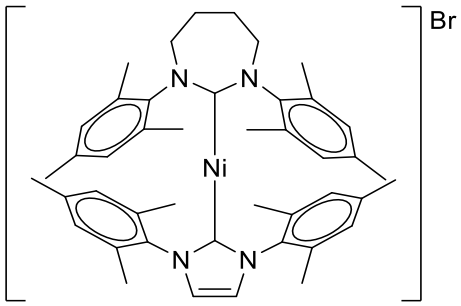

Method as for **3.1** (section 7.8.1), but using compound **2.5** (250 mg, 0.34 mmol) and IMes (155 mg, 0.51 mmol) in THF (30 mL). Recrystallisation from CH_2Cl_2/hexane at room temperature yielded pale-yellow crystals. Yield: 175 mg (66%). ^{1}H NMR (CD_2Cl_2, 500 MHz, 298 K): δ 43.4 (br s), 35.2 (br s), 31.1 (br s), -3.0 (br s), -3.6 (br s), -3.7 (br s), -4.6 (br s), -16.3 (br s).

7.9.12 Synthesis of Other Heteroleptic [Ni(RE-NHC)(NHC')]Br Compounds with Only ^{1}H NMR Data

The following reactions were NMR tube scale reactions, running through most of the permutations of different RE-NHCs on Ni(I). All ^{1}H NMR signals given are of crude reaction mixtures that show new products formed, any unsuccessful reactions are left out of this list. No yields or elemental analyses were obtained.

7.9.12.1 Synthesis of [Ni(6Xyl)(6Xyl-p-Br)]Br

A flame-dried J. Young's NMR tube was charged with [6Xyl-*p*-BrH]PF_6 (19 mg, 0.03 mmol) and $KN(SiMe_3)_2$ (7 mg, 0.03 mmol) in THF (1 mL) and the contents shaken for 30 min to form an off-white suspension. After the precipitate was allowed to settle, the THF filtrate was decanted away into a second flame-dried NMR tube that contained compound **2.2** (15 mg, 0.02 mmol). The mixture of *in-situ* generated 6Xyl-*p*-Br and **2.2** was shaken for 16 hrs, forming a dark yellow suspension. The precipitate was isolated by cannula filtration, washed with Et_2O (2 × 1 mL), and dried under reduced pressure. ^{1}H NMR (CD_2Cl_2, 500 MHz, 298 K): δ 53.6 (br s), 53.4 (br s), 51.1 (br s), -12.0 (br s), -13.2 (br s), -16.1 (s), -20.5 (br s), -21.0 (br s).

7.9.12.2 Synthesis of [Ni(6Xyl)(7Xyl-p-Br)]Br

Method as for section 7.9.12.1 above, but with [7Xyl-*p*-BrH]PF_6 (20 mg, 0.03 mmol) and $KN(SiMe_3)_2$ (7 mg, 0.03 mmol) in THF (1 mL), followed by compound **2.2** (15 mg, 0.02 mmol). ^{1}H NMR (CD_2Cl_2, 500 MHz, 298 K): δ 52.3 (br s), 49.7 (br s), 48.1 (br s), 41.6 (br s), -11.2 (br s), -12.0 (br s), -12.8 (s), -17.8 (br s), -20.1 (br s).

7.9.12.3 Synthesis of [Ni(6Xyl)(IMes)]Br

Method as for section 7.9.12.1 above, but with IMes (10 mg, 0.03 mmol) and compound **2.2** (15 mg, 0.02 mmol) in THF (1 mL). ^{1}H NMR (CD_2Cl_2, 500 MHz, 298 K): δ 58.5 (br s), 50.8 (br s), 45.1 (br s), -7.0 (br s), -7.8 (s), -10.5 (br s), -10.6 (br s), -20.5 (br s), -23.0 (br s).

7.9.12.4 Synthesis of [Ni(7Mes)(6Xyl-p-Br)]Br

Method as for section 7.9.12.1 above, but with [6Xyl-*p*-BrH]PF_6 (18 mg, 0.03 mmol) and $KN(SiMe_3)_2$ (6 mg, 0.03 mmol) in THF (1 mL), followed by compound **2.5** (15 mg, 0.02 mmol). ^{1}H NMR (CD_2Cl_2, 500 MHz, 298 K): δ 49.1 (br s), 46.7 (br s), 45.1 (br s), 39.6 (br s), -7.9 (br s), -8.2 (br s), -9.2 (br s), -12.0 (br s), -15.4 (br s), -19.5 (br s).

7.9.12.5 Synthesis of [Ni(7Mes)(7Xyl-p-Br)]Br

Method as for section 7.9.12.1 above, but with [7Xyl-*p*-BrH]PF_6 (19 mg, 0.03 mmol) and $KN(SiMe_3)_2$ (6 mg, 0.03 mmol) in THF (1 mL), followed by compound **2.5** (15 mg, 0.02 mmol). ^{1}H NMR (CD_2Cl_2, 500 MHz, 298 K): δ 49.3 (br s), 49.1 (br s), 38.9 (br s), 38.5 (br s), -8.0 (s), -9.6 (s), -12.0 (br s), -16.7 (br s), -18.2 (br s).

7.9.12.6 Synthesis of [Ni(7Xyl)(6Xyl-p-Br)]Br

Method as for section 7.9.12.1 above, but with [6Xyl-*p*-BrH]PF_6 (19 mg, 0.03 mmol) and $KN(SiMe_3)_2$ (6 mg, 0.03 mmol) in THF (1 mL), followed by compound **2.6** (15 mg, 0.02 mmol). ^{1}H NMR (CD_2Cl_2, 500 MHz, 298 K): δ 50.6 (br s), 47.9 (br s), 46.4 (br s), 40.6 (br s), -10.1 (br s), -12.0 (br s), -16.2 (br s), -17.5 (br s), -19.8 (br s).

7.9.12.7 Synthesis of [Ni(7Xyl)(IMes)]Br

Method as for section 7.9.12.1 above, but with IMes (10 mg, 0.03 mmol) and compound **2.6** (15 mg, 0.02 mmol) in THF (1 mL). ^{1}H NMR (CD_2Cl_2, 500 MHz, 298 K): δ 44.1 (br s), 35.8 (br s), 31.6 (br s), -3.7 (br s), -3.9 (s), -4.6 (br s), -16.5 (br s), -20.5 (br s).

7.9.12.8 Synthesis of [Ni(6Xyl-p-Br)(IMes)]Br

Method as for section 7.9.12.1 above, but with IMes (8 mg, 0.03 mmol) and compound **2.4** (15 mg, 0.02 mmol) in THF (1 mL). ^{1}H NMR (CD_2Cl_2, 500 MHz, 298 K): δ 60.4 (br s), 52.5 (br s), 47.0 (br s), -6.4 (br s), -8.0 (br s), -8.3 (br s), -11.4 (br s), -23.4 (br s).

7.10 Synthesis of [Ni(RE-NHC)(PCy_3)]Br Compounds

7.10.1 Synthesis of [Ni(6Mes)(PCy_3)]BAr^F_4 (4.12)

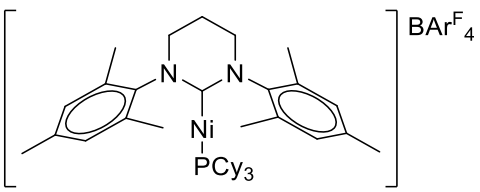

A flame-dried J. Young's ampoule was charged with **2.20** (100 mg, 0.14 mmol) and $NaBAr^F_4$ (126 mg, 0.14 mmol) and the suspension stirred in Et_2O (3 mL) for 16 hrs

at room temperature. The ether solution was cannula filtered to a clean ampoule and immediately layered with pentane (10 mL) to form analytically pure pale-yellow crystalline material. Yield: 172 mg (83%). ^{1}H NMR (THF-d_8, 500 MHz, 298 K): δ 39.6 (br s), 33.3 (br s), 28.9 (br s), 7.75 (s, 8H, BAr^F_4), 7.52 (s, 4H, BAr^F_4), 4.6 (br s), 2.2 (s), -1.1 (br s), -1.3 (br s), -1.4 (br s), -3.1 (s), -12.2 (br s). Anal. calcd. (found) for $C_{72}H_{73}N_2BF_{24}NiP$ (%): C 56.79 (56.44), H 4.83 (4.76), N 1.84 (1.94). Solution magnetic moment (Evans method, THF): 2.6 μ_B.

7.10.2 Synthesis of [Ni(6Xyl)(PCy$_3$)]BAr$^F_4$ (4.13)

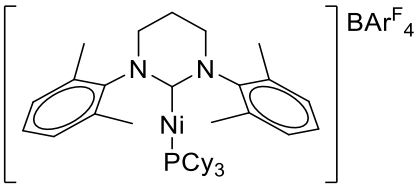

Same method as for **4.12** (section 7.10.1), but using compound **2.21** (100 mg, 0.14 mmol) and $NaBAr^F_4$ (125 mg, 0.14 mmol). Yield: 118 mg (56%). ^{1}H NMR (THF-d_8, 500 MHz, 298 K): δ 40.7 (br s), 33.7 (br s), 30.0 (br s), 7.74 (s, 8H, BAr^F_4), 7.52 (s, 4H, BAr^F_4), 4.6 (br s), 2.2 (s), -1.0 (br s), -1.3 (br s), -2.0 (br s), -12.0 (br s), -13.6 (br s). Anal. calcd. (found) for $C_{70}H_{69}N_2BF_{24}NiP$ (%): C 56.25 (56.00), H 4.65 (4.61), N 1.87 (2.00). Solution magnetic moment (Evans method, THF): 2.5 μ_B.

7.10.3 Synthesis of [Ni(7Mes)(PCy$_3$)]BAr$^F_4$ (4.14)

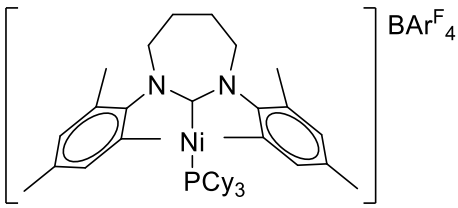

Same method as for **4.12** (section 7.10.1), but using compound **2.22** (100 mg, 0.13 mmol) and $NaBAr^F_4$ (118 mg, 0.13 mmol). Yield: 142 mg (70%). ^{1}H NMR (THF-d_8, 500 MHz, 298 K): δ 27.7 (br s), 23.3 (br s), 21.7 (br s), 7.78 (s, 8H, BAr^F_4), 7.55 (s, 4H, BAr^F_4), 4.5 (br s), 4.0 (br s), 2.7 (s), 2.6 (s), 0.3 (br s), -0.2 (br s), -8.5 (br s). Anal. calcd. (found) for $C_{73}H_{75}N_2BF_{24}NiP$ (%): C 57.05 (56.76), H 4.92 (4.84), N 1.82 (1.95). Solution magnetic moment (Evans method, THF): 2.5 μ_B.

7.10.4 Synthesis of [Ni(7Xyl)(PCy$_3$)]BAr$^F_4$ (4.15)

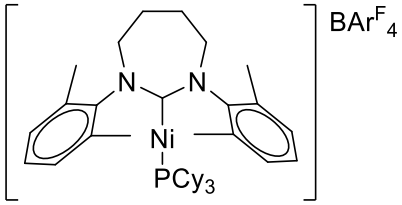

Same method as for **4.12** (section 7.10.1), but using compound **2.23** (100 mg, 0.14 mmol) and NaBAr$^F_4$ (122 mg, 0.14 mmol). Yield: 166 mg (80%). ^{1}H NMR (THF-d_8, 500 MHz, 298 K): δ 30.1 (br s), 25.1 (br s), 22.8 (br s), 7.76 (s, 8H, BAr$^F_4$), 7.54 (s, 4H, BAr$^F_4$), 4.2 (br s), 2.6 (s), 0.2 (br s), -0.2 (br s), -9.4 (br s), -17.1 (br s). Anal. calcd. (found) for $C_{71}H_{71}N_2BF_{24}NiP$ (%): C 56.52 (56.37), H 4.74 (4.67), N 1.86 (2.12). Solution magnetic moment (Evans method, THF): 2.6 μ_B.

7.11 Reactivity of [Ni(NHC)(PCy$_3$)]BAr$^F_4$ Compounds

7.11.1 Synthesis of [Ni(7Xyl)(P^{t}Bu$_3$)]BAr$^F_4$ (4.16)

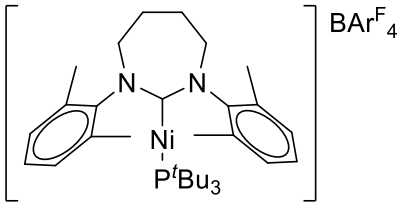

Compound **4.15** (20 mg, 0.01 mmol) and P^{t}Bu$_3$ (13 mg, 0.06 mmol) were charged into a J. Young's NMR tube and dissolved in THF (0.5 mL) before shaking for 24 hrs at room temperature. The pale-yellow suspension was pumped down to dryness, the residue washed with pentane (2 × 1 mL) to remove any free trialkylphosphine, before extraction into Et_2O (0.5 mL) and layering with pentane (1 mL) to form pale-yellow crystalline material. Yield: 8 mg (42%). ^{1}H NMR (THF-d_8, 500 MHz, 298 K): δ 31.8 (br s), 27.9 (br s), 7.76 (s, 8H, BAr$^F_4$), 7.54 (s, 4H, BAr$^F_4$), -12.7 (br s), -18.7 (br s). Anal. calcd. (found) for $C_{65}H_{65}N_2BF_{24}NiP$ (%): C 54.57 (54.58), H 4.58 (4.48), N 1.96 (2.22). Solution magnetic moment (Evans method, THF): 2.2 μ_B.

7.11.2 Synthesis of [Ni(6Xyl)(PCy$_3$)(CO)]BAr$^F{}_4$ (4.17)

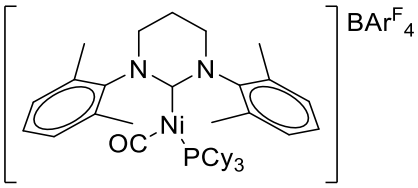

A J. Young's NMR tube containing **4.13** (5 mg, 0.003 mmol) in Et_2O (0.5 mL) was degassed before charging with 1 atm of CO. An immediate colour change from pale yellow to pale green accompanied coordination of CO. Green crystals were formed upon adding pentane (1 mL) to the Et_2O solution. IR (KBr): ν_{CO} = 2027 cm^{-1}.

7.11.3 Synthesis of [Ni(7Mes)(PCy$_3$)(CO)]BAr$^F{}_4$ (4.18)

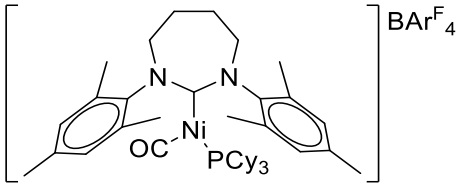

Same method as for **4.17** (section 7.11.2), but starting with compound **4.14** (5 mg, 0.003 mmol) in Et_2O (0.5 mL). Green crystals were formed from Et_2O/pentane. IR (KBr): ν_{CO} = 2027 cm^{-1}.

7.11.4 Synthesis of [Ni(7Xyl)(PCy$_3$)(CO)]BAr$^F{}_4$ (4.19)

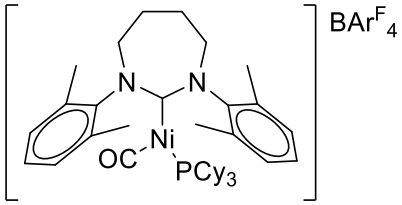

Same method as for **4.17** (section 7.11.2), but starting with compound **4.15** (20 mg, 0.01 mmol) in Et_2O (0.5 mL). Green crystals were formed from Et_2O/pentane. Yield: 16 mg (79%). ^{1}H NMR (THF-d_8, 500 MHz, 298 K): δ 8.2 (br s), 7.79 (s, 8H, BAr$^F{}_4$), 7.57 (s, 4H, BAr$^F{}_4$), 6.6 (br s), 4.6 (br s), 1.7 (br s), 1.2 (br s). IR (THF): ν_{CO} = 2025 cm^{-1}. IR (KBr): ν_{CO} = 2028 cm^{-1}. Anal. calcd. (found) for $C_{72}H_{71}N_2BF_{24}NiOP$ (%): C 56.27 (56.36), H 4.66 (4.64), N 1.82 (2.03). Solution magnetic moment (Evans method, THF): 1.5 μ_B.

7.11.5 Synthesis of [Ni(7Xyl)(P^{t}Bu$_3$)(CO)]BAr$^F{}_4$ (4.20)

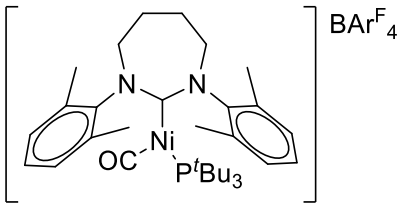

Same method as for **4.17** (section 7.11.2), but starting with compound **4.16** (5 mg, 0.003 mmol) in Et_2O (0.5 mL). Green crystals were formed from Et_2O/pentane. IR (KBr): ν_{CO} = 2023 cm^{-1}.

7.11.6 Synthesis of [PCy$_3$Me][Ni(PCy$_3$)I$_3$] (4.21)

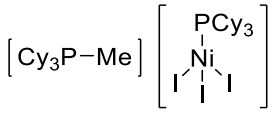

CH_3I (0.4 μL, 0.01 mmol) was added to a J. Young's NMR tube of **4.15** (10 mg, 0.007 mmol) in THF-d_8. Initially the solution goes green in colour, but after 3.5 hrs, the tube contained a deep red suspension. All the volatiles were removed under vacuum and the residue extracted in Et_2O (0.5 mL). Deep red crystals formed upon crystallisation from Et_2O and pentane. $^{31}P\{^1H\}$ NMR (THF-d_8, 202 Hz, 298 K): δ 37.6 (s).

7.11.7 Synthesis of [{Ni(PCy$_3$)}$_2$(μ-I)$_3$] (4.22)

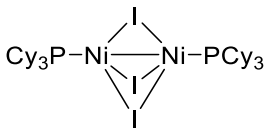

4-fluoroiodobenzene (1.5 μL, 0.01 mmol) was added to a J. Young's NMR tube of **4.15** (10 mg, 0.007 mmol) in THF-d_8 and the tube shaken for 24 hrs. Initially the solution goes dark green in colour, and deep green crystals formed from Et_2O and pentane crystallisation. $^{31}P\{^1H\}$ NMR (THF-d_8, 202 Hz, 298 K): δ 28.5 (s).

7.11.8 Synthesis of [7Xyl·C$_6$H$_4$F]BAr$^F_4$ (4.23)

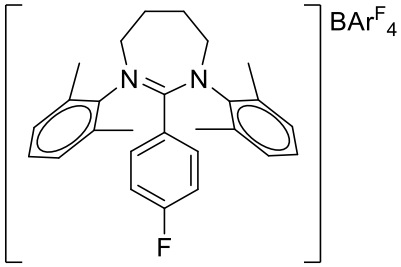

During crystallisation of **4.22**, colourless crystals also formed. X-ray diffraction revealed them to be the diazepinium salt **4.23**. ^{1}H NMR (THF-d_8, 500 MHz, 298 K): δ 7.79 (s, 8H, BAr$^F_4$), 7.57 (s, 4H, BAr$^F_4$), 7.35 (m, 2H, C$_6$*H*$_4$F), 7.10 – 7.00 (m, 6H, *o*,*p*-C*H*$_{aryl}$), 6.82 (m, 2H, C$_6$*H*$_4$F), 4.49 (s, 4H, NC*H*$_2$), 2.57 (s, 4H, NCH$_2$C*H*$_2$), 2.50 (s, 12H, *o*-C*H*$_3$). ^{19}F{^{1}H} NMR (THF-d_8, 471 MHz, 298 K): δ 65.31 (s, BAr$^F_4$), -107.81 (s, C$_6$H$_4$*F*).

7.12 Hydrophosphination of Alkynes with PPh$_2$H using NHCs/CAACs

7.12.1 Stoichiometric Reactions Between NHCs and Substrates

*7.12.1.1 IMe$_4$ + diphenylphosphine - Synthesis of IMe$_4$-H$_2$ (**5.10**)*

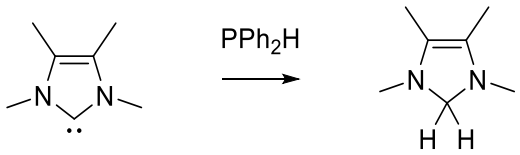

IMe$_4$ (75 mg, 0.60 mmol) and PPh$_2$H (105 µL, 0.60 mmol) were charged to a flame-dried ampoule in THF (2 mL) and the solution stirred at room temperature for 69 hrs. The volatiles were vacuum transferred to a J. Young's NMR tube. NMR showed formation of the aminal product, with data matching that in the literature.[19] ^{1}H NMR (THF-d_8, 500 MHz, 298 K): δ 3.56 (s, 2H, NC*H*$_2$N), 2.30 (s, 6H, NC*H*$_3$), 1.59 (s, 6H, CC*H*$_3$). ^{13}C{^{1}H} NMR (THF-d_8, 125 MHz, 298 K): δ 124.0 (s, *C*CH$_3$), 81.6 (s, N*C*H$_2$N), 38.0 (s, N*C*H$_3$), 9.6 (s, C*C*H$_3$).

*7.12.1.2 IMe_4 + phenylacetylene – Synthesis of IMe_4-(H)(C≡CPh) (**5.11**)*

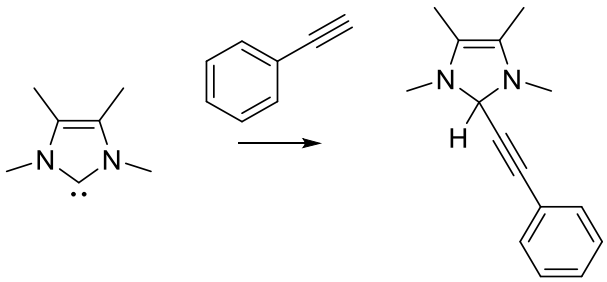

IMe_4 (75 mg, 0.60 mmol) and PhC≡CH (105 µL, 0.60 mmol) were charged to a flame-dried J. Young's resealable ampoule in THF (0.5 mL) and the contents shaken at room temperature for 20 min. ^{1}H NMR (THF-d_8, 500 MHz, 298 K): δ 7.44 – 7.30 (m, CH_{aryl}), 3.76 (s, 1H, C*H*), 2.44 (s, 6H, NCH_3), 1.63 (s, 6H, CCH_3).

*7.12.1.3 I^tBu + diphenylphosphine – Synthesis of I^tBu-H_2 (**5.12**)*

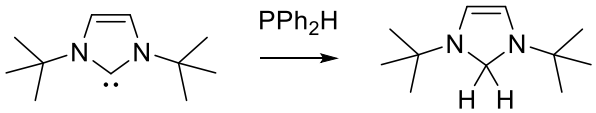

I^tBu (7 mg, 0.04 mmol) and PPh_2H (77 µL, 0.44 mmol) were charged to a flame-dried J. Young's resealable ampoule in THF (0.5 mL) and the solution shaken at room temperature for 24 hrs. NMR showed formation of the aminal product, with spectroscopic data which matched literature spectra.[20] ^{1}H NMR (THF-d_8, 500 MHz, 298 K): δ 5.44 (s, 2H, C*H*), 4.20 (s, 2H, CH_2), 1.06 (s, 18H, C(CH_3)$_3$).

*7.12.1.4 ^{Et2}CAAC + diphenylphosphine – Synthesis of ^{Et2}CAAC(H)(PPh_2) (**5.13**)*

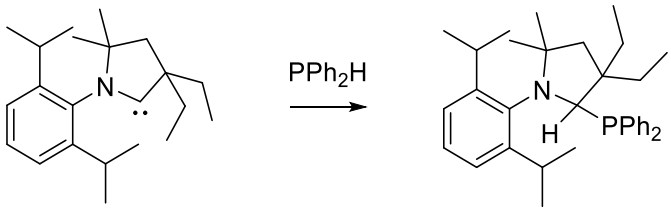

^{Et2}CAAC (20 mg, 0.06 mmol) and PPh_2H (11 µL, 0.06 mmol) were charged to a flame-dried J. Young's NMR tube and dissolved in THF-d_8. Integration of inverse gated ^{31}P{^{1}H} NMR spectra after 20 min at room temperature showed 78% consumption of the phosphine, with no further consumption occurring over the next 24 hrs. NMR showed formation of oxidative addition product **5.13**, with precedent for this formation known in the literature for the analogous ^{Me2}CAAC system.[21] Addition of PhC≡CH (1 equiv.) to the reaction mixture showed no hydrophosphination occurring after 72 hrs at room

temperature. ^{1}H NMR (THF-d_8, 500 MHz, 298 K): δ 7.43 (m, 2H, CH_{Ph}), 7.28 (m, 1H, CH_{dipp}), 7.18 (m, 1H, CH_{dipp}), 7.11 (m, 2H, CH_{Ph}), 7.03 (m, 1H, CH_{Ph}), 6.90 (m, 2H, CH_{Ph}), 6.84 (m, 1H, CH_{Ph}), 6.72 (m, 2H, CH_{Ph}), 6.67 (m, 1H, CH_{dipp}), 4.88 (d, J_{PH} = 4.5 Hz, 1H, CPH), 3.76 (sept, J_{HH} = 6.6 Hz, 1H, CH(CH$_3$)$_2$), 3.41 (sept, J_{HH} = 6.6 Hz, 1H, CH(CH$_3$)$_2$), 2.22 (d, J_{HH} = 13.0. Hz, CH_2), 1.90 (d, J_{HH} = 13.0 Hz, CH_2), 1.62 (d, J_{HH} = 6.7 Hz, 3H, CH(CH_3)$_2$), 1.61 (s, 3H, C(CH_3)$_2$), 1.35 (m, 2H, C(CH_2CH$_3$)$_2$), 1.28 (d, J_{HH} = 6.7 Hz, 3H, CH(CH_3)$_2$), 1.21 (m, 2H, C(CH_2CH$_3$)$_2$), 1.03 (d, J_{HH} = 6.7 Hz, 3H, CH(CH_3)$_2$), 0.94 (s, 3H, C(CH_3)$_2$), 0.92 (t, J_{HH} = 7.4 Hz, 3H, C(CH$_2$CH_3)$_2$), 0.63 (t, J_{HH} = 7.5 Hz, 3H, C(CH$_2$CH_3)$_2$), 0.37 (d, J_{HH} = 6.7 Hz, 3H, CH(CH_3)$_2$). ^{13}C{^{1}H} NMR (THF-d_8, 125 MHz, 298 K): δ 152.3 (s, C_{Ph}), 148.7 (s, C_{dipp}), 144.1 (s, C_{dipp}), 141.8 (d, J_{PC} = 22.1 Hz, C_{Ph}), 140.4 (d, J_{PC} = 19.1 Hz, C_{Ph}), 136.1 (d, J_{PC} = 20.8 Hz, C_{Ph}), 133.3 (d, J_{PC} = 19.6 Hz, C_{Ph}), 129.1 (s, CH$_{dipp}$), 128.8 (s, CH$_{dipp}$), 128.2 (d, J_{PC} = 7.5 Hz, C_{Ph}), 127.6 (d, J_{PC} = 7.5 Hz, C_{Ph}), 127.2 (s), 125.3 (s, CH$_{dipp}$), 124.6 (s, CH$_{dipp}$), 74.2 (d, J_{PC} = 8.4 Hz, CPH), 63.9 (s, C(CH$_3$)$_2$), 51.0 (d, J_{PC} = 11.5 Hz, C(CH$_2$CH$_3$)$_2$), 50.5 (s, CH$_2$), 35.6 (s, C(CH$_2$CH$_3$)$_2$), 31.4 (s, C(CH$_3$)$_2$), 28.9 (s, CH(CH$_3$)$_2$), 28.5 (s, C(CH$_3$)$_2$), 28.0 (s, CH(CH$_3$)$_2$), 27.4 (s, CH(CH$_3$)$_2$), 25.5 (s, CH(CH$_3$)$_2$), 25.4 (s, CH(CH$_3$)$_2$). 23.3 (s, CH(CH$_3$)$_2$), 11.1 (s, C(CH$_2$$CH_3$)$_2$), 10.3 (s, C(CH$_2$$CH_3$)$_2$). ^{31}P{^{1}H} NMR (THF-d_8, 202 MHz, 298 K): δ -11.2 (s, CPH).

7.13 References

1. N. A. Yakelis and R. G. Bergman, *Organometallics*, 2005, **24**, 3579-3581.
2. K. M. Kuhn and R. H. Grubbs, *Org. Lett.*, 2008, **10**, 2075-2077.
3. N. Kuhn and T. Kratz, *Synthesis*, 1993, **6**, 561-562.
4. A. J. Arduengo, III, S. F. Gamper, J. C. Calabrese and F. Davidson, *J. Am. Chem. Soc.*, 1994, **116**, 4391-4394.
5. N. Ortega, C. Richter and F. Glorius, *Org. Lett.*, 2013, **15**, 1776-1779.
6. A. J. Arduengo, III, H. V. R. Dias, R. L. Harlow and M. Kline, *J. Am. Chem. Soc.*, 1992, **114**, 5530-5534.
7. L. Jafarpour, E. D. Stevens and S. P. Nolan, *J. Organomet. Chem.*, 2000, **606**, 49-54.
8. J. K. Mahoney, D. Martin, C. E. Moore, A. L. Rheingold and G. Bertrand, *J. Am. Chem. Soc.*, 2013, **135**, 18766-18769.

9. V. Lavallo, Y. Canac, C. Präsang, B. Donnadieu and G. Bertrand, *Angew. Chem. Int. Ed.*, 2005, **44**, 5705-5709.
10. G. R. Fulmer, A. J. M. Miller, N. H. Sherden, H. E. Gottlieb, A. Nudelman, B. M. Stoltz, J. E. Bercaw and K. I. Goldberg, *Organometallics*, 2010, **29**, 2176-2179.
11. D. F. Evans, *J. Chem. Soc*, 1959, 2003-2005.
12. G. M. Sheldrick, *Acta. Crystallogr.*, 1990, 467-473.
13. W. J. M. Blackaby, S. Sabater, R. C. Poulten, M. J. Page, A. Folli, V. Krewald, M. F. Mahon, D. M. Murphy, E. Richards and M. K. Whittlesey, *Dalton Trans.*, 2018, **47**, 769-782.
14. R. C. Poulten, M. J. Page, A. G. Algarra, J. J. Le Roy, I. Lopez, E. Carter, A. Llobet, S. A. Macgregor, M. F. Mahon, D. M. Murphy, M. Murugesu and M. K. Whittlesey, *J. Am. Chem. Soc.*, 2013, **135**, 13640-13643.
15. M. Iglesias, D. J. Beetstra, J. C. Knight, L. L. Ooi, A. Stasch, S. Coles, L. Male, M. B. Hursthouse, K. J. Cavell, A. Dervisi and I. A. Fallis, *Organometallics*, 2008, **27**, 3279-3289.
16. J. J. Dunsford, D. S. Tromp, K. J. Cavell, C. J. Elsevier and B. M. Kariuki, *Dalton Trans.*, 2013, **42**, 7318-7329.
17. V. Cesar, N. Lugan and G. Lavigne, *Eur. J. Inorg. Chem.*, 2010, 361-365.
18. A. Aidouni, S. Bendahou, A. Demonceau and L. Delaude, *J. Comb. Chem.*, 2008, **10**, 886-892.
19. D. Franz and S. Inoue, *Chem. Asian J.*, 2014, **9**, 2083-2087.
20. A. Jana, C. Schulzke and H. W. Roesky, *J. Am. Chem. Soc.*, 2009, **131**, 4600-4601.
21. G. D. Frey, J. D. Masuda, B. Donnadieu and G. Bertrand, *Angew. Chem. Int. Ed.*, 2010, **49**, 9444-9447.

APPENDICES

1 CRYSTAL STRUCTURES

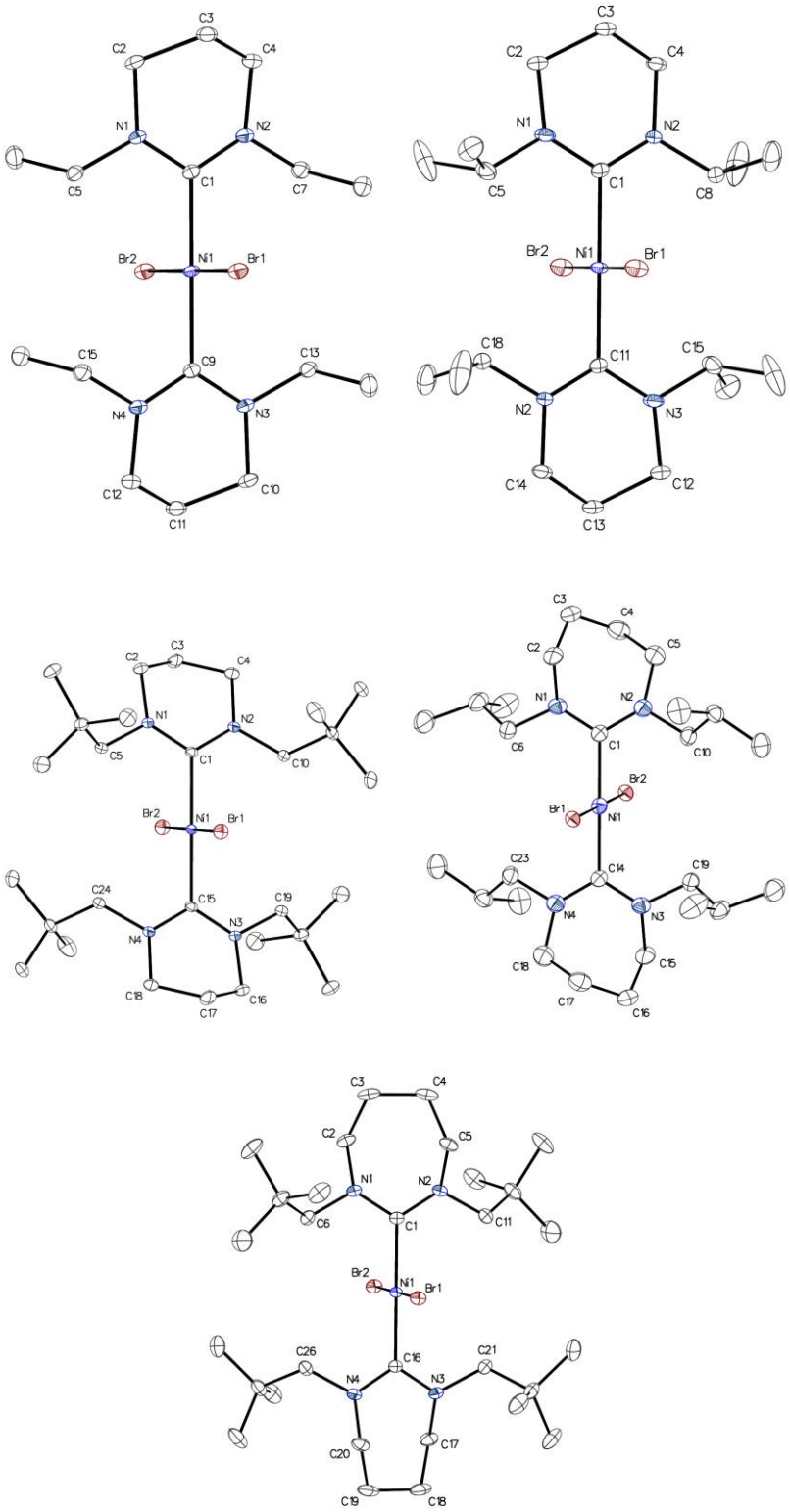

Figure A1.1 Molecular structures of **2.10**, **2.11**, Ni(6^{n}Pent)$_2$Br$_2$, Ni(7^{i}Bu)$_2$Br$_2$, and Ni(7^{n}Pent)$_2$Br$_2$. Thermal ellipsoids are set at 30% probability. All hydrogen atoms have been omitted for clarity.

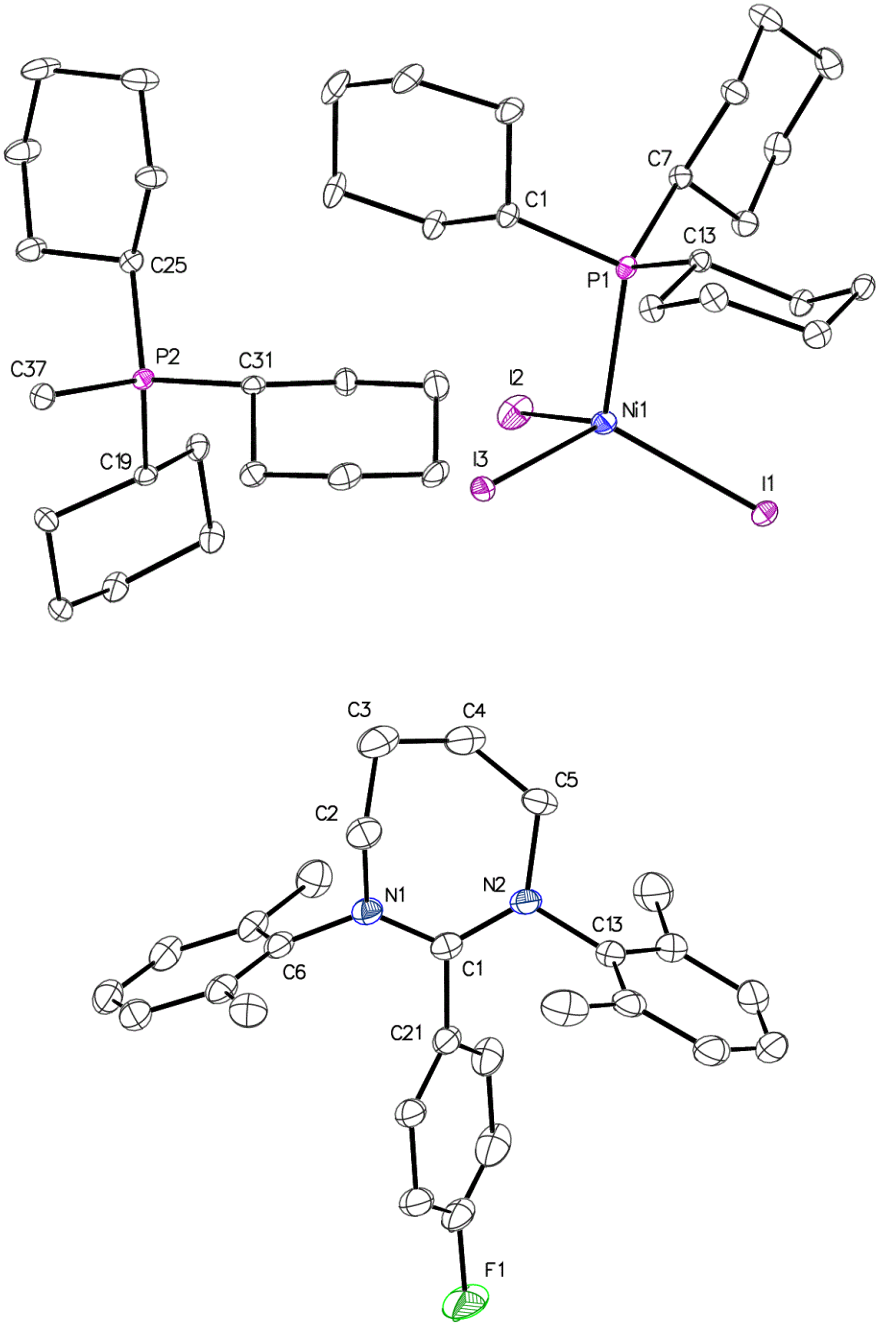

Figure A1.2 Molecular structures of **4.21** and the cation in **4.23**. Thermal ellipsoids are set at 30% probability. All hydrogen atoms have been omitted for clarity.

2 CRYSTALLOGRAPHIC DATA

	Ni(6Xyl)(PPh_3)Br (2.2)	**Ni(6Xyl-*p*-Br)(PPh_3)Br (2.4)**	**Ni(7Xyl)(PPh_3)Br (2.6)**
Identification code	e16mkw4	e17mkw31	e16mkw3
Empirical formula	$C_{38}H_{39}BrN_2NiP$	$C_{38}H_{37}Br_3N_2NiP$	$C_{48}H_{50}BrN_2NiP$
Formula weight	693.30	851.10	824.49
Temperature/K	150.02(11)	150.00(10)	150.00(10)
Crystal system	triclinic	monoclinic	monoclinic
Space group	P-1	$P2_1/n$	$P2_1/n$
Unit cell dimensions/Å, °	a = 10.0658(3), α = 90.258(2)	11.0562(8), 90	9.9401(2), 90
	b = 10.4271(3), β = 92.694(3)	17.2369(9), 102.261(8)	23.4907(4), 105.451(2)
	c = 16.3374(4), γ = 107.240(3)	19.2965(17), 90	17.9641(4), 90
Volume/Å^3	1635.57(9)	3593.5(5)	4043.01(16)
Z	2	4	4
Density ρ_{calc}g/cm^3	1.408	1.573	1.355
Absorption coefficient/mm^{-1}	1.893	3.949	1.544
F(000)	718.0	1708.0	1720.0
Crystal size/mm^3	0.456 × 0.365 × 0.167	0.451 × 0.323 × 0.175	0.407 × 0.301 × 0.257
Radiation	MoKα (λ = 0.71073)	MoKα (λ = 0.71073)	MoKα (λ = 0.71073)
2Θ range for data collection/°	6.518 to 54.958	6.686 to 57.06	6.72 to 54.964
Index ranges	$-13 \le h \le 13, -13 \le k \le 13, -21 \le l \le 21$	$-14 \le h \le 9, -15 \le k \le 22, -23 \le l \le 23$	$-11 \le h \le 12, -30 \le k \le 30, -23 \le l \le 23$
Reflections collected	54485	12284	39111
Independent reflections	7496 [R_{int} = 0.0364, R_{sigma} = 0.0227]	7196 [R_{int} = 0.0649, R_{sigma} = 0.1722]	9249 [R_{int} = 0.0335, R_{sigma} = 0.0322]
Data/restraints/parameters	7496/96/466	7196/0/410	9249/0/482
Goodness-of-fit on F^2	1.062	0.995	1.041
Final R indexes [I>=2σ (I)]	R_1 = 0.0294, wR_2 = 0.0695	R_1 = 0.0893, wR_2 = 0.1932	R_1 = 0.0345, wR_2 = 0.0804
Final R indexes [all data]	R_1 = 0.0394, wR_2 = 0.0739	R_1 = 0.1928, wR_2 = 0.2530	R1 = 0.0488, wR2 = 0.0873
Largest diff. peak/hole / e Å^{-3}	0.47/-0.31	2.37/-0.74	0.86/-0.63

	Ni(6Et)$_2$Br$_2$ (2.10)	**Ni(6^{i}Pr)$_2$Br$_2$ (2.11)**	**Ni(6^{i}Bu)(PPh$_3$)Br (2.13)**
Identification code	s16mkw75	e17mkw2	e17mkw9
Empirical formula	$C_{16}H_{32}Br_2N_4Ni$	$C_{26}H_{46}N_4NiBr_2$	$C_{30}H_{39}BrN_2NiP$
Formula weight	498.98	586.82	597.22
Temperature/K	150.00(10)	150.0(2)	150.00(11)
Crystal system	triclinic	triclinic	monoclinic
Space group	P-1	P-1	$P2_1/c$
Unit cell dimensions/Å, °	7.6056(6), 71.647(6) 8.4267(6), 75.582(6) 8.4507(6), 79.426(6)	8.3642(6), 88.886(5) 8.7185(6), 74.988(6) 10.5300(7), 80.203(6)	8.6093(7), 90 27.246(2), 109.035(10) 13.1292(12), 90
Volume/Å^3	494.60(7)	730.61(9)	2911.3(5)
Z	1	1	4
Density ρ_{calc}g/cm^3	1.675	1.3336	1.363
Absorption coefficient/mm^{-1}	6.169	3.414	2.114
F(000)	254.0	281.9	1244.0
Crystal size/mm^3	0.278 × 0.167 × 0.12	0.235 × 0.136 × 0.12	0.195 × 0.16 × 0.091
Radiation	CuKα (λ = 1.54184)	Mo Kα (λ = 0.71073)	MoKα (λ = 0.71073)
2Θ range for data collection/°	11.136 to 146.868	6.84 to 58.08	6.722 to 54.966
Index ranges	$-6 \le h \le 9, -10 \le k \le 10, -10 \le l \le 10$	$-10 \le h \le 11, -11 \le k \le 11, -13 \le l \le 14$	$-10 \le h \le 11, -34 \le k \le 35, -16 \le l \le 15$
Reflections collected	3992	5746	27051
Independent reflections	1973 [R_{int} = 0.0202, R_{sigma} = 0.0234]	3269 [R_{int} = 0.0279, R_{sigma} = 0.0598]	6523 [R_{int} = 0.0699, R_{sigma} = 0.0828]
Data/restraints/parameters	1973/0/108	3269/0/151	6523/555/434
Goodness-of-fit on F^2	1.075	1.018	1.032
Final R indexes [I>=2σ (I)]	R_1 = 0.0246, wR_2 = 0.0654	R_1 = 0.0526, wR_2 = 0.1340	R_1 = 0.0510, wR_2 = 0.0757
Final R indexes [all data]	R_1 = 0.0253, wR_2 = 0.0659	R_1 = 0.0686, wR_2 = 0.1440	R_1 = 0.0917, wR_2 = 0.0857
Largest diff. peak/hole / e Å^{-3}	0.57/-0.58	1.04/-0.71	0.50/-0.48

	Ni(6^{n}Pent)(PPh_3)Br (2.14)	Ni(7^{n}Pent)(PPh_3)Br (2.16)	Ni(6^{n}Pent)$_2$$Br_2$
Identification code	s17mkw1	e17mkw15	s16mkw95
Empirical formula	$C_{32}H_{43}BrN_2NiP$	$C_{33}H_{45}BrN_2NiP$	$C_{28}H_{56}Br_2N_4Ni$
Formula weight	625.27	639.30	667.29
Temperature/K	150.00(10)	150.00(10)	150.10(10)
Crystal system	orthorhombic	monoclinic	monoclinic
Space group	$Cmc2_1$	$P2_1/n$	C2/c
Unit cell dimensions/Å, °	18.61276(9), 90 9.44335(4), 90 17.74036(7), 90	10.7151(3), 90 18.6310(5), 91.792(3) 16.0526(5), 90	17.4247(2), 90 14.4402(2), 106.2660(10) 13.4557(2), 90
Volume/Å^3	3118.17(2)	3203.06(16)	3250.15(8)
Z	4	4	4
Density ρ_{calc}g/cm^3	1.332	1.326	1.364
Absorption coefficient/mm^{-1}	3.039	1.927	3.890
F(000)	1308.0	1340.0	1400.0
Crystal size/mm^3	0.283 × 0.247 × 0.130	0.855 × 0.575 × 0.521	0.351 × 0.294 × 0.231
Radiation	CuKα (λ = 1.54184)	MoKα (λ = 0.71073)	CuKα (λ = 1.54184)
2Θ range for data collection/°	9.504 to 146.598	6.802 to 54.968	8.088 to 146.472
Index ranges	$-23 \leq h \leq 22$, $-11 \leq k \leq 11$, $-22 \leq l \leq 22$	$-13 \leq h \leq 13$, $-24 \leq k \leq 23$, $-20 \leq l \leq 20$	$-21 \leq h \leq 20$, $-16 \leq k \leq 17$, $-16 \leq l \leq 16$
Reflections collected	56284	27970	16384
Independent reflections	3229 [R_{int} = 0.0398, R_{sigma} = 0.0118]	7184 [R_{int} = 0.0302, R_{sigma} = 0.0319]	3263 [R_{int} = 0.0327, R_{sigma} = 0.0189]
Data/restraints/parameters	3229/1/181	7184/0/349	3263/0/166
Goodness-of-fit on F^2	1.056	1.061	1.167
Final R indexes [I>=2σ (I)]	R_1 = 0.0226, wR_2 = 0.0606	R_1 = 0.0618, wR_2 = 0.1861	R_1 = 0.0289, wR_2 = 0.0755
Final R indexes [all data]	R_1 = 0.0227, wR_2 = 0.0606	R_1 = 0.0729, wR_2 = 0.1950	R_1 = 0.0294, wR_2 = 0.0759
Largest diff. peak/hole / e Å^{-3}	0.26/-0.23	2.67/-1.78	0.41/-0.56

	Ni(7^{i}Bu)$_2$Br$_2$	**Ni(7^{n}Pent)$_2$Br$_2$**	**[{Ni(6Mes)(PPh$_3$)}$_2$(μ-Br)]BAr$^{F}_4$ (2.18)**
Identification code	e17mkw17	e17mkw5	e17mkw42
Empirical formula	$C_{26}H_{52}N_4NiBr_2$	$C_{30}H_{60}Br_2N_4Ni$	$C_{116}H_{108}BBrF_{24}N_4Ni_2OP_2$
Formula weight	631.17	695.35	2300.14
Temperature/K	150.00(10)	150.00(10)	150.00(10)
Crystal system	monoclinic	orthorhombic	triclinic
Space group	$P2_1/c$	Fddd	P-1
Unit cell dimensions/Å, °	8.3131(8), 90 8.9516(7), 90 20.607(3), 90	20.3492(5), 90 23.3391(6), 90 15.1384(5), 90	12.9050(4), 75.082(2) 17.3278(5), 84.432(2) 25.2732(6), 87.444(2)
Volume/Å^3	1533.5(3)	7189.7(3)	5434.1(3)
Z	2	8	2
Density ρ_{calc}g/cm^3	1.3668	1.285	1.406
Absorption coefficient/mm^{-1}	3.257	2.785	0.836
F(000)	651.8	2928.0	2364.0
Crystal size/mm^3	0.919 × 0.675 × 0.577	0.476 × 0.373 × 0.341	1.045 × 0.77 × 0.563
Radiation	Mo Kα (λ = 0.71073)	MoKα (λ = 0.71073)	MoKα (λ = 0.71073)
2Θ range for data collection/°	6.98 to 58.9	6.71 to 54.956	6.908 to 54.968
Index ranges	$-11 \leq h \leq 10$, $-11 \leq k \leq 12$, $-24 \leq l \leq 27$	$-25 \leq h \leq 26$, $-30 \leq k \leq 26$, $-15 \leq l \leq 19$	$-16 \leq h \leq 16$, $-22 \leq k \leq 17$, $-32 \leq l \leq 32$
Reflections collected	13132	17752	46948
Independent reflections	3744 [R_{int} = 0.0547, R_{sigma} = 0.0574]	2064 [R_{int} = 0.0194, R_{sigma} = 0.0106]	24033 [R_{int} = 0.0376, R_{sigma} = 0.0887]
Data/restraints/parameters	3744/0/164	2064/0/89	24033/121/1365
Goodness-of-fit on F^2	1.129	1.041	1.023
Final R indexes [I>=2σ (I)]	R_1 = 0.0778, wR_2 = 0.2043	R_1 = 0.0175, wR_2 = 0.0411	R_1 = 0.0635, wR_2 = 0.1396
Final R indexes [all data]	R_1 = 0.0911, wR_2 = 0.2158	R_1 = 0.0242, wR_2 = 0.0440	R_1 = 0.1297, wR_2 = 0.1745
Largest diff. peak/hole / e Å^{-3}	1.67/-2.69	0.28/-0.21	1.19/-0.93

	Ni(6Mes)(PCy_3)Br (2.20)	**[Ni(6Xyl)$_2$]Br (3.2)**	**[Ni(7Mes)$_2$]Br (3.3)**
Identification code	s16mkw74	s16mkw45	s16mkw46
Empirical formula	$C_{40}H_{61}BrN_2NiP$	$C_{42}H_{52}N_4NiBrCl_4$	$C_{47}H_{62}BrCl_2N_4Ni$
Formula weight	739.49	893.29	892.52
Temperature/K	150.00(10)	150.00(10)	150.01(10)
Crystal system	orthorhombic	monoclinic	orthorhombic
Space group	$Pca2_1$	C2/c	$Pca2_1$
Unit cell dimensions/Å, °	32.3207(2), 90 9.93930(10), 90 23.77980(10), 90	15.41478(14), 90 13.97716(11), 105.2482(10) 20.40543(19), 90	17.55756(9), 90 12.09149(6), 90 21.14171(10), 90
Volume/Å^3	7639.15(10)	4241.67(7)	4488.32(4)
Z	8	4	4
Density ρ_{calc}g/cm^3	1.286	1.399	1.321
Absorption coefficient/mm^{-1}	2.558	4.340	3.030
F(000)	3144.0	1852.0	1876.0
Crystal size/mm^3	0.619 × 0.333 × 0.32	0.265 × 0.207 × 0.16	0.264 × 0.152 × 0.088
Radiation	CuKα (λ = 1.54184)	CuKα (λ = 1.54184)	CuKα (λ = 1.54184)
2Θ range for data collection/°	5.468 to 148.628	8.682 to 144.904	7.31 to 145.032
Index ranges	$-40 \le h \le 40$, $-12 \le k \le 8$, $-29 \le l \le 29$	$-15 \le h \le 19$, $-17 \le k \le 17$, $-25 \le l \le 25$	$-21 \le h \le 21$, $-14 \le k \le 14$, $-26 \le l \le 19$
Reflections collected	110800	22050	57741
Independent reflections	15449 [R_{int} = 0.0496, R_{sigma} = 0.0241]	4197 [R_{int} = 0.0203, R_{sigma} = 0.0129]	6924 [R_{int} = 0.0345, R_{sigma} = 0.0215]
Data/restraints/parameters	15449/849/1069	4197/0/240	6924/1/508
Goodness-of-fit on F^2	1.030	1.022	1.033
Final R indexes [I>=2σ (I)]	R_1 = 0.0472, wR_2 = 0.1258	R_1 = 0.0381, wR_2 = 0.0927	R_1 = 0.0308, wR_2 = 0.0821
Final R indexes [all data]	R_1 = 0.0479, wR_2 = 0.1264	R_1 = 0.0392, wR_2 = 0.0934	R_1 = 0.0315, wR_2 = 0.0827
Largest diff. peak/hole / e Å^{-3}	1.74/-0.65	1.02/-1.02	0.72/-0.53

	[Ni(7Xyl)$_2$]Br (3.4)	**[Ni(6Mes)(6Xyl)]Br (4.1)**	**[Ni(6Mes)(7Mes)]Br (4.2)**
Identification code	e16mkw5	s16mkw42	e17mkw16
Empirical formula	$C_{44}H_{56}N_4Cl_4NiBr$	$C_{44}H_{56}BrCl_4N_4Ni$	$C_{46}H_{60}BrN_4NiCl_2$
Formula weight	921.34	921.34	878.50
Temperature/K	149.9(3)	150.00(10)	150.00(10)
Crystal system	monoclinic	monoclinic	monoclinic
Space group	C2/c	$P2_1$	$P2_1/c$
Unit cell dimensions/Å, °	15.7903(3), 90 13.6094(2), 105.989(2) 21.2365(5), 90	10.28064(11), 90 21.43518(19), 96.6170(9) 10.28913(11), 90	14.6633(5), 90 15.0292(4), 107.793(4) 21.2991(8), 90
Volume/Å^3	4387.11(16)	2252.29(4)	4469.3(3)
Z	4	2	4
Density ρ_{calc}g/cm^3	1.395	1.359	1.306
Absorption coefficient/mm^{-1}	1.632	4.103	1.483
F(000)	1916.0	958.0	1844.0
Crystal size/mm^3	0.332 × 0.278 × 0.203	0.222 × 0.176 × 0.115	0.36 × 0.35 × 0.301
Radiation	MoKα (λ = 0.71073)	CuKα (λ = 1.54184)	MoKα (λ = 0.71073)
2Θ range for data collection/°	6.57 to 54.968	8.25 to 146.35	6.748 to 54.966
Index ranges	$-20 \le h \le 20$, $-17 \le k \le 17$, $-27 \le l \le 27$	$-12 \le h \le 12$, $-24 \le k \le 26$, $-12 \le l \le 12$	$-19 \le h \le 18$, $-19 \le k \le 19$, $-23 \le l \le 26$
Reflections collected	21856	25257	42518
Independent reflections	5036 [R_{int} = 0.0261, R_{sigma} = 0.0222]	7802 [R_{int} = 0.0338, R_{sigma} = 0.0329]	10140 [R_{int} = 0.0395, R_{sigma} = 0.0437]
Data/restraints/parameters	5036/0/249	7802/1/515	10140/6/475
Goodness-of-fit on F^2	1.038	1.108	1.052
Final R indexes [I>=2σ (I)]	R_1 = 0.0287, wR_2 = 0.0716	R_1 = 0.0415, wR_2 = 0.1135	R_1 = 0.0773, wR_2 = 0.2174
Final R indexes [all data]	R_1 = 0.0401, wR_2 = 0.0774	R_1 = 0.0429, wR_2 = 0.1144	R_1 = 0.1044, wR_2 = 0.2369
Largest diff. peak/hole / e Å^{-3}	0.45/-0.48	0.59/-0.60	1.13/-2.14

	[Ni(6Mes)(7Xyl)]Br (4.3)	**[Ni(6Mes)(6Xyl-*p*-Br)]Br (4.4)**	**[Ni(6Mes)(IMes)]Br (4.6)**
Identification code	s16mkw41	e17mkw26	s17mkw8
Empirical formula	$C_{45}H_{58}BrCl_4N_4Ni$	$C_{44}H_{54}Br_3Cl_4N_4Ni$	$C_{44}H_{54}BrCl_2N_4Ni$
Formula weight	935.37	1079.15	848.43
Temperature/K	150.00(10)	150.00(10)	150.00(10)
Crystal system	monoclinic	monoclinic	monoclinic
Space group	$P2_1$	$P2_1/c$	$P2_1/c$
Unit cell dimensions/Å, °	10.10569(8), 90 21.63897(18), 98.0393(8) 10.44124(9), 90	13.4533(4), 90 13.7830(3), 90.019(3) 25.3976(9), 90	14.96206(18), 90 14.45183(11), 108.0635(13) 20.9775(3), 90
Volume/Å^3	2260.82(3)	4709.4(2)	4312.38(9)
Z	2	4	4
Density ρ_{calc}g/cm^3	1.374	1.522	1.307
Absorption coefficient/mm^{-1}	4.095	3.219	3.128
F(000)	974.0	2188.0	1772.0
Crystal size/mm^3	0.246 × 0.153 × 0.086	0.417 × 0.304 × 0.124	0.311 × 0.204 × 0.066
Radiation	CuKα (λ = 1.54184)	MoKα (λ = 0.71073)	CuKα (λ = 1.54184)
2Θ range for data collection/°	8.552 to 146.126	6.642 to 54.966	6.214 to 146.38
Index ranges	$-12 \leq h \leq 10$, $-26 \leq k \leq 26$, $-12 \leq l \leq 12$	$-16 \leq h \leq 17$, $-17 \leq k \leq 17$, $-31 \leq l \leq 32$	$-18 \leq h \leq 18$, $-17 \leq k \leq 12$, $-25 \leq l \leq 25$
Reflections collected	26415	50848	62774
Independent reflections	8761 [R_{int} = 0.0299, R_{sigma} = 0.0324]	10646 [R_{int} = 0.0521, R_{sigma} = 0.0588]	8621 [R_{int} = 0.0594, R_{sigma} = 0.0304]
Data/restraints/parameters	8761/1/515	10646/19/542	8621/6/487
Goodness-of-fit on F^2	1.031	1.067	1.041
Final R indexes [I>=2σ (I)]	R_1 = 0.0252, wR_2 = 0.0627	R_1 = 0.0662, wR_2 = 0.1299	R_1 = 0.0506, wR_2 = 0.1464
Final R indexes [all data]	R_1 = 0.0259, wR_2 = 0.0634	R_1 = 0.1165, wR_2 = 0.1465	R_1 = 0.0550, wR_2 = 0.1525
Largest diff. peak/hole / e Å^{-3}	0.29/-0.22	0.93/-0.60	1.00/-1.05

	[Ni(6Mes)(SIMes)]Br (4.7)	**[Ni(6Xyl)(7Mes)]Br (4.8)**	**[Ni(6Xyl)(7Xyl)]Br (4.9)**
Identification code	e17mkw11	e17mkw8	e17mkw4
Empirical formula	$C_{44}H_{56}BrCl_2N_4Ni$	$C_{45}H_{58}BrCl_4N_4Ni$	$C_{43}H_{54}BrCl_4N_4Ni$
Formula weight	850.44	935.37	907.32
Temperature/K	150.00(10)	150.01(12)	150.00(10)
Crystal system	monoclinic	monoclinic	monoclinic
Space group	$P2_1/c$	$P2_1$	C2/c
Unit cell dimensions/Å, °	14.7805(6), 90 14.5235(5), 107.554(4) 21.2216(9), 90	10.0860(2), 90 21.4874(4), 97.762(2) 10.5800(2), 90	15.6080(5), 90 13.7916(4), 105.804(4) 20.8868(7), 90
Volume/Å^3	4343.4(3)	2271.91(8)	4326.1(3)
Z	4	2	4
Density ρ_{calc}g/cm^3	1.301	1.367	1.393
Absorption coefficient/mm^{-1}	1.524	1.577	1.654
F(000)	1780.0	974.0	1884.0
Crystal size/mm^3	0.601 × 0.338 × 0.287	0.31 × 0.259 × 0.25	0.565 × 0.5 × 0.382
Radiation	MoKα (λ = 0.71073)	MoKα (λ = 0.71073)	MoKα (λ = 0.71073)
2Θ range for data collection/°	6.66 to 54.966	6.89 to 54.968	7.166 to 54.968
Index ranges	$-19 \leq h \leq 19$, $-18 \leq k \leq 18$, $-27 \leq l \leq 27$	$-12 \leq h \leq 12$, $-27 \leq k \leq 27$, $-13 \leq l \leq 13$	$-20 \leq h \leq 19$, $-15 \leq k \leq 17$, $-27 \leq l \leq 27$
Reflections collected	51918	18572	17937
Independent reflections	9800 [R_{int} = 0.0485, R_{sigma} = 0.0432]	9323 [R_{int} = 0.0302, R_{sigma} = 0.0647]	4876 [R_{int} = 0.0262, R_{sigma} = 0.0271]
Data/restraints/parameters	9800/18/499	9323/7/509	4876/3/261
Goodness-of-fit on F^2	1.042	1.044	1.046
Final R indexes [I>=2σ (I)]	R_1 = 0.0521, wR_2 = 0.1162	R_1 = 0.0410, wR_2 = 0.0841	R_1 = 0.0400, wR_2 = 0.1114
Final R indexes [all data]	R_1 = 0.0862, wR_2 = 0.1333	R_1 = 0.0570, wR_2 = 0.0921	R_1 = 0.0512, wR_2 = 0.1201
Largest diff. peak/hole / e Å^{-3}	1.01/-0.88	0.65/-0.75	0.49/-1.10

	[Ni(7Mes)(7Xyl)]Br (4.10)	[Ni(7Mes)(IMes)]Br (4.11)	[Ni(6Mes)(PCy_3)]BAr^F_4 (4.12)
Identification code	e17mkw3	e17mkw10	e18mkw9
Empirical formula	$C_{46}H_{60}BrCl_4N_4Ni$	$C_{45}H_{56}BrCl_2N_4Ni$	$C_{72}H_{73}BF_{24}N_2NiP$
Formula weight	949.40	862.45	1522.81
Temperature/K	150.0(2)	150.01(10)	150.0(3)
Crystal system	monoclinic	monoclinic	monoclinic
Space group	$P2_1$	$P2_1/c$	Pn
Unit cell dimensions/Å, °	10.0856(5), 90 21.6495(9), 98.223(4) 10.6295(4), 90	14.6077(4), 90 14.6052(3), 107.734(3) 21.5929(6), 90	13.2409(5), 90 13.1959(4), 90.374(3) 20.5534(5), 90
Volume/Å^3	2297.07(17)	4387.9(2)	3591.13(19)
Z	2	4	2
Density ρ_{calc}g/cm^3	1.373	1.306	1.408
Absorption coefficient/mm^{-1}	1.561	1.509	0.397
F(000)	990.0	1804.0	1566.0
Crystal size/mm^3	0.346 × 0.272 × 0.247	0.364 × 0.279 × 0.245	0.566 × 0.413 × 0.179
Radiation	MoKα (λ = 0.71073)	MoKα (λ = 0.71073)	MoKα (λ = 0.71073)
2Θ range for data collection/°	6.426 to 54.966	6.566 to 54.964	6.486 to 54.968
Index ranges	$-11 \leq h \leq 12$, $-27 \leq k \leq 27$, $-13 \leq l \leq 9$	$-18 \leq h \leq 18$, $-18 \leq k \leq 18$, $-27 \leq l \leq 27$	$-17 \leq h \leq 15$, $-17 \leq k \leq 17$, $-24 \leq l \leq 26$
Reflections collected	19955	40142	32226
Independent reflections	10087 [R_{int} = 0.0262, R_{sigma} = 0.0497]	9919 [R_{int} = 0.0448, R_{sigma} = 0.0494]	12351 [R_{int} = 0.0362, R_{sigma} = 0.0599]
Data/restraints/parameters	10087/1/515	9919/34/543	12351/116/970
Goodness-of-fit on F^2	1.027	1.022	1.021
Final R indexes [I>=2σ (I)]	R_1 = 0.0374, wR_2 = 0.0686	R_1 = 0.0537, wR_2 = 0.1255	R_1 = 0.0677, wR_2 = 0.1892
Final R indexes [all data]	R_1 = 0.0461, wR_2 = 0.0718	R_1 = 0.0968, wR_2 = 0.1487	R_1 = 0.0865, wR_2 = 0.1966
Largest diff. peak/hole / e Å^{-3}	0.46/-0.36	0.61/-0.80	0.91/-0.56

	[Ni(6Xyl)(PCy_3)]BAr^F_4 (4.13)	**[Ni(7Mes)(PCy_3)]BAr^F_4 (4.14)**	**[Ni(7Xyl)(PCy_3)]BAr^F_4 (4.15)**
Identification code	e18mkw13	e18mkw17	e18mkw12
Empirical formula	$C_{70}H_{69}BF_{24}N_2NiP$	$C_{73}H_{75}BF_{24}N_2NiP$	$C_{71}H_{71}BF_{24}N_2NiP$
Formula weight	1494.76	1536.84	1508.78
Temperature/K	150.0(3)	149.99(10)	150.00(10)
Crystal system	orthorhombic	monoclinic	monoclinic
Space group	$Pca2_1$	$P2_1$	$P2_1/n$
Unit cell dimensions/Å, °	19.8983(4), 90	12.5661(3), 90	14.4404(3), 90
	12.5762(2), 90	15.8229(4), 93.742(2)	12.6335(3), 95.383(2)
	27.8673(4), 90	37.1513(10), 90	38.6694(8), 90
Volume/Å^3	6973.7(2)	7371.1(3)	7023.5(3)
Z	4	4	4
Density ρ_{calc}g/cm^3	1.424	1.385	1.427
Absorption coefficient/mm^{-1}	0.408	0.388	0.406
F(000)	3068.0	3164.0	3100.0
Crystal size/mm^3	0.591 × 0.421 × 0.341	0.54 × 0.409 × 0.346	0.595 × 0.484 × 0.401
Radiation	MoKα (λ = 0.71073)	MoKα (λ = 0.71073)	MoKα (λ = 0.71073)
2Θ range for data collection/°	6.82 to 58.85	6.772 to 58.988	7.018 to 59.138
Index ranges	$-25 \le h \le 25$, $-16 \le k \le 17$, $-38 \le l \le 38$	$-15 \le h \le 17$, $-21 \le k \le 19$, $-49 \le l \le 49$	$-19 \le h \le 18$, $-15 \le k \le 17$, $-52 \le l \le 51$
Reflections collected	60383	65065	59981
Independent reflections	16654 [R_{int} = 0.0289, R_{sigma} = 0.0351]	32008 [R_{int} = 0.0414, R_{sigma} = 0.0878]	17113 [R_{int} = 0.0422, R_{sigma} = 0.0623]
Data/restraints/parameters	16654/461/1088	32008/519/2049	17113/659/1112
Goodness-of-fit on F^2	1.024	1.011	1.035
Final R indexes [I>=2σ (I)]	R_1 = 0.0420, wR_2 = 0.0845	R_1 = 0.0660, wR_2 = 0.1246	R_1 = 0.0578, wR_2 = 0.1062
Final R indexes [all data]	R_1 = 0.0608, wR_2 = 0.0929	R_1 = 0.1017, wR_2 = 0.1425	R_1 = 0.0958, wR_2 = 0.1222
Largest diff. peak/hole / e Å^{-3}	0.38/-0.38	0.62/-0.39	0.50/-0.46

	[Ni(7Xyl)(P^{t}Bu$_3$)]BAr$^F_4$ (4.16)	**[Ni(7Xyl)(PCy$_3$)(CO)]BAr$^F_4$ (4.19)**	**[Ni(7Xyl)(P^{t}Bu$_3$)(CO)]BAr$^F_4$ (4.20)**
Identification code	e19mkw12	e19mkw14	e19mkw18
Empirical formula	$C_{65}H_{65}BF_{24}N_2NiP$	$C_{72}H_{71}BF_{24}N_2NiOP$	$C_{66}H_{65}BF_{24}N_2NiOP$
Formula weight	1430.68	1536.79	1458.69
Temperature/K	150.00(13)	150.00(10)	150.01(11)
Crystal system	monoclinic	triclinic	monoclinic
Space group	$P2_1/c$	P-1	$P2_1/c$
Unit cell dimensions/Å, °	12.8141(1), 90 27.3944(4), 93.118(1) 18.4571(2), 90	13.2285(5), 90.250(2) 13.6683(4), 98.884(3) 19.8178(6), 95.342(3)	12.7782(2), 90 27.5727(5), 93.7550(10) 18.6212(3), 90
Volume/Å^3	6469.49(13)	3524.3(2)	6546.71(19)
Z	4	2	4
Density ρ_{calc}g/cm^3	1.469	1.448	1.480
Absorption coefficient/mm^{-1}	0.436	0.407	0.433
F(000)	2932.0	1578.0	2988.0
Crystal size/mm^3	0.464 × 0.276 × 0.256	0.622 × 0.447 × 0.314	0.516 × 0.322 × 0.176
Radiation	MoKα (λ = 0.71073)	MoKα (λ = 0.71073)	MoKα (λ = 0.71073)
2Θ range for data collection/°	6.748 to 59.448	6.874 to 58.876	6.742 to 59.118
Index ranges	$-16 \le h \le 17$, $-37 \le k \le 34$, $-25 \le l \le 22$	$-18 \le h \le 16$, $-17 \le k \le 18$, $-25 \le l \le 27$	$-16 \le h \le 11$, $-38 \le k \le 36$, $-22 \le l \le 25$
Reflections collected	62757	34140	63663
Independent reflections	16158 [R_{int} = 0.0325, R_{sigma} = 0.0387]	16395 [R_{int} = 0.0277, R_{sigma} = 0.0552]	15935 [R_{int} = 0.0340, R_{sigma} = 0.0417]
Data/restraints/parameters	16158/637/1076	16395/496/995	15935/188/1004
Goodness-of-fit on F^2	1.079	1.023	1.021
Final R indexes [I>=2σ (I)]	R_1 = 0.0482, wR_2 = 0.1082	R_1 = 0.0558, wR_2 = 0.1210	R_1 = 0.0619, wR_2 = 0.1511
Final R indexes [all data]	R_1 = 0.0725, wR_2 = 0.1191	R_1 = 0.0864, wR_2 = 0.1368	R_1 = 0.0946, wR_2 = 0.1724
Largest diff. peak/hole / e Å^{-3}	0.88/-0.58	1.05/-0.47	1.56/-1.43

	[PCy_3Me][$Ni(PCy_3)I_3$] (4.21)	**[{$Ni(PCy_3)$}$_2$(μ-I)$_3$] (4.22)**	**[7Xyl·C_6H_4F]BAr^F_4 (4.23)**
Identification code	e19mkw16	e19mkw19	e19mkw20
Empirical formula	$C_{37}H_{69}I_3NiP_2$	$C_{36}H_{66}I_3Ni_2P_2$	$C_{59}H_{42}BF_{25}N_2$
Formula weight	1015.27	1058.94	1264.75
Temperature/K	150.01(10)	150.00(10)	149.89(10)
Crystal system	triclinic	triclinic	triclinic
Space group	P-1	P-1	P-1
Unit cell dimensions/Å, °	12.0599(4), 78.572(3) 13.3517(5), 78.451(3) 13.4206(5), 89.107(3)	8.5985(3), 74.147(3) 13.9712(6), 89.723(3) 17.9705(7), 82.276(3)	12.5305(1), 90.191(1) 12.7623(2), 91.337(1) 35.3003(5), 92.431(1)
Volume/Å^3	2074.61(13)	2056.72(14)	5638.48(13)
Z	2	2	4
Density ρ_{calc}g/cm^3	1.625	1.710	1.490
Absorption coefficient/mm^{-1}	2.800	3.268	0.145
F(000)	1016.0	1054.0	2560.0
Crystal size/mm^3	0.504 × 0.41 × 0.34	0.286 × 0.171 × 0.122	0.461 × 0.449 × 0.245
Radiation	MoKα (λ = 0.71073)	MoKα (λ = 0.71073)	MoKα (λ = 0.71073)
2Θ range for data collection/°	6.9 to 59.04	6.826 to 58.858	6.786 to 59.182
Index ranges	$-16 \leq h \leq 15$, $-18 \leq k \leq 17$, $-17 \leq l \leq 18$	$-11 \leq h \leq 10$, $-18 \leq k \leq 17$, $-24 \leq l \leq 24$	$-16 \leq h \leq 14$, $-14 \leq k \leq 17$, $-44 \leq l \leq 46$
Reflections collected	17603	20234	51180
Independent reflections	9618 [R_{int} = 0.0251, R_{sigma} = 0.0514]	9599 [R_{int} = 0.0254, R_{sigma} = 0.0424]	26294 [R_{int} = 0.0309, R_{sigma} = 0.0659]
Data/restraints/parameters	9618/0/389	9599/0/388	26294/507/1839
Goodness-of-fit on F^2	1.039	1.025	1.014
Final R indexes [I>=2σ (I)]	R_1 = 0.0386, wR_2 = 0.0711	R_1 = 0.0289, wR_2 = 0.0488	R_1 = 0.0772, wR_2 = 0.1659
Final R indexes [all data]	R_1 = 0.0528, wR_2 = 0.0774	R_1 = 0.0413, wR_2 = 0.0529	R_1 = 0.1278, wR_2 = 0.1968
Largest diff. peak/hole / e Å^{-3}	2.21/-1.08	0.76/-0.97	0.58/-0.52

3 NMR SPECTROSCOPY

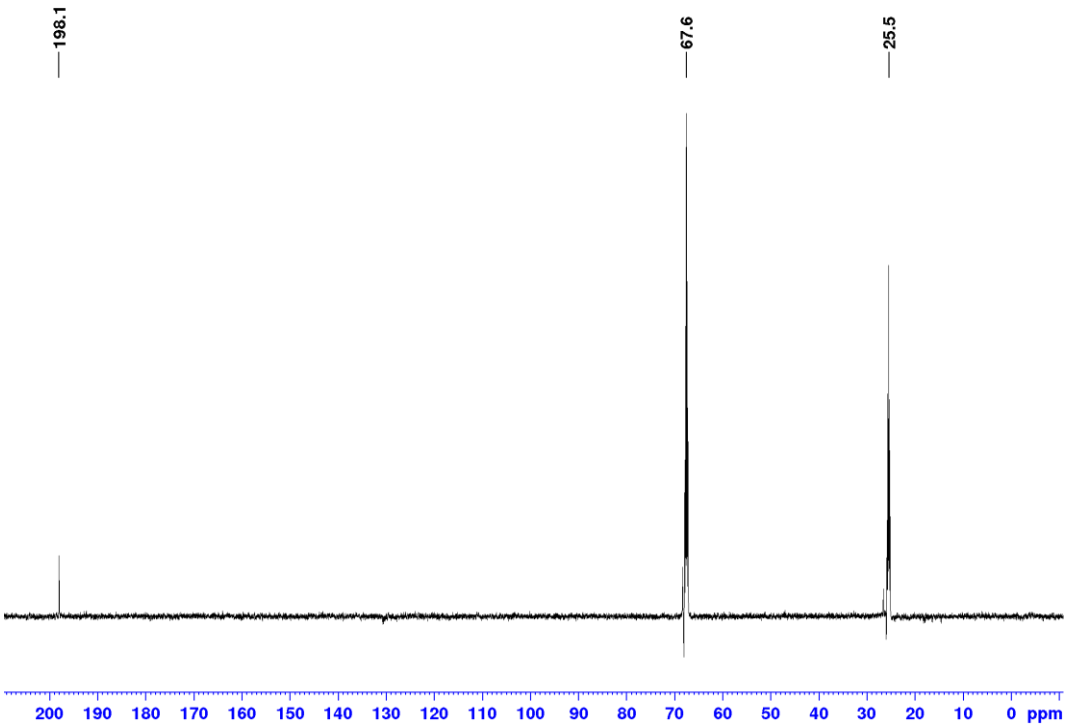

Figure A3.1 $^{13}C\{^{1}H\}$ NMR spectrum (THF-d_8, 126 MHz, 298 K) recorded 5 min after addition of 1 atm ^{13}CO to a THF-d_8 solution of compound **2.19**.

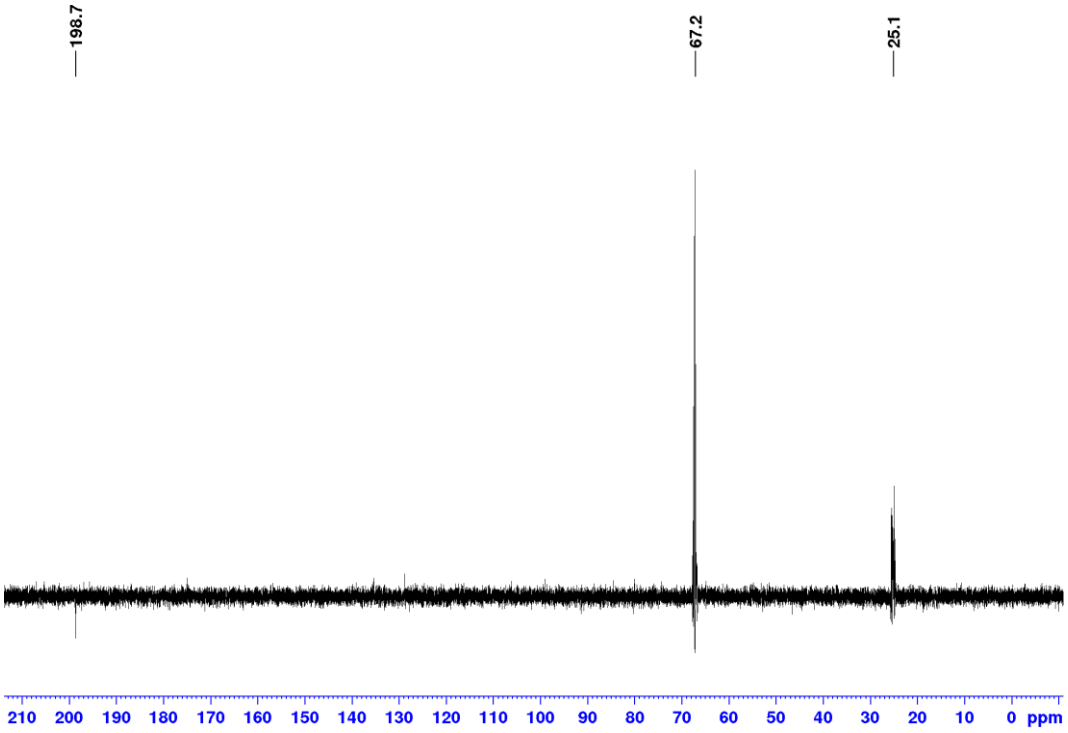

Figure A3.2 $^{13}C\{^{1}H\}$ NMR spectrum (THF-d_8, 126 MHz, 298 K) recorded 30 min after addition of 1 atm ^{13}CO to a THF-d_8 solution of compound **4.20**.

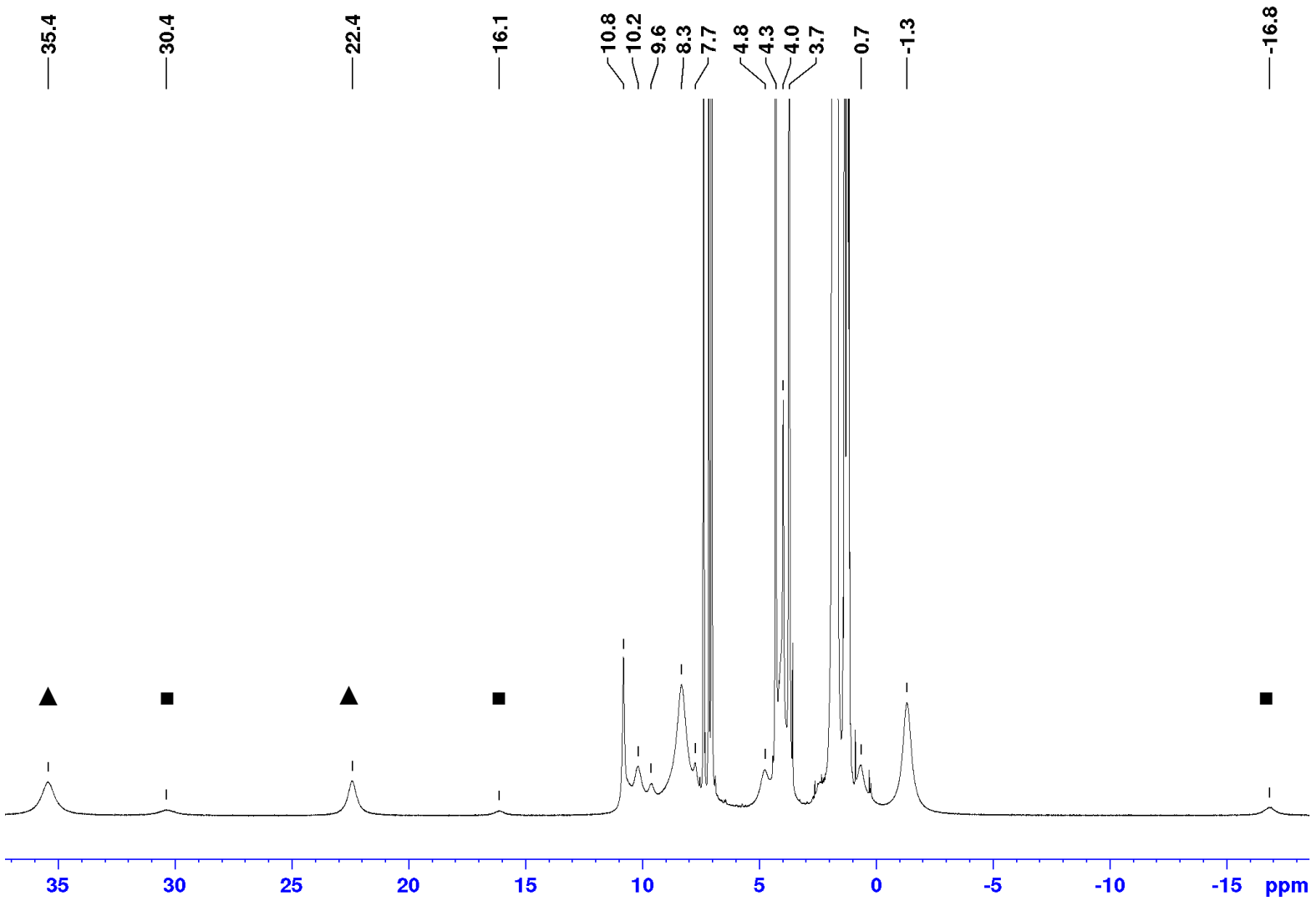

Figure A3.3 ^{1}H NMR spectrum (C_6D_6, 500 MHz, 298 K) of reaction between **2.1** (■) and PCy_3, showing formation of Ni(6Mes)(PCy_3)Br (▲).

4 IR SPECTROSCOPY

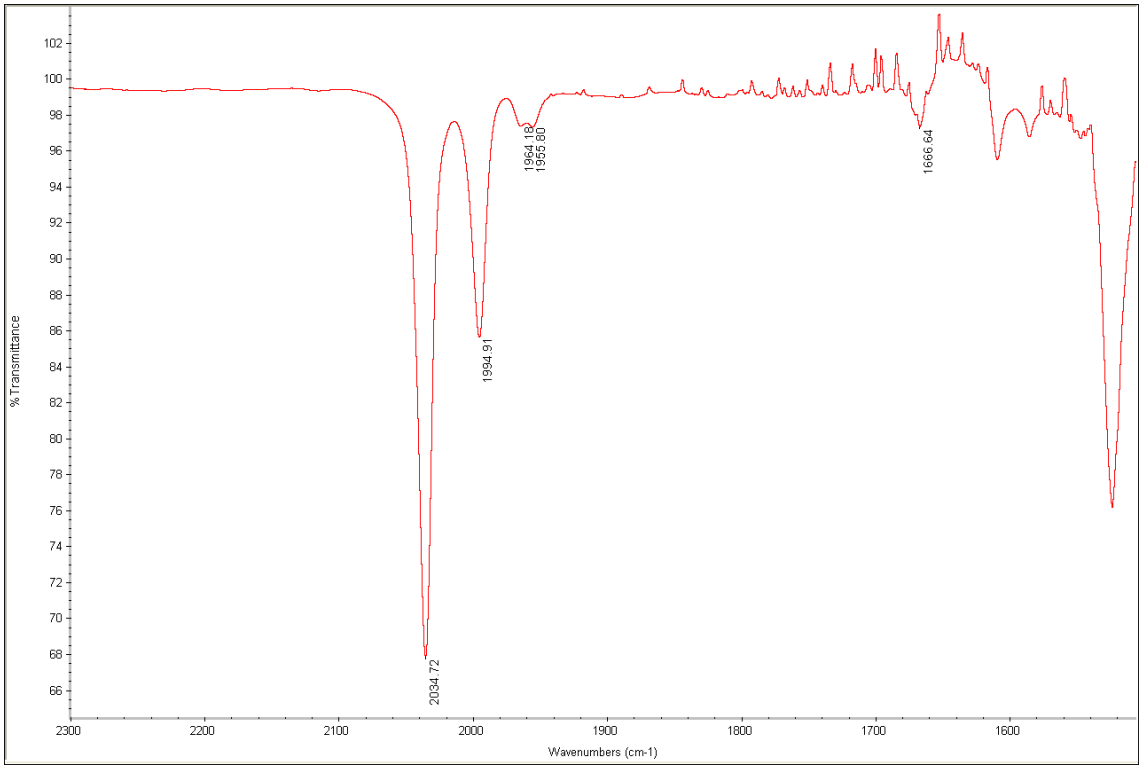

Figure A4.1 FTIR spectrum (THF) of compound **2.19**.

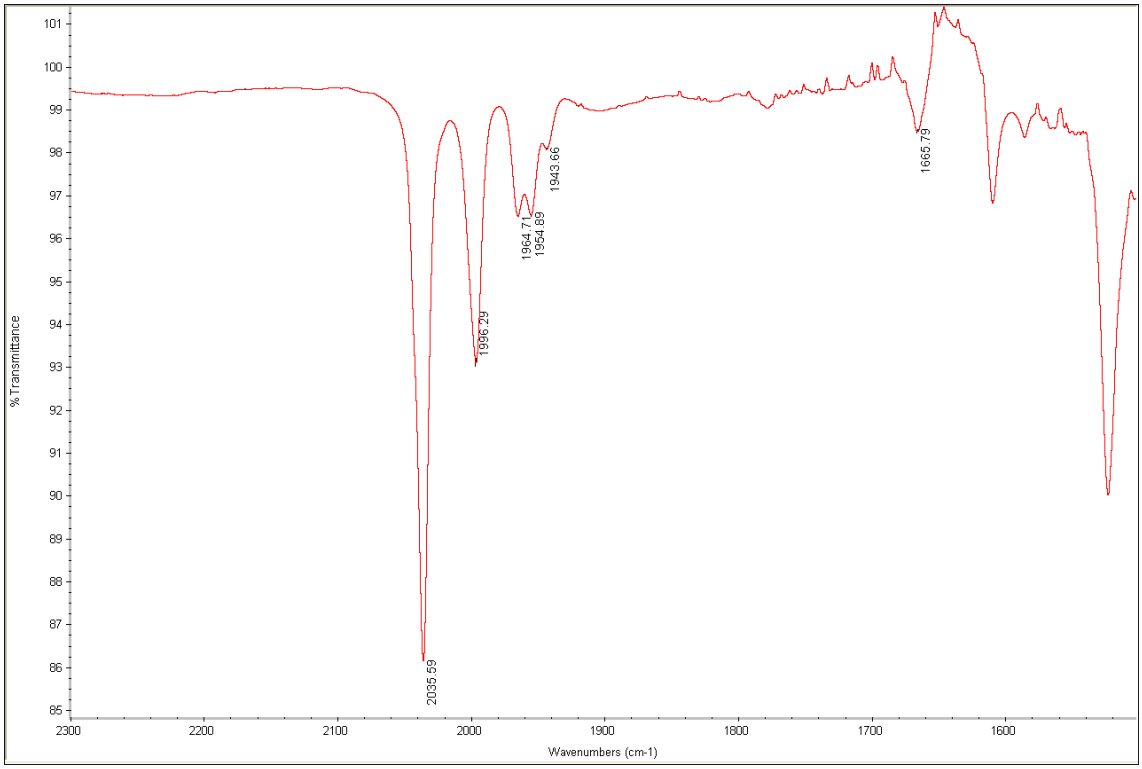

Figure A4.2 FTIR spectrum (THF) of [Ni(6Mes)(PPh_3)(CO)]BAr^F_4.

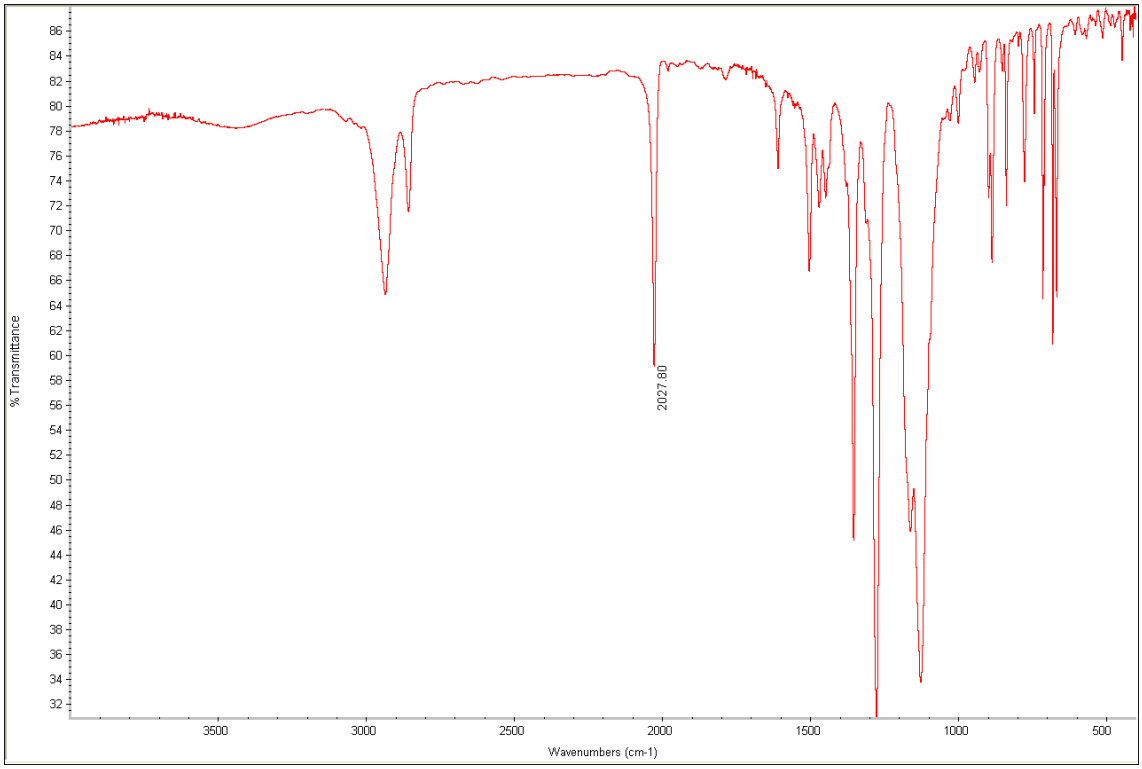

Figure A4.3 FTIR spectrum (KBr) of compound **4.19**.

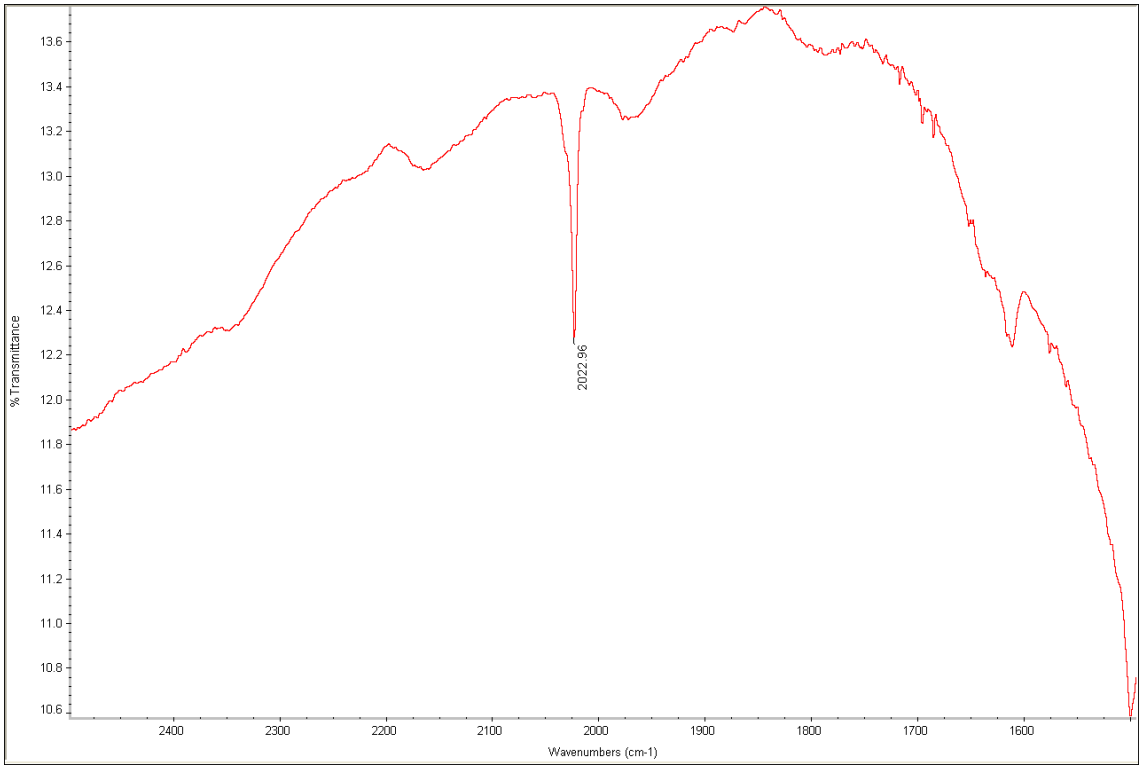

Figure A4.4 FTIR spectrum (KBr) of compound **4.20**.

5 CYCLIC VOLTAMMETRY

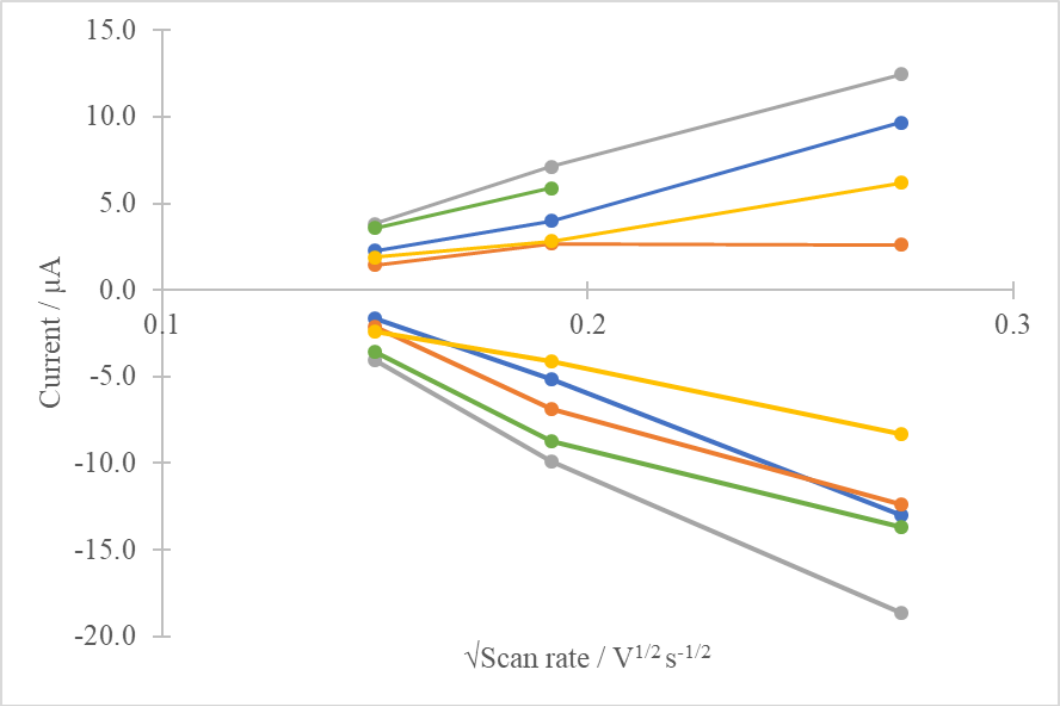

Figure A5.1 Peak current *vs*. square root of scan rate for compounds **4.12** – **4.16**.

6 DFT

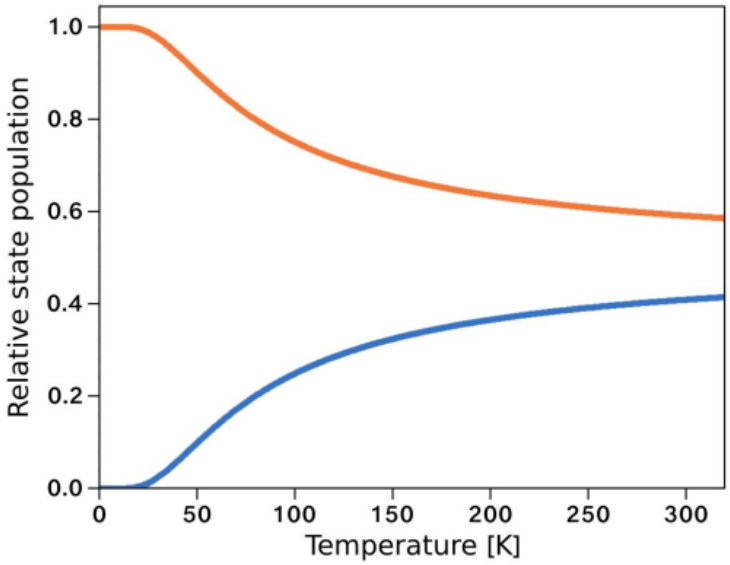

Figure A6.1 Boltzmann population distribution of the high spin (S = 1, ferromagnetically coupled) and broken-symmetry (S = 0, antiferromagnetically coupled) states of compound **2.18** based on the molecular structure coordinates with optimised hydrogen atom positions. The energy difference between the states is taken from the B3LYP BS-DFT calculation

7 SQUID

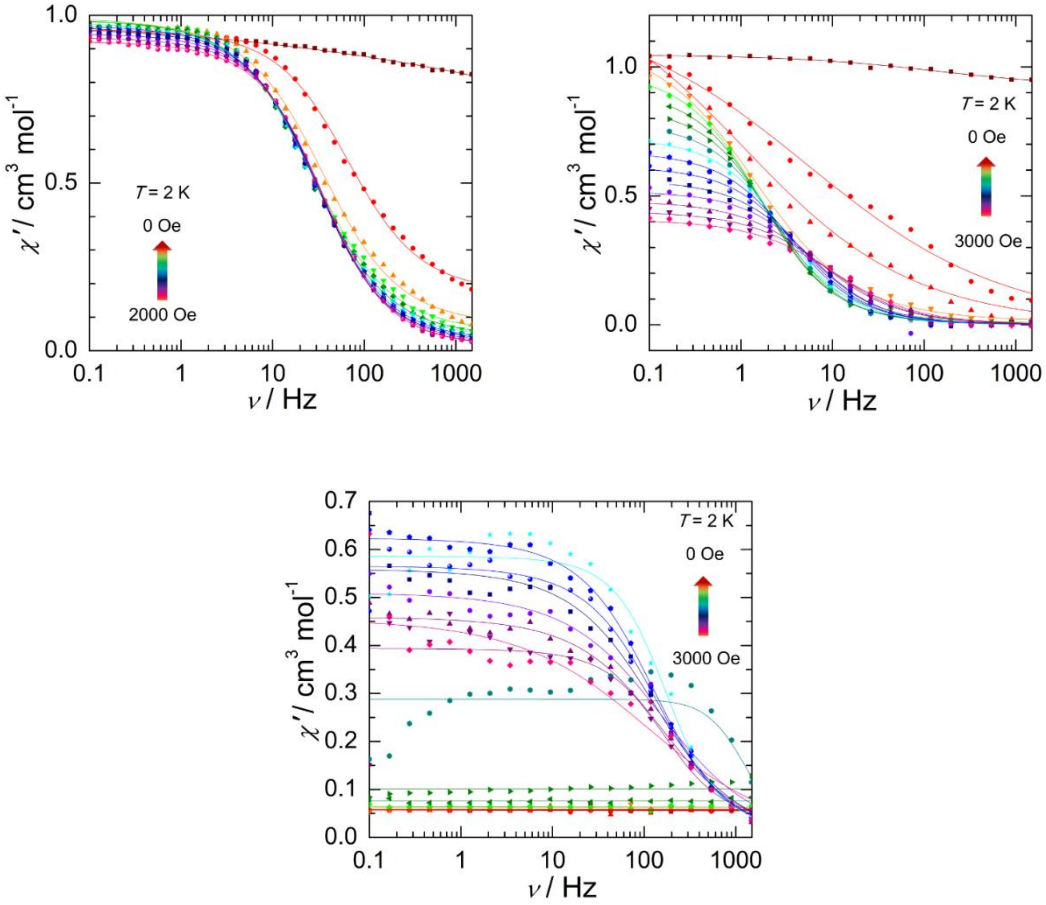

Figure A7.1 Frequency dependence of the in-phase (χ') magnetic susceptibility of compounds **3.1** (left), **3.2** (right), and **3.4** (middle) as a function of applied dc field at 2 K. Solid lines represent generalised Debye fits at each field strength.

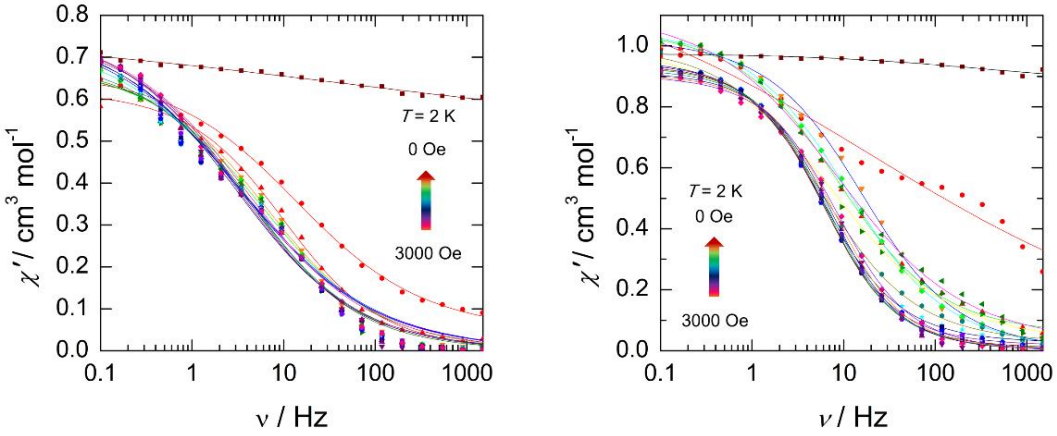

Figure A7.2 Frequency dependence of the in-phase (χ') magnetic susceptibility of compound **4.2** (left) and **4.6** (right) as a function of applied dc field at 2 K. Solid lines represent generalised Debye fits at each field strength.

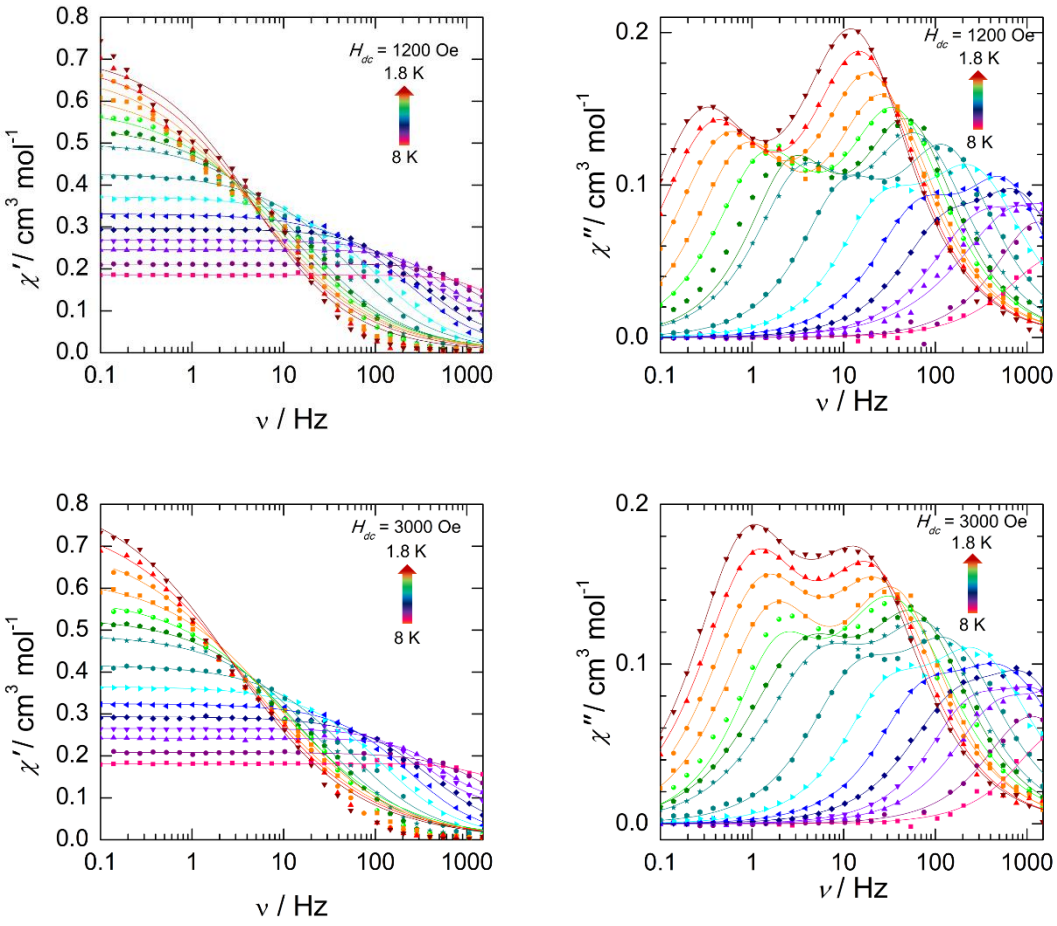

Figure A7.3 Frequency dependence of the in-phase (χ') and out-of-phase (χ'') magnetic susceptibility of compound **4.2** as a function of temperature under 1200 and 3000 Oe applied dc fields. Solid lines represent generalised double Debye fits at each temperature.

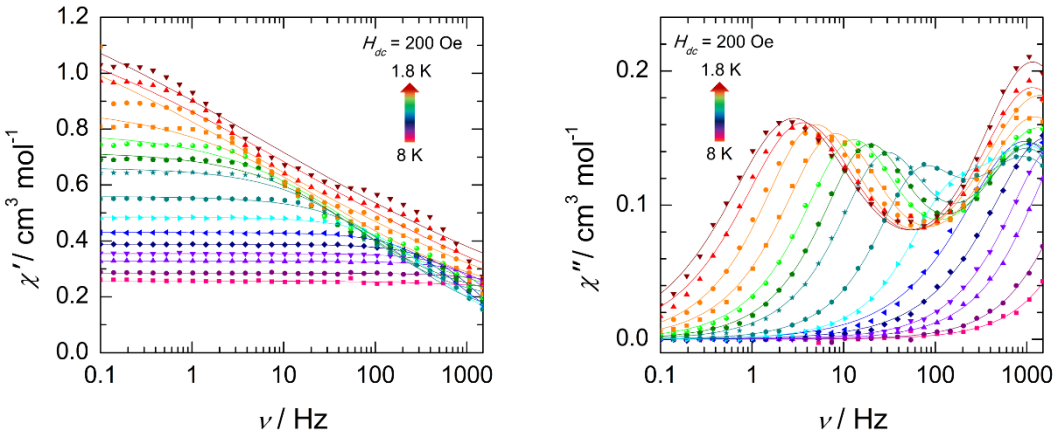

Figure A7.4 Frequency dependence of the in-phase (χ') and out-of-phase (χ'') magnetic susceptibility of compound **4.6** as a function of temperature under a 200 Oe applied dc fields. Solid lines represent generalised double Debye fits at each temperature.

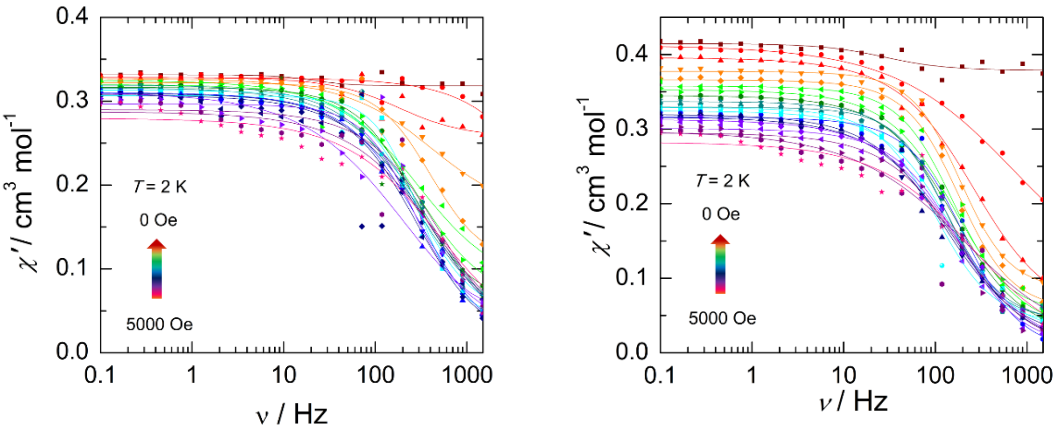

Figure A7.5 Frequency dependence of the in-phase (χ') magnetic susceptibility of compound **4.12** (left) and **4.13** (right) as a function of applied dc field at 2 K. Solid lines represent generalised Debye fits at each field strength.

Parameters fitted of the χ' and χ'' magnetic susceptibility plot of compound **3.1** to a generalised Debye model at i) 2 K under varying dc fields, and ii) 600 Oe dc field at varying temperatures.

		χ'				χ''			
		τ (s)	α	χ_S	χ_T	τ (s)	α	χ_S	χ_T
Field (Oe)	**0**	9.09E-09	0.84499	0	1.0096	0.00031	0.45456	0.01563	0.14320
	200	0.00238	0.24859	0.17257	0.95833	0.00220	0.30321	0.00174	0.85180
	400	0.00452	0.27031	0.07437	0.98634	0.00442	0.30028	0.00367	0.95397
	600	0.00566	0.27067	0.05276	0.99171	0.00562	0.28613	0.00010	0.95977
	800	0.00568	0.25855	0.04017	0.9871	0.00571	0.26711	0.00079	0.95732
	1000	0.00556	0.24394	0.03568	0.97803	0.00557	0.25302	0.00085	0.95363
	1200	0.00535	0.23514	0.02805	0.96947	0.00540	0.23953	0.00288	0.94873
	1400	0.00519	0.22142	0.02485	0.95716	0.00519	0.23138	0.00153	0.93768
	1600	0.00493	0.22084	0.01871	0.94678	0.00497	0.21943	0.00080	0.92716
	1800	0.00473	0.21389	0.01343	0.93486	0.00470	0.21425	0.16979	1.08877
	2000	0.00451	0.21257	0.01143	0.92248	0.00449	0.20763	0.00360	0.91074
T (K)	**9**	8.61E-06	0	0	0.21573	5.84E-06	0.09239	0	0.32915
	8.5	0.0107	0	0.228	0.23087	1.68E-05	0	0	0.20144
	8	1.44E-08	0.63444	0	0.24707	2.14E-06	0.09928	0	1.43151
	7.5	1.30E-05	0.1147	0.00894	0.26286	3.21E-05	0	0	0.19516
	7	1.25E-05	0.20785	0	0.2825	1.49E-05	0.05965	0	0.49258
	6.5	5.18E-05	0.02344	0	0.30201	3.50E-05	0.08544	0	0.33268
	6	5.63E-05	0.02409	0	0.32738	5.33E-05	0.03323	2.28E-05	0.33332
	5.5	7.79E-05	0.05201	0	0.35743	7.82E-05	0.04385	0.00465	0.36462
	5	0.00013	0.03413	0.0193	0.39289	0.00013	0.03127	0.00016	0.37062
	4.5	0.00021	0.03619	0.0327	0.44316	0.00021	0.03407	0.00081	0.41318
	4	0.00037	0.03075	0.04785	0.49524	0.00035	0.0487	0.00297	0.46591
	3.75	0.00050	0.03494	0.0561	0.528	0.00047	0.06279	0.00021	0.49099
	3.5	0.00067	0.0543	0.0549	0.56519	0.00064	0.08008	0.0109	0.54213
	3.25	0.00093	0.07721	0.0579	0.60867	0.00090	0.10397	0.00323	0.57897
	3	0.00132	0.10246	0.0596	0.65832	0.00127	0.12872	0.00671	0.63037
	2.75	0.00189	0.13609	0.06056	0.72038	0.00186	0.16156	0.00020	0.68232
	2.5	0.00279	0.17342	0.06313	0.79425	0.0027	0.20407	0.00048	0.7601
	2.25	0.00407	0.22142	0.05914	0.88571	0.00401	0.24662	0.00049	0.85728
	2	0.0057	0.27093	0.05182	0.99454	0.00564	0.28513	0.0027	0.96266
	1.8	0.00707	0.29379	0.04799	1.07483	0.00704	0.30595	0.00393	1.04607

Parameters fitted of the χ' and χ'' magnetic susceptibility plot of compound **3.2** to a generalised Debye model at i) 2 K under varying dc fields, and ii) 600 Oe dc field at varying temperatures.

		χ'				χ''			
		τ (s)	α	χ_S	χ_T	τ (s)	α	χ_S	χ_T
Field (Oe)	**0**	0.00111	0.53695	0.91886	1.04752	0.00069	0.53694	0.00421	0.12744
	200	0.02993	0.63104	0	1.24034	0.02218	0.64635	0.00069	1.24703
	400	0.14658	0.58213	0	1.37171	0.08353	0.5345	0.00634	1.19864
	600	0.11493	0.38058	0.0124	1.11353	0.10518	0.34128	6.37E-05	1.02911
	800	0.10089	0.27302	0.00693	0.99252	0.10311	0.26125	0.00139	0.97156
	1000	0.08831	0.23136	0.00434	0.91336	0.09075	0.25142	0.00248	0.93631
	1200	0.0758	0.21916	0.00311	0.84559	0.07871	0.23236	0.13314	1.00079
	1400	0.06407	0.21712	0	0.78282	0.06709	0.25497	0.01257	0.84276
	1600	0.05409	0.22801	0	0.72757	0.05919	0.2673	0.00211	0.77952
	1800	0.04581	0.23763	0	0.67348	0.04931	0.30771	0.00551	0.74507
	2000	0.03753	0.23255	0	0.61524	0.04147	0.32042	0.00219	0.69545
	2200	0.03129	0.24149	0	0.56202	0.0344	0.31189	0.00416	0.62418
	2400	0.02663	0.23024	0	0.51816	0.02893	0.36106	0.00028	0.5975
	2600	0.02233	0.28606	0	0.48224	0.02622	0.37151	0.00341	0.5482
	2800	0.01825	0.28629	0	0.44075	0.02099	0.39442	0.00363	0.51605
	3000	0.01557	0.30476	0	0.40844	0.01856	0.41465	0.0024	0.47515
T (K)	**12**	6.76E-05	0.05607	0.0753	0.17657	4.62E-05	0	0	0.18322
	11	6.77E-05	0.01457	0	0.19166	6.37E-05	0.05312	0.00028	0.20767
	10	0.00010	0.0154	0	0.21151	0.00011	0	0	0.20433
	9	0.00017	0.0319	0	0.23631	0.00017	0.01644	0.00052	0.23576
	8	0.00029	0.02692	0.00531	0.26561	0.00028	0.01289	0.00274	0.25996
	7	0.00054	0.0134	0.00754	0.30225	0.00054	0.02638	0.00019	0.30243
	6	0.00114	0.04377	0.00378	0.35362	0.0011	0.06175	0.00021	0.35521
	5.5	0.00178	0.06709	0.00362	0.38591	0.00172	0.07455	0.0119	0.40143
	5	0.00298	0.07456	0.00456	0.42496	0.00289	0.08411	0.00335	0.4268
	4.5	0.00496	0.10822	0.00476	0.47253	0.00498	0.11156	0.00418	0.48001
	4	0.00918	0.13134	0.0111	0.53485	0.00905	0.14346	0.00139	0.53265
	3.5	0.0172	0.18355	0.0108	0.61705	0.0174	0.17718	0.00212	0.60279
	3	0.0336	0.26393	0.0101	0.73775	0.0335	0.2323	0.0414	0.74167
	2.8	0.0431	0.28486	0.0109	0.79064	0.0427	0.25991	0.00304	0.75923
	2.6	0.058	0.31882	0.0109	0.8704	0.054	0.28854	0.0442	0.86411
	2.4	0.0717	0.33359	0.0123	0.93473	0.0675	0.30252	0.00429	0.88385
	2.2	0.09492	0.36492	0.0111	1.03655	0.08607	0.3252	3.63E-05	0.9606
	2	0.13548	0.40264	0.00829	1.1764	0.1007	0.32072	0.0129	1.01858
	1.8	0.14117	0.396	0.014	1.19322	0.12397	0.35597	0.00175	1.1004

Parameters fitted of the χ' and χ'' magnetic susceptibility plot of compound **3.3** to a generalised Debye model at i) 2 K under varying dc fields, and ii) 600 Oe dc field at varying temperatures.

		χ'				χ''			
		τ (s)	α	χ_S	χ_T	τ (s)	α	χ_S	χ_T
Field (Oe)	**0**					0.00088	0.02333	0.15983	0.20106
	200					0.00382	0.15284	0.0163	0.63973
	400					0.01028	0.15647	0.00567	0.68192
	600					0.01621	0.16915	0.00358	0.70815
	800					0.01882	0.18001	0.0244	0.69826
	1000					0.02251	0.17282	0.0684	0.73465
	1200					0.02326	0.16937	0.00544	0.65927
	1400					0.02273	0.14802	0.02183	0.62919
	1600					0.0222	0.15642	0.00087	0.59035
	1800					0.02366	0.19228	0.00114	0.57021
	2000					0.02385	0.21182	0.0562	0.60826
	2200					0.02145	0.19725	0.00012	0.51695
	2400					0.0212	0.24282	0.0112	0.51538
	2600					0.01984	0.21511	0.11444	0.58145
	2800					0.01704	0.24751	0.05404	0.50198
	3000					0.01504	0.21818	0.03059	0.43723
T (K)	**8**	0	3.18E-05	0	0.19388	1.77E-05	0	0	0.2194
	7.5	0.02687	8.50E-05	0.12456	0.22135	4.85E-05	0.03512	0	0.21644
	7	0.04717	9.61E-05	0	0.25703	0.00011	0.03365	0.00288	0.26387
	6.5	0	0.00019	0.01592	0.27986	0.00017	0.05148	0.00972	0.29811
	6	0.0192	0.00031	0.00187	0.30776	0.00032	0.0305	0.00431	0.30875
	5.5	0.03536	0.00057	0.00459	0.34043	0.00056	0.03057	0.00036	0.34283
	5	0.03453	0.00111	0.00948	0.38108	0.00112	0.00112	0.00024	0.37549
	4.5	0.06359	0.00223	0.00393	0.43326	0.00229	0.04612	0.00166	0.42534
	4	0.09013	0.0049	0.00883	0.50457	0.00463	0.08561	1.96E-05	0.49727
	3.5	0.10231	0.00642	0.00714	0.53566	0.00631	0.10020	0.00442	0.53521
	3	0.12789	0.00845	0.00614	0.57598	0.00826	0.11623	0.00068	0.568
	2.8	0.13447	0.01091	0.00623	0.61878	0.01081	0.13855	0.01289	0.6226
	2.6	0.16372	0.01393	0.00215	0.67142	0.01371	0.16001	4.15E-07	0.66188
	2.4	0.16854	0.01683	0.00437	0.71529	0.01654	0.17313	0.02943	0.73355
	2.2	0.19535	0.01863	0.00074	0.74039	0.01815	0.1581	0.11263	0.83078
	2	0	3.18E-05	0	0.19388	1.77E-05	0	0	0.2194
	1.8	0.02687	8.50E-05	0.12456	0.22135	4.85E-05	0.03512	0	0.21644

Parameters fitted of the χ' and χ'' magnetic susceptibility plot of compound **3.4** to a generalised Debye model at i) 2 K under varying dc fields, and ii) 600 Oe dc field at varying temperatures.

		χ'				χ''			
		τ (s)	**α**	**χ_S**	**χ_T**	**τ (s)**	**α**	**χ_S**	**χ_T**
Field (Oe)	**0**	6.46E-24	0.99478	0	0.1	8.65E-07	0	0	0.10001
	200	0.00071	1	0.0139	0.10001	0	0	10	0.1
	400	8.30E+27	0.99961	0.01743	0.1	0	0	10	0.1
	600	0.00104	1	0.0235	0.10004	0	0	10	0.1
	800	3.81E+40	0.99205	0.0419	0.11199	0	0	10	0.1
	1000	1.48E-35	0.99962	0.0486	0.10223	0	0	10	0.1
	1200	0	0	0	0.10101	5.61E-06	0	2.87E-05	0.10022
	1400	0.00012	0	0	0.28805	0.00019	0	0.00199	0.31393
	1600	0.00092	0.11423	0.0204	0.58574	0.00113	0.17114	0.0362	0.65871
	1800	0.00128	0.2578	0	0.62342	0.00121	0.27624	0.00051	0.65269
	2000	0.00115	0.25022	0	0.56541	0.00118	0.30217	0.00411	0.59844
	2200	0.00125	0.30777	0	0.55861	0.00108	0.30757	0.0113	0.57156
	2400	0.00104	0.3611	0	0.50987	0.001	0.33426	0.00024	0.52292
	2600	0.00106	0.31763	0	0.45915	0.00085	0.35622	0.00187	0.50603
	2800	0.00097	0.17271	0.03251	0.39381	0.00078	0.3456	1.62E-05	0.45308
	3000	0.00144	0.48435	0	0.45512	0.00078	0.34684	0.00997	0.42893
T (K)	**8**	0	5.13E-19	10	0.24176	1.28E-05	0.03	0	0.51907
	7.5	0.00013	0	0.206	0.2585	3.62E-05	0.00185	0	0.27865
	7	5.48E-05	0.04851	0.0603	0.27586	8.28E-05	0	1.14E-10	0.1813
	6.5	6.73E-05	0.04423	0	0.29898	8.35E-05	0	0.00079	0.25237
	6	0.00011	0.01304	0.0756	0.31948	9.80E-05	0.02269	0.00148	0.29089
	5.5	0.00015	0.00482	0.0693	0.34902	0.00014	0.04027	0.00058	0.3191
	5	0.00020	0.02248	0.0598	0.38319	0.00018	0.0561	0.0252	0.38945
	4.5	0.00025	0.09169	0.0301	0.43042	0.00025	0.06882	0.0248	0.4211
	4	0.00036	0.09316	0.0401	0.47815	0.00034	0.12655	0.00082	0.47274
	3.5	0.00047	0.14016	0.0131	0.5423	0.00046	0.15364	0.00771	0.55081
	3	0.00065	0.17513	0.00185	0.626	0.00067	0.17678	0.00069	0.62442
	2.8	0.00075	0.17636	0	0.66601	0.00076	0.19009	0.00882	0.67933
	2.6	0.00089	0.1864	0	0.71135	0.00090	0.18448	0.00032	0.71472
	2.4	0.00105	0.18745	0	0.76185	0.00106	0.19038	0.00042	0.76426
	2.2	0.00127	0.20375	0	0.82273	0.00128	0.18576	0.0163	0.83518
	2	0.00149	0.18971	0	0.86442	0.00149	0.18444	0.00046	0.86668
	1.8	0.0017	0.19149	0	0.9035	0.00171	0.19666	0.00027	0.91471

8 HYDROPHOSPHINATION DATA

IMe_4 catalysed hydrophosphination of alkenes with PPh_2H.[a]

Entry	Alkene	Conversion (%)[b]	Hydrophosphination product (%) of all products
1	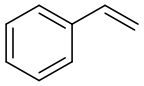	82	93
2[c]	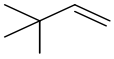	10	0[d]
3[c]	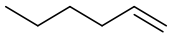	11	0[d]

[a] Conditions: IMe_4 (0.04 mmol), alkene (0.40 mmol) and PPh_2H (0.44 mmol), THF (0.5 mL), 298 K, 2 hrs. [b] Based on phosphine consumption quantified by integration of inverse-gated $^{31}P\{^1H\}$ NMR spectra. [c] 24 hr reaction. [d] Only dehydrocoupled product formed.

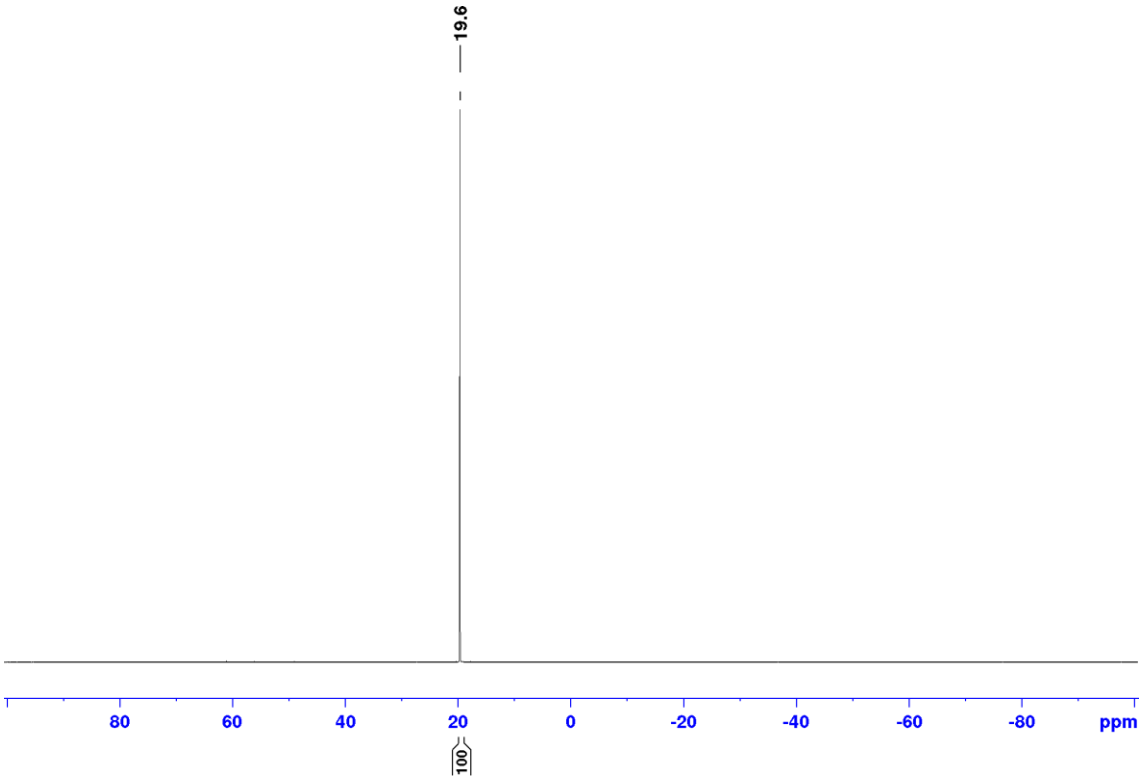

Figure A8.1 Inverse-gated $^{31}P\{^1H\}$ NMR spectrum (THF, 202 MHz, 298 K) of attempted I^{t}Bu (10 mol%) catalysed hydrophosphination of PhC≡CH with P^{t}Bu$_2$H.